

**Measurement of Z -Boson Production in Pb+Pb and $p + p$ Collisions
via the Electron and Muon Decay Channels at $\sqrt{s_{NN}} = 2.76$ TeV**

By

MICHAEL DAVID GARDNER

B.S. (Westmont College, Santa Barbara) 2009

M.S. (University of California, Davis) 2010

DISSERTATION

Submitted in partial satisfaction of the requirements for the degree of

DOCTOR OF PHILOSOPHY

in

Physics

in the

OFFICE OF GRADUATE STUDIES

of the

UNIVERSITY OF CALIFORNIA

DAVIS

Approved:

Prof. Manuel Calderón de la Barca Sánchez, Chair

Prof. Daniel Cebra

Prof. Ramona Vogt

Committee in Charge

2014

Measurement of Z -Boson Production in Pb+Pb and $p + p$ Collisions via the Electron and Muon Decay Channels at $\sqrt{s_{NN}} = 2.76$ TeV

Abstract

Experiments over the last decade at the Relativistic Heavy Ion Collider (RHIC) at the Brookhaven National Laboratory have yielded evidence for the formation of the new state of matter called the quark-gluon plasma (QGP). Normally, quarks (and their associated gluons) are found only in colorless doublets (mesons) or triplets (baryons), but when raised above the cross-over threshold at a temperature of ~ 175 MeV, a strongly-coupled partonic medium of asymptotically free quarks and gluons is expected to form. The focus of heavy-ion physics at both the RHIC and Large Hadron Collider (LHC) experiments has been to study physical processes that allow for a better grasp of the properties of this medium.

Because of the large center-of-mass energy per nucleon pair ($\sqrt{s_{NN}}$) of 2.76 TeV in Pb+Pb collisions at the LHC and substantial delivered integrated luminosities, the study of new processes in nucleus-nucleus collisions has become possible. One of those processes is Z -boson production, which due to the Z -boson not interacting strongly, being produced in hard collisions and having a decay channel that does not interact with the QGP, can act as a control in understanding the cold nuclear matter effects present in heavy-ion collisions.

This dissertation presents the measurement of the production of Z bosons in the dimuon and dielectron decay channels in Pb+Pb and $p + p$ collisions at $\sqrt{s_{NN}} = 2.76$ TeV obtained by the CMS experiment at the LHC. The analysis is based on the data sample collected during the Pb+Pb run in 2011, which corresponds to an integrated luminosity of $150 \mu\text{b}^{-1}$ and on the $p + p$ data sample collected in 2013, at the same center-of-mass energy, with an integrated luminosity of 5.4 pb^{-1} . The ratio of Pb+Pb to $p + p$ yields, scaled by the number of incoherent nucleon-nucleon collisions, R_{AA} , is expected to be equal to unity if there are no nuclear effects modifying the production of the Z boson in the Pb+Pb collisions.

The R_{AA} for centrality-integrated Z -boson production is found to be 1.06 ± 0.05 (stat) ± 0.08 (syst) in the dimuon channel and 1.02 ± 0.08 (stat) ± 0.15 (syst) in the dielectron channel, and shows no nuclear modification across the rapidity, transverse momentum and centrality bins measured. This result demonstrates that the binary-collision scaling is seen to hold in the kinematic region studied, which is expected for a colorless probe that is unaffected by a deconfined QGP. It also opens avenues to study processes that are strongly modified by the QGP, by using Z production as a control.

Para minha linda, paciente e generosa Emily.
Eu sei que você me ama, mesmo se voc nunca lês isto!

Foreword

Just as when you take ice, and heat it up, it will go from a solid to a liquid, to a gas, and then at some point to plasma, you can change the state of matter at the nuclear level. When you take lead particles, accelerate them to high speeds and energies, and collide them, the extremely high energy and density in the center of the collision forms a new state of matter called the “Quark-Gluon Plasma” (QGP) and can be thought of as a “soup of quarks and gluons.”

Usually quarks and gluons (called partons) are only found bound together inside of a nucleon or a type of particle called a meson, but in the QGP you can see free partons. This medium is extremely hot (2×10^{12} degrees Kelvin), and extremely dense (10 times denser than a nucleus), and studying the interesting processes that occur in the medium, require controls in order to understand what would happen if no QGP was formed. One of the controls needed is to measure the production of a particle known as a Z boson, which does not interact with the QGP medium.

This dissertation is focused on detailing the study of Z production as a control for the QGP, using the data from the Compact Muon Solenoid (CMS) detector at the Large Hadron Collider (LHC), as part of the heavy-ion group here. For my research, I take the data produced in these collisions, and study the effects that these Hard Probes experience when they interact with the QGP medium.

The results of my analysis confirm predictions, and show that the effects of the QGP on Z s produced in collisions and passing through the QGP are small, and they help to set limits on the level of the effect expected on other signals measured at the LHC. This opens the doors for new analyses that can use this result as a baseline in understanding the properties of the QGP matter.

Acknowledgments

This Dissertation was a result of a great deal of work over 5 years, and so much support from others. To start, I want to thank some of the people who were part of this journey.

Manuel, I wouldn't have made it through grad school without your encouragement and support. There are so many times I felt frustrated, or stuck, and you always had time to sit down, answer questions I was worried were too basic, and go through next steps with me. Dan, you walked me through my first quarter of TAing and lead TAing Physics 7, and showed me how to embrace the different. Thank you for all of the long TA and research conversations. Dan and Manuel, thank you for your generosity through the parties, barbecues, dinners, and outings we have had throughout the past 5 years.

Wes Loewer, thank you for introducing me to Calculus and Physics. You were right when you said I would never look at the world the same again! Michael, Ken and Warren, thank you for how you challenged me to grow while learning Physics. And Warren, I am so thankful for the summers of research at Westmont and MSU!

To the CMS heavy-ion and dilepton group, thank you for the support and opportunities during research. Anna and Lamia, it has been a pleasure working on analyses. Mihee and Dong Ho, thank you for the endless Skype help sessions. Shalhout, Justin, Joe, and Dustin, I'm glad I got to meet and work with you while in Geneva. Torsten and Camelia, without the two of you, I still wouldn't know which globaltag and CMSSW version to use.

Rylan, Evan, and Tony! You have been there to challenge me or help me as I have needed it. Rylan, thank you for your CMS expertise, and all of your help while moving to Geneva! Guillermo and Jorge, thanks for your help on both sides of the grad school transition. Chris and Chad, I always looked forward to coming into the office, and getting help for random ROOT and computer questions.

Bret, Kent, and Andy, playing games on weekends has been so great. Kevin, Mccullen, Chris, Aaron, Jiayin, and the rest of our grad school class, you have all been great encouragement throughout. To all of the members of our UCC family, you have helped us make Davis home.

Mom, Dad, and Jonathan, thank you for always believing in me more than I believe in myself.

You have always helped to ground me and given me the bigger perspective when I have gotten tunnel vision. Pop and Dot, I'm so glad that Emily and I ended up in Davis for grad school. The first year was so tough, and having Sunday lunches and dinner parties at your place have made such a big difference. Jeane and B, I'm so glad that the two of you moved to Tiburon! It has been great getting to know you more, and getting to join you in so many trips you have taken Emily and I on. Thank you for all of your generosity!

Thank you Emily for everything you've done for me over the last 5 year. There's no one I would rather have gone on our Geneva journey with! Thank you for the ways that you've encouraged me, balanced me out, and given me grace during the rough weeks.

Andy finally, thank you God for a beautiful world, and the creativity you have given us to learn about it and explore it in new ways.

Contents

| | | |
|----------|--|-----------|
| 1 | Introduction | 1 |
| 2 | Theory Overview | 4 |
| 2.1 | The Standard Model of Particle Physics | 4 |
| 2.2 | Electroweak Theory | 6 |
| 2.3 | QCD | 7 |
| 2.4 | Formation of the QGP | 8 |
| 2.4.1 | Heavy Quarkonia Suppression | 9 |
| 2.4.2 | Away-side Jet Suppression | 10 |
| 2.5 | Electroweak Probes and the QGP at the LHC | 12 |
| 2.5.1 | Glauber Model | 13 |
| 2.5.2 | Cold Nuclear Matter Effects | 13 |
| 2.5.3 | Heavy Electroweak Probes: A Control Experiment | 14 |
| 2.6 | Z Bosons in Heavy-Ion Collisions at the LHC | 15 |
| 2.6.1 | Z Boson Production and Decay | 15 |
| 2.6.2 | Initial State Modification | 16 |
| 3 | Experimental Facilities | 20 |
| 3.1 | LHC | 20 |
| 3.1.1 | LHC Layout and Design | 20 |
| 3.1.2 | LHC Injection Chain | 22 |
| 3.1.3 | LHC as a Heavy-Ion Collider | 24 |

| | | |
|----------|--|-----------|
| 3.2 | The CMS Detector | 24 |
| 3.2.1 | CMS Coordinate System | 26 |
| 3.2.2 | Inner Tracker | 27 |
| 3.2.3 | Electromagnetic Calorimeter | 29 |
| 3.2.4 | Hadronic Calorimeter | 31 |
| 3.2.5 | The Magnet | 31 |
| 3.2.6 | Muon Systems | 32 |
| 3.2.7 | Forward Detectors | 39 |
| 4 | Data Selection, Simulation and Reconstruction | 42 |
| 4.1 | Triggering | 42 |
| 4.1.1 | The Muon Trigger System | 45 |
| 4.1.2 | The Electron Trigger System | 51 |
| 4.2 | Event Selection and Cleaning | 53 |
| 4.2.1 | Event Selection and Cleaning in Pb+Pb | 53 |
| 4.2.2 | Event Selection and Cleaning in $p + p$ | 55 |
| 4.3 | Centrality Determination | 56 |
| 4.4 | Simulation | 59 |
| 4.5 | Lepton Reconstruction | 61 |
| 4.5.1 | Muon Reconstruction | 61 |
| 4.5.2 | Electron Reconstruction | 63 |
| 5 | Analysis of $Z \rightarrow l^+l^-$ in Pb+Pb at $\sqrt{s_{NN}} = 2.76$ TeV | 65 |
| 5.1 | Lepton Selection and Identification | 66 |
| 5.1.1 | Muon Identification | 66 |
| 5.1.2 | Electron Identification | 68 |
| 5.2 | Resolution Corrections | 74 |
| 5.2.1 | Resolution Study | 75 |
| 5.2.2 | Invariant Mass Comparison | 79 |

| | | |
|----------|--|------------|
| 5.2.3 | Energy Correction | 81 |
| 5.2.4 | Oversmearing of the MC | 82 |
| 5.2.5 | Unfolding | 86 |
| 5.3 | Raw Yields | 88 |
| 5.3.1 | Raw Yields in Dimuon Channel | 89 |
| 5.3.2 | Raw Yields in Dielectron Channel | 89 |
| 5.4 | Acceptance and Efficiency | 89 |
| 5.4.1 | Acceptance and Efficiency Corrections for Dimuons | 91 |
| 5.4.2 | Acceptance and efficiency corrections for dielectrons | 92 |
| 5.5 | Uncertainties | 93 |
| 5.5.1 | Background Studies | 96 |
| 5.5.2 | Acceptance and Efficiency Uncertainty from Shape Variation | 96 |
| 5.5.3 | Uncertainty on T_{AA} | 101 |
| 5.6 | Tag and Probe Method | 101 |
| 5.6.1 | TNP Method for Muons | 102 |
| 5.6.2 | TNP Method for Electrons | 111 |
| 6 | Analysis of $Z \rightarrow l^+l^-$ in $p + p$ at $\sqrt{s} = 2.76$ TeV | 117 |
| 6.1 | Lepton Selection and Identification | 118 |
| 6.1.1 | Muon Identification | 118 |
| 6.1.2 | Electron Identification | 119 |
| 6.2 | Resolution Corrections | 121 |
| 6.2.1 | Resolution Study | 124 |
| 6.2.2 | Invariant Mass Comparison | 127 |
| 6.2.3 | Energy Correction | 129 |
| 6.2.4 | Oversmearing of the MC | 129 |
| 6.2.5 | Unfolding | 130 |
| 6.3 | Raw Yields | 131 |
| 6.3.1 | Raw Yields in Dimuon Channel | 132 |

| | | |
|----------|---|------------|
| 6.3.2 | Raw Yields in Dielectron Channel | 132 |
| 6.4 | Acceptance and Efficiency | 133 |
| 6.4.1 | Efficiency Corrections for Dimuons | 133 |
| 6.4.2 | Efficiency Corrections for Dielectrons | 134 |
| 6.5 | Uncertainties | 134 |
| 6.5.1 | Background Studies | 135 |
| 6.6 | Tag and Probe Method | 135 |
| 6.6.1 | TNP Method for Muons | 137 |
| 6.6.2 | TNP Method for Electrons | 140 |
| 7 | Results and Discussion | 145 |
| 7.1 | Z Yields in Pb+Pb Collisions vs. p_T , y , and Centrality | 145 |
| 7.2 | Z-Boson Production Cross Section in $p + p$ Collisions | 147 |
| 7.3 | Nuclear Modification Factor | 150 |
| 7.4 | Combination of the Results | 150 |
| 8 | Conclusion | 157 |
| A | Mass and p_T resolution distributions | 159 |
| A.1 | Mass Resolution Plots - Pb+Pb | 159 |
| A.2 | Mass Resolution Plots - $p + p$ | 162 |
| A.3 | Transverse Momentum Resolution Plots - Pb+Pb | 164 |
| A.4 | Transverse Momentum Resolution Plots - $p + p$ | 166 |
| B | Tag and Probe | 168 |
| B.1 | Tag and Probe Mass Plots - Muons in Pb+Pb | 169 |
| B.2 | Tag and Probe Mass Plots - Muons in $p + p$ | 175 |
| B.3 | Tag and Probe Mass Plots - Electrons in Pb+Pb | 181 |
| B.4 | Tag and Probe Mass Plots - Electrons in $p + p$ | 187 |

List of Figures

| | | |
|------|--|----|
| 2.1 | The Standard Model of elementary particles. | 5 |
| 2.2 | QCD coupling constant as a function of energy. | 8 |
| 2.3 | Di-hadron correlations in STAR in $p + p$, d+Au and Au+Au collisions. | 11 |
| 2.4 | Di-jet imbalance in CMS: signature for away-side jet suppression. | 12 |
| 2.5 | Nuclear PDFs at 10 GeV and 10 TeV. | 15 |
| 2.6 | Production and decay of the Z Feynman Diagrams. | 16 |
| 2.7 | Nuclear modification general line shape in EPS09. | 17 |
| 2.8 | EPS09 NPDFs based on DIS data. | 18 |
| 3.1 | Schematic and photographic view of the LHC. | 21 |
| 3.2 | CERN experiments and LHC injection chain path. | 23 |
| 3.3 | Schematic of the CMS detector. | 25 |
| 3.4 | View of z and η range of the CMS detector. | 27 |
| 3.5 | Particle paths through CMS detector. | 29 |
| 3.6 | ECAL crystals with photodetectors attached. | 30 |
| 3.7 | Solenoid magnet being inserted into CMS. | 33 |
| 3.8 | Picture of me in front of an opened up CMS. | 34 |
| 3.9 | The muon p_T resolution as a function of p_T | 35 |
| 3.10 | Drift tube chamber cell. | 36 |
| 3.11 | Layout of the double gap in an RPC module. | 37 |
| 3.12 | Side view of the CSC stations in CMS. | 38 |

| | | |
|------|---|----|
| 3.13 | Picture of the full CSC ME2 station. | 39 |
| 3.14 | Layout of CSC chambers. | 40 |
| 3.15 | Forward detector layout in CMS. | 41 |
| 4.1 | Higgs $\rightarrow ZZ$ candidate event in $p + p$ collisions at $\sqrt{s} = 8$ TeV in CMS. | 44 |
| 4.2 | Central Pb+Pb collision at $\sqrt{s_{NN}} = 2.76$ TeV in CMS. | 44 |
| 4.3 | $\Upsilon \rightarrow \mu^+\mu^-$ candidate event in Pb+Pb collisions at $\sqrt{s_{NN}} = 2.76$ TeV in CMS. | 47 |
| 4.4 | $W \rightarrow \mu\nu$ candidate event in Pb+Pb collisions at $\sqrt{s_{NN}} = 2.76$ TeV in CMS. | 48 |
| 4.5 | $Z \rightarrow \mu^+\mu^-$ candidate event in Pb+Pb collisions at $\sqrt{s_{NN}} = 2.76$ TeV in CMS. | 49 |
| 4.6 | Dimuon invariant mass for Pb+Pb collisions at $\sqrt{s_{NN}} = 2.76$ TeV in CMS. | 50 |
| 4.7 | $Z \rightarrow e^+e^-$ candidate event in Pb+Pb collisions at $\sqrt{s_{NN}} = 2.76$ TeV in CMS. | 52 |
| 4.8 | Centrality determination in CMS based on E_T deposit in the HF. | 57 |
| 4.9 | Centrality distribution of the muon triggered events. | 59 |
| 4.10 | Distribution of $Z p_T$ for $\simeq 500,000$ Z bosons generated in PYTHIA. | 61 |
| 5.1 | Muon quality distributions in Pb+Pb: MC vs. data. | 69 |
| 5.2 | Electron quality distributions in Pb+Pb: MC vs. data. | 72 |
| 5.3 | Electron quality distributions in Pb+Pb (sideband subtracted): MC vs. data. | 73 |
| 5.4 | Decomposition of dilepton p_T into a_l and a_t | 75 |
| 5.5 | a_t vs. a_l distribution for dimuons in Pb+Pb in MC and data. | 76 |
| 5.6 | Mean and RMS of a_t and a_l for dimuons in Pb+Pb for MC and data. | 77 |
| 5.7 | Resolution in Pb+Pb as a function of Gen p_T for dimuons from Z bosons. | 77 |
| 5.8 | Mean and RMS of a_t and a_l for dielectrons in Pb+Pb for MC and data. | 78 |
| 5.9 | Resolution in Pb+Pb as a function of Gen p_T for dielectrons from Z bosons. | 79 |
| 5.10 | $Z \rightarrow \mu^+\mu^-$ invariant mass in Pb+Pb for MC and data. | 80 |
| 5.11 | Original $Z \rightarrow e^+e^-$ invariant mass in Pb+Pb for MC and data. | 81 |
| 5.12 | Reconstructed p_T compared to generated p_T for dielectrons in Pb+Pb. | 82 |
| 5.13 | Energy scale and resolution of reconstructed electrons. | 83 |
| 5.14 | $Z \rightarrow e^+e^-$ invariant mass after energy corrections in Pb+Pb for MC and data. | 83 |

| | | |
|------|--|-----|
| 5.15 | Kolmogorov-Smirnov statistic illustration. | 84 |
| 5.16 | P-value from the X^2 test as a function of energy shift. | 85 |
| 5.17 | Final $Z \rightarrow e^+e^-$ invariant mass in Pb+Pb for MC and data. | 86 |
| 5.18 | Generated vs. Reconstructed Z boson p_T in the dimuon channel in Pb+Pb. | 87 |
| 5.19 | Generated vs. Reconstructed Z boson p_T in the dielectron channel in Pb+Pb. | 88 |
| 5.20 | Acceptance for dimuons in Pb+Pb as a function of Z p_T and y | 91 |
| 5.21 | Efficiency for dimuons in Pb+Pb as a function of Z p_T , y , and centrality. | 91 |
| 5.22 | Acceptance for dielectrons in Pb+Pb as a function of Z p_T and y | 92 |
| 5.23 | Efficiency for dielectrons in Pb+Pb as a function of Z p_T , y , and centrality. | 92 |
| 5.24 | Invariant mass of dielectrons in MC, showing SS and OS pairs. | 93 |
| 5.25 | Charge misidentification rate as a function of η , p_T , and centrality. | 94 |
| 5.26 | Background systematic estimation for dimuons in Pb+Pb. | 97 |
| 5.27 | Background systematic estimation for dielectrons in Pb+Pb. | 97 |
| 5.28 | Variation of p_T shapes for generated dimuons in Pb+Pb. | 98 |
| 5.29 | Variation of y shapes for generated dimuons in Pb+Pb. | 99 |
| 5.30 | Variation of p_T shapes for generated dielectrons in Pb+Pb. | 99 |
| 5.31 | Variation of y shapes for generated dielectrons in Pb+Pb. | 100 |
| 5.32 | Single muon triggering efficiency in Pb+Pb for dimuon trigger. | 104 |
| 5.33 | Single muon triggering efficiency in Pb+Pb for single and di-muon trigger. | 106 |
| 5.34 | Single muon ID efficiency in Pb+Pb. | 108 |
| 5.35 | Gen vs. Standalone muon p_T comparison in Pb+Pb. | 110 |
| 5.36 | Plot showing p_T dependent invariant mass bump for Standalone muons. | 110 |
| 5.37 | Single muon tracking efficiency in Pb+Pb. | 111 |
| 5.38 | Single electron triggering efficiency in Pb+Pb. | 113 |
| 5.39 | Single electron ID efficiency in Pb+Pb. | 115 |
| 5.40 | Single electron tracking efficiency in Pb+Pb. | 116 |
| 6.1 | Muon quality distributions in $p + p$: MC vs. data. | 120 |
| 6.2 | Electron quality distributions in $p + p$: MC vs. data. | 122 |

| | | |
|------|--|-----|
| 6.3 | Electron quality distributions in $p + p$ (sideband subtracted): MC vs. data. | 123 |
| 6.4 | Mean and RMS of a_t and a_l for dimuons in $p + p$ for MC and data. | 125 |
| 6.5 | Resolution in $p + p$ as a function of Gen p_T for dimuons from Z bosons. | 125 |
| 6.6 | Mean and RMS of a_t and a_l for dielectrons in $p + p$ for MC and data. | 126 |
| 6.7 | Resolution in $p + p$ as a function of Gen p_T for dielectrons from Z bosons. | 127 |
| 6.8 | $Z \rightarrow \mu^+ \mu^-$ invariant mass in $p + p$ for MC and data. | 128 |
| 6.9 | $Z \rightarrow e^+ e^-$ invariant mass in $p + p$ for MC and MC and data. | 129 |
| 6.10 | Generated vs. Reconstructed Z boson p_T in the dimuon channel in $p + p$ | 130 |
| 6.11 | Generated vs. Reconstructed Z boson p_T in the dielectron channel in $p + p$ | 131 |
| 6.12 | Efficiency for dimuons in $p + p$ as a function of Z p_T , and y | 133 |
| 6.13 | Efficiency for dielectrons in $p + p$ as a function of Z p_T , and y | 134 |
| 6.14 | Background systematic estimation for dimuons in $p + p$ | 136 |
| 6.15 | Background systematic estimation for dielectrons in $p + p$ | 136 |
| 6.16 | Single-muon triggering efficiency in $p + p$ | 138 |
| 6.17 | Single-muon ID efficiency in $p + p$ | 139 |
| 6.18 | Single-muon tracking efficiency in $p + p$ | 140 |
| 6.19 | Single-electron triggering efficiency in $p + p$ | 142 |
| 6.20 | Single-electron ID efficiency in $p + p$ | 143 |
| 6.21 | Single-electron tracking efficiency in $p + p$ | 144 |
| 7.1 | Centrality dependence of the Z -boson production yield in Pb+Pb collisions. | 146 |
| 7.2 | Z -boson production yield in Pb+Pb collisions as a function of p_T and y | 148 |
| 7.3 | Z -boson production cross section in $p + p$ collisions as a function of p_T and y | 149 |
| 7.4 | R_{AA} for Z -boson production as a function of y , p_T , and centrality. | 151 |
| 7.5 | $Z \rightarrow l^+ l^-$ yield in Pb+Pb collisions as a function of y , p_T , and centrality. | 154 |
| 7.6 | $Z \rightarrow l^+ l^-$ cross section in $p + p$ collisions as a function of y , and p_T | 155 |
| 7.7 | R_{AA} for $Z \rightarrow l^+ l^-$ as a function of y , p_T , and centrality. | 156 |

List of Tables

| | | |
|-----|--|-----|
| 4.1 | Table of Centrality parameters based on Glauber model. | 58 |
| 5.1 | Quality cuts applied to global muons. | 68 |
| 5.2 | Quality cuts applied to global electrons. | 71 |
| 5.3 | Raw yield of Z s in dimuon channel in Pb+Pb in p_T , y , and centrality bins. | 89 |
| 5.4 | Raw yield of Z s in dielectron channel in Pb+Pb in p_T , y , and centrality bins. | 90 |
| 5.5 | Systematic uncertainty values for $Z \rightarrow \mu^+\mu^-$ and $Z \rightarrow e^+e^-$ in Pb+Pb. | 95 |
| 5.6 | Acc and eff uncertainties due to shape variation for dimuons in Pb+Pb. | 99 |
| 5.7 | Acc and eff uncertainties due to shape variation for dielectrons in Pb+Pb. | 100 |
| 5.8 | Uncertainty on T_{AA} | 101 |
| 6.1 | Quality cuts applied to global muons. | 118 |
| 6.2 | Quality cuts applied to global electrons. | 121 |
| 6.3 | Raw yield of Z bosons in dimuon channel in $p + p$ in p_T and y bins. | 132 |
| 6.4 | Raw yield of Z bosons in dielectron channel in $p + p$ in p_T and y bins. | 132 |
| 6.5 | Systematic uncertainty values for $Z \rightarrow \mu^+\mu^-$ and $Z \rightarrow e^+e^-$ in $p + p$ | 135 |
| 7.1 | R_{AA} for $Z \rightarrow l^+l^-$ processes as a function of y , p_T , and centrality. | 152 |

Chapter 1

Introduction

The Z boson was first observed by the UA1 and UA2 experiments at CERN over thirty years ago in proton-antiproton collisions at a center-of-mass energy of 540 GeV [1, 2]. Since then, its properties have been characterised in detail by a succession of collider experiments [3–10]. These properties have been well measured at different center-of-mass energies in electron-positron, proton-proton, and proton-antiproton collisions, and those measured values play an important role in this dissertation:

- **Decay channels:** the fact that the Z -boson decays into lepton pairs (dileptons) makes the measurement of the Z accessible to the CMS detector in both the muon and electron decay channels.
- **Mass:** the mass of the Z ($m_Z \approx 90 \text{ GeV}/c^2$) sets the momentum scale for the daughter leptons ($p_T^{\mu e}$) measured in the detector.
- **Decay width:** since the decay width of the Z boson is comparable to the detector resolution, the shape measured in real data, and generated in simulated data, needs to be specified by physics as well as detector contributions.

Once produced, electroweak bosons such as the Z -boson decay with a typical lifetime of $0.1 \text{ fm}/c$, which is well within the medium formed in nucleus-nucleus collisions, whose transverse length is on the order of 10 fm . Leptonic decays are thus of particular interest since leptons pass through the

medium being probed without strong interaction, regardless of whether it is partonic or hadronic. Dileptons from Z bosons can thus serve as an *in situ* control for the processes expected to be heavily modified in the QGP, such as quarkonium production or the production of an opposite-side jet in Z + jet processes [11–13]. However, in heavy-ion collisions, Z -boson production can be affected by initial-state effects. The modification of the yield in heavy-ion collisions is expected to be about 3% due to the combination of the following: isospin effects resulting from the proton-neutron (or u - d quark) ratio not being equal to one in the Pb nuclei [14], and multiple scattering and energy loss of the initial partons [15]. In addition, the nuclear modification of parton distribution functions (PDF) can lead to changes on the order of 5% in the observed Z -boson yield in Pb+Pb collisions, depending on the dilepton rapidity [16].

Based on the first Pb+Pb collisions at the LHC, with an integrated luminosity of $7.2 \mu\text{b}^{-1}$, the Compact Muon Solenoid (CMS) collaboration at the LHC reported first results on the $Z \rightarrow \mu^+\mu^-$ [17], $W^\pm \rightarrow \mu^\pm\nu$ [18] and isolated photon [19] production in Pb+Pb collisions. These results showed that within the errors of the experiments, electroweak bosons are essentially unmodified by the QGP.

The measurement of the Z was a proof-of-principle measurement with a statistical uncertainty of 25% for the centrality-integrated point. In late 2011, CMS collected a factor of 20 times more Pb+Pb collision data at $\sqrt{s_{NN}} = 2.76 \text{ TeV}$, corresponding to an integrated luminosity of about $150 \mu\text{b}^{-1}$. In 2013, CMS recorded at the same center-of-mass energy, a total integrated luminosity of 5.4 pb^{-1} of $p + p$ data. By using these higher-statistics data, more detailed studies as a function of transverse momentum (p_T), rapidity (y), and collision centrality can be made.

It is the purpose of this thesis to use these two data sets to measure the nuclear modification factor (R_{AA}), defined as the ratio of Pb+Pb and $p + p$ yields scaled by the number of incoherent nucleon-nucleon collisions, for the Z boson as a function of p_T , y , and collision centrality. The electron channel is used for the first time to measure Z -boson production in heavy-ion collisions in CMS, and, along with the muon channel, this measurement will provide a measurement of the cold nuclear matter (CNM) effects present in heavy-ion collisions for the kinematic regions studied.

This thesis is organized in the following manner. In Chapter 2, the underlying theory is presented including the production of electroweak probes and the study of the formation of the Quark-Gluon Plasma. Chapter 3 covers the Experimental facilities of the LHC as well as the CMS detector. Chapter 4 covers the data collection and reconstruction process, as well as the creation of the simulated datasets used in the analysis. Chapter 5 focuses on the analysis of the Z decaying to the dimuon and dielectron channels in Pb+Pb collisions, and Chapter 6 covers the analysis in $p + p$ collisions. The results are discussed in Chapter 7, including the measurement of the R_{AA} and the combination of the two channels, and the thesis ends with the conclusions in Chapter 8.

Chapter 2

Theory Overview

2.1 The Standard Model of Particle Physics

Physics is essentially the study of forces. Throughout this past century, physicists have studied four forces: the strong force, weak force, electromagnetic force and gravitational force. In the second half of the 20th century, physicists developed the Standard Model of particle physics in an effort to combine the strong, weak and electromagnetic forces in a simple and meaningful way. This model, which has been around in its current form since the 1970s, has been extremely successful, not only in explaining the phenomena we see in the universe, but also in predicting the presence of new particles and phenomena.

At its essence, the Standard Model states that the strong, weak and electromagnetic interactions occur between spin- $\frac{1}{2}$ particles by exchanging spin-one bosons amongst themselves. Figure 2.1 shows the structure of the Standard Model of particle physics, with the spin-half particles called *fermions* on the left and the integer spin particles called *bosons* on the right. The fermions are split into two categories: quarks on the top, and leptons on the bottom. The quarks interact strongly via gluons, electromagnetically through photons, and weakly via the massive electroweak bosons (W^\pm and Z -bosons). Since leptons do not carry color charge (the charge associated with the strong force), they do not interact strongly. The leptons can interact weakly, but only the electron, muon and tau leptons interact electromagnetically, as they carry electric charge.

The final boson which is left on its own is the Higgs boson. It is an excitation in the Higgs field, whose interaction provides particles with their various masses [20–23].

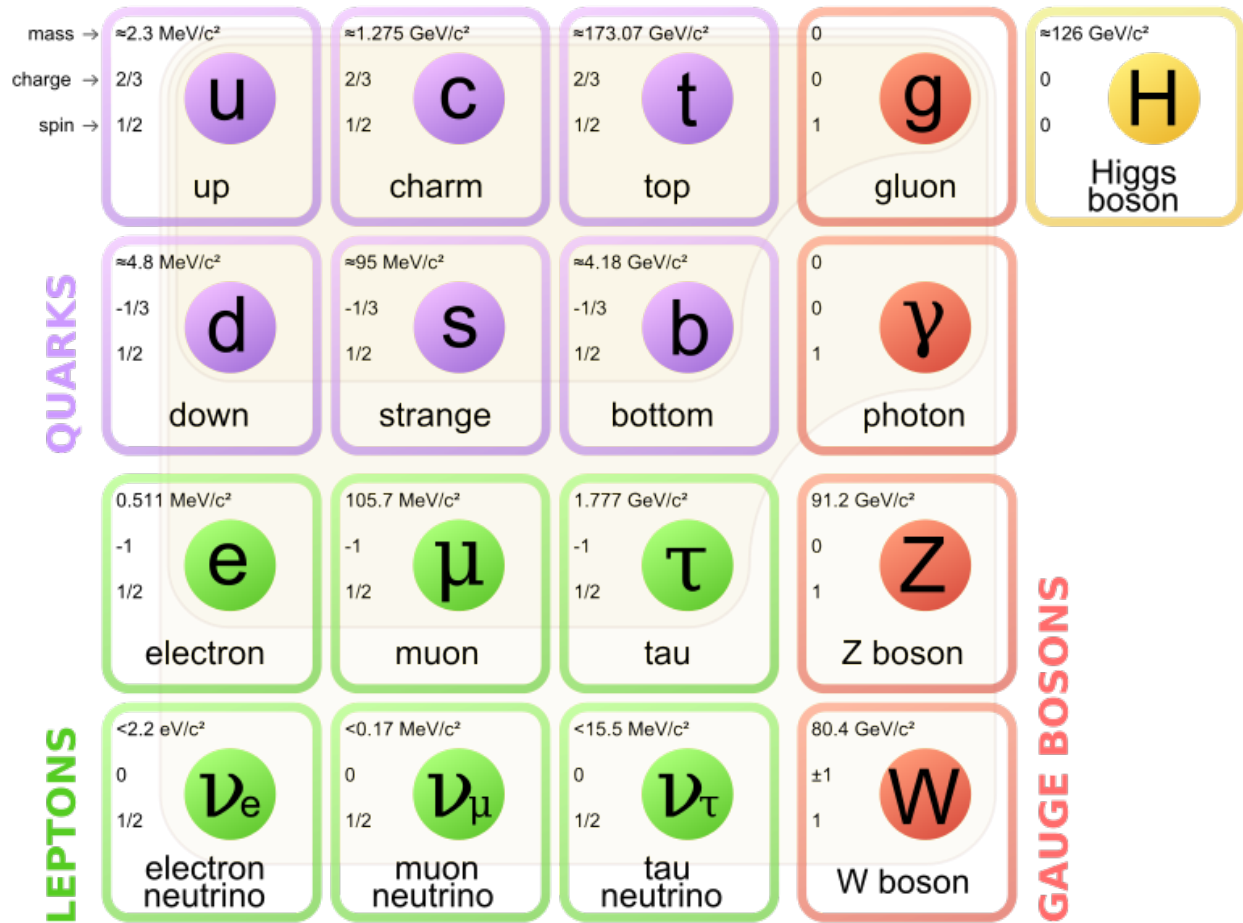


Figure 2.1: The Standard Model of elementary particles [24].

Although the electroweak theory is well understood and predictive in the sense that theory and experiment agree very well, it is more challenging to develop models for the strong force. For this reason, the study of the strongly interacting Quark-Gluon Plasma (QGP) medium is very challenging, and severely limited by the complexity of the strong force. In order to simplify the study of the properties the QGP, it is important to first study well-understood and controlled signals such as the heavy electroweak bosons passing through the strongly-interacting medium. To understand Z-boson production in the QGP, an understanding of Electroweak Theory and Quantum Chromodynamics (QCD) is necessary.

2.2 Electroweak Theory

The electroweak theory was proposed as a unification of the electromagnetic and the weak interactions by Glashow, Salam, and Weinberg, for which they received the Nobel Prize in Physics in 1979 [25–27]. Electroweak theory describes how the electroweak bosons (the photon (γ), the W^\pm , and the Z boson) interact with matter. The major pieces of evidence that helped solidify this theory came first with the discovery of neutral currents by the Gargamelle bubble chamber, which was interpreted as a neutrino interacting via the exchange of a Z boson [28], followed by the observation of W^\pm and Z boson decays at the Super Proton Synchrotron. Carlo Rubbia and Simon van der Meer shared the Nobel Prize in Physics in 1984 for their work leading to the discovery of the W and Z bosons [1, 2, 29, 30].

The electromagnetic force is mediated by the photon, and acts upon all particles that carry electric charge. The electromagnetic force follows the $1/r^2$ law originally discovered by Coulomb, in the sense that particles having the same electric charge are repelled and particles having opposite charge are attracted to each other with a force that falls off as the square of the distance between them. The strength of the interaction is characterized by the fine structure constant, α , which is known to 0.25 parts per billion, and is on the order of $1/137$.

The weak force is mediated by the Z and W^\pm bosons. These bosons interact with all quarks and leptons, although due to the large masses of the mediating bosons, weak interactions occur only over a short distance. This is in contrast to the electromagnetic force, mediated by massless photons, which has an infinite range. The weak force is the “weakest” force described in the Standard Model, with the coupling constant, $\alpha_W \sim 10^{-6}$. The weak force is known for the role it plays in decays, as it is the only force that induces flavor-changing currents through W^\pm interactions. This swapping of flavors in the quark and lepton sectors allows for processes such as beta decay ($n \rightarrow pe\bar{\nu}_e$), which requires the change of a down quark to an up quark, and muon decay ($\mu \rightarrow e\bar{\nu}_e\nu_\mu$), which requires the change of a muon to an electron and two neutrinos.

2.3 QCD

In the theory of QCD, particles with “color” charge interact via the strong force through the exchange of mediators with “color” charge. The idea of “color” was chosen in analogy with the three primary colors, resulting in the “chromo” root of Quantum Chromodynamics. Each quark carries one of three color charges (red, green, or blue), and each mediator gluon carries one color charge and one anti-color charge. Together, the quarks and gluons are referred to as *partons* and comprise the group of objects that interact strongly.

Several characteristics of QCD are crucial in distinguishing it from QED. First of all, QCD is a non-Abelian gauge theory, which among other things results in gluons being able to interact with other gluons, resulting in increasing interaction strength at increasing distance scales. This fact results in two crucial and intimately related characteristics of QCD: asymptotic freedom and confinement [31].

Asymptotic freedom states that the force between two color carrying particles will go to zero as the distance between them goes to zero, and becomes very strong as that distance increases. This can be seen in the strong coupling constant α_s , which to leading order is derived from the properties of QCD to be:

$$\alpha_s(Q^2) = \frac{12\pi}{(11N_c - 2n_f) \log(Q^2/\Lambda^2)} \quad (2.1)$$

where Λ is the QCD scale parameter, $N_c = 3$ is the number of quark colors, $n_f = 6$ is the number of quark flavors, and Q^2 is the value of the momentum transfer squared in a $2 \rightarrow 2$ process. This equation demonstrates that at small distance scales, corresponding to large momentum transfer, as $Q^2 \rightarrow \infty$, $\alpha_s \rightarrow 0$, and at large distance scales, corresponding to small momentum transfer, $\alpha_s \rightarrow \infty$, $Q^2 \rightarrow \Lambda^2$. The calculation and experimental measurement of this running constant can be seen in Fig. 2.2.

Asymptotic freedom leads directly to confinement, which is simply the fact that solitary partons are forbidden. Quarks can therefore only be found in either color neutral doublets called mesons, which are quark-antiquark pairs, or triplets called baryons such as protons and neutrons.

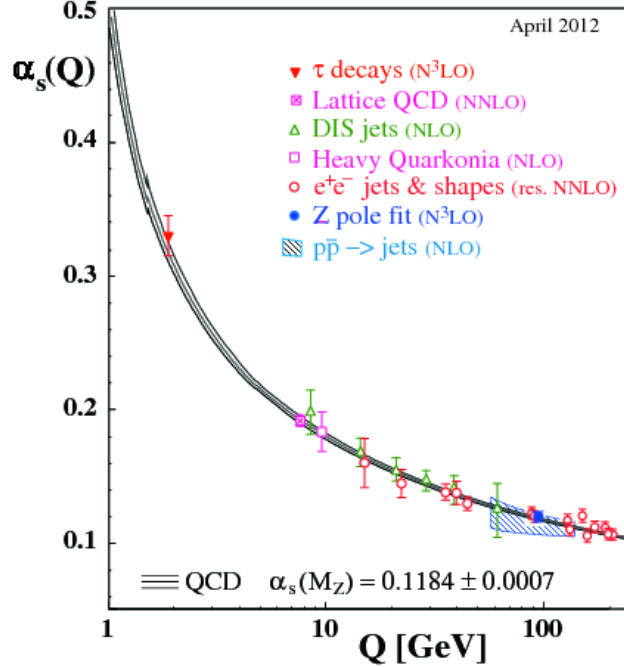


Figure 2.2: Measurement and theoretical prediction of the QCD coupling constant as a function of energy [32].

2.4 Formation of the QGP

In hadronic collisions, such as proton-proton ($p + p$) collisions at the Large Hadron Collider (LHC) as two partons get further and further apart, the bond between them gets stronger and it becomes energetically favorable to form quark-antiquark pairs, which result in the formation of new mesons and baryons. Although these parton collisions and the resulting particles may be challenging to measure fully in an experiment, the theory of QCD can be used consistently in providing a theoretical framework and predictions for the processes that occur.

Once QCD is taken into an extremely hot and dense medium, such as the state of the universe 10^{-6} seconds after the big bang, and such as the medium formed in ultra-relativistic heavy-ion collisions, the picture becomes much more complicated. At temperatures above the critical temperature ($T_c \sim 175$ MeV) and at large energy densities ($\epsilon > 1$ GeV/fm³), a new state of matter known as QGP is predicted to be formed which is characterized by the following:

- strongly interacting medium: the medium formed is strongly coupled, which results in hadronic

matter produced in or passing through the medium being significantly modified via the strong force.

- deconfined partons: since outside of the QGP, partons are only found within doublet or triplet states, the relevant degrees of freedom are those states. Within the QGP, the partons move independently and the relevant degrees of freedom for the medium are the quarks and gluons themselves.

These properties of the medium result in several major signatures (two of which are described here) for the formation of the QGP, which are not only useful in demonstrating the formation of the medium, but also in measuring the properties of the QGP.

2.4.1 Heavy Quarkonia Suppression

One of the first processes to be introduced as a signature for the formation of the QGP was heavy quarkonia suppression, introduced by Matsui and Satz in 1986 [33]. Quarkonia, mesons made up of charm or bottom quarks, are produced in ultrarelativistic collisions. Originally looking at the J/ψ , Matsui and Satz proposed that, according to lattice QCD calculations, there is a temperature above which the J/ψ will dissociate, resulting in the melting of the J/ψ state in the QGP and a suppression of the production compared to what is seen when no QGP is formed.

Although the situation turns out to be much less “unambiguous” than was originally thought for claiming the observation of this signature as an observation of QGP formation, measuring quarkonia suppression has played a crucial part in understanding the properties of the QGP. In particular the recent measurements at the LHC and RHIC [34, 35] of the suppression of the Upsilon meson (Υ), a bottom/anti-bottom quark bound state, have been significant in testing our understanding of quarkonia suppression. According to lattice QCD calculations, due to the different binding energies of the ground state ($1S$) and two excited states ($2S$ and $3S$) of the Υ , the states experience sequential suppression where the more excited states dissociate at lower temperatures than the ground state [36].

Since quarkonia have large masses compared to the light mesons, they are not significantly modified as they pass through the QGP, and since their production primarily comes from gluon-gluon

fusion, they are predominantly produced in the early stages of the collision. These two factors combined with the differing binding energies of the three states contribute to the relative suppression of the states being useful as a thermometer for the medium formed in the collision.

2.4.2 Away-side Jet Suppression

Jets are produced in a collision when an energetic parton resulting from the collision begins hadronizing by pulling particles out of the vacuum and forming a narrow cone of collinear particles [37]. As jets pass through the QGP where color fields are manifest, it is expected that the energetic partons will radiate gluons and the jets end up being broader and possibly softer than those passing through a vacuum. The induced energy loss via gluon bremsstrahlung depends on the medium density. The study of jets is therefore crucial in studying the energy density of the QGP, looking at the energy loss of partons passing through the strongly-coupled medium [38].

One of the earliest major results demonstrating the energy loss of partons passing through the QGP came from the Solenoidal Tracker at RHIC (STAR), which showed evidence for the suppression of high- p_T hadrons in heavy-ion collisions (specifically gold-gold (Au+Au) collisions) relative to proton-proton ($p + p$) and deuteron-gold (d+Au) collisions. Figure 2.3 [39] shows the dihadron correlations between particles in a single heavy-ion collision. The x -axis is the azimuthal separation ($\Delta\phi$) between the leading (highest p_T) hadron and another measured hadron. The red (green) points represent central (minimum bias) d+Au collisions, the blue stars represent central Au+Au collisions, the line histogram represents the minimum bias $p + p$ collisions, and the vertical lines represent the statistical errors in the measurement. In the figure, the points near $\Delta\phi \sim 0$ show the near-side peak of hadrons which represent collimated hadrons in the leading jet and the points near $\Delta\phi \sim \pi$ show the away-side peak of hadrons which represent collimated hadrons in the jet traveling opposite to the leading jet. The near-side peak is prominent in all collision geometries whereas the away-side peak is seen in the $p + p$ and d+Au collisions, but is suppressed in central Au+Au collisions. This suppression is understood as being due to energy loss of strongly interacting particles in the sub-leading jet passing through more of the QGP than those in the leading jet.

Due to the luminosities that have been achieved and the great increase in center of mass energy

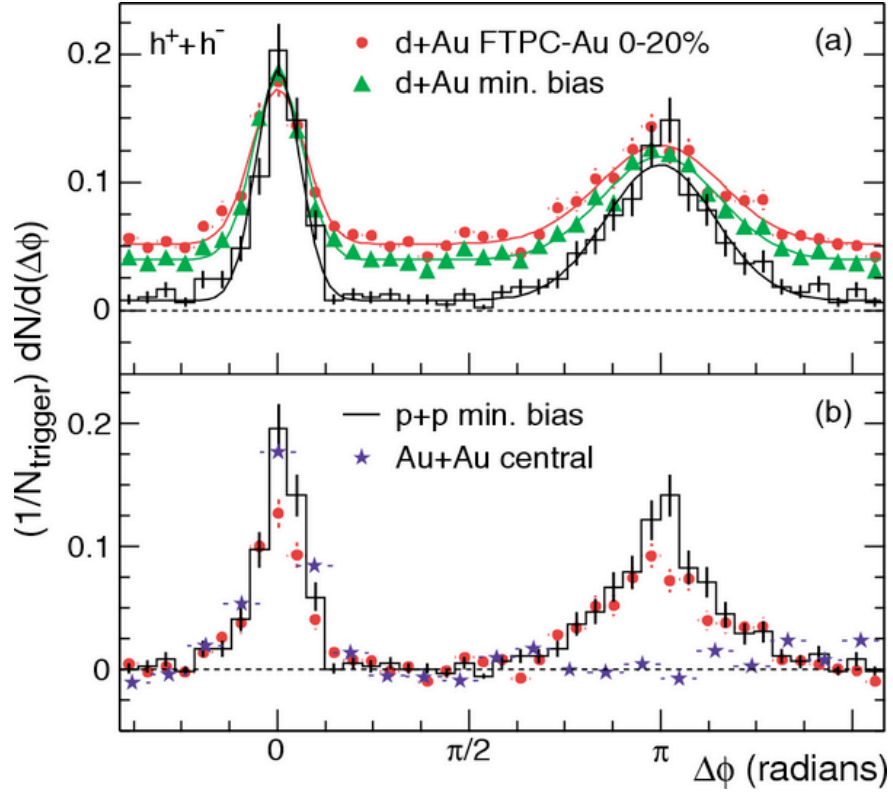


Figure 2.3: STAR results showing the away-side peak in di-hadron correlations in proton-proton and d+Au collisions, with the away-side peak suppressed in Au+Au collisions [39].

($\sqrt{s_{NN}}$) available at the LHC, the process of studying jets has moved to tagging and studying the jets themselves, allowing for impressive event displays such as the ones shown in Fig. 2.4 and to eventually study in detail jet hadronization and energy loss in the QGP.

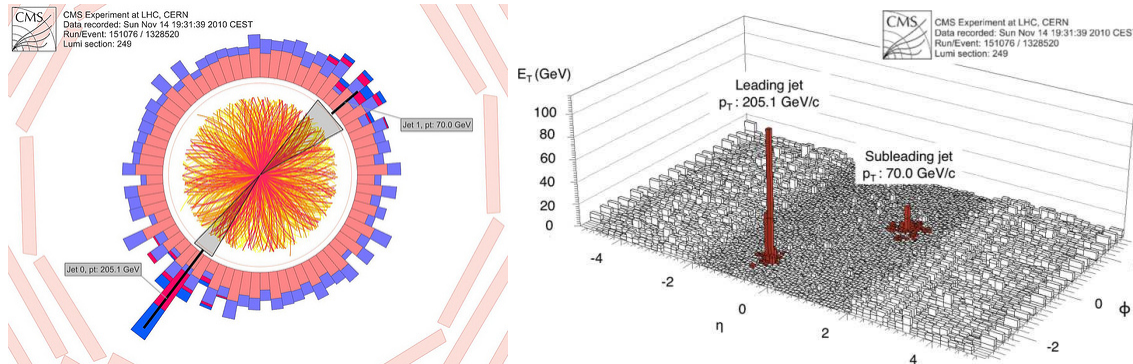


Figure 2.4: CMS event showing a large dijet imbalance, the signature for away-side jet suppression [40].

2.5 Electroweak Probes and the QGP at the LHC

With the unprecedented energies achieved at the LHC, the major focus of the LHC Physics program is in High Energy Physics and the search for new particles, including the recent discovery of a Higgs Boson [41]. In High Energy Physics, the 7 TeV center-of-mass energy achieved once the collider started running was a factor of 3.5 increase in energy over the previous record holder, the Tevatron, which reached an energy of 1.96 TeV. In heavy-ion physics, the 2.76 TeV center-of-mass per nucleon-nucleon pair in the Pb+Pb collisions is a factor of ≈ 14 increase in energy over the 200 GeV available at the Relativistic Heavy Ion Collider (RHIC).

This increase in energy results in a significant increase in production cross section for rare hard probes that have been crucial for the study of the QGP at lower center-of-mass energies, such as the J/ψ and Υ mesons. The increase has also made probes available that were unavailable at lower energies, such as the W^\pm and Z bosons. These bosons are not only interesting to study on their own, but are also useful as controls for understanding the complexity of QGP formation in heavy-ion collisions.

2.5.1 Glauber Model

In order to understand the effect that the QGP has on the production and transport of partons passing through the medium, there must first be some control with which to compare what is expected when no QGP is formed. The first control that is used is taking $p + p$ collisions and scaling them by the geometry of the collision. Since a lead nucleus colliding with another lead nucleus involves a much greater number of participating nucleons compared to a $p + p$ collision, and a different distribution of partons than a proton colliding with a proton, a model must be developed to scale $p + p$ collisions to what would be expected if a heavy-ion collision were just a superposition of nucleon-nucleon collisions. The model used in this thesis is the Glauber model, described in Ref. [42].

The Glauber model is crucial in setting the scaling required to compare the production of particles such as the Υ mesons and the Z bosons. In order to determine whether what is seen in a heavy-ion collision is what would be expected by scaling the $p + p$ collisions given the geometry of the heavy-ion collision or whether it is different than expected and may be of interest in the study of the QGP, the scaling must be accurate and reflective of what actually occurs in a collision.

2.5.2 Cold Nuclear Matter Effects

Although scaling $p+p$ collisions by the number of nucleon-nucleon collisions can model the heavy-ion collision as a system of independent NN collisions, there are significant initial-state effects that are not reflected by just scaling the $p + p$ reference. Put simply, a lead nucleus colliding with a lead nucleus is not the same thing as 208 protons and neutrons colliding with 208 protons and neutrons. The effects resulting from this difference are called cold nuclear matter (CNM) effects, and are challenging to decouple from the differences that result from the formation of the QGP, which are called hot nuclear matter (HNM) effects. More controls are needed in order to separate these effects.

The first control used that can assist in the understanding of CNM effects is that of looking at proton-nucleus ($p+A$) collisions. These collisions explore how a proton colliding with a nucleus is different than taking a collision between two protons and scaling by the number of binary

nucleon-nucleon collisions that occur when a proton collides with a nucleus, without needing to take into account the formation of the QGP (since no QGP is expected to form in a $p+A$ collision). This control has the added benefit of taking into account CNM effects, but can be challenging to study due to ambiguities that come up in the understanding of the geometry and centrality of a $p+A$ collision, as well as requiring a separate run that can be technically challenging to carry out.

The second set of controls that can be used to understand CNM effects are particles produced in heavy-ion collisions that are not significantly modified by the strongly interacting medium. Leptons and the electroweak bosons are good candidates for these controls, although particles such as photons and electrons are produced in such abundance that getting a clean signal in $p+p$ and Pb+Pb collisions from these individual particles would be impossible. Instead we turn to the W^\pm and Z bosons.

2.5.3 Heavy Electroweak Probes: A Control Experiment

Electroweak boson production is rare, but these bosons are useful because these should only be affected by initial-state effects. The W and Z bosons decay within the medium with a typical lifetime of 0.1 fm/c but, since they have leptonic decay channels where the daughter leptons will also not be affected by the strongly interacting medium, they can be cleanly reconstructed without being affected by the formation of the QGP. This makes them excellent candidates for acting as controls for understanding CNM effects and decoupling CNM and HNM effects in heavy-ion collisions. The main production mechanisms for the Z , and the decay of the Z to dileptons are discussed in Section 2.6.1, and shown in Fig. 2.6.

The measurement of W^\pm and Z boson production gives us a way of testing the Glauber model scaling of $p+p$ collisions since only CNM effects will modify their production. They also serve as a control within an event to study heavily-modified processes such as jet production and quenching, by looking at Z +jet events to measure energy loss in a jet in an unbiased manner. Thus, the heavy electroweak probes can have a unique role in disentangling the CNM and HNM effects experienced by particles modified by the formation of the QGP.

2.6 Z Bosons in Heavy-Ion Collisions at the LHC

2.6.1 Z Boson Production and Decay

The mass of the Z boson is 91.2 GeV [31], requiring a very hard and rare process to produce it. Figure 2.5 shows the parton distribution functions (PDF) of gluons, sea quarks and valence quarks in a proton and their associated uncertainties using the NNLO MSTW2008 parameterization at a scale of 10 GeV and 10 TeV. The PDFs are shown as a function of Bjorken x (denoted as x in the plots), which represents the fraction of the total proton momentum that the colliding parton carries. Given the mass of the Z ($m_Z \sim 90$ GeV), and the beam energy ($\sqrt{s_{NN}} = 2.76$ TeV), the momentum fraction carried by the partons involved in the collision will be on the order of $x \sim m_Z/\sqrt{s_{NN}} \sim 0.03$, and therefore will involve a collision of sea-quarks and/or gluons.

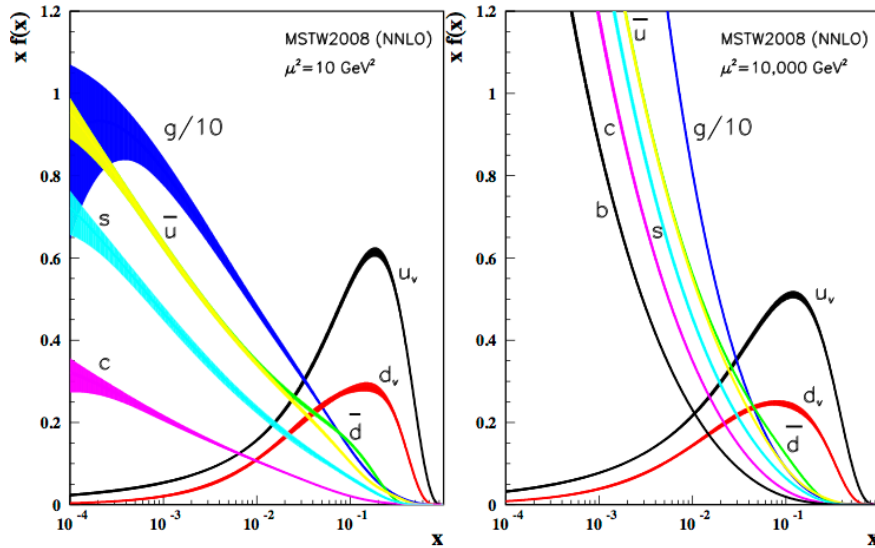


Figure 2.5: Structure functions of the proton and their associated uncertainties using the NNLO MSTW2008 parameterization at a scale of 10 GeV and 10 TeV [43].

Since the Z boson does not couple to the gluon, the dominant production mechanisms are the ones shown in Fig. 2.6. The main decay channels for the Z are those to hadrons and neutrinos, but the e^+e^- , $\mu^+\mu^-$, and $\tau^+\tau^-$ decay modes each occur 3.4% of the time.

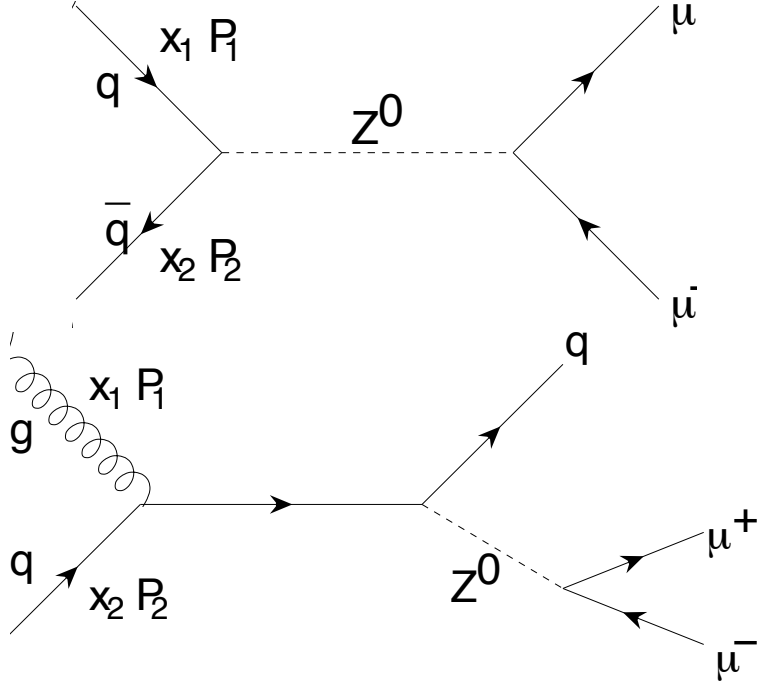


Figure 2.6: Feynman diagrams for the Production of the Z and decay to dimuons in the $q\bar{q} \rightarrow Z \rightarrow \mu^+\mu^-$ (top) and $qg \rightarrow qZ \rightarrow q\mu^+\mu^-$ (bottom)

2.6.2 Initial State Modification

After the Z boson is produced, it and the dileptons it decays into are unmodified by the QGP formed in the heavy-ion collision. When compared to production in $p + p$ scaled by the number of binary nucleon-nucleon collisions, there will be some modification due to the fact that the nuclear parton distribution functions (nPDFs) will have modified relative distributions from those shown in Fig. 2.5. As mentioned before, these are CNM effects, which are a combination of a variety of effects.

One of the most important CNM effects is the difference in isospin between protons and neutrons. Since the Pb nucleus is composed of a combination of 82 protons and 126 neutrons, the distribution of up and down quarks will be significantly different from those in protons. This results in a significantly modified PDF from that shown in Fig. 2.5. This effect must be accounted for in predictions and simulations, by using the up and down quark distributions expected in the Pb nucleus.

One model which attempts to take into account the remaining CNM effects on the PDFs, to obtain nPDFs, is EPS09 [44], whose general assumed shape is shown in Fig. 2.7. In the figure, R_i^A refers to the nuclear modification of PDFs in a free proton compared to a nucleus. The i refers to the parton type (gluon, valence quark or sea quark) and A refers to the type of nucleus. The downward trend as $x \rightarrow 0$ (shadowing) is in part due to the fact that a parton in that x -region that has already scattered will be less likely to be involved in another collision, with the upward trend at mid- x (anti-shadowing) being the inverse. The dip at high- x (EMC effect) refers to an effect that has been seen in nuclear deep inelastic scattering for over 30 years. There are a large number of competing explanations related to the local and global nuclear structure on the market [45–51]. Finally, the peak at high- x (Fermi motion) is related to the quantum motion of nucleons bound inside the nucleus.

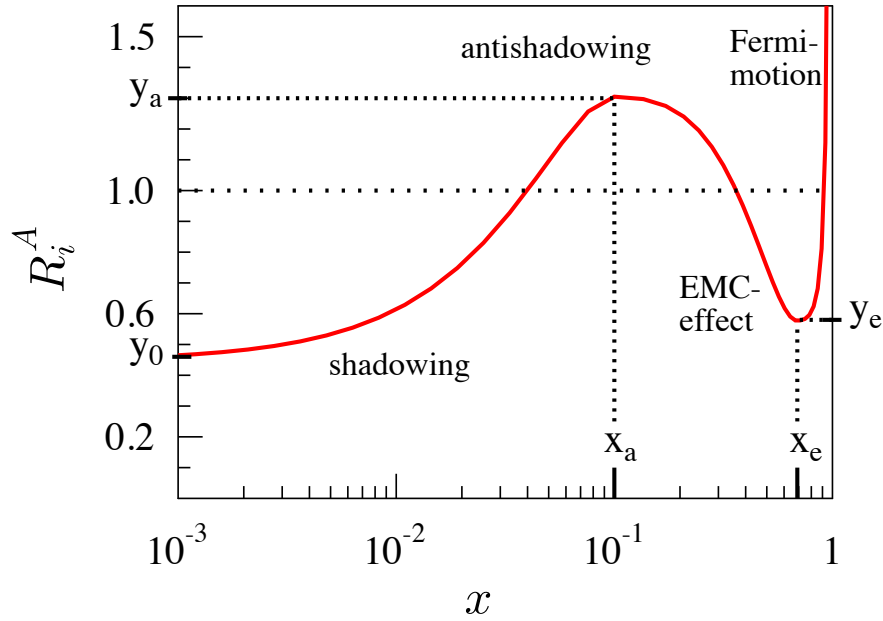


Figure 2.7: General line shape description for the EPS09 model describing the R_i^A or nuclear modification to the free proton PDFs [44].

The modification seen in Fig. 2.7 is a general description, so in Fig. 2.8 are shown fits to a combination of actual nuclear deep inelastic scattering (nDIS) data, Drell-Yan results in fixed-target collisions and π^0 measurements from RHIC. These data illustrate the level of modification expected in the nPDFs.

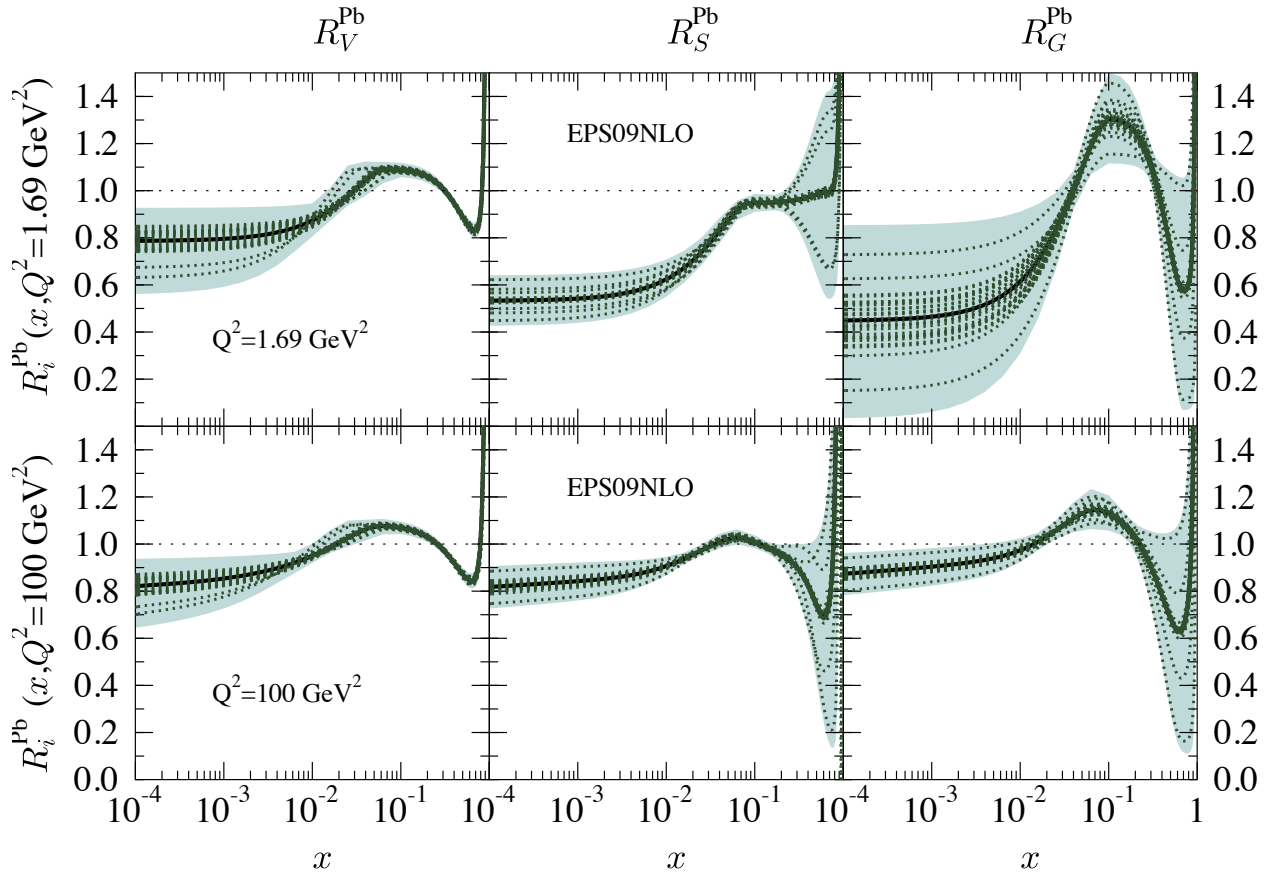


Figure 2.8: The nuclear modifications R_V , R_S , and R_G for Lead at scales of $Q^2 = 1.69$ (top) and 100 GeV^2 (bottom). The thick black lines indicate the best-fit results of DIS data, whereas the dotted green curves denote the errors [44].

For the sea quarks (S) and gluons (G) involved in the production of the Z , the expected modification for $x \sim 3 \times 10^{-2}$ is small, since $R_S^{\text{Pb}}(3 \times 10^{-2}) \sim 1$, and $R_G^{\text{Pb}}(3 \times 10^{-2}) \sim 1$. However, as the x decreases, the PDF are more strongly modified, which means that production of the Z from balanced partons (where both partons have about the same x) is not to be heavily modified by CNM effects, while imbalanced partons (where the partons have very different x) are expected to be more heavily modified by CNM effects. This effect can be measured by looking at the Z production as a function of x , which is possible by looking at the final direction of motion of the Z in terms of being in the direction of the original motion of one of the partons involved in the collision. The parameter of interest that describes that direction is called rapidity, and will be defined and discussed in Chapter 3.

The modification of Z boson production in Pb+Pb collisions measured in CMS relative to the production seen in $p + p$ collisions is expected to be small and due to shadowing effects of order $\sim 10\%$ and possible rapidity dependencies. The measurement of these effects can then be used to constrain the Pb nPDFs, allowing for the decoupling of hot and cold nuclear matter effects in heavy-ion collisions. Further discussion on these effects can be found Reference [52, 53].

The details of the CMS measurement are described in the following chapter.

Chapter 3

Experimental Facilities

3.1 LHC

The Large Hadron Collider is a two-ring accelerator and collider installed in the tunnels originally built for the Large Electron-Positron Collider (LEP) at the European Organization for Nuclear Research (CERN) in the 1980s. The tunnel has a circumference of 26.7 km and is located between 45 and 170 m below the surface of both French and Swiss territory.

3.1.1 LHC Layout and Design

As can be seen in Fig. 3.1, the LHC is split into 8 different Octants. The stations set up to manage that section of the LHC are referred to by point N, where N is a reference to the number of the Octant it is in. The LHC is currently set up as two rings where beams in one ring travel in a clockwise direction, beams in the second ring travel in the counterclockwise direction, and the two rings intersect at four interaction points (IPs). At each of these points there is a detector that is used to observe the collisions that occur as the beams cross. A Toroidal Large LHC Apparatus (ATLAS) is at point 1. ATLAS is the largest general purpose detector built to discover the Higgs Boson, and any other new physics that may be in reach at the energies reached. A Large Ion Collider Experiment (ALICE) detector is at point 2. ALICE is a detector dedicated to studying heavy-ion collisions at the LHC. The Compact Muon Solenoid (CMS) detector is at point 5. CMS

is a compact general purpose detector built to compete with ATLAS in discovering the Higgs Boson and looking for new physics beyond the standard model. Due to the general construction of the detector, it is also fit for measuring heavy-ion collisions. The Large Hadron Collider Beauty (LHCb) experiment is at point 8 and is focused entirely on studying beauty production and decay in an effort to understand the particle-antiparticle asymmetry observed in nature [54–57].

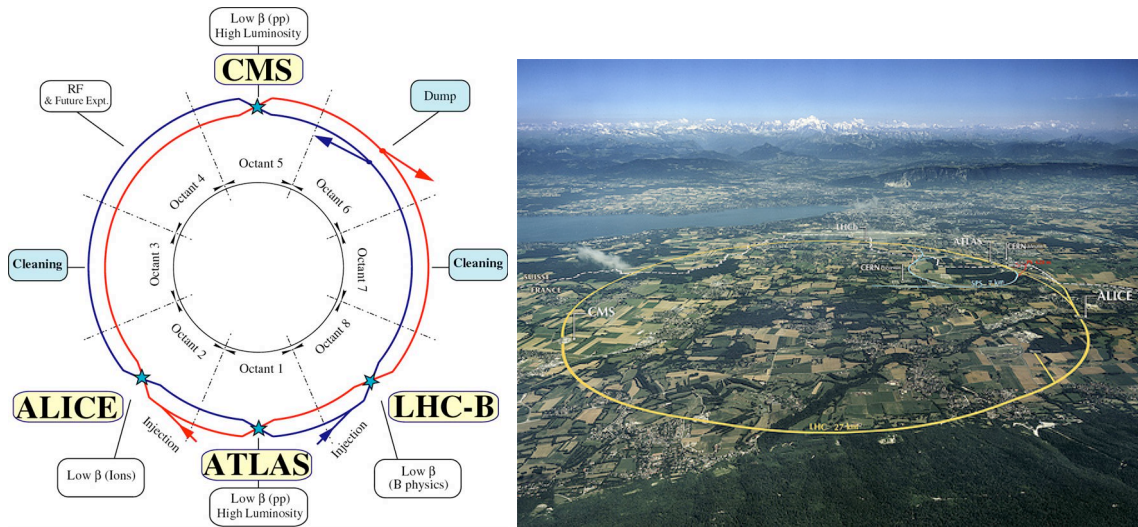


Figure 3.1: Schematic layout of the LHC (left) and photographic view from above (right) [58].

The LHC accelerator was designed to run two beams of protons in opposite directions which would collide at $\sqrt{s} = 14$ TeV. Due to significant damage done to the accelerator near the beginning of running at that energy, when a magnet quenched and dumped a significant amount of energy into the accelerator, the LHC has run proton-proton collisions at more conservative energies of $\sqrt{s} = 7$ TeV and 8 TeV. During Long Shutdown 1 (February 2013 - November 2015), the accelerator is undergoing repairs, maintenance and upgrades that will allow the safe running of $\sqrt{s} = 13$ TeV $p + p$ collisions.

Not only is the LHC a large step up in beam energy, but it is also designed to reach staggering peak luminosities, which results in an increase in the number of collisions occurring per second. The number of events generated per second (N_{event}) in collisions is given by:

$$N_{\text{event}} = L\sigma_{\text{event}} \quad (3.1)$$

In this equation σ_{event} is the cross section for an event occurring, and L corresponds to the luminosity, which is given by the equation:

$$L = \frac{N_b^2 n_b f_{rev} \gamma_r}{4\pi \epsilon_n \beta^*} F \quad (3.2)$$

Here, N_b is the number of particles in a bunch, n_b is the number of bunches in one beam, f_{rev} is the number of revolutions per second, γ_r is the relativistic gamma factor, ϵ_n is the normalized transverse beam emittance corresponding to how tight the bunch is in the transverse plane, β^* is the beta function at the collision point which refers to how tight the beam is squeezed by the quadrupole magnets at the IP, and F is the geometric luminosity reduction factor due to the crossing angle at the IP. Over the course of the LHC running, the accelerator physicists have tuned the parameters of the collider to increase the peak luminosity of the machine, which has almost reached the design luminosity of $L = 10^{34} \text{ cm}^{-2} \text{ s}^{-1}$. Although the same beams intersect at each collision point along the ring, parameters like β^* are different at each intersection point, making it possible to provide each experiment with a luminosity specific to its needs. In particular, luminosities are smaller for ALICE and LHCb during the $p + p$ running than for CMS and ATLAS whereas in Pb+Pb running ALICE, ATLAS, and CMS have similar peak luminosities.

3.1.2 LHC Injection Chain

The series of steps required to take protons from the hydrogen gas at the beginning of the injection chain to a beam of protons at an energy of 3.5 TeV (designed to reach an energy of 7 TeV) is shown in Fig. 3.2. The protons begin as hydrogen gas which is grouped into particle bunches. These particle bunches have their electrons stripped off and are taken through a series of accelerators that boost the protons to a specific energy, and then feed those proton bunches into the next accelerator in the chain. Once the protons have gone through the booster, proton synchrotron (PS) and super proton synchrotron (SPS) they are fed into the LHC as bunches in two beams revolving in opposite directions. The beams are then boosted on every pass around the ring by the RF cavity of Octant 4, and cleaned and focused by the magnets, until the beams are at the desired collision energy. Then the beams are focused together at the IPs.

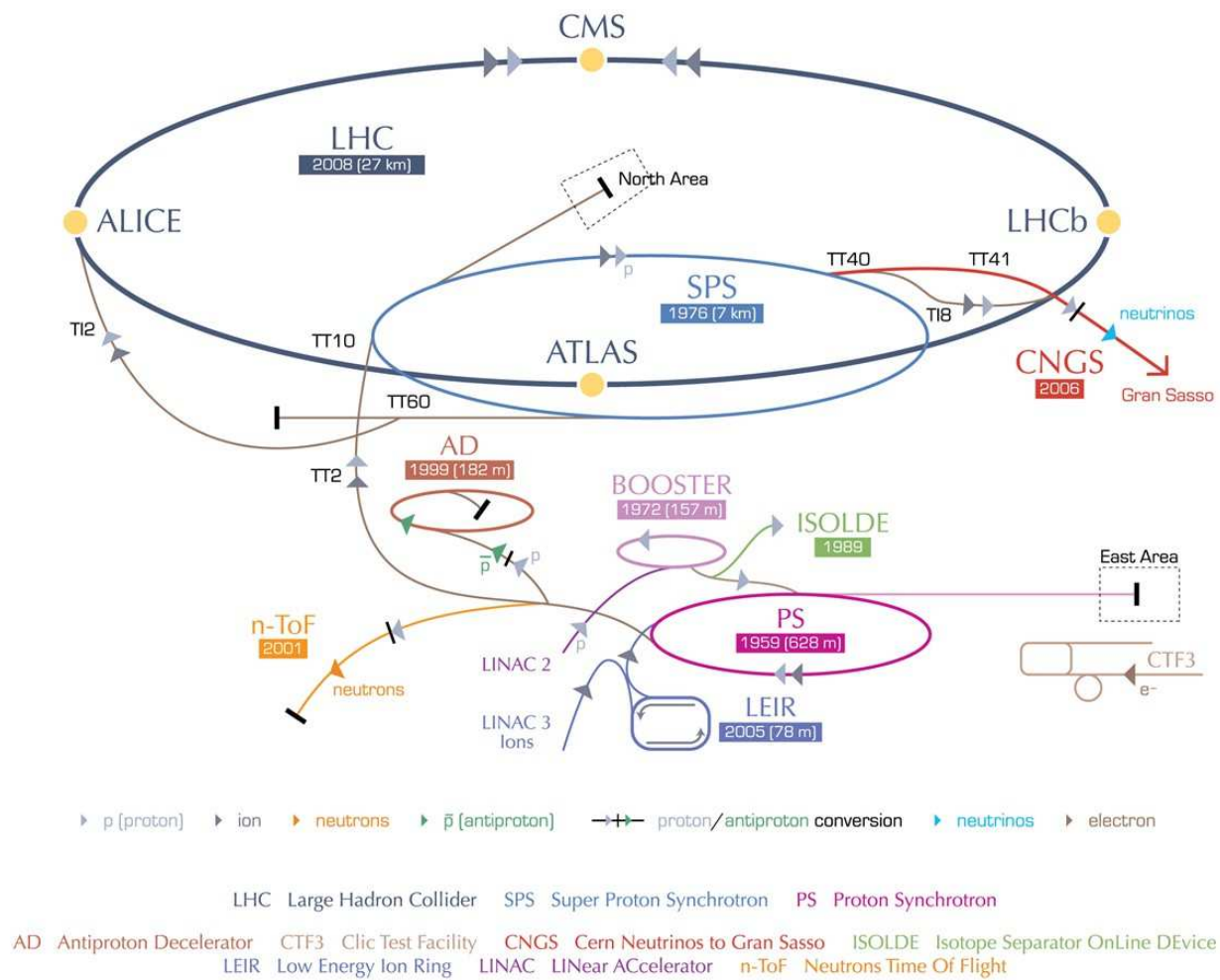


Figure 3.2: Schematic showing the various CERN experiments, along with the injection chain path for beams colliding in the LHC [58].

3.1.3 LHC as a Heavy-Ion Collider

Although the LHC was built for running proton-proton ($p + p$) collisions, the accelerator was designed to be flexible enough to carry out collisions with nuclear beams. The strength of the magnets determine the energy of the beams that can be kept in the ring. Since the force of the magnet relative to the mass of the nuclear species scales with Z/A , where Z is the number of protons in the nucleus, and A is the mass number, using the same magnets, the center-of-mass per nucleon energy decreases going from protons to lead-208 nuclei, which have 82 protons and 126 neutrons.

In 2010 and late 2011 the LHC ran Pb+Pb collisions at an energy of $\sqrt{s_{NN}} = 2.76$ TeV. In 2013 the LHC ran p +Pb collisions, where the proton beam had an energy of 4 TeV, and the lead beam had an energy of 1.58 TeV. When boosted into the center-of-mass frame, the resulting collisions are at a center-of-mass energy of 5.02 TeV. In these collisions, the center-of-mass frame is shifted from the lab frame in the direction of motion of the proton.

The injection chain for the lead beam begins with evaporated lead that is bunched together in groups. Some of the electrons are stripped from the atoms, at which point the lead atoms are fed into the linear accelerator set up for ions (LINAC 3 in Fig. 3.2). The bunches are then sent to the Low Energy Ion Ring (LEIR), which is an upgrade of the original Low Energy Antiproton Ring (LEAR), where they are accelerated to a high energy that they can be injected into the PS. The rest of injection chain matches what is done for the proton beams.

3.2 The CMS Detector

The CMS detector, shown in Fig. 3.3, was designed as a multi-purpose detector that could run at, and take advantage of, the energies and luminosities supplied by the LHC. It was designed to be a detector that could be run in parallel with the ATLAS detector and act both as competition and a cross-check for the new physics discoveries that the LHC collisions could provide. The main distinctions between the two detectors are summarized in CMS's name. CMS was designed with the following characteristics:

CMS DETECTOR

Total weight : 14,000 tonnes
 Overall diameter : 15.0 m
 Overall length : 28.7 m
 Magnetic field : 3.8 T

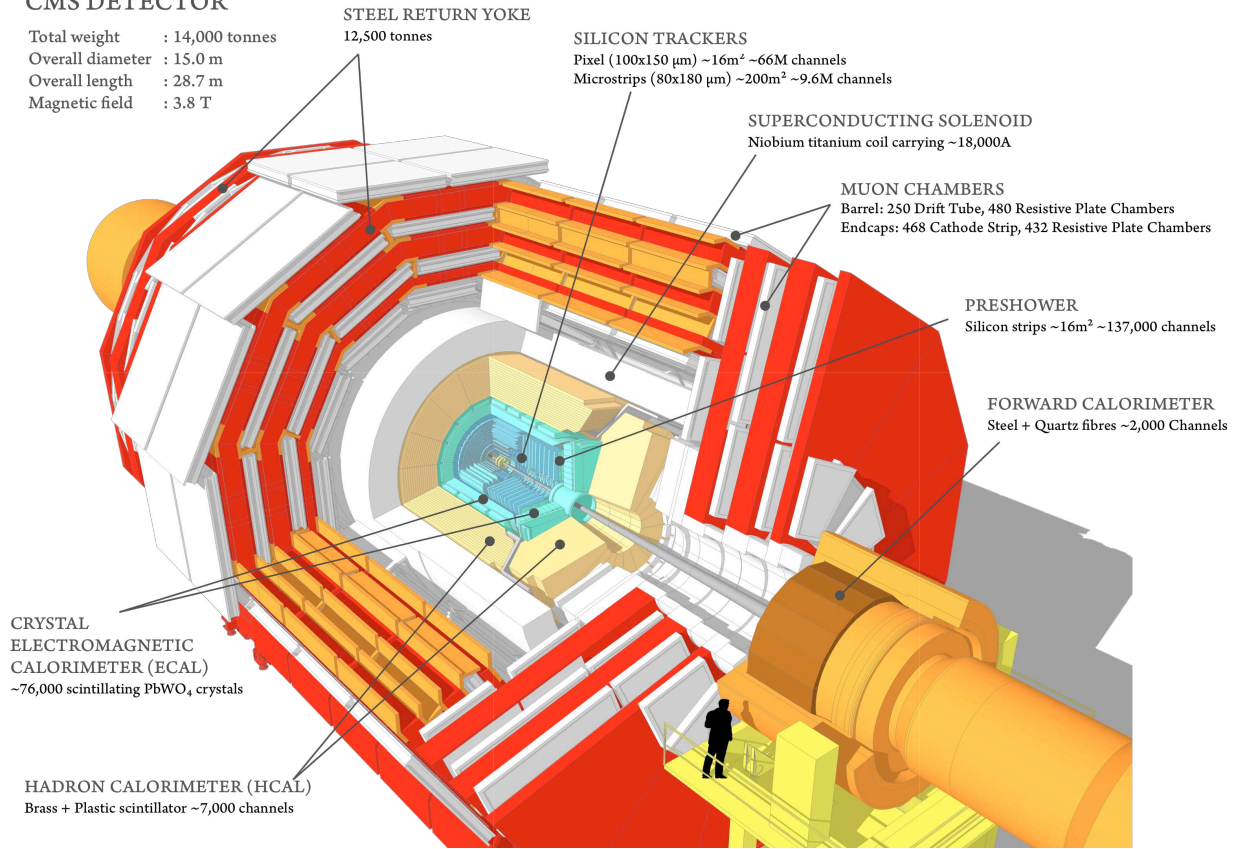


Figure 3.3: Schematic of the CMS detector [56].

- **Compact:** When designs for the CMS detector were first proposed, there were two competing designs whose distinguishing feature was their size. Specifically, the question was whether the tracker and calorimeters should all be built to fit within the magnet, or whether the calorimeters would be split up. In the end the more compact design was chosen. The ATLAS experiment weighs 7,000 tons, is 46 m long and 25 m in diameter, taking up a volume of 23,000 m³, and resulting in a density of ~ 300 kg/m³. The CMS detector weighs 12,500 tons, is 21.6 m long and 15 m in diameter, taking up a volume of 3,800 m³, resulting in a density of ~ 3000 kg/m³.
- **Muon:** Although built to be as versatile as possible, the CMS detector was built with muons at heart. Specifically the detector has three overlapping muon sub-detectors using three different technologies that provide full azimuthal coverage, fast triggering, good momentum resolution, and very little background. Its muon capabilities are a huge step up from previous experiments, and provides a clean signal for analyses requiring the detection of a muon.
- **Solenoid:** The central feature of CMS is the 4 Tesla (T) solenoidal magnet (run at 3.8 T in order to increase longevity), which provides excellent momentum resolution, as well as much of the detector's structural support. Whereas the toroidal magnet in ATLAS produces a complex magnetic field, which changes throughout the entire volume, the solenoid magnet produces a near uniform 3.8 T field within the volume and a 2 T field that radially falls off slowly outside of the magnet.

These three features make CMS a powerful discovery machine that has been used to discover the Higgs, and is well suited to measure Z production in a heavy-ion environment.

3.2.1 CMS Coordinate System

CMS uses a right-handed coordinate system, set up so that the origin is at the nominal interaction point. The x -axis points to the center of the LHC, the y -axis points up (perpendicular to the LHC plane), and the z -axis points along the anticlockwise-beam direction. Due to the cylindrical symmetry of the detector and spherical symmetry of the collisions originating at the center of the

detector, the set of coordinates most heavily used is with the z -axis in the anticlockwise-beam direction, θ as the polar angle which goes from 0 to π as it sweeps from the $+z$ direction to the $-z$ direction, and ϕ as the azimuthal angle which goes from 0 to 2π as it travels azimuthally around the detector. As is commonly done in collider physics, instead of using θ , pseudorapidity (η) is used, defined as:

$$\eta = -\ln[\tan(\theta/2)] \quad (3.3)$$

This set of coordinates (z , η , and ϕ) allows for the simplest description of motion and detection of particles in the CMS detector. Figure 3.4 shows a side view of the CMS detector in terms of these coordinates, where the detector is identical for all values of ϕ .

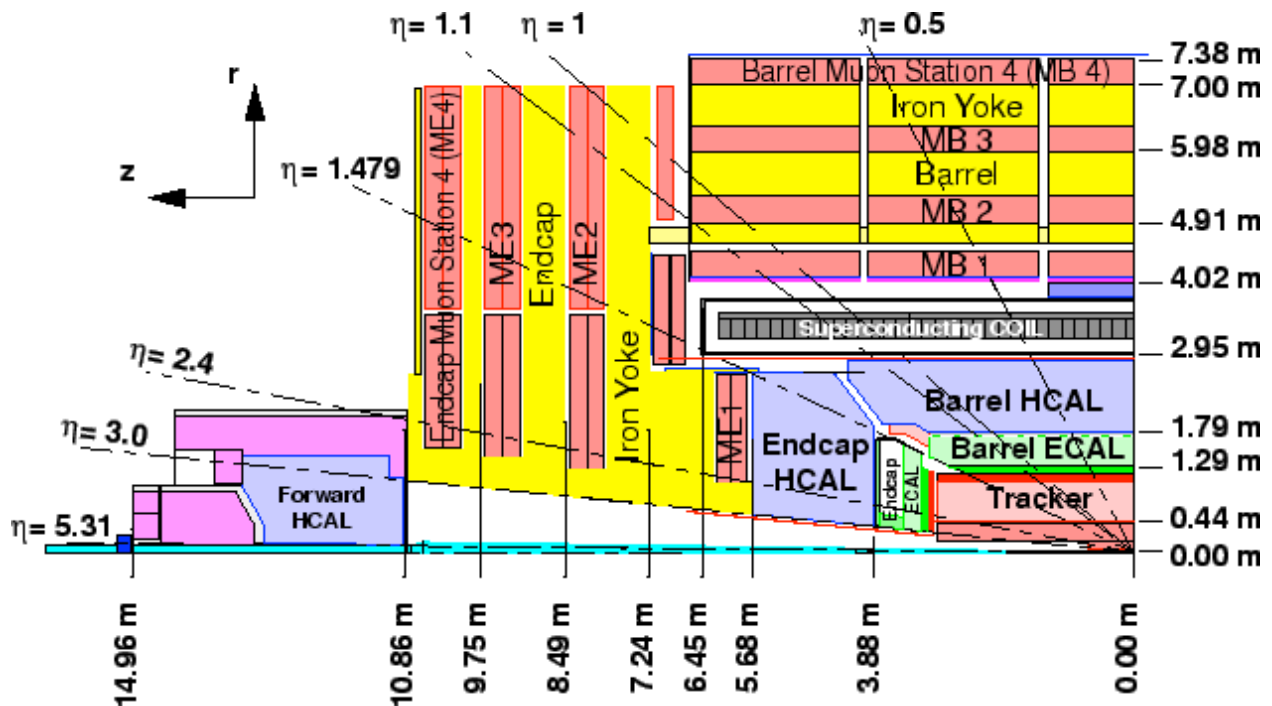


Figure 3.4: Side view of the CMS detector, showing the z and η range of each portion of the detector [56].

3.2.2 Inner Tracker

The inner tracker is housed within a cylinder that is 5.8 m long and 2.6 m in diameter. It is the sub-detector that is closest to the interaction region, and which receives both the largest amount of

information, as well as the largest amount of damage from particles passing through the material of the detector. When deciding on the design of the tracker, several major competing concerns needed to be taken into account:

- **Lifetime:** technologies that are radiation hard are required, due to the intense amount of radiation that would be experienced over the 10 year expected lifetime of the tracker. Even designs that would allow for quick change weren't enough, since during the long running period of the LHC, there are only a few periods where dead channels and parts can be replaced.
- **High granularity:** the goal of the tracker is to provide high precision measurements of charged-particle tracks as well as the ability to reconstruct secondary vertices with high precision. This requires a tracker with extremely fine segmentation and high granularity.
- **Fast:** at the LHC design luminosity of $10^{34} \text{ cm}^{-2} \text{ s}^{-1}$, bunch crossings occur every 25 ns, and therefore the tracker response must be fast. For many of the triggers used in CMS, the information in the tracker is crucial in determining whether or not the event is interesting.
- **Minimizing material:** although there must be material in the tracker in order to measure particles produced in the collision, extra material will result in interactions that will complicate the measurement of particles passing through CMS. Thus, minimizing the amount of material used is important in removing background interactions.
- **Cost:** the tracker is very important, and is a priority in the detector budget, but since the tracker is enormous (the CMS tracker is $\sim 200 \text{ m}^2$), keeping the cost to a workable amount is challenging.

Compromises were needed in order for the tracker to be acceptable in all of these areas, and in the end the current design was agreed upon. The 3 inner layers of the tracker are silicon pixel detectors which provide high precision measurements of charged-particle tracks as well as the ability to reconstruct secondary vertices with high precision. Outside of the pixel layers, there are 10 layers of silicon microstrip detectors which are crucial for precisely measuring the momentum of charged particles passing through the tracker. The silicon material used allows for fast triggering and fine

granularity but, due to the power density of the material, significant cooling is required, which adds considerably to the amount of material in the tracker.

As seen in Fig. 3.5, not only is the inner track crucial for measuring the kinematic properties of charged particles with good resolution, but it is also crucial to particle identification for distinguishing between charged and non-charged particles which hit in the calorimeters. Applying “track vetoes” is especially important in identifying photons as opposed to electrons, since their signatures in the calorimeters can be challenging to distinguish.

Since the tracker is such a crucial component for identifying and measuring particle motion in the detector, the inner tracker coverage of $|\eta| < 2.5$ sets the η range for most analyses at CMS.

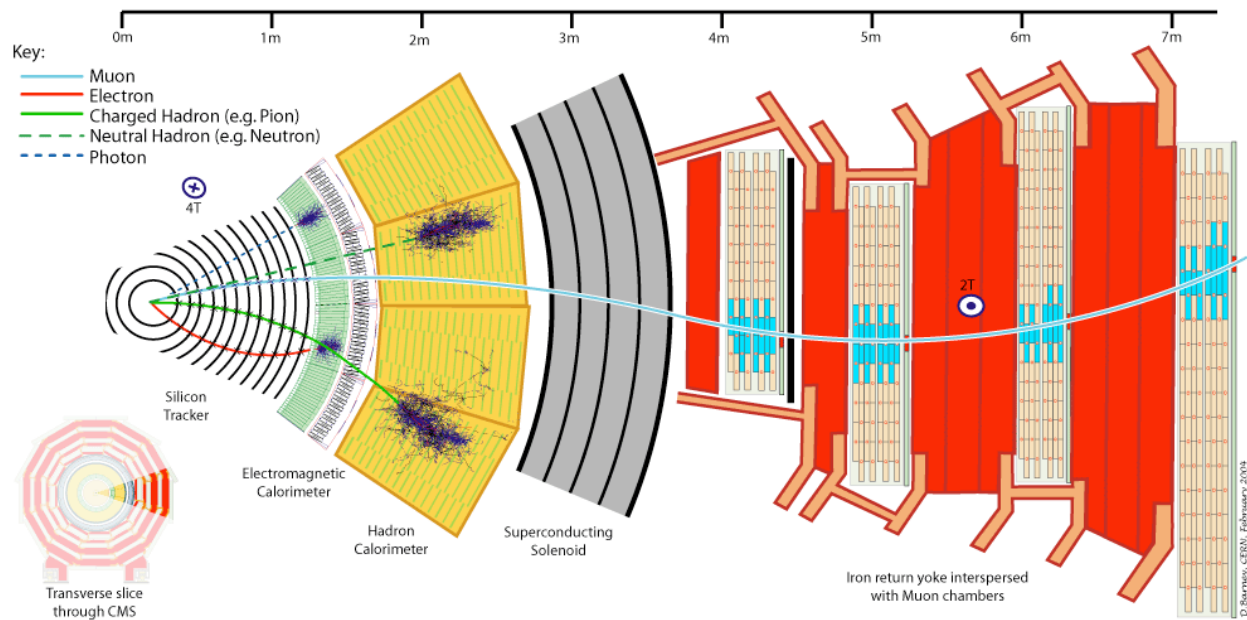


Figure 3.5: Side view of the CMS detector, showing the path traveled by various particles passing through the various portions of the detector [56].

3.2.3 Electromagnetic Calorimeter

The electromagnetic calorimeter (ECAL) is composed of 75 848 lead tungstate (PbWO_4) crystals which provide coverage in pseudorapidity $|\eta| < 1.48$ in the barrel region and $1.48 < |\eta| < 3.0$ in the two endcap regions. The main distinctions for the ECAL in these two regions is the presence of a

preshower detector in the endcap ECAL used for π^0 rejection, and the type of photodetector used to measure the scintillation light from the particles passing through the crystals, shown in Fig. 3.6.

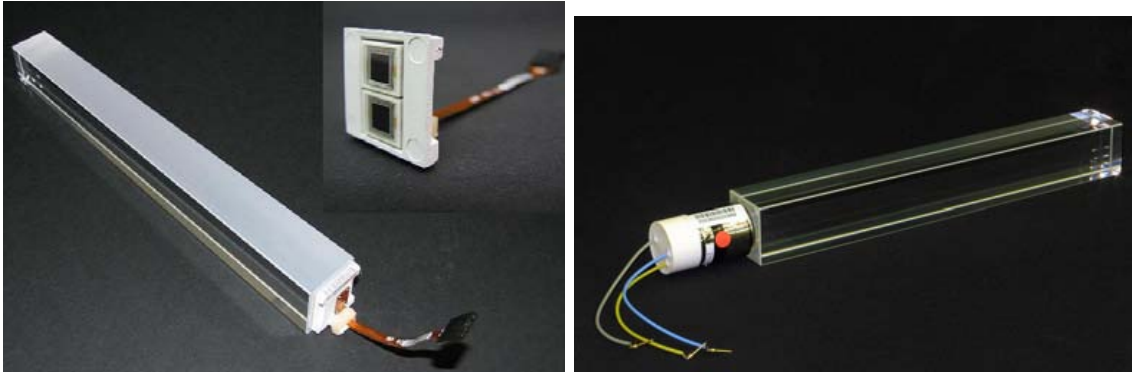


Figure 3.6: Barrel (left) and endcap (right) ECAL crystals with their respective photodetectors attached [56].

The criteria that set the design of the ECAL was the desire to detect the Higgs boson decaying to two photons. The PbWO_4 crystals that make up the ECAL are extremely dense and scintillate when particles pass through them, which produce short, well-defined photon bursts that allow for precise, and fairly fast detection. The ECAL’s thickness is chosen to be over 25 radiation lengths (X_0) in order to fully stop high energy electrons and photons passing through the calorimeter. The characteristics of the ECAL provide the energy resolution, efficiency and speed required to detect the signal defined by the criteria.

Unlike the tracker, the energy of a particle passing through the ECAL is measured by the amount of energy deposited in the calorimeter as opposed to the motion of the particle passing through the detector. This means that the efficient collection of energy deposited in the crystal is critical, as well as correctly grouping energy clusters, called “super clusters” that come from the same particles passing through the crystals. Although the ECAL crystals are very radiation hard, over time their ability to collect light decreases. The importance of energy collection in the ECAL pushes the need for the laser-monitoring system that is set up to continuously monitor the efficiencies of the crystals to transmit light. This monitoring system allows for the correction of efficiency losses, which allows the ECAL to run well over the course of CMS’s lifetime.

In $p + p$ collisions at $\sqrt{s} = 7$ TeV, the ECAL energy resolution for electrons with a transverse

energy $E_T \approx 45$ GeV typical of $Z \rightarrow e^+e^-$ decays is better than 2% in the central region of the ECAL barrel ($|\eta| < 0.8$), and is between 2% and 5% elsewhere. For low-bremsstrahlung electrons, where 94% or more of their energy is contained within a 3×3 array of crystals, the energy resolution improves to 1.5% for $|\eta| < 0.8$ [59]. Matching ECAL clusters to tracks measured in the silicon tracker is used to differentiate electrons from photons.

3.2.4 Hadronic Calorimeter

The hadronic calorimeter (HCAL) surrounds the ECAL, and provides coverage in $|\eta| < 3.0$. Since electrons will almost always be stopped in the ECAL, large energy deposits in the HCAL can be used to veto on hadronic energy. This cut is very effective in cleaning up hadronic background that may otherwise appear to be signal from an electron, which makes the HCAL an important part of electron analyses.

The HCAL is set up as a sampling calorimeter, made up of alternating layers of scintillator and brass. This allows for the slowing down and absorption of energy in the brass layers and the measurement of tracks and deposited energy in the scintillation layers. The measurement of the energy of hadrons passing through the calorimeter is particularly important for measuring hadron jets, and particles resulting in missing transverse energy such as neutrinos and invisible exotic particles, and the absorption is crucial in cutting down on high energy hadrons reaching the muon stations. The thickness of the HCAL varies between 7 and 11 interaction lengths (λ_I), depending on η , which keeps high energy hadrons from reaching the muon stations.

3.2.5 The Magnet

A crucial part of the design of the detector is the magnetic field map. The ability of the magnetic field to bend charged particles is crucial in measuring the momentum of particles passing through the detector. In order to achieve the level of resolution required for discovering new physics, the magnetic field must be strong, which is why a superconducting magnet is used in CMS. This requires the magnet to be kept at a constant temperature of 2 K. Several other choices were made to achieve the level of magnetic field desired:

- **Number of turns:** the winding of previous magnets have been done in 1 or 2 layers, but due to the number of ampere-turns needed for a 4 tesla field (41.7 MA-turn) the CMS solenoid is made up of 4 layers.
- **Reinforcement:** the combined aluminum and Rutherford-type cable is mechanically reinforced with an aluminum alloy.
- **Size:** The magnet is enormous, with a length of 12.5 m, an inner diameter of 6.3 m and a mass of 220 tons.

Within the superconducting solenoid volume, referred to as the barrel region of CMS, and shown in Fig. 3.7 are the silicon pixel and strip tracker, the lead tungstate crystal ECAL, and the brass/scintillator HCAL. These portions of the detector experience a 3.8 T magnetic field. The return field of the magnet saturates 1.5 m of iron outside of the magnet, which allows the placement of gas-ionization muon detectors which experience a magnetic field of ~ 1.9 T.

At large z values, which is referred to as the end cap region, the magnetic field becomes weaker and less uniform, which results in a decrease of momentum resolution at greater η .

3.2.6 Muon Systems

Measuring muons in CMS comes with a significant set of benefits:

- **Clean Signal:** due to the significant absorption of energy from electrons and photons in the ECAL and from hadrons in the HCAL, the vast majority of tracks seen in CMS’s muon chambers come from muons. Although some “punch-through” hadrons make it out to the muon chambers, basic muon identification cuts eliminate nearly all fake muons from the analysis.
- **Resolution:** as can be seen in Fig. 3.9, the muon resolution at CMS varies as a function of p_T and η , with 10 GeV/c muons at midrapidity having resolution less than 1%, and 1 TeV/c muons at forward rapidity having resolution $\sim 10\%$. This excellent resolution is due not only to the tracker, strong magnetic field and muon detectors, but also due to the fact



Figure 3.7: The CMS solenoid magnet in gray is shown being inserted into CMS. The iron return yoke which holds the barrel muon chambers, is shown in red [56].



Figure 3.8: During Long Shutdown 1 (February 2013 - November 2015), the LHC and the detectors underwent significant repairs. During this time, I was allowed to go down into the viewing area of the detector to see CMS pulled apart, with a good view of the return yoke (in red), the magnet (in silver) and all of the cabling [60].

that bremsstrahlung radiation is suppressed for muons compared to electrons by a factor of $m_\mu/m_e \sim 200$. This results in muons being less affected by radiative losses than particles such as electrons.

- **Trigger:** the combination of very low background and therefore low occupancy in the muon chambers, along with fast muon and tracker detectors allows CMS to run a dedicated and unprescaled trigger set to trigger on interesting single and multi-muon events with specific p_T cuts over the full η range.

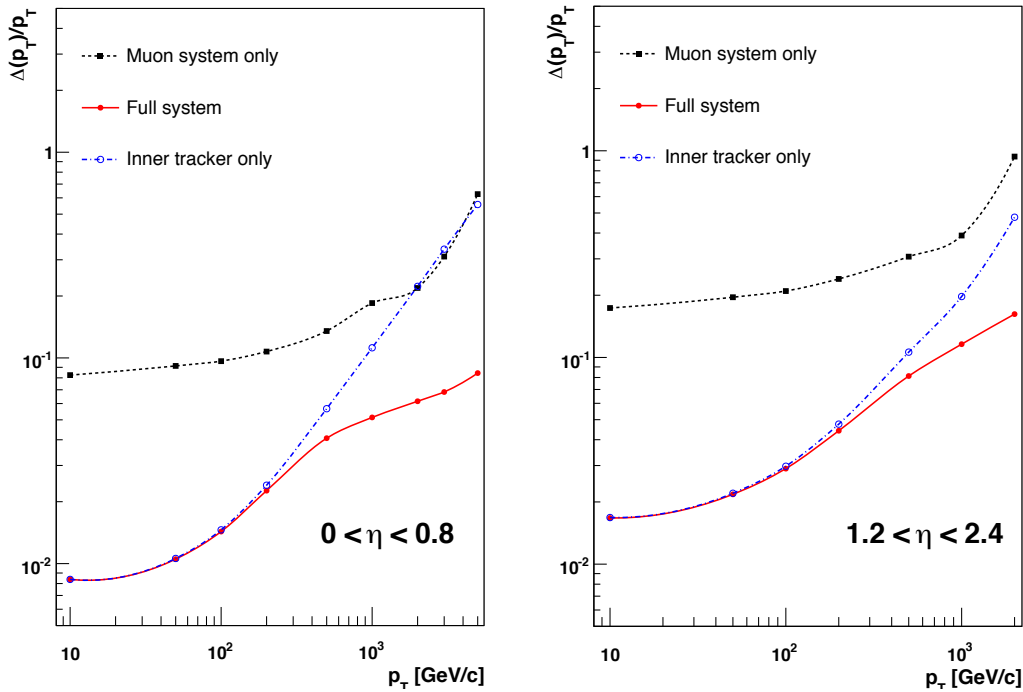


Figure 3.9: The muon p_T resolution as a function of the transverse momentum (p_T) using the muon system only, the inner tracking only, and both. The left panel shows the resolution in the $|\eta| < 0.8$ region, and the right panel shows the resolution in the $1.2 < |\eta| < 2.4$ region [56].

There are three different muon subdetectors that contribute to CMS's success as a muon detector: the drift tubes, resistive plate capacitors, and cathode strip chambers. The subdetectors are chosen to provide full η coverage, flexibility, and robustness in order to detect muons quickly and accurately as they pass through the muon stations.

3.2.6.1 Drift tubes

Due to the low background and uniform magnetic field in the barrel region, drift tube (DT) chambers work well in covering the $|\eta| < 1.2$ region of CMS. The chambers are housed in the iron flux-return plate of the magnet and are split into 4 stations. The first 3 stations are used to measure muons traveling through the detector in all three dimensions whereas the final station does not measure the travel along the direction of the beam line.

Each of the first 3 stations contain 8 chambers. Four of the chambers are used to measure the muons in the $r - \phi$ plane. The other 4 chambers provide the measurement in the z plane. The cells in the chambers are tiled in order to remove dead spots in the chamber efficiency.

The measurement of the muon passing through the drift tube is shown in Fig. 3.10. The muon passing through the cell induces a charge while the position of the cell and the amount of time for the wire to receive the signal provides a 2-D measurement of the muon trajectory. Measurements from hits in the drift tube cells provide excellent time resolution for triggering and, when linked together with other hits, can be used to create muon tracks and reject background hits.

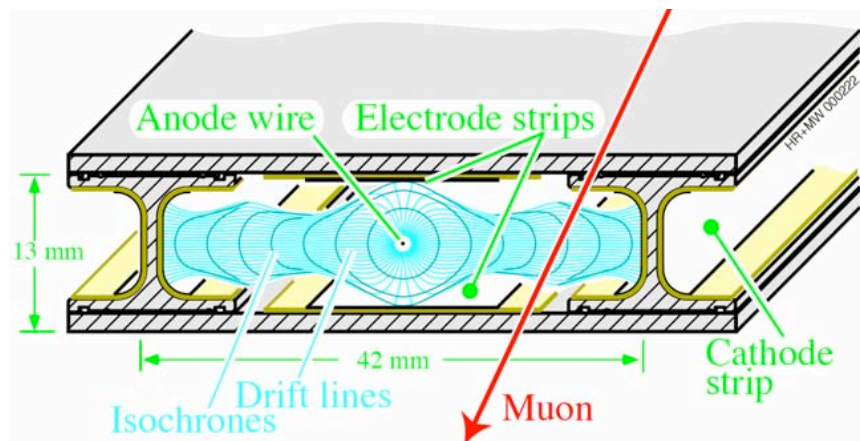


Figure 3.10: One cell from the drift tube chambers. A muon passing through the chamber induces a charge which drifts to the wire [56].

3.2.6.2 Resistive Plate Capacitors

In order to deal with the eventual collision rates once the LHC reaches full luminosity and to provide a complementary system dedicated to triggering, the resistive plate chambers (RPCs) were added in both the barrel and endcap regions. They provide a fast triggering system independent of the other two systems which can tag the time of an event faster than the minimum bunch crossing time of 25 ns at the LHC which results in an unambiguous tagging of the relevant bunch crossing. This triggering system also has a sharp p_T threshold and covers the range $|\eta| < 1.6$. The RPCs provide good time resolution but lower spatial resolution than the DTs and CSCs, which results in the need for the RPC overlap with the other two muon systems.

There are 6 layers of RPCs in the barrel muon system and 3 layers in the endcap muon system. The layers in the barrel and endcap are denser in the first few stations, in order to trigger on the lower p_T muons which may not make it to the outer muon stations. The RPC is a gaseous parallel-plate detector whose layout is shown in Fig. 3.11. The double-gap modules have two gaps with a strip in between which measures the induced signal from a muon passing through the module.

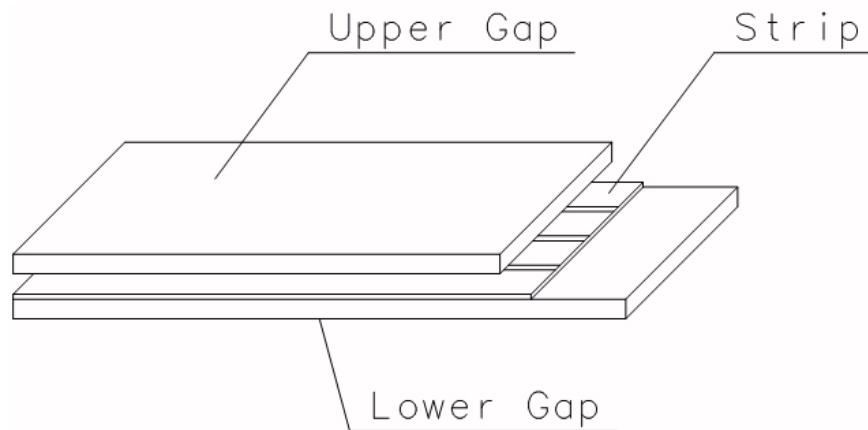


Figure 3.11: Layout of the double gap in an RPC module [56].

3.2.6.3 Cathode Strip Chambers

Since the two endcap regions of CMS receive high signal and background rates and are in the presence of a large non-uniform magnetic field, a different technology than that used in the drift

tubes must be used for achieving high resolution muon measurements. The cathode strip chambers (CSC) are chosen to accomplish this task, covering $0.9 < |\eta| < 2.4$ with 4 CSC stations on each side of CMS. The overall layout of the CSCs is shown in Fig. 3.12, showing the position of the four CSC stations in the detector.

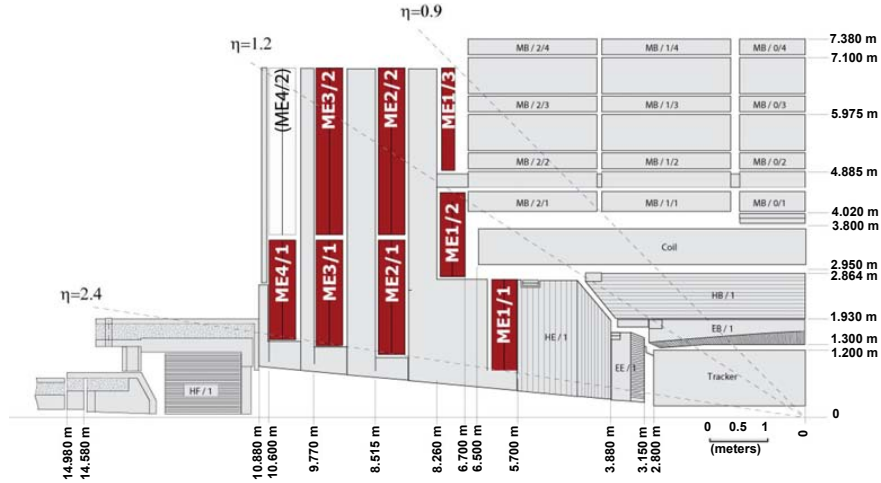


Figure 3.12: Side view of the CSC stations (in maroon) in CMS. The CSCs are split into four stations which have inner and outer disks [56].

The first station on each side is split into 3 sections of 36 chambers each, which receive the highest muon and background rates, and therefore the highest levels of radiation. The second and third stations each have an inner ring made up of 18 chambers and an outer ring made up of 36 chambers. The fourth station is made up of an inner ring of 18 chambers. Figure 3.13 shows the head-on view of the ME2 station, which provides full coverage in ϕ , and coverage of $1.0 < |\eta| < 2.4$.

Each CSC is made up of 7 panels with strips running lengthwise and wires running azimuthally within the gas gaps between panels. As a muon passes through the chamber, the induced charge on a wire and strip provide a coordinate which specifies the trajectory of the muon through the chamber. This layout is shown in the left panel of Fig. 3.14. This setup provides great resolution and efficiency for detecting muons passing through the chambers as well as durable radiation hard detectors in the most active η region of the detector.

In order to further improve on the performance of the CSC chambers, there have been two major upgrades done on the CSCs during the Long Shutdown 1 (LS1 refers to the period from

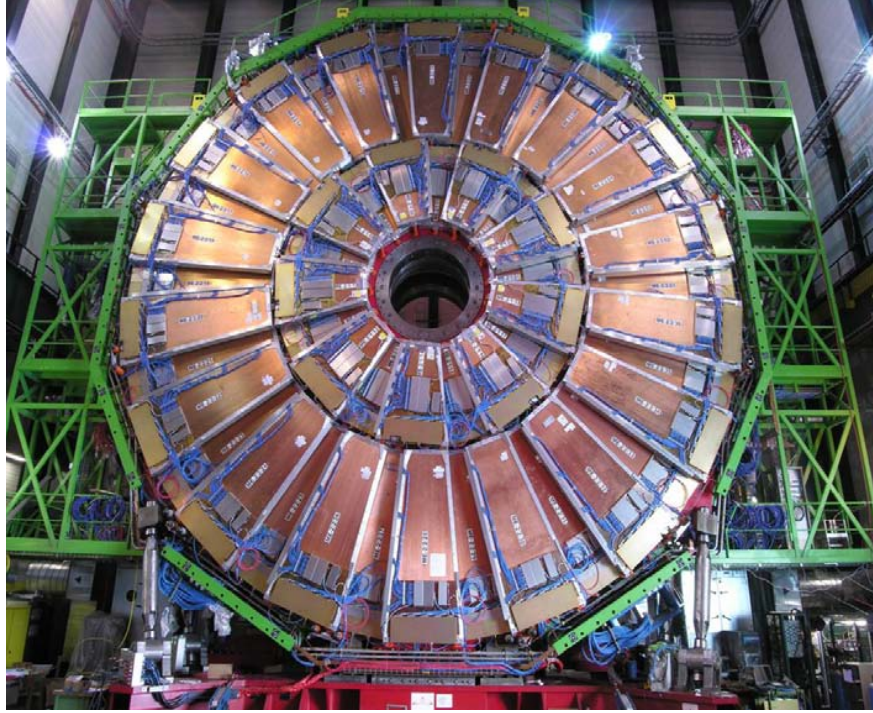


Figure 3.13: Picture of the full CSC ME2 station [56].

February 2013 - November 2015). The first is the addition of the ME 4/2 chamber, which improves the robustness of the CSCs. The second is the upgrade of the ME 1/1 station with new digital readout chips and optical fibers that allow for readout rates that match those required in the higher luminosity environment in the next stage of LHC running. The right panel in Fig. 3.14 shows an open upgraded chamber from the ME 1/1 station.

3.2.7 Forward Detectors

CMS has extensive forward calorimetry, shown in Fig. 3.15. Two steel/quartz-fiber Cherenkov hadron forward calorimeters (HF) are located on each side of the interaction point, covering the region $2.9 < |\eta| < 5.2$. The Centauro and strange object research (CASTOR) detector is a quartz-tungsten calorimeter which is extremely radiation hard and covers the range $5.2 < |\eta| < 6.6$. The Zero degree calorimeter (ZDC) is a quartz-tungsten calorimeter placed 150 m on either side of CMS which covers the range $|\eta| \geq 8.3$ and is designed to measure diffractive collisions and spectator particles. Although the TOTAL Elastic and diffractive cross section Measurement

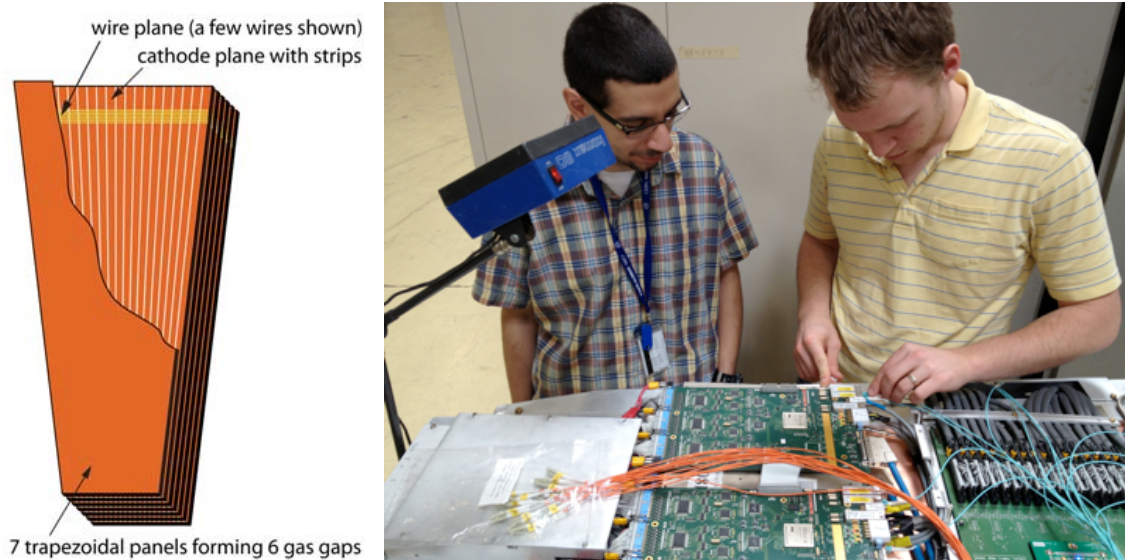


Figure 3.14: Left: layout of CSC chamber, showing the panels made up of strips and wires which detect muons passing through the chamber [56]. Right: picture of me (right) and Shalhout Z. Shalhout (left) working on the upgrade of a ME+1/1 chamber [60].

(TOTEM) detector is separate from CMS, there is a close partnership between the experiments, as they share the same interaction point.

In $p + p$ collisions, nearly 90% of the energy deposited in the detector is in the HF (in heavy-ion collisions this value heavily depends on the geometry of the collision). Although much of the interesting and usable information from the collisions is at midrapidity, the information obtained by the HF is critical in reconstructing collisions and triggering. By looking at the distribution of the sum of the transverse energy deposited in the HF, heavy-ion collisions can be split into fractions of the total hadronic inelastic cross section. Looking at the energy deposited in the HF is also used to determine whether a collision is interesting enough to keep or if it is an event coming from a beam gas collision.

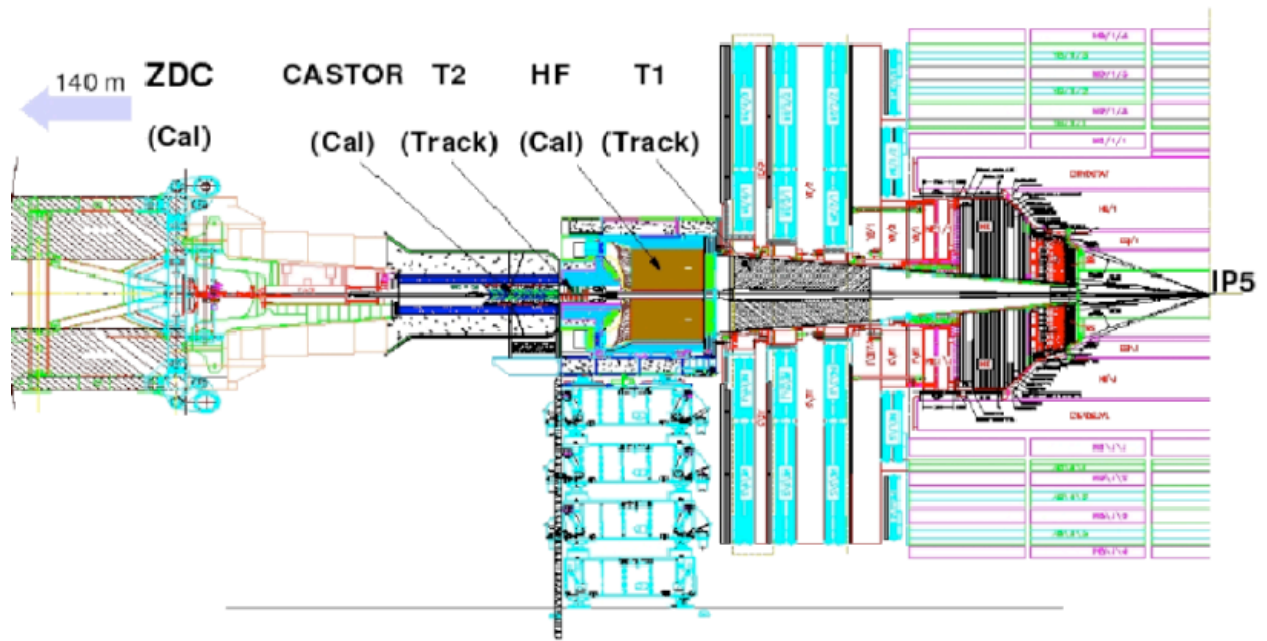


Figure 3.15: Layout of the detectors in the CMS/TOTEM forward region at the LHC point 5. TOTEM is made up of trackers T1 and T2, as well as the Roman Pots which are placed 147 m and 220 m from the interaction point [56].

Chapter 4

Data Selection, Simulation and Reconstruction

4.1 Triggering

The LHC has and will continue to reach collision levels that push the boundaries of the ability of current technology to record, interpret and process data. With approximately 600 million collisions occurring every second, determining what events are important to record becomes crucial for using resources wisely. Having a system that can handle this level of decision making is therefore central to discovering new physics from the collisions occurring at CMS. CMS has developed a multi-tiered trigger system built to handle the maximum crossing frequencies of 40 MHz reached with the crossing interval of 25 ns for $p + p$ collisions. This trigger system is also designed to be flexible enough to run in p +Pb and Pb+Pb environments while selecting the events of interest.

For the purposes of describing the general trigger system, the relevant parameters stated will be those from high luminosity $p + p$ running (at a bunch crossing frequency of 40 MHz). In the heavy-ion group's running of $p + p$, p +Pb and Pb+Pb, the frequency of collisions is decreased due to a significant decrease in instantaneous luminosity. In the high luminosity $p + p$ collisions, since the overall output capability of the read-out system is 150 Hz, the combined level-1 (L1) trigger and high-level trigger (HLT) systems are responsible for reducing the rate by over a factor of 10^6 .

This enormous reduction is done through prioritizing the physics signals of interest and creating trigger menus that achieve those goals by balancing background reduction while still keeping a high signal efficiency.

The L1 trigger is based on programmable electronics that make fast decisions depending on the hits in various subdetectors. The general idea is that coarse information from the tracker, calorimeters and muon chambers is used to make the initial L1 decision. The higher resolution data is stored in a pipeline for later use in the HLT if the L1 requirements are met. Since the design of L1 can handle a trigger output rate of 100 kHz, we run L1 at 30 kHz in order to be safe. The events that pass the L1 trigger have their full read-out data sent to the data acquisition (DAQ) system where the HLT takes over. The HLT uses a large cluster (over 10K cores) of workstations with vast computing power (50 TFlops, or the equivalent of 12K 1.8 GHz CPUs) to run offline reconstruction algorithms on fully-assembled event information and make software-based trigger decisions to determine which events will be recorded. After the HLT, the maximum designed output for the entire menu is 150 Hz for $p + p$ collisions. Once an event is triggered, the DAQ records the event (which is on the order of 1 MByte for $p + p$ collisions and 12 MBytes for Pb+Pb collisions) locally, where it is either permanently stored directly at CERN, or sent to a storage facility in the tiered data storage system set up for CMS. This event data can then be grouped into datasets that can be studied with the hopes of further understanding QCD.

Although the functions of the trigger systems are very similar when running Pb+Pb and $p + p$ collisions, the events themselves differ greatly. Figure 4.1 shows an interesting event in $p + p$ at a center-of-mass energy of 8 TeV, showing the ability of CMS to resolve electrons and muons. In heavy-ion collisions, the level of background in the detector makes discovering the signal much more challenging, as can be seen from a central Pb+Pb collision in Fig. 4.2. Due to the larger data size, the number of heavy-ion events that CMS is able to write out is smaller than for $p + p$ but, since the event frequency is much lower in heavy ions, the fraction of events that are read out compared to the total number of minimum bias (MB) events is on the order of 10^3 .

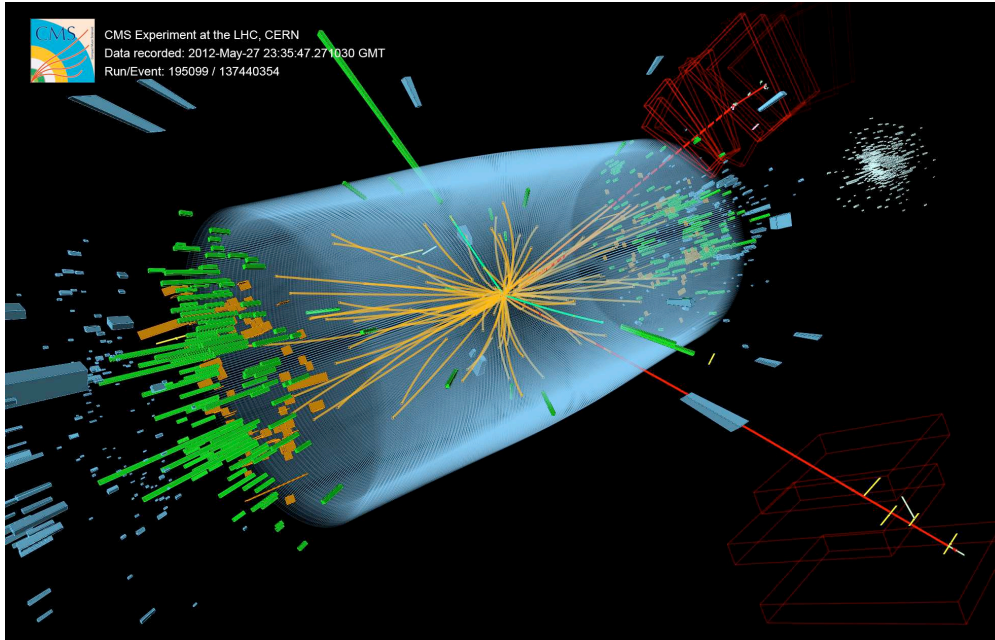


Figure 4.1: Event recorded with the CMS detector in 2012 at a proton-proton centre-of-mass energy of 8 TeV. The event shows characteristics expected from the decay of the Higgs boson to a pair of Z bosons, one of which subsequently decays to a pair of electrons (green lines and green towers) and the other Z decays to a pair of muons (red lines). The event could also be due to known Standard Model background processes [61].

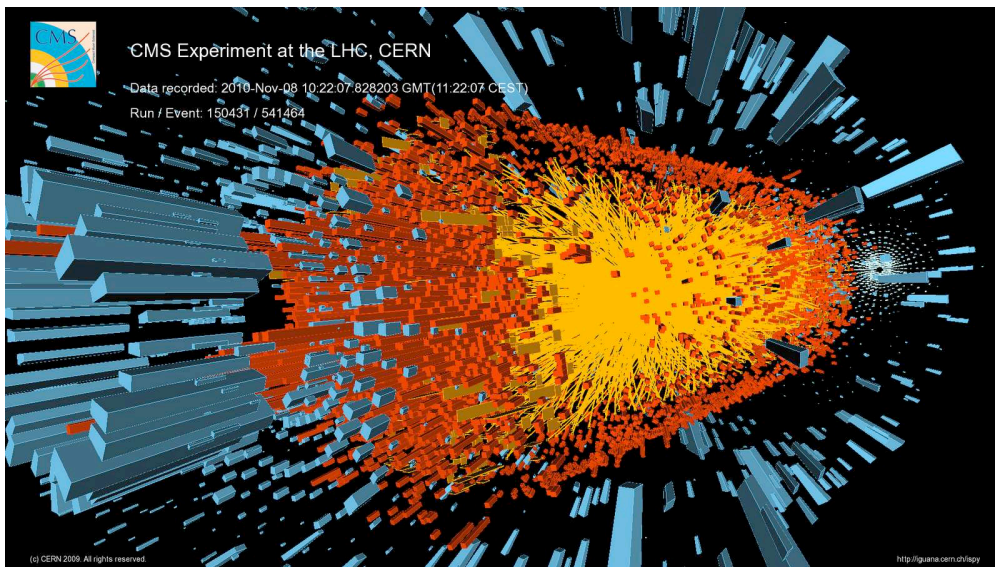


Figure 4.2: Central Pb+Pb event in the CMS detector in 2011 at a centre-of-mass per-nucleon energy of 2.76 TeV. The yellow tracks show the tracks in the inner tracker, the red bars show the energy deposited in the ECAL and the blue bars show the energy deposited in the HCAL [62].

4.1.1 The Muon Trigger System

The muon triggers rely on information from all three muon systems. The hits detected in the DT chambers provide information that can be combined in order to reconstruct muon-track segments in the barrel, the CSCs provide information to form muon track segments in the endcaps and the RPC trigger chambers provide hits with excellent timing resolution. Each system uses different requirements to determine whether a muon hit has occurred at which point, muon-track segments are formed from a combination of those hits. The muon triggers were initially limited to $|\eta| \leq 2.1$ although, for the $p + p$ and Pb+Pb runs analyzed in this dissertation, the limitations of the muon triggers are $|\eta| \leq 2.4$.

Each of the tracks formed is identified as a muon candidate. The DTs, barrel RPCs, CSCs and endcap RPCs each send up to four muon candidates ordered by their quality to the Global Muon Trigger (GMT). The GMT then sends this information to the Global Trigger (GT) which either accepts or rejects the event based on whether the muon candidates satisfy any triggers on the L1 menu. This L1 trigger may be entirely based off the coarse information from the muon system or may require a coincidence with information from other sub-detectors. For the purposes of this thesis, the L1 muon triggers used were based entirely on the information from the muon systems.

If the event is accepted at the L1 level, the data from the detector is sent to the DAQ. Common HLT algorithms for the muon trigger menu take information from the tracker and the muon chambers to create global muons. In order to pass an HLT trigger, these global muons may either have kinematic conditions on them (single muon with $p_T > 20$ GeV), or may be counted in order to have a minimum number of particles (two electrons and two muons which each have $p_T > 10$ GeV), or may be combined with other physics objects (including other muons) to form physics objects of interest (four leptons with an invariant mass greater than 50 GeV). If the muon objects satisfy a trigger that is part of the trigger menu, the event is accepted and the DAQ records the event.

4.1.1.1 Muon Triggers in Pb+Pb

During the 2011 Pb+Pb run, the muon HLT menu contained a combination of double and single muon triggers in order to select events for the dimuon analyses. Out of the 100 Hz trigger output

allotment during the heavy-ion run, the dilepton group was given a quarter. This allotment was used for collecting all of the data used by the dilepton group. Signals are prioritized in a way that each analysis receives enough statistics to do a meaningful study for that signal. In some cases this means pre-scaling triggers for high statistics signals that will take up the full trigger bandwidth by some factor N (pre-scaling means sequentially ignoring $(N-1)/N$ of the events when looking at that trigger). The main priorities for the dimuon group in choosing the trigger menu were the following signals:

- **J/ψ :** the J/ψ has a small mass (~ 3 GeV), and can decay to two oppositely charged muons. In order to detect a J/ψ , the best trigger is one that requires two muons with no p_T cut. Due to the frequency of having two muons in the chambers during an event, a combination of a heavily pre-scaled trigger with two muons with no p_T cut and a less heavily pre-scaled trigger with two muons with a p_T cut of 3 GeV are chosen for the J/ψ analysis.
- **Υ :** the Υ has a mass of ~ 9.5 GeV, and can decay to two oppositely charged muons. The unrescaled trigger chosen for measuring Υ production requires two muons with a p_T cut of 3 GeV. The p_T cut is set at 3 GeV in order to keep the number of background events down while keeping the efficiency high for measuring the Υ . Figure 4.3 shows an Υ candidate decaying to two muons in a Pb+Pb collision.
- **W^\pm bosons:** the W^\pm bosons have a mass of ~ 80 GeV. A W boson can decay to one muon which carries the charge of the W , and one muon neutrino. Since the signal that the neutrino leaves in the detector is missing energy, it is easier to set up the trigger to collect events with one high- p_T muon. The trigger chosen for measuring W^\pm production requires one muon with a p_T cut of 15 GeV. This p_T cut is high but, due to the large mass of the W boson, 97% of muons coming from the W satisfy the trigger requirement. A W boson event candidate can be seen in Fig. 4.4, showing the high p_T muon (red line on the display) in an event with a large momentum imbalance which is the signal for a muon neutrino coming from the W decay.
- **Z boson:** the Z boson has a mass of ~ 90 GeV and can decay to two oppositely charged

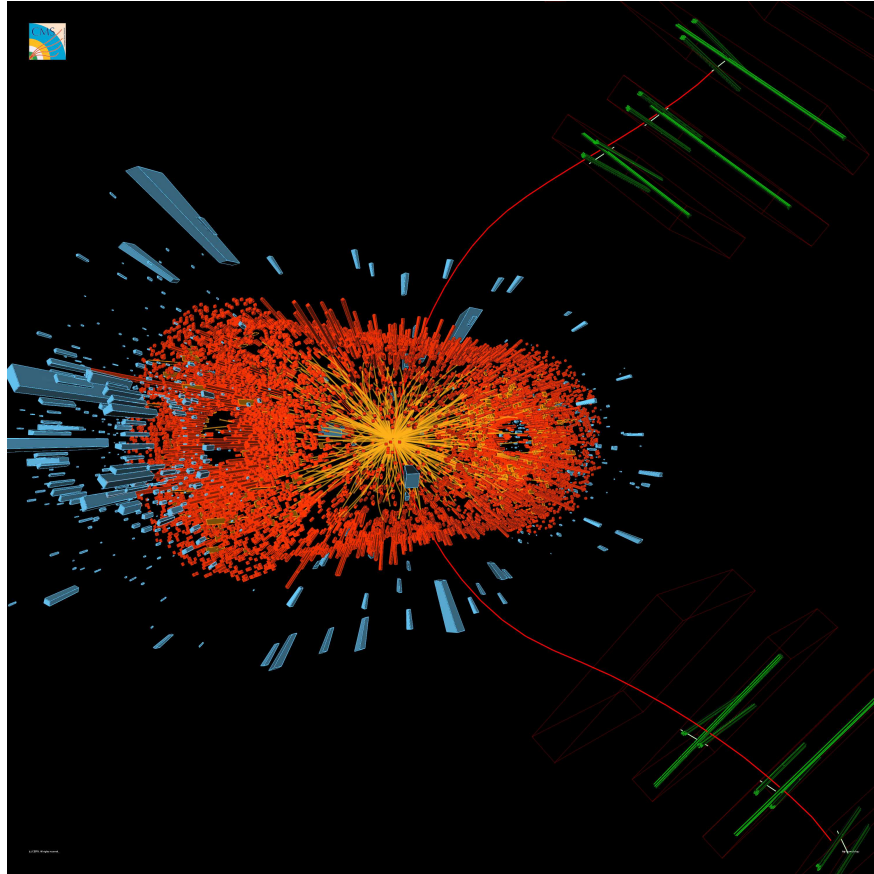


Figure 4.3: Candidate for Υ production and decay to two muons observed in a Pb+Pb collision at the LHC. The two red lines (tracks) are the two muons, the mass of orange lines are tracks from other particles produced in the collision, whose energy is measured in the electromagnetic calorimeter (red parallelepiped) and the hadron calorimeter (blue parallelepiped) [63].

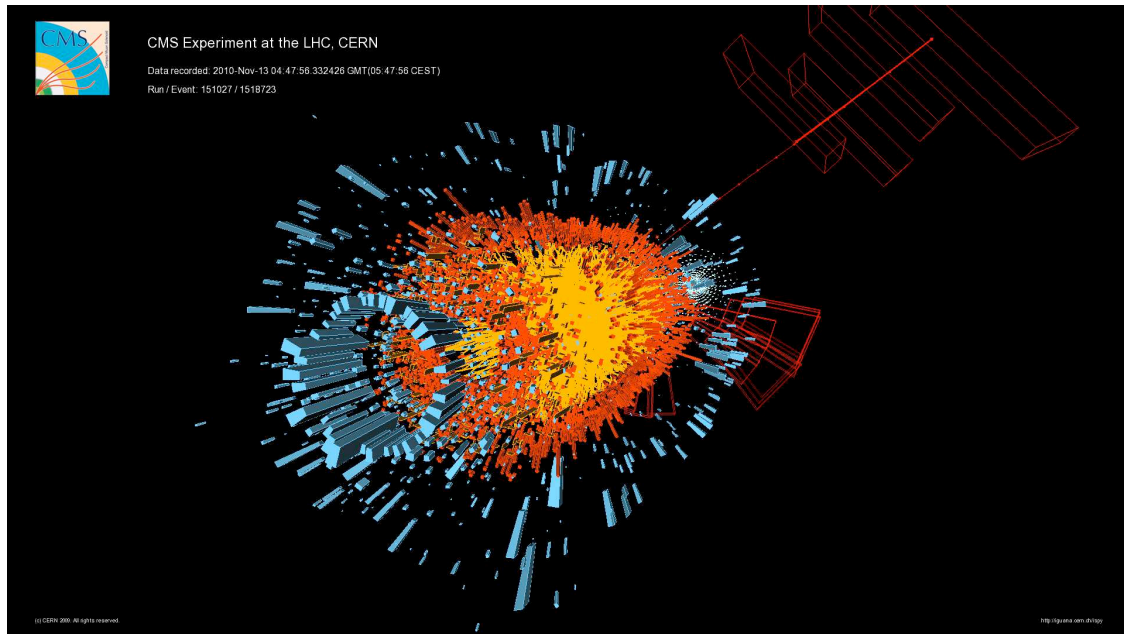


Figure 4.4: Event display in a central Pb+Pb collision showing an event triggered by the Single Muon 15 trigger, which is consistent with W boson production. The momentum imbalance measured in the transverse plane is $43 \text{ GeV}/c$ and the muon (red line on the display), which is detected in the Muon Drift Chambers, is produced with a $\eta = -0.7$ [18].

muons. The trigger chosen for measuring Z production requires one of the decay muons to have a p_T greater than 15 GeV. Since both muons from the Z typically have $p_T > 40$ GeV/ c , this trigger is 99% efficient and significantly cuts background events. A Z boson event candidate can be seen in Fig. 4.5, showing the high p_T muons (two red lines) and the calorimeter background in green. This demonstrates that although the Pb+Pb events display a large amount of activity since a central Pb+Pb event can have the equivalent of ~ 2000 binary nucleon-nucleon collisions, the signal from the Z boson is clean and clear.

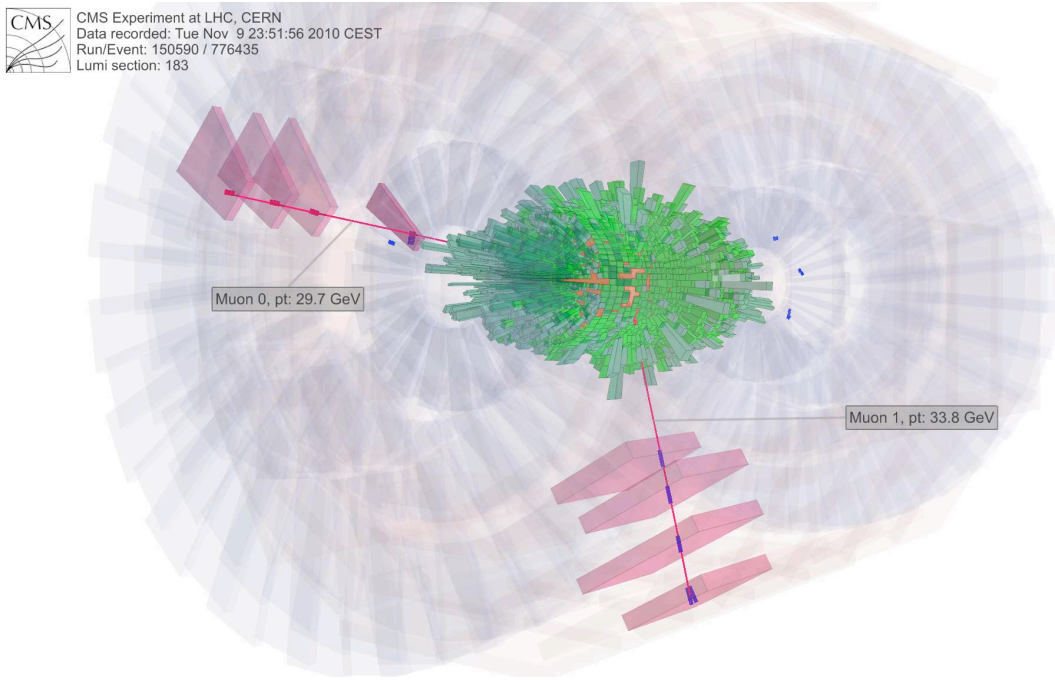


Figure 4.5: Candidate Z boson decaying to two muons (two red lines) in a Pb+Pb heavy-ion collision at CMS. The green indicates energy deposits in CMS from other particles produced. Note that the high- p_T muon tracks are basically straight, compared to those of the Υ shown in Fig. 4.3 [64].

For the 2011 run, the overall performance of the muon systems and triggers in Pb+Pb were phenomenal, resulting in high resolution measurements of the signals mentioned. Most of the particles and resonances that can be seen in the dimuon invariant mass spectrum are shown in Fig. 4.6. Specifically, during the Pb+Pb run there were 1022 events triggered by Z bosons decaying to two muons.

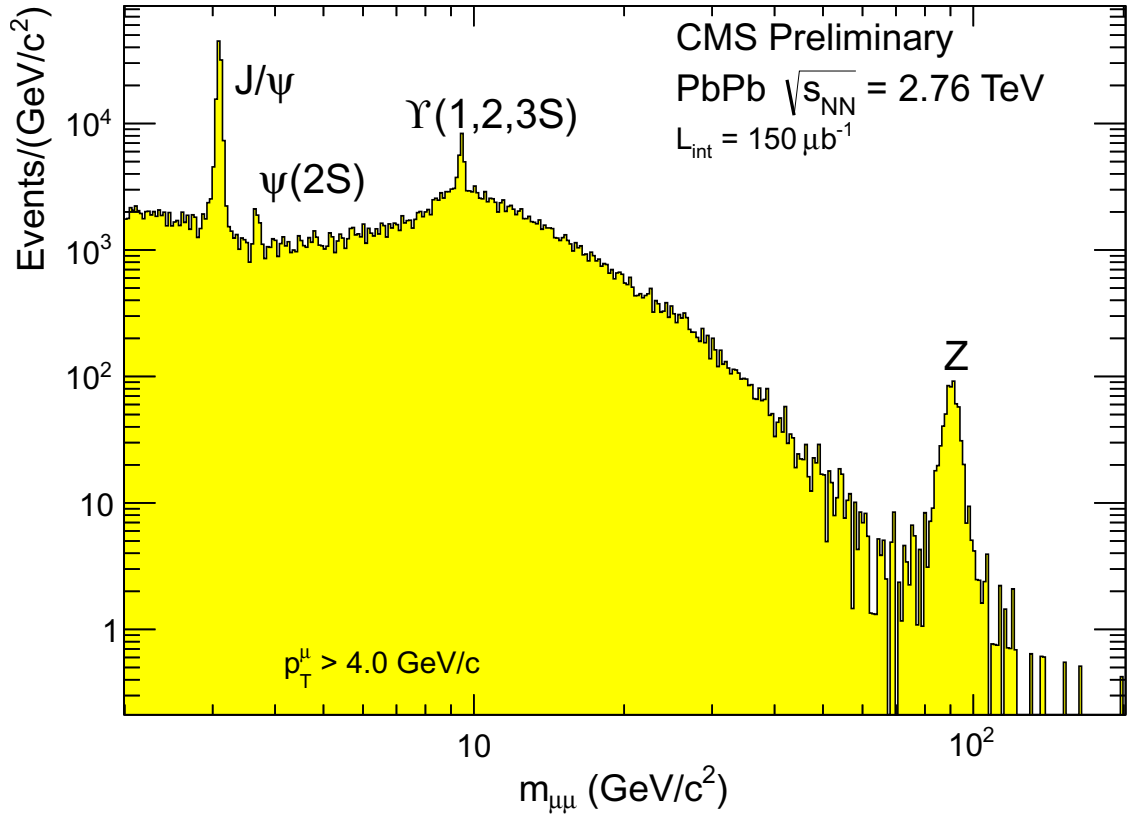


Figure 4.6: The standard “Yellow Plot” shown at conferences by the dilepton group, showing the dimuon invariant mass spectrum from the events collected with the dilepton trigger menu. The ρ , ω and ϕ are shown at low mass, the quarkonia peaks at intermediate mass, and the Z boson peak at high mass. Since the W bosons do not decay to 2 muons, there is not a visible peak associated with W boson production and decay [65].

4.1.1.2 Muon Triggers in $p + p$

Overall, the trigger menu used during the $p + p$ run in 2012 was chosen with the same priorities as those in the Pb+Pb run. Due to the lower background rates in $p + p$, the pre-scale levels for the lower- p_T muon triggers were significantly decreased. The trigger chosen for the measurement of Z boson production in the dimuon decay channel in $p + p$ collisions required two muons with no explicit p_T requirement, and had a trigger efficiency of 99%. This trigger had no prescale during the entire run, resulting in a total of 830 Z bosons produced in $p + p$ collisions decaying to two muons.

4.1.2 The Electron Trigger System

The electron triggers rely on information from the tracker, the ECAL, and the HCAL systems. The energy measurement from the ECAL is the most important for triggering on a high energy electron. The ECAL is divided into regions, with each region consisting of trigger towers. When an event occurs, all of the energy deposited in the calorimeters is added up to obtain trigger tower transverse-energy (E_T) measurements. The trigger algorithm for the ECAL begins by finding hot areas in each ECAL region. This is done by finding the largest trigger tower E_T deposit, and adding the E_T from the neighboring tower with the most energy deposited.

At this point, depending on the trigger, these deposits are sent to the Regional Calorimeter Trigger (RCT), where the trigger will either be accepted or rejected based on the size of the energy deposits in the ECAL and the size of the energy deposits in the HCAL. Those triggers that are designed to only get photons or electrons will require a large deposit in the ECAL without having a significant energy deposit in the same kinematic region of the HCAL. This veto is referred to as an *isolation cut* since the desire is to isolate electrons and photons from hadronic background.

4.1.2.1 Electron Triggers in Pb+Pb

Due to the large background in Pb+Pb events, calorimeter triggers must either be heavily pre-scaled, or be very selective and only select events requiring large energy deposits. At the trigger level, it is nearly impossible to distinguish between a high energy electron or photon depositing a large

amount of energy in the ECAL. For this reason, a diphoton trigger was used for measuring the Z decaying to two electrons. A trigger requiring two significant energy deposits in the ECAL was chosen where one deposit had an $E_T > 20$ GeV and the other one an $E_T > 15$ GeV. Although the ECAL extends to $|\eta| \leq 3.0$, the electron and photon triggers used in this analysis were limited to $|\eta| \leq 1.44$.

The efficiency for this trigger in keeping events where the Z boson decays to two electrons was approximately 96%. One of these events is shown in Fig. 4.7, where the two large energy deposits show the trajectory of the two electrons coming from Z boson decay.

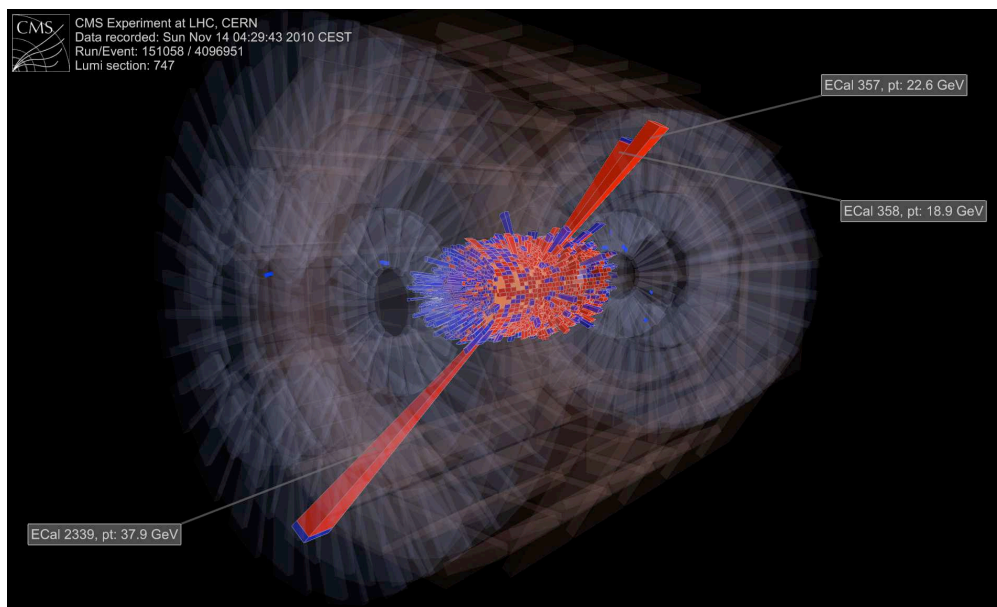


Figure 4.7: Candidate Z boson decaying to two electrons (two tallest red tower groups) in a Pb+Pb heavy-ion collision at CMS. The other red and blue towers indicate energy deposits in CMS from other particles produced [64].

4.1.2.2 Electron Triggers in $p + p$

In order to stay consistent with the trigger used in Pb+Pb, the same trigger requirements were used for the measurement in $p + p$, as well as the same η limitations. The efficiency of this $p + p$ trigger for keeping Z boson decays to two electrons was approximately 99%. The difference in the efficiency comes from the fact that an improved energy-clustering algorithm was developed and

used in the $p + p$ collisions, compared to the one used during the Pb+Pb run.

4.2 Event Selection and Cleaning

The trigger menu is set up to only select physics signals of interest in the detector. Unfortunately, during the running of the LHC, there are several background processes that can satisfy those triggers and fill up the trigger menu bandwidth without giving any useful physics. Each of these backgrounds must be understood in order to set up trigger vetoes to save precious space in the trigger menu and space in the final storage systems. Some of these processes, such as cosmic rays passing through the detector or beam gas events, are constantly occurring but have signals that can be used to recognize them and remove them either online or offline. Others such as power failures or software update errors in the subdetector systems cannot be solved with simple gating and must instead be marked and removed from the final analysis datasets.

CMS has extensive online and offline data quality monitoring for the data collected during running. Each luminosity section used in analyses is validated by the respective subdetector systems personnel for the respective subdetector systems, in order to be confident that the data collected comes from a fully functioning CMS detector. For the Z to dimuon analyses in Pb+Pb and $p + p$, only data where the tracker and muon systems were fully functioning are used, while, for the Z to dielectron analyses in Pb+Pb and $p + p$, only data where the tracker, ECAL and HCAL were fully functioning are used.

4.2.1 Event Selection and Cleaning in Pb+Pb

During the running of CMS, there is the need to select “in time” events which occur when two beams are actually crossing as well as collision events that deposit sufficient amounts of energy in both forward calorimeters. These two conditions are very effective for removing much of the background processes that occur during collisions. Specifically, the triggers used were gated on a combination of information from the beam pick-up timing detector (BPTX) which determines when a bunch crossing occurs, and the beam scintillation counter (BSC) and HF which collect energy from the underlying event in order to make sure the event was not obviously a beam-gas event.

There are also several offline cuts that are made after the datasets are recorded. Some of these repeat what was done at the trigger level but using more information from the detector. Other cuts are used to remove specific types of background that were recognized after the runs were completed. These backgrounds include beam gas, PKAM (Previously Known As Monsters) and UPC (ultra-peripheral collisions) events, and are described below. These cleaning cuts have only a small effect on the number of selected events and are standard selection cuts used by all heavy-ion analyzers:

- **BSC halo-filter:** events in which any of the BSC halo bits fired are excluded from the analysis. These are events that have very small HF energy and quite a large number of pixel hits. These events are due to the beam halo extending out to the radius of the pixel detector but not reaching the HF. This filter removes most of the beam gas events not removed by the HF coincidence condition.
- **HF energy:** An additional offline HF coincidence condition is imposed. This is made by requiring at least 3 towers on each side of the interaction point in the HF with at least 3 GeV energy deposited per tower. This condition is most effective in removing UPC events.
- **Primary vertex condition:** The requirement of a reconstructed primary vertex with two or more tracks is imposed. In peripheral events, all tracks above 75 MeV/ c transverse momentum were used to reconstruct the vertex. In central events, the minimum p_T cut was increased to 700 MeV/ c and the tracking region was narrowed in η to keep the maximum number of fitted tracks stable around 40–60, ensuring time-efficient reconstruction.
- **PKAM removal:** These events were originally called “monster events” as the large number of hits in a single pixel readout channel leading to timeouts were not understood. They were later recognized as tracks that hit the pixel sensors, resulting in a large number of pixels above threshold and renamed PKAM events. In PKAM events, the HF energy deposits are much smaller for a given number of pixel hits than for normal Pb+Pb collisions. To remove these events, we require that the pixel cluster length in the tracker is compatible with the vertex. This cut, in combination with the BSC halo-filter cut, eliminates all of the PKAM

events. The compatibility variable is the number of clusters that have a length (in global z direction) that is compatible with the reconstructed vertex, divided by the number of hits that are compatible with an artificially displaced vertex position (that is offset by ± 10 cm). If this ratio is high, that indicates a well defined vertex and a good collision. If the ratio is about unity, that indicates that the vertex is ill-defined, a characteristic feature of PKAM events. At very low pixel multiplicity values, the compatibility is allowed to be low in order to keep events that have a little larger background hit fluctuation but otherwise good collisions. Therefore a cut is applied to remove events with high number of pixel hits and a low value of the compatibility variable.

In order to keep consistency among all analyses, the CMS heavy-ion group created JavaScript Object Notation (JSON) files that represent the “golden” luminosity sections for the Pb+Pb run which are used to remove those luminosity sections where CMS was not functioning at full capacity. The appropriate JSON files were used for the Z to dimuon and dielectron analyses. The combination of the selection and cleaning cuts made verifies that the data used in this analysis came from Pb+Pb collisions recorded in a fully functioning CMS detector.

These criteria select $97 \pm 3\%$ of hadronic Pb+Pb collisions, corresponding to a number of efficiency corrected MB events, $N_{\text{MB}} = (1.16 \pm 0.04) \times 10^9$ for the sample analyzed. The predicted cross section for Pb+Pb hadronic inelastic collisions at $\sqrt{s_{NN}} = 2.76$ TeV is 7.65 ± 0.42 b, according to a Glauber Monte Carlo (MC) simulation [42, 66] with the same parameters as in Ref. [40], which results in an integrated luminosity of about $150 \mu\text{b}^{-1}$.

4.2.2 Event Selection and Cleaning in $p + p$

Due to the cleaner $p + p$ running environment, there are fewer background events to be removed. The beam-gas and cosmic ray filtering are done in the same way as in Pb+Pb, where there are vetoes set up both in the triggering and in offline cuts.

For the $p + p$ run, the CMS heavy-ion group also created JSON files that represent the “golden” luminosity sections for the $p + p$ run, and the appropriate JSON files were used for the Z to dimuon and dielectron analyses. Again, the combination of the selection and cleaning cuts made verifies

that the data used for the $p + p$ analysis came from $p + p$ collisions recorded in a fully functioning CMS detector.

The $p + p$ data set corresponds to an integrated luminosity of 5.4 pb^{-1} , known to an accuracy of 3.7% based on a van der Meer scan [67]. The uncertainty on the luminosity is due to the uncertainty in the calibration of the beam cross section.

4.3 Centrality Determination

The centrality of a collision is an important parameter for Pb+Pb collisions. It is defined by the geometrical overlap of the incoming nuclei and allows the Pb+Pb data to be split into centrality classes ranging from peripheral, where there is little overlap in the colliding nuclei, to central, where there is nearly complete overlap in the colliding nuclei. In CMS, the centrality of a Pb+Pb collision is defined through bins that correspond to fractions of the total hadronic inelastic cross section as observed in the distribution of the sum of the transverse energy deposited in the HF calorimeters. Figure 4.8 shows how the events are split up in centrality in CMS. The centrality classes used in this analysis are 50–100% (most peripheral), 40–50%, 30–40%, 20–30%, 10–20%, and 0–10% (most central), ordered from the lowest to the highest HF energy deposited.

Each centrality class will select a distribution of impact parameters (b). The average b of the distribution is monotonically related to each centrality class. Each class results in a different average number of participating nucleons ($\langle N_{\text{part}} \rangle$) and a different number of average binary collisions ($\langle N_{\text{coll}} \rangle$). There is a commonly used theoretical model, the Glauber model, for estimating the $\langle N_{\text{part}} \rangle$, $\langle N_{\text{coll}} \rangle$ and $\langle b \rangle$ values for the centrality classes. If an effect is expected to scale with N_{part} or N_{coll} , such a hypothesis can be tested using the calculated values of N_{part} or N_{coll} for a given centrality class.

More binary collisions and participating nucleons will result in an increase in most physics processes for that event, regardless of whether or not a QGP is formed. The Glauber model allows the study of differences between centrality classes to give information about the formed QGP instead of effectively just showing that more central events involve higher values of N_{part} and N_{coll} . The centrality-related quantities calculated in the Glauber model, as described in Ref. [42, 66], are

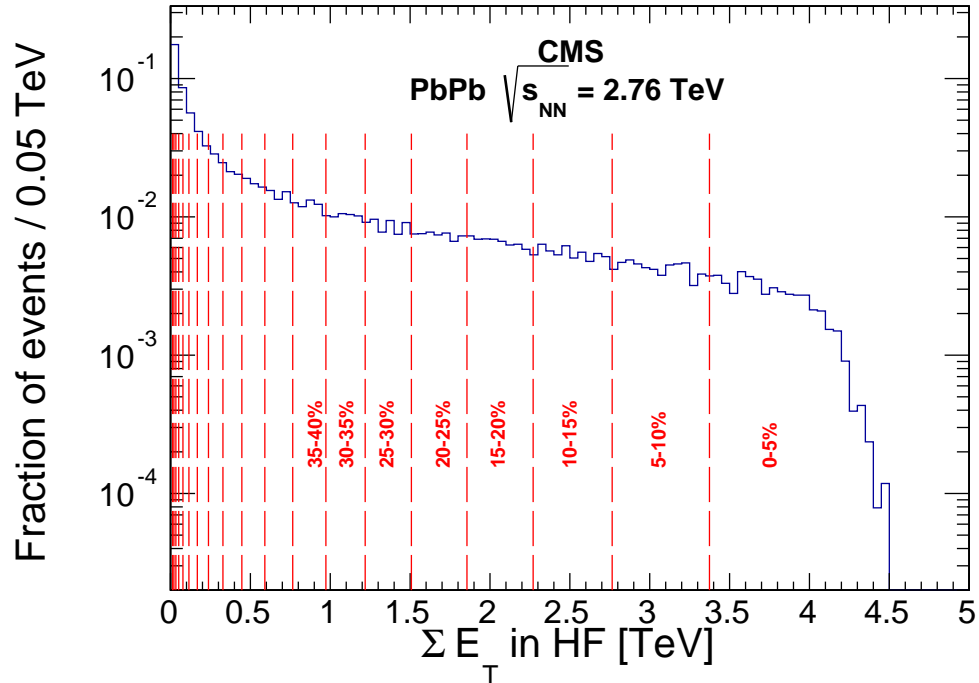


Figure 4.8: Fraction of events as a function of the sum of E_T deposited in the HF. The red lines show how the Pb+Pb centrality bins are split up, in order to distinguish between more central events (those near 0-5%) and more peripheral events (those with less E_T deposited in the HF, and near 100%) [68].

summarized in Table 4.1. The same Glauber model parameters are used as in Ref. [40], namely standard parameters for the Woods-Saxon function that distributes the nucleons in the Pb nuclei, and a nucleon-nucleon inelastic cross section of $\sigma_{NN}^{\text{inel}} = 64 \pm 5$ mb, based on a fit to the existing data for total and elastic cross sections in proton-proton and proton-antiproton collisions [69].

When measuring the nuclear modification factor, R_{AA} , the corrected Z -boson yields in Pb+Pb collisions are compared to those in $p+p$ collisions, by scaling the $p+p$ yields by the nuclear overlap function, T_{AA} . The scaling by T_{AA} accounts for the increased probability of hard scattering in the nucleus-nucleus collision compared to $p+p$ collisions. At a given centrality, T_{AA} -scaled Z -boson yields can be directly compared with the Z -boson production cross sections in $p+p$ collisions. In units of mb^{-1} , the average T_{AA} goes from 0.47 ± 0.07 to 23.2 ± 1.0 , from the peripheral 50–100% to the central 0–10% centrality ranges.

Table 4.1: The average numbers of participating nucleons ($\langle N_{\text{part}} \rangle$), binary nucleon-nucleon collisions ($\langle N_{\text{coll}} \rangle$), and the nuclear overlap function ($\langle T_{AA} \rangle$), corresponding to the centrality ranges used in this analysis.

| Centrality | $\langle N_{\text{part}} \rangle$ | $\langle N_{\text{coll}} \rangle$ | $\langle T_{AA} \rangle$ (mb^{-1}) |
|------------|-----------------------------------|-----------------------------------|---|
| [50, 100]% | 22 ± 2 | 30 ± 5 | 0.47 ± 0.07 |
| [40, 50]% | 86 ± 4 | 176 ± 21 | 2.75 ± 0.30 |
| [30, 40]% | 130 ± 5 | 326 ± 34 | 5.09 ± 0.43 |
| [20, 30]% | 187 ± 4 | 563 ± 53 | 8.80 ± 0.58 |
| [10, 20]% | 261 ± 4 | 927 ± 81 | 14.5 ± 0.80 |
| [0, 10]% | 355 ± 3 | 1484 ± 120 | 23.2 ± 1.00 |
| [0, 100]% | 113 ± 3 | 363 ± 32 | 5.67 ± 0.32 |

Although each centrality bin of $X\%$ contains the same number of events, regardless of whether they are central or peripheral events, production of hard probes such as Z bosons scales with N_{coll} , leading to the shape shown in Fig. 4.9. In the figure, bin 0 corresponds to the top 2.5% most central events and bin 40 corresponds to the 5% most peripheral events. A strong centrality dependence is seen since, in central collisions, the number of colliding nucleon-nucleon pairs is much larger than that expected peripheral collisions, and the number of muon-triggered events is mostly driven by $\langle N_{\text{coll}} \rangle$. Once the number of muon triggered events is scaled down based on $\langle N_{\text{coll}} \rangle$, resulting in the average production per binary collision, the distribution versus centrality will be effectively flat.

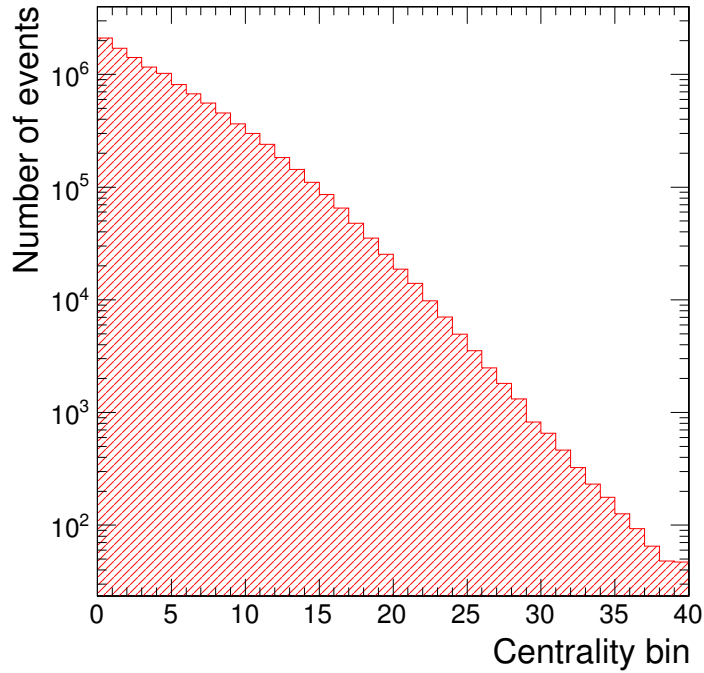


Figure 4.9: Centrality distribution of the muon triggered events.

4.4 Simulation

On top of the data that is collected at CMS, the $Z \rightarrow \mu^+\mu^-$ and $Z \rightarrow e^+e^-$ analyses require simulated datasets in order to correct the data yields for losses in efficiency due to acceptance effects and the cuts that are applied. The simulation scheme used is the Monte Carlo (MC) method which simulates data by either applying random sampling of flat distributions and weighing the sample to match predicted distributions, or by applying random sampling directly to predicted distributions. The method used for the simulation of this data is the latter, using random sampling of the predicted distributions relevant to Z production and decay. These simulated MC datasets must be validated by being compared to what is actually seen in data and can then be used to correct for effects seen in the data.

Although the simulated Z boson signal will be similar in $p+p$ and Pb+Pb events, the backgrounds will be very different due to the large multiplicities seen in the CMS detector during Pb+Pb collisions. For this reason, both $p+p$ and Pb+Pb event simulation begins with simulating a

$p + p$ collision where a Z boson is produced and decays to two muons or electrons. This is done by simulating the electroweak processes $Z \rightarrow \mu^+\mu^-$ and $Z \rightarrow e^+e^-$ using the PYTHIA 6.424 [70] next-to-next-to-leading-order (NNLO) generator with the $Z2^*$ tune. This tune is designed to match the charged particle multiplicity measured by CMS at \sqrt{s} values of 0.9, 2.36, and 7 TeV. The processes used in the PYTHIA simulation were those specific to Z boson production in combination with the interference term from Drell-Yan, and the decays were constrained to be only to dimuons or dielectrons. The detector response to each PYTHIA signal event is simulated with a realistic simulation of the CMS detector using GEANT4 [71].

For the $p + p$ event, this is the end of the simulation step, but for the Pb+Pb event, the signal is taken and embedded in a realistic heavy-ion background event. These background events are produced with the HYDJET 1.8 next-to-leading-order (NLO) event generator [72] and then simulated with GEANT4 as well. The HYDJET parameters are tuned to reproduce the measured particle multiplicity for different centralities. The embedding is done at the level of detector hits, and the signal and background events share the same generated vertex location. After the simulation step is carried out, the simulated events are processed through the trigger emulation and the full event reconstruction chain in order to match as closely as possible what is carried out in getting the data from CMS.

For each decay channel, and for each collision system, Z bosons are simulated in six different $Z p_T$ bins. These bins are $[0 - 20]$, $[20 - 40]$, $[40 - 60]$, $[60 - 80]$, $[80 - 100]$, $[100 - \infty]$ GeV/ c . Although one bin with a $Z p_T$ of $[0 - \infty]$ GeV/ c could have been used, the vast majority of the simulated Z s would be at low p_T , as can be seen in Fig. 4.10, resulting in larger uncertainties for the corrections applied to the high p_T Z s. A different solution to this is to simulate an even larger amount of events but, due to the significant cost to simulate and store these events, this solution does not end up being a good choice. Instead 20,000 simulated events are generated in each $Z p_T$ bin previously mentioned by changing the \hat{p}_T parameter in PYTHIA. Each dataset is then weighted based on the relative cross section in order to match the predicted $Z p_T$ distribution. This provides large statistics for the entire range of $Z p_T$ while keeping the datasets a reasonable size.

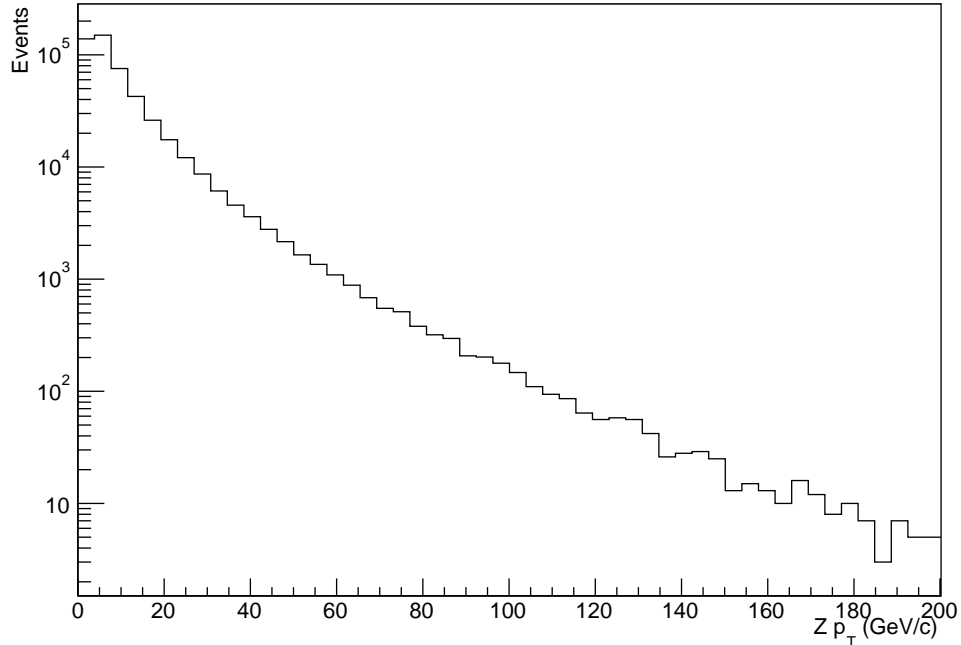


Figure 4.10: Distribution of $Z p_T$ for $\simeq 500,000$ Z bosons generated in PYTHIA.

4.5 Lepton Reconstruction

After the data from the collisions have been recorded, and the MC events have been simulated, these data must be converted from a series of numbers recorded by each subdetector to a meaningful and detailed picture of an event. This process is called reconstruction and often involves taking information from various subdetectors and combining it into physics objects that contain their energy and trajectory information. Since the physics objects of interest for these analyses are muons and electrons, these will be the focus of the reconstruction description.

4.5.1 Muon Reconstruction

Muons are reconstructed using a global fit to a track reconstructed in the muon detectors matched to a track reconstructed in the silicon tracker.

The process begins with reconstructing tracks in the muon detectors, known as “standalone muons” (STA muons). In order to form these tracks, an algorithm is used to take the hits from all three muon systems and form tracks using a series of iterations of fitting hits to a track and

removing those hits from the list of available hits. The iterations continue until all hits are part of the track of an STA muon.

These STA muons are then matched to tracks reconstructed in the silicon tracker using an algorithm optimized for the heavy-ion environment. Due to the difference in multiplicity in the tracker during Pb+Pb and $p + p$ collisions, the tracker reconstruction algorithms are significantly different for the two collision systems. Although the algorithms from $p + p$ work in Pb+Pb, the time required for running the reconstruction is prohibitively expensive. Therefore the main difference between the algorithms relates to the track clustering, which begins with doublet seeds (two hits in the tracker that are close together in (η, ϕ)) in $p + p$ collisions, and begins with triplet seeds (three hits in the tracker that are close together) in Pb+Pb collisions.

In the previous measurement of Z production in the dimuon channel by CMS [17], the tracker reconstruction algorithm in Pb+Pb carried out three iterations combining hits in the tracker to form track segments where hits that were part of formed tracks were removed after each iteration. The first two iterations began with triplet seeds, while the third formed tracks using a heavily limited set of doublet seeds. These limitations allowed for the fast reconstruction of tracks but came at the cost of only achieving a single-muon reconstruction efficiency of $\simeq 85\%$ for muons from Z -boson decays with $p_T^\mu > 20 \text{ GeV}/c$. The regional iterative (RegIt) tracking algorithm, designed for optimized tracker reconstruction in Pb+Pb, improved the efficiency by increasing the number of iterations carried out using an expanded set of doublet seeds compared to the previous reconstruction algorithm. This improved the single-muon reconstruction efficiency to $\simeq 98\%$ for muons from the Z -boson decays with $p_T^\mu > 20 \text{ GeV}/c$, reaching the efficiency level of the algorithm used for $p + p$ collisions.

The algorithm that actually matches the STA muon to the tracker tracks does so by first taking the STA muons and matching them with tracks in the tracker in a specific $\eta - \phi$ range to minimize the χ^2 for the global fit of these two tracks. Once this matching is done, a *Global muon* is formed, which contains all the information from the tracker and the muon systems. These Global muons are the physics objects used in the Z to dimuon analysis, and further cuts based on the information contained in these objects can be used to remove “fake muons”.

4.5.2 Electron Reconstruction

Electrons are reconstructed using a global fit to a *supercluster* of energy deposits in the ECAL matched to a track reconstructed in the silicon tracker.

The first step is to create the superclusters in the ECAL. Electrons traversing the silicon tracker emit bremsstrahlung photons and deposit energy in the ECAL with a significant spread in the azimuthal direction. An algorithm for clustering E_T deposits from particles passing through the ECAL and building the superclusters is used in order to estimate the proper energy of electrons in the ECAL, as in Ref. [19]. It also takes into account the bremsstrahlung emissions as it attempts to reconstruct the electron energy [73]. Due to the significant amount of energy deposited by the underlying Pb+Pb event in the ECAL, background subtraction is also required to get the energy scale correct. Energy scale corrections based on MC are also applied in Section 5.2.3 to improve the final measurement of electrons from the Z boson decay.

The track reconstruction in the tracker is done in the same manner as described in the muon reconstruction section. The only difference is that for the electron reconstruction in Pb+Pb, the original lower efficiency track reconstruction algorithm is used. The RegIt tracking was done on the data that was filtered for the muon analyses and, although the reconstruction time was more manageable, it still required a great deal more offline resources than the original reconstruction. Since this analysis was done on a separate set of skimmed data, the RegIt reconstruction would need to be done separately. Since the dielectron channel has significantly lower statistics than the dimuon channel, the decision was made not to run the RegIt reconstruction.

Combining the superclusters with tracks in the tracker is also done in a similar way to what is done for muon reconstruction. The tracks in the pixel detector closest in kinematic space (p_T , η and ϕ) to the superclusters are found and used to construct the *Global electron*, which contains all the information from the tracks in the tracker and the supercluster that make it up. These Global electrons are the physics objects used in the Z to dielectron analysis. Further cuts based on the information contained in these objects can be used to remove “fake electrons”.

The standard algorithms and identification criteria presented in Ref. [74] are used for the $p + p$ sample, resulting in a reconstruction efficiency of about 98% for $p_T^e > 20$ GeV/ c electrons from

the Z -boson decays. For Pb+Pb collisions, the electron reconstruction efficiency is about 85% for $p_T^e > 20$ GeV/ c electrons from the Z -boson decays due to the lower tracking efficiency for Pb+Pb collisions without RegIt tracking.

Chapter 5

Analysis of $Z \rightarrow l^+l^-$ in Pb+Pb at

$$\sqrt{s_{NN}} = 2.76 \text{ TeV}$$

Once the data have been recorded, cleaned, and reconstructed, they are ready to be analyzed. The first step of this analysis is to set the cuts to be used in order to remove as much background as possible from fake leptons while still keeping a high efficiency. The effect of these cuts is then compared to what is seen in data and what is seen in MC. This process is described in Section 5.1. The next step is to look at the energy scale and resolution seen in data compared to MC. Depending on how different the resolution is in data and MC resolution corrections, in the form of energy scale corrections, MC oversmearing, and resolution unfolding, may need to be applied. These steps are described in Section 5.2.

After the resolution corrections have been applied, defining and measuring the signal and background in bins of p_T , y and centrality is carried out in Section 5.3. The final part of measuring the yields is measuring the overall acceptance and efficiency corrections required to correct for losses in the signal, shown in Section 5.4. Although the uncertainties in the measurement are described in some detail throughout the chapter, Section 5.5 summarizes the measurement of the uncertainties for this measurement.

Each section will describe what is done in general, and then will be split into the treatment for muons relative to that for electrons.

Since the Tag and Probe (TNP) method used to compare efficiencies seen in data compared to MC is essential for this study, a large fraction of the effort for the completion of this thesis was devoted to the estimation of efficiencies via the TNP method. Therefore, Section 5.6 presents a detailed exposition of the method as used for the present work.

5.1 Lepton Selection and Identification

In order to keep as much signal as possible, the strategy for this analysis is to apply loose cuts. This approach is possible due to the relatively clean signal the Z provides once a high- p_T lepton cut is made. Especially in the muon channel, the low occupancy of the CMS muon chambers from the relatively low rate of high- p_T muons in Pb+Pb at 2.76 TeV provides a nearly pure Z signal in the dimuon channel.

5.1.1 Muon Identification

In order to remove objects that reach the muon stations that are not muons (such as high- p_T “punch through” hadrons), muon identification cuts must be made which require a set of selection criteria on each muon track. Although there are muons from background sources that are present even with optimized cuts, a significant amount of these background processes, such as cosmic rays and heavy-quark semileptonic decays, can be rejected by an appropriate selection of cut variables. For the purpose of this analysis, the muons used are prompt high p_T muons with cuts matching those recommended for high- p_T muons in the heavy-ion environment by the CMS Muon Physics Object Group (POG). They differ slightly from the cuts used in the latest Z boson measurement in $p+p$ collisions [9] in that no isolation cuts are used. The isolation cuts used in the $p+p$ collision environment rely on a sufficiently low occupancy in the calorimeters which is not the case in the heavy-ion environment.

- $|\eta^\mu| < 2.4$: this cut on the η of the muon is due to the limit of the muon station coverage.
- $p_T > 20$ GeV/ c : this removes a small portion of the generated Z s, but keeps the muon spectrum above the trigger efficiency turn-on curve. This cut is the most effective cut in

reducing the background while keeping the efficiency high.

- The muon must be found by both the global and tracker muon algorithms. Asking for the latter helps reject decays-in-flight, punch-through, and matching with noise, background tracks, or segments.
- The global muon must have at least one valid hit in the muon chamber once the final fit is preformed ($N_{\text{hit}} > 0$).
- The global muon must be matched to more than one muon station, which cuts down on the possibility of punch-through.
- The global muon must have hits in at least 1 pixel layer.
- The global muon must have hits in more than 4 tracker layers.
- $\chi^2/\text{ndf} < 10$ for the global fit. This cut is chosen to be very loose, and removes some fake tracks from real data. This cut has the least correlation with the rest of the cuts since events removed by this cut are not taken out by the other cuts.
- $|d_z(\text{prim_vtx})| < 0.5$ mm (inner track), the longitudinal distance of closest approach to the primary vertex.
- $|d_{xy}(\text{prim_vtx})| < 0.02$ mm (inner track), the transverse distance of closest approach to the primary vertex.

The cuts listed are studied in the reconstructed MC simulated dataset and the effects of all quality cuts are shown in Table 5.1. The table summarizes the values of the cuts for the analysis and the percentile of signal in simulation kept independently by each cut in the third column and after all the other cuts are applied in the last column. All cuts are applied after applying the trigger selection of one muon with a $p_T > 15$ GeV/c.

In order to make sure the generated MC is representative of the data, Fig. 5.1 shows the MC distributions plotted together with the distributions from real data. The reconstructed MC muons coming from the Z are shown in the green histogram and the reconstructed global muons from

Table 5.1: Quality cuts applied to global muons.

| Cut variable | Cut value | Only this cut | All except this cut |
|------------------|----------------------|---------------|------------------------|
| IsTrackerMuon | true | 99.07 % | 95.41% |
| Muon Valid Hits | > 0 | 99.11 % | 96.21% |
| Matched Stations | > 1 | 97.68 % | 96.70% |
| Tracker Layers | > 4 | 99.98 % | 95.42% |
| Pixel Layers | > 0 | 99.63 % | 95.77 % |
| GlobalChi2 | < 10 | 98.80 % | 96.47% |
| | $ d_z $ < 0.5 mm | 99.99% | 95.40% |
| | $ d_{xy} $ < 0.02 mm | 99.98 % | 95.42% |
| All cuts applied | | 95.40 % | |

the Z candidate muon pairs in data are shown with the red points. For each variable plotted, all cuts were applied except for the cut on the variable shown. All of the variable distributions are normalized to unity. For most of the variables, the muons from HI data Z candidates (red points) match the distributions from MC Z s (green histogram). When a discrepancy between the two is seen, the cut on the variable is made loose enough so as not to affect the results. This can be shown by taking the ratio of the integral of the distribution passing the cut in both MC and real data (RD), shown on each plot. For perfectly matching distributions, this ratio should be equal to 1. The vertical dashed purple lines give the cut values used in the analysis.

Table 5.1 shows that $< 5\%$ of the signal is lost when applying all of the quality cuts. The largest loss comes from requiring more than one matched station. This is also the muon quality cut responsible for the largest cut on the background.

5.1.2 Electron Identification

Electron candidates are built from the reconstruction of superclusters and their associated tracks. Unlike the muons, the electrons have a significant amount of background from hadrons and photons. Thus tighter cuts are required on the electron candidates in order to achieve a significant decrease in the background. The electron identification variables used in the Pb+Pb analyses were the same as those used in the $\sqrt{s} = 7$ TeV $p + p$ analyses [7, 8] although the cut values were optimized for the Pb+Pb environment. The requirements used in the selection process that have been found to

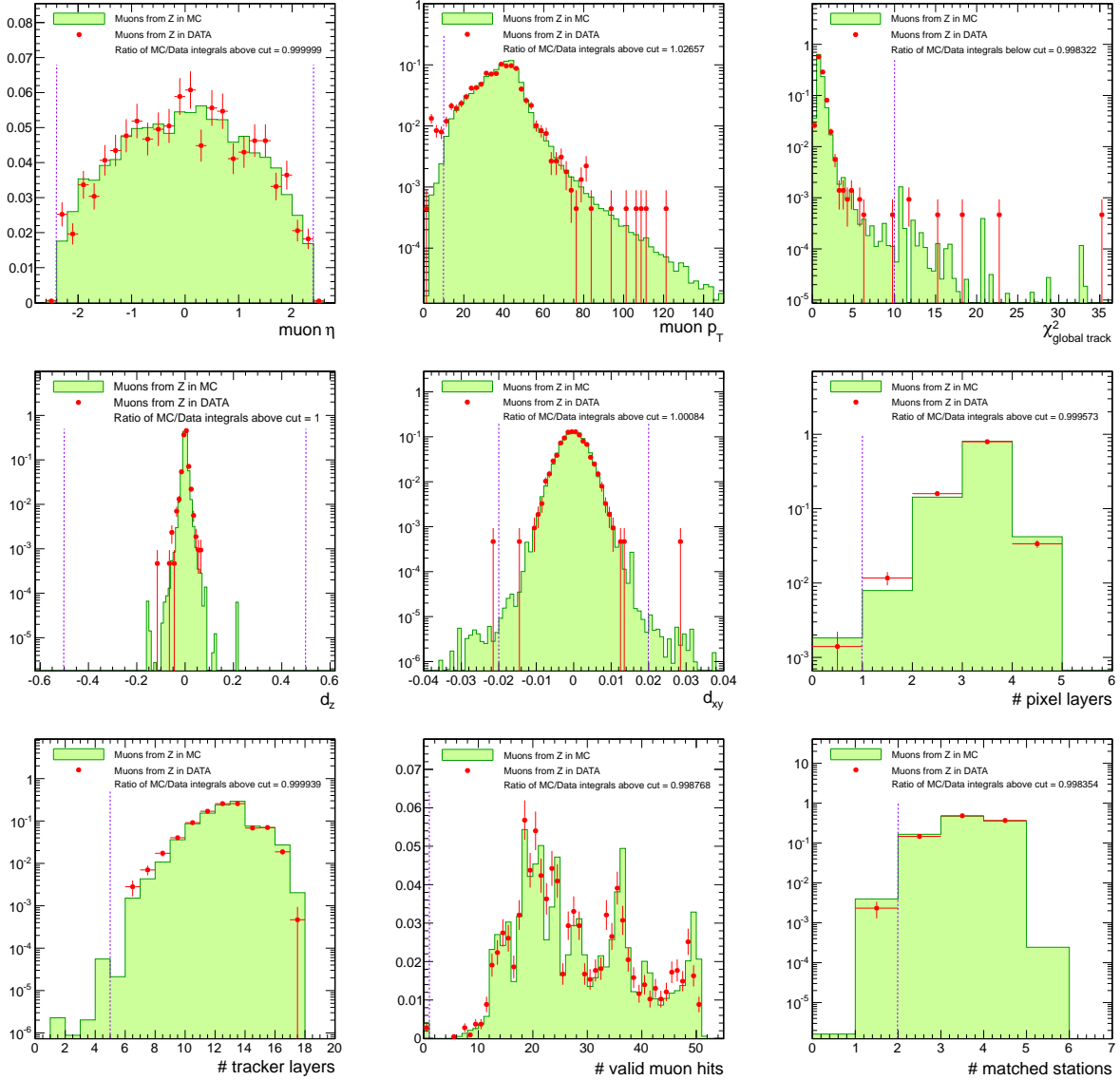


Figure 5.1: Single global muon quality distributions in the Pb+Pb collision system, from HYDJET background events with one Z embedded per event (green histogram) and from the real data Z candidates (red points). All other cuts are applied to the muons but the one displayed. The histograms are normalized to unit area. The vertical dashed bars indicate the cut values used.

be the most effective in reducing the background while keeping the largest signal (see Ref. [74] for a more detailed definition of the variables) are:

- $p_T^e > 20 \text{ GeV}/c$, p_T^e is the p_T of the electron used in the analysis. The trigger used effectively sets an online cut requiring one supercluster with $E_T > 20 \text{ GeV}$ and one with $E_T > 15 \text{ GeV}$, based on energy deposited in the ECAL. After reconstruction, an offline cut requiring electrons to have $p_T > 20 \text{ GeV}/c$ is set.
- $|\eta_e| < 1.44$ where η_e is the η of the electrons. This cut was made based on the limitation of the trigger used to this η region.
- $|1/E_{sc} - 1/p_{T_track}| < 0.05$ characterizes the combined cut on supercluster energy and track p_T that identifies the track and superCluster as coming from an electron. These are expected to be close. A large distance represents a difference in the measured supercluster and track energy which likely means the track was incorrectly matched to the supercluster.
- $|d_{xy}(\text{prim_vtx})| < 0.02 \text{ mm}$ (inner track), characterizes the distance of closest approach of the electron track to the primary vertex in the transverse direction. A large distance usually is a result of an electron resulting from a secondary decay, or a poor global fit.
- $H/E < 0.2$, where H is the energy deposited in the HCAL towers in a cone of radius $R = 0.15$ centered on the electromagnetic supercluster position and E is the energy of the electromagnetic supercluster. This variable is useful to reject the candidates originating from jets, which carry not only electromagnetic energy, but also hadronic energy.
- $|\Delta\eta_{in}| = |\eta_{sc} - \eta_{in}^{\text{extrap}}| < 0.03$, where η_{sc} is the energy-weighted position in η of the supercluster and $\eta_{in}^{\text{extrap}}$ is the η coordinate of the position of closest approach to the supercluster position, extrapolating from the innermost track position and direction. This is also a measure of how well the track from the tracker and the supercluster match.
- $|\Delta\Phi_{in}| = |\Phi_{sc} - \Phi_{in}^{\text{extrap}}| < 0.15$, where Φ_{sc} is the energy weighted position in Φ of the supercluster and $\Phi_{in}^{\text{extrap}}$ is the Φ coordinate of the position of closest approach to the supercluster

position, extrapolating from the innermost track position and direction. Along with $\Delta\eta_{in}$, it helps to determine how well the track and supercluster match.

- $\sigma_{i\eta i\eta} < 0.011$ characterizes the shower shape in the η direction. The larger the value of $\sigma_{i\eta i\eta}$, the larger the energy spread of the energy deposited in the ECAL. For a high- p_T electron hitting the ECAL, the energy spread is fairly tight. Further description is found in Section 5.1.2.1.

The cuts listed are studied in the reconstructed MC simulated dataset. The effects of all quality cuts are shown in Table 5.2. The table summarizes the values of the cuts for the analysis. The percent of the simulated signal kept by each cut independently is given in the third column while the signal remaining after all other cuts are applied is given in the last column. All cuts are applied after the trigger selection is complete.

Table 5.2: Quality cuts applied to global electrons.

| Cut variable | Cut value | Only this cut | All except this cut |
|-------------------------------|-------------|---------------|---------------------|
| H/E | < 0.2 | 98.68% | 78.88 % |
| $ \sigma_{i\eta i\eta} $ | < 0.011 | 86.19% | 88.97 % |
| $ \Delta\eta_{in} $ | < 0.03 | 98.66% | 78.22 % |
| $ \Delta\Phi_{in} $ | < 0.15 | 96.86% | 80.44 % |
| $ d_{xy} $ | < 0.02 mm | 94.89% | 79.81 % |
| $ 1/E_{sc} - 1/p_{T_track} $ | < 0.05 | 93.40% | 80.44 % |
| All cuts applied | | | 78.21 % |

In order to make sure the generated MC is representative of the data, Fig. 5.2 shows the MC distributions plotted together with the distributions from real data without any background subtracted. The reconstructed MC muons coming from the Z are shown in the green histogram and the reconstructed global muons from the Z candidate muon pairs in data are shown with the red points. For each variable plotted, all cuts were applied except for the cut on the variable shown. All of the variable distributions are normalized to unity.

The plot comparing electron $\sigma_{i\eta i\eta}$ in data and MC are significantly different because there is a background present in the data that has a fundamentally different shower shape. In order to subtract the background, sideband subtraction is performed. In this case the mass bins 40 – 70

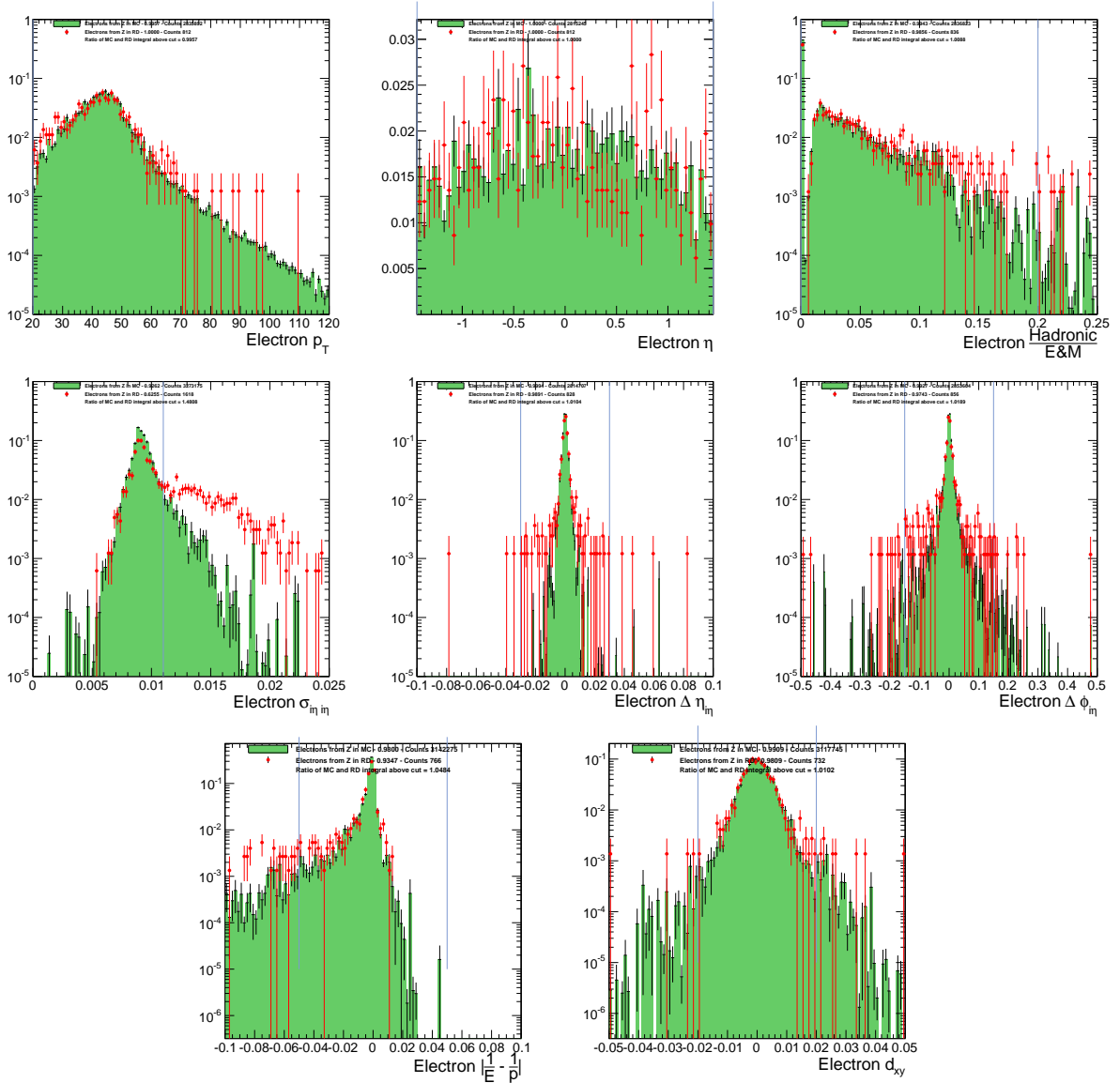


Figure 5.2: Single global electron quality distributions in the Pb+Pb collision system, from HYDJET background events with one Z embedded per event (green histogram) and from the real data Z candidates (red points). All other cuts are applied to the electrons except the one displayed. The histograms are normalized to unity. The vertical bars indicate the actual cuts used.

and $110 - 140 \text{ GeV}/c^2$ are used as the sideband regions representing the background. These values are subtracted from those in the $60 - 120 \text{ GeV}/c^2$ mass bin. The sideband subtracted results are shown in Fig. 5.3, demonstrating that the removal of background events removes the discrepancy between the data and MC.

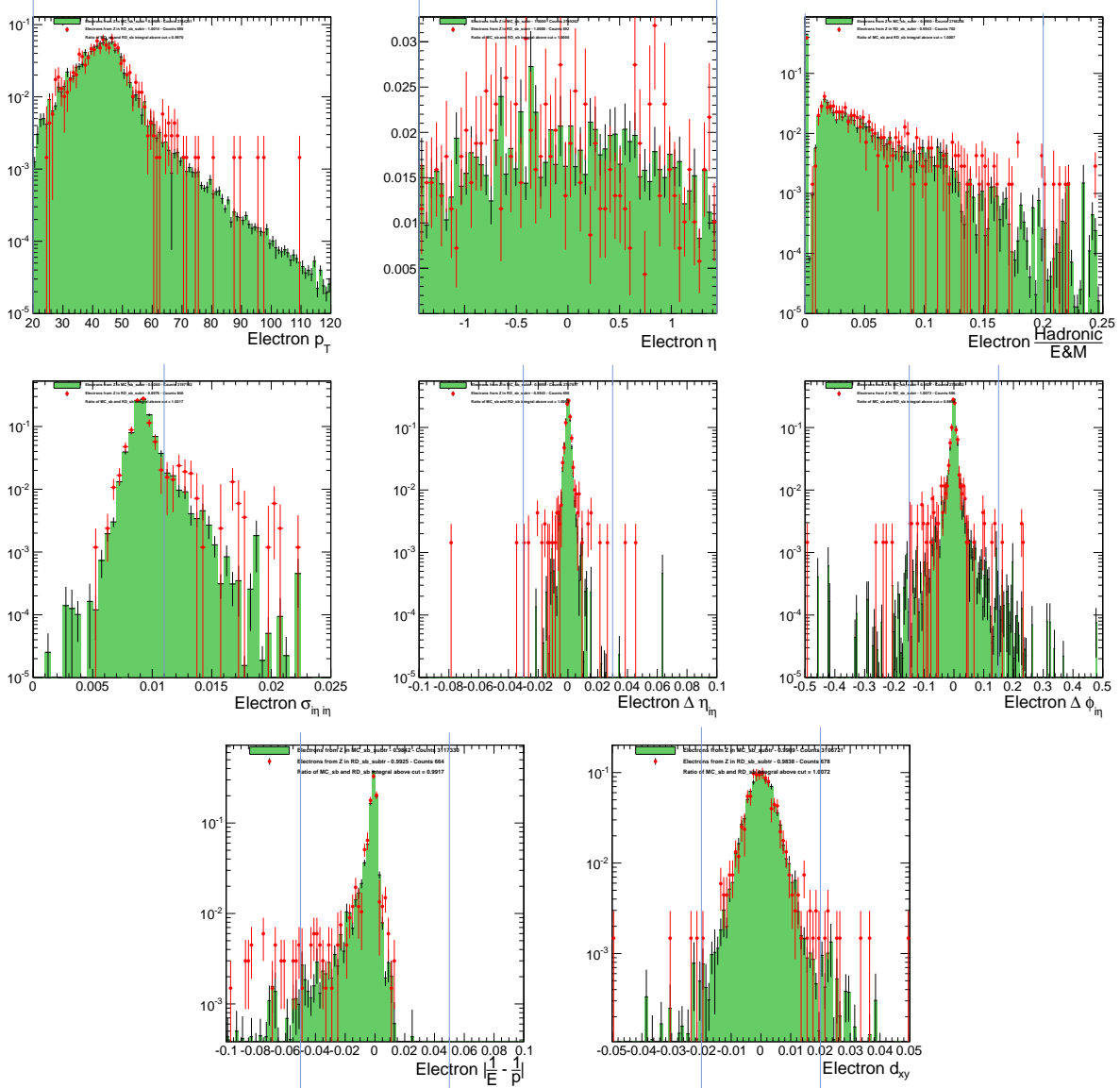


Figure 5.3: Single global electron quality distributions in the Pb+Pb collision system, from HYDJET background events with one Z embedded per event (green histogram) and from the real data Z candidates (red points). All other cuts are applied to the electrons but the one displayed. Side-band subtraction is performed, using the mass bins $40 - 70$, and $110 - 140 \text{ GeV}/c^2$ as the sideband regions. The histograms are normalized to unity. The vertical dashed bars indicate the actual cuts used.

5.1.2.1 Shower Shape Variable

To study the properties of an electron candidate, we need to investigate the cluster shape variables provided by the crystals assigned to a given cluster. The $\sigma_{i\eta i\eta}$ variable characterizes the shower shape in the η direction, defined as:

$$\sigma_{i\eta i\eta}^2 = \frac{\sum_i^{5 \times 5} w_i (\eta_i - \eta_{5 \times 5})^2}{\sum_i^{5 \times 5} w_i}, w_i = \max(0, c + \ln \frac{E_i}{E_{5 \times 5}}), \quad (5.1)$$

where E_i and η_i are the energy and pseudorapidity of the i^{th} crystal within the 5×5 electromagnetic cluster. $E_{5 \times 5}$ and $\eta_{5 \times 5}$ are the energy sum and energy-weighted average η of the 5×5 crystals. Here c is a constant effective cut on the crystal energy, fixed to 4.7 in $p + p$, studies.

The electron candidates tend to have smaller $\sigma_{i\eta i\eta}$ while hadrons and π^0 's tend to have larger $\sigma_{i\eta i\eta}$.

5.2 Resolution Corrections

In order for the MC to be trusted, it must faithfully reflect the characteristics of the data. An important aspect of the data and MC is the resolution of the mass and p_T of the Z . If these are significantly different, then the difference must be accounted for either through a correction or through assigning an uncertainty associated with that difference.

The first step is to compare the resolutions in data and MC in a data-driven way following the analysis done in Ref. [75]. This gives a general sense of the agreement between the two, as well as an idea of the level of resolution effects being dealt with. The next step is to look at the peak and resolution of the invariant mass in data compared to MC, in order to determine the need for either energy scale corrections to the data or MC oversmearing.

Finally, due to the significant p_T resolution effects that are present due to a combination of detector and final state radiation effects, unfolding is introduced in order to get a final Z p_T spectrum that can be compared to theoretical predictions.

5.2.1 Resolution Study

The resolution study was done by following the analysis done in Ref. [75]. To begin, a dilepton thrust axis is defined that maximizes the scalar sum of the projections of the p_T of the two leptons onto the axis. This axis is defined since the single-muon resolution effects occur dominantly along this axis. The dilepton p_T is then decomposed into a component parallel (a_l) and another one perpendicular (a_t) to this new axis, as shown in Fig. 5.4. In case of big resolution differences between data and MC, the mean and RMS values of these two variables will be very different with the a_l component most affected, resulting in the need for energy corrections.

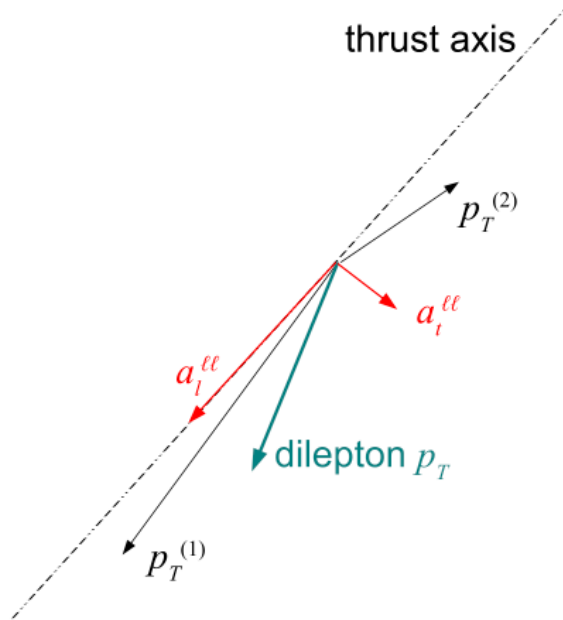


Figure 5.4: Representation of the transverse plane of the event and of the decomposition of the dilepton transverse momentum along the thrust axis [75].

5.2.1.1 Resolution Study for Dimuons

Because the dimuon signal is very clean, the dimuon channel is expected to have a high resolution with the MC and data agreeing within statistics. We plot a_l and a_t for all Z candidates from data (RD) and MC simulation in Fig. 5.5. When no p_T selection is applied to the sample, the RMS of the two variables is comparable.

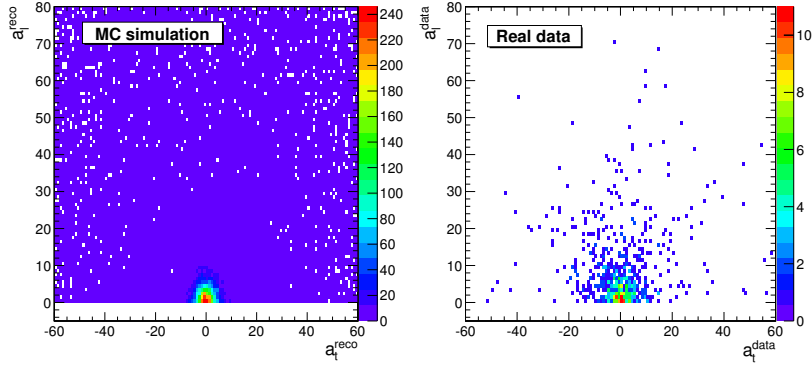


Figure 5.5: a_t versus a_l distribution for MC simulation on the left and for Z candidates from real data on the right for dimuons in the Pb+Pb collision system.

The next step is to analyze the data in p_T bins while comparing to the expectations from MC simulations. The RD and MC samples are split in the p_T bins of the analysis and the RMS and mean value of the a_l and a_t distributions are computed. Figure 5.6 shows the mean and the RMS of the a_l and a_t distributions for MC truth, MC simulation, and Z candidates in RD.

Finally, the values of the dimuon mass and p_T resolution are calculated. The results presented in Fig. 5.7 are obtained by splitting into 9 p_T bins and fitting the difference between the generated Z mass or p_T and the reconstructed value to a Gaussian. The individual fit results can be found in Appendix A and are shown in Figs. A.1 and A.5. We find a p_T resolution of better than 3% for $p_T > 40$ GeV/ c and a mass resolution better than 1.8%.

In the end, although there are some differences between the data and MC, these differences are not significant given the errors on the resolution measurement.

5.2.1.2 Resolution Study for Dielectrons

When comparing to the dimuon signal, the dielectron channel is expected to have lower resolution. The MC should reflect this decrease in resolution. The a_l and a_t for all Z candidates from real data (RD) and MC simulation look similar to those shown for the muons in Fig. 5.5, although there are fewer statistics for the data. When no p_T selection is applied to the sample, the RMS of the two variables is comparable.

The next step is to analyze the data in p_T bins while comparing to the expectations from MC

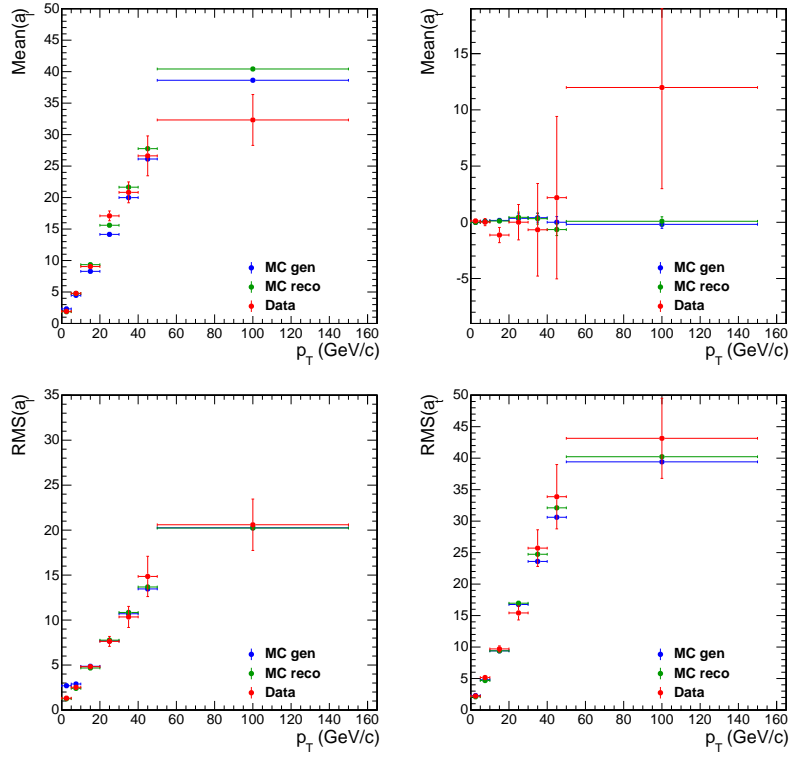


Figure 5.6: The mean (top) and the RMS (bottom) of the a_t (left) and a_l (right) distributions for MC truth, for MC simulation and for Z candidates from real data (blue squares, green triangles, and red circles, respectively), for dimuons in the Pb+Pb collision system.

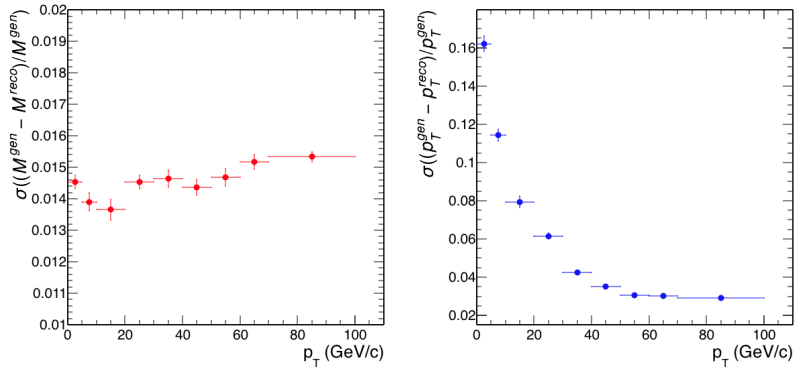


Figure 5.7: The mass resolution (left) and the p_T resolution (right) as a function of the generated p_T of the Z boson from dimuons in the Pb+Pb collision system.

simulations. The RD and MC samples are split in the p_T bins of the analysis and the RMS and mean values of the a_l and a_t distributions are computed. Figure 5.8 shows the mean and the RMS of the a_l and a_t distributions for MC truth, MC simulation, and Z candidates in RD.

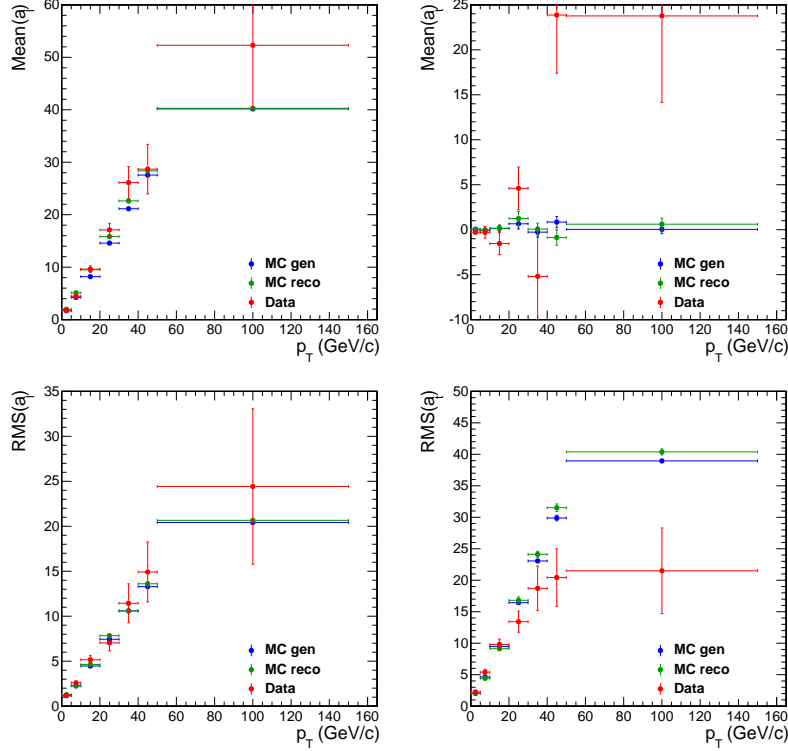


Figure 5.8: The mean (top) and the RMS (bottom) of the a_t (left) and a_l (right) distributions for MC truth, for MC simulation and for Z candidates from real data for dielectrons in the Pb+Pb collision system.

Finally, the values of the dielectron mass and p_T resolution are calculated. The results presented in Fig. 5.9 are obtained by splitting into 9 p_T bins and fitting the difference between the generated Z mass or p_T and the reconstructed value to a Gaussian. The individual fit results can be found in Appendix A and are shown in Figs. A.2 and A.6. We find a p_T resolution of better than 5% for $p_T > 40$ GeV/ c , and a mass resolution better than 3%.

The RMS a_l is the most significant value representing the resolution. It shows that the data and MC distributions match within statistics. The other values have some significant differences, although they have large statistical limitations as well. These differences will be addressed by

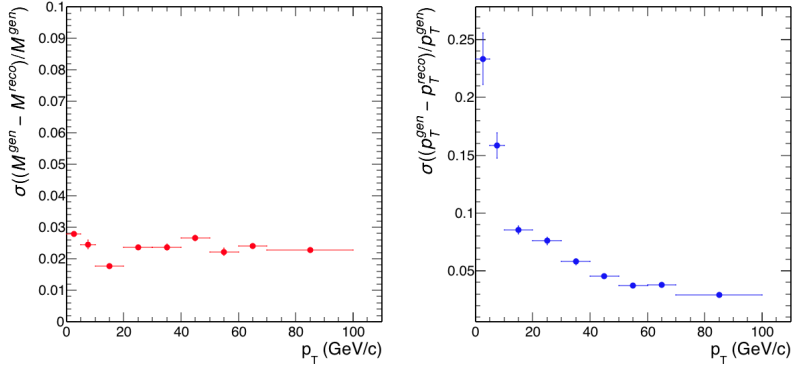


Figure 5.9: The mass resolution (left) and the p_T resolution (right) as a function of the generated p_T of the Z boson from dielectrons in the Pb+Pb collision system.

applying an energy correction to the data, and oversmearing the MC.

5.2.2 Invariant Mass Comparison

Studying the Z boson comes with the bonus that it provides a prominent peak compared to background processes. It is thus possible to compare the invariant mass distribution seen in data compared to that of the MC. If energy scale corrections are needed, the Z boson peak will be at a different mass in the data compared to MC and, if the resolution differs between the two, then the MC must be oversmeared.

5.2.2.1 Invariant Mass for Dimuons

Figure 5.10 shows the invariant mass distribution for global-global muon pairs from real data after all cuts are made. The solid points are the opposite-sign (OS) pairs, the open points represent the same-sign (SS) pairs (of which there are none in the dimuon channel). The red, filled histogram shows the invariant mass distribution seen in the MC. Since the background is negligible in the Z mass range, we can directly get the number of Z s from counting: $N_Z = 1022$ in the $[60-120]$ GeV/c^2 mass range. The number of background events from muons not coming from a Z that get matched together with other muons and fall within that mass range can be estimated by looking at the number of same-sign pairs.

Comparing data and MC, the peaks match, confirming that the muons are reconstructed with

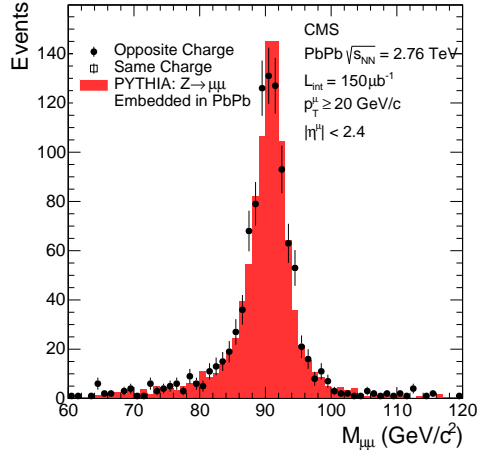


Figure 5.10: Invariant mass of global-global muon pairs in the Pb+Pb collision system, after all cuts are made. The solid points represent “Opposite charge” muon pairs in data, and the open points would represent the “Same charge” muon pairs, but none were observed in this mass range. The filled, red histogram represents the MC.

the correct energy. The MC appears to have a slightly higher resolution than the data although, given the statistics, the resolutions are reasonably similar.

5.2.2.2 Invariant Mass for Dielectrons

Figure 5.11 shows the invariant mass distribution for electron pairs from real data. The solid points are the opposite-sign pairs, the open points are the same-sign pairs and the blue, filled histogram shows the invariant mass in the MC. For Z bosons decaying into two electrons, the background is well represented by the same-sign pairs (although a charge misidentification correction will be applied later on). We can get the number of Z s from counting the number of opposite-sign pairs: $N_Z(\text{OS}) = 355$ and subtracting the number of same-sign pairs: $N_Z(\text{SS}) = 27$, resulting in $N_Z(\text{OS} - \text{SS}) = 328$ in the $[60 - 120]$ GeV/c^2 mass range.

Comparing data and MC, the peak of the data is shifted, which confirms that there is a need for an energy scale correction for the electron case. The MC also appears to have a higher resolution than the data, which may require oversmearing after the energy correction is applied.

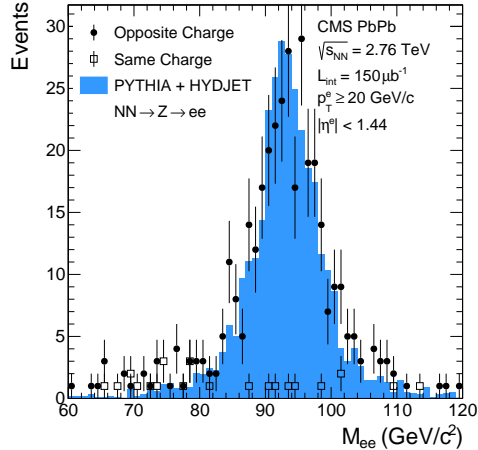


Figure 5.11: Invariant mass of electron pairs in the Pb+Pb collision system, after all cuts are made. The solid points represent “Opposite charge” electron pairs in data, and the open points represent the “Same charge” electron pairs. The blue, filled histogram represents the MC.

5.2.3 Energy Correction

Since the resolution of the muon systems is really good, and the background in the muon stations is low, little or no energy correction is expected to be needed. Due to the high background in the electron stations, it is expected that an energy correction will be needed in order to account for the background increasing the average energy present in the ECAL. By looking at the invariant mass distributions in the two decay channels, these expectations are validated. Therefore energy corrections are carried out in the electron channel.

5.2.3.1 Energy Correction for Dielectrons

Due to the underlying heavy-ion event, there can be significant differences in the average energy deposited in the calorimeters between peripheral and central events. Figure 5.12 shows the difference in reconstructed p_T compared to generated p_T for peripheral and central collisions. Electrons in central heavy-ion events are on average reconstructed with higher p_T than those reconstructed in peripheral events. This shift must be corrected for.

Although the correction due to the energy scaling has a small effect on the yield of the Z s, it will significantly change the distribution of the Z s with respect to the Z p_T and y , as well

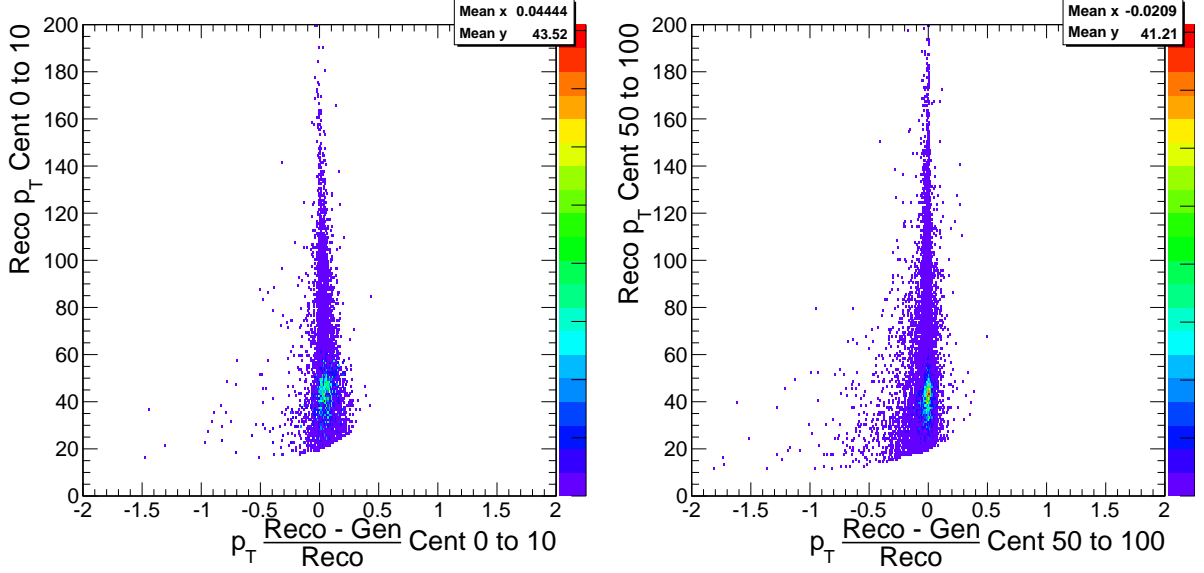


Figure 5.12: Left: 10% most central events, where on average, the p_T of reconstructed electrons is 5% greater than the generated p_T . Right: 50% most peripheral events, where on average, the p_T of reconstructed electrons is 2% smaller than the generated p_T .

as correcting the shift in the invariant mass peak. Thus, this difference needs to be corrected for. This correction is determined by taking every electron generated and comparing it to its reconstructed kinematics, $E_T(\text{reco})/E_T(\text{gen})$. Figure 5.13 shows the mean and standard deviations, sigma, of $E_T(\text{reco})/E_T(\text{gen})$ binned in centrality and E_T . The electrons are corrected by this factor, depending on their energy and event centrality.

Figure 5.14 shows the invariant mass after the energy scale correction is applied to each electron, given its reconstructed p_T and centrality.

5.2.4 Oversmearing of the MC

Once the data has been corrected, the Z boson peaks should match. When comparing the resolution of the peak, there may still be a significant difference between data and MC. If so this difference either needs to be corrected for or taken into account in the uncertainties. The first step is to determine, given the statistics of the measurement, whether or not the distributions really are different.

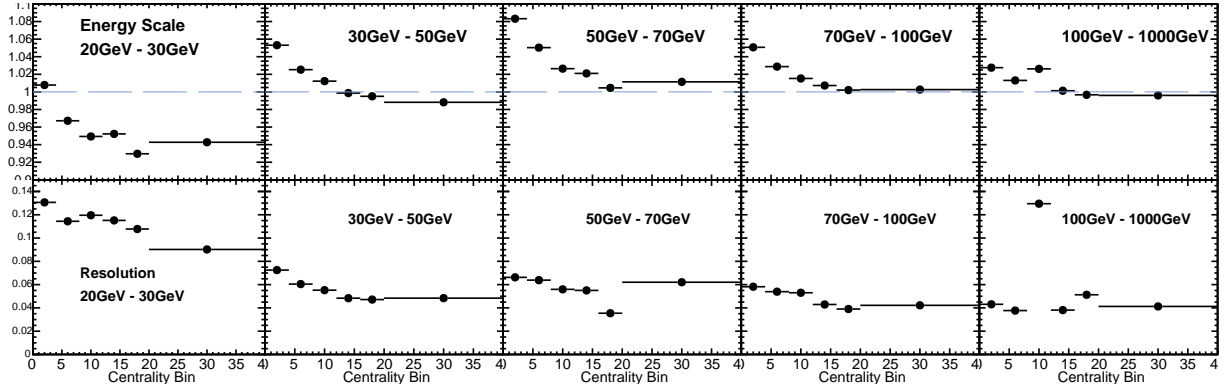


Figure 5.13: Energy scale and resolution of reconstructed electrons in the Pb+Pb collision system. MC electrons embedded in heavy-ion data were used. The energy binning used is based on the reconstructed kinematics of the electron

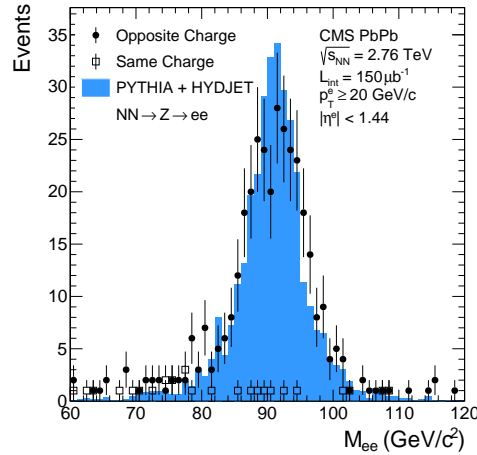


Figure 5.14: Invariant mass of electron pairs in the Pb+Pb collision system, after all cuts are made, and after the energy-scale correction is applied. The solid points represent “Opposite charge” electron pairs in data, and the open points represent the “Same charge” electron pairs. The blue, filled histogram represents the MC.

5.2.4.1 Kolmogorov-Smirnov Test

One test that can be done to determine how likely it is that the data distribution came from the underlying MC distribution is the Kolmogorov-Smirnov (KS) test [76]. This test can be used to compare either a cumulative distribution function of reference (CDF) to an empirical distribution function of the sample (ECDF) or two ECDFs. In this case, it makes sense to compare the MC as the CDF and the data as the ECDF in order to determine the likelihood that the data came from the MC distribution. If the likelihood is high, then there is no need for further correcting or smearing the energy.

The KS test is set up to be run as an unbinned test so that the goodness of fit will not change based on the chosen binning. The test steps through the cumulative probability of the two distributions. The statistic that measures the goodness of fit is the maximum distance between the two plots, as shown in Fig. 5.15.

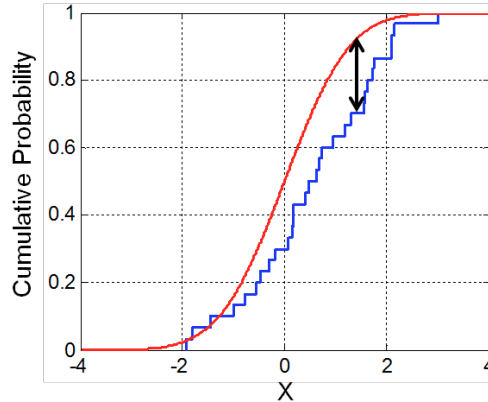


Figure 5.15: Illustration of the Kolmogorov-Smirnov statistic. The red line is CDF (MC), the blue line is an ECDF (data), and the black arrow is the KS statistic [77].

The result of the KS test comparing the data and MC in the dimuon channel is that 20% of randomly drawn distributions from the MC will fit either as well or more poorly than the recorded data. Although this is not excellent agreement, it is good enough to justify keeping the MC resolution as is, without oversmearing, and that the oversmearing correcting this difference (as described for the electron MC in Pb+Pb in Section 5.2.4.2) is insignificant.

The result of the KS test comparing the data and MC in the dielectron channel is that 6% of

randomly drawn distributions from the MC will fit as well or more poorly than the recorded data. This is poorer agreement than that in the dimuon channel. Thus oversmearing is needed to correct the MC to match the data.

5.2.4.2 Oversmearing of the Electron MC

Although the resolution does not change the overall yields, the fact that the MC has a better resolution than the data can affect the p_T unfolding to correct for resolution effects. Hence, in order to correct for this, each MC electron p_T is smeared by adding a random number from a Gaussian distribution of mean 0, and $\sigma = x$. For each smear of $\sigma = x$, the smeared MC is compared to the data. The best smearing is the one that gives the largest p -value for the KS test, in the mass range $80 - 100 \text{ GeV}/c^2$. The p -values for the various levels of oversmearing are shown in Fig. 5.16.

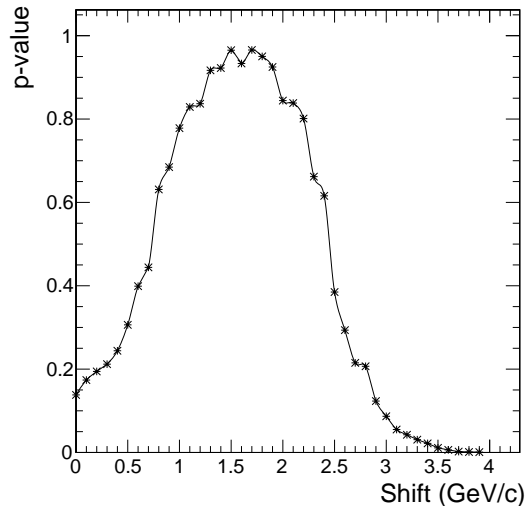


Figure 5.16: Plot shows the p -value from the χ^2 test for the MC and data distributions in the Pb+Pb collision system, showing the peak value at $1.7 \text{ GeV}/c$.

The p -value is a maximum at $\sigma = 1.7 \text{ GeV}/c$. The effect is insignificant in the overall efficiency, vs. centrality and vs. y (on the order of 0.1%). The effect is more significant in p_T due to the unfolding of resolution effects. After the oversmearing is carried out in the MC, the results of the data and MC invariant mass comparison are shown in Fig. 5.17.

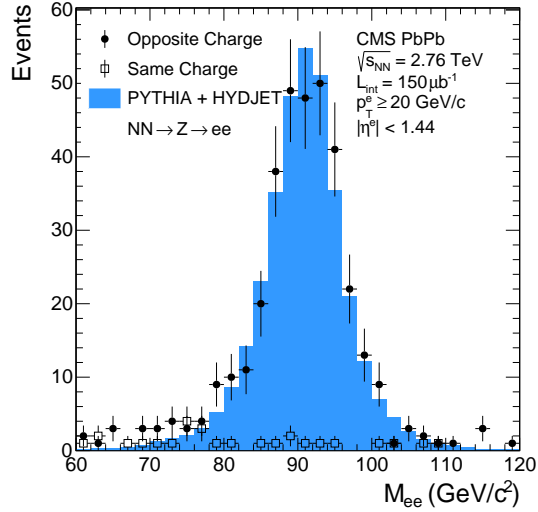


Figure 5.17: Invariant mass of electron pairs in the Pb+Pb collision system, after all cuts are made, the energy correction is applied to the data, and oversmearing is applied to the MC.

5.2.5 Unfolding

The p_T that a Z boson is produced with and the p_T that it is reconstructed with can be different for a variety of reasons. Some of these reasons involve final or initial state energy loss from the leptons that the Z boson decays into. In addition, the detector does not have perfect resolution. In order to compare the final measured Z p_T spectrum to theoretical predictions, these resolution effects must be corrected for. Such a procedure is sometimes referred to as *unfolding*.

In the method applied to this analysis, the effect of bin migration (a Z being reconstructed at a slightly different p_T due to finite resolution) is separated from other effects and a correction is applied to the data. The TUnfold package in ROOT is employed, using the following method:

1. Take the MC sample that has undergone a similar reconstruction to that of the data.
2. Create a response matrix that holds the information of how the generated kinematic values were transformed into reconstructed kinematic values.
3. “Unfold” that response matrix to get a matrix that can be used to transform the reconstructed kinematic values of particles in data back to the original kinematic values of that particle.

4. Regularization as explained below is applied.

To zeroth-order, “unfolding” the response matrix is just taking the inverse of the response matrix. The problem with this method is that statistical fluctuations are amplified during the inversion unless smoothness conditions are applied. These conditions, known as regularization conditions, are an attempt at making the unfolded distributions look smooth and remove the amplified statistical fluctuations that occur if one just uses the inverse of the response matrix. For the TUnfold method, Thikonov regularization is done, using the standard scheme based on the curvature of the difference between the output and bias distributions. The TUnfold method is applied to both the dielectron and dimuon channels for the p_T spectrum. The Z y distribution does not show significant need for unfolding due to the relatively flat y distribution.

5.2.5.1 Resolution Unfolding for Dimuons

Using the MC that has been generated, the response matrix shown in Fig. 5.18 is created.

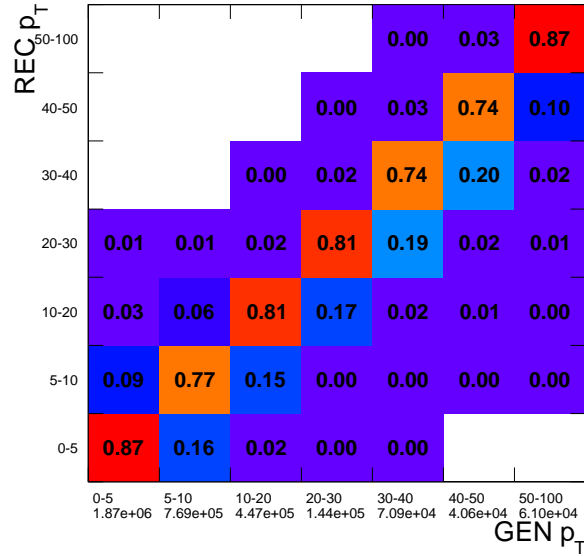


Figure 5.18: Matrix of generated versus reconstructed p_T for the Z boson in the dimuon channel in Pb+Pb collisions. This matrix is obtained from the MC used in this analysis.

The response matrix is unfolded, and applied to the data binned in Z boson p_T in order to transform the reconstructed Z boson p_T spectrum to the originally produced Z boson p_T spectrum.

5.3.1 Raw Yields in Dimuon Channel

The Z candidates in the dimuon channel are split into bins of p_T , $|y|$, and centrality, as shown in Table 5.3. The total integrated value is 1022 ± 32 Z bosons. There are no same charge dimuons so no background subtraction is needed.

Table 5.3: Raw number of Z boson candidates in the dimuon channel in the p_T , y , and centrality bins used for the analysis, including statistical uncertainties for $p_T^\mu > 20$ GeV/ c , $|\eta^\mu| < 2.4$ and $|y_{\mu\mu}| < 2.0$

| | | | | | | | | |
|-------|--------------|--------------|--------------|--------------|--------------|--------------|------------|------------|
| p_T | 0 – 5 | 5 – 10 | 10 – 20 | 20 – 30 | 30 – 40 | 40 – 50 | 50 – 100 | |
| N_Z | 298 ± 16 | 291 ± 17 | 225 ± 15 | 108 ± 10 | 40 ± 6 | 27 ± 5 | 29 ± 5 | |
| $ y $ | 0 – 0.25 | 0.25 – 0.5 | 0.5 – 0.75 | 0.75 – 1.0 | 1.0 – 1.25 | 1.25 – 1.5 | 1.5 – 1.75 | 1.75 – 2.0 |
| N_Z | 165 ± 13 | 150 ± 12 | 153 ± 12 | 147 ± 12 | 143 ± 12 | 129 ± 11 | 91 ± 9 | 44 ± 7 |
| Cent | 0 – 10% | 10 – 20% | 20 – 30% | 30 – 40% | 40 – 50% | 50 – 100% | | |
| N_Z | 396 ± 20 | 284 ± 17 | 154 ± 12 | 98 ± 10 | 45 ± 7 | 45 ± 7 | | |

5.3.2 Raw Yields in Dielectron Channel

The Z candidates in the dielectron channel are split into the same bins of p_T , and centrality as the dimuon channel, but different bins of $|y|$, as shown in Table 5.4. There are 355 ± 19 opposite charge dielectrons and 27 ± 5 same charge dielectrons, resulting in a background subtracted raw yield of 328 ± 20 Z bosons.

5.4 Acceptance and Efficiency

Once all of the resolution corrections have been applied and the raw signal and background yields have been measured, the acceptance and efficiency corrections required to correct for losses in the signal are calculated. These corrections are calculated as functions of p_T , y and centrality in order to look at the corrected yields.

The acceptance factor can be calculated by dividing the number of generated Z s by the number of accepted Z s in our MC sample. The acceptance cuts are as shown in the following equation,

Table 5.4: Raw number of Z boson candidates in the dielectron channel in the p_T , y , and centrality bins used for the analysis, including statistical uncertainties for $p_T^e > 20$ GeV/ c , $|\eta^e| < 1.44$ and $|y_{ee}| < 1.44$

| | | | | | | | |
|-------------------|----------|------------|------------|------------|------------|-----------|----------|
| p_T (GeV/ c) | 0 – 5 | 5 – 10 | 10 – 20 | 20 – 30 | 30 – 40 | 40 – 50 | 50 – 100 |
| N_Z^{OS} | 96±10 | 95±10 | 86±9 | 38±6 | 19±4 | 12±3 | 9±3 |
| N_Z^{SS} | 2±1 | 4±2 | 9±3 | 6±2 | 3±2 | 0±0 | 2±1 |
| N_Z^{OS-SS} | 94±10 | 91±10 | 77±10 | 32±7 | 16±5 | 12±3 | 7±3 |
| $ y $ | 0 – 0.25 | 0.25 – 0.5 | 0.5 – 0.75 | 0.75 – 1.0 | 1.0 – 1.44 | | |
| N_Z^{OS} | 106±10 | 78±9 | 86±9 | 48±7 | 37±6 | | |
| N_Z^{SS} | 9±3 | 6±2 | 8±3 | 2±1 | 2±1 | | |
| N_Z^{OS-SS} | 97±10 | 72±9 | 78±9 | 46±7 | 35±6 | | |
| Centrality | 0 – 10% | 10 – 20% | 20 – 30% | 30 – 40% | 40 – 50% | 50 – 100% | |
| N_Z^{OS} | 131±11 | 92±9 | 66±8 | 30±5 | 19±4 | 17±4 | |
| N_Z^{SS} | 7±2 | 4±2 | 7±2 | 2±1 | 3±2 | 4±2 | |
| N_Z^{OS-SS} | 124±12 | 88±10 | 59±9 | 28±6 | 16±5 | 13±5 | |

where e refers to electrons and μ to muons:

$$\alpha = \frac{N^Z(|y_Z^{\mu\mu(ee)}| < 2.0(1.44), |\eta^{\mu(e)}| < 2.4(1.44), p_T^{\mu(e)} \geq 20 \text{ GeV}/c)}{N^Z(|y_Z^{\mu\mu(ee)}| < 2.0(1.44))}. \quad (5.2)$$

The efficiency corrections are done so that the denominator is based on the number of generated Z events that survive the selection on kinematical quantities whereas the numerator is based on the number of reconstructed dimuon (dielectron) events after applying the selection criteria to the dimuon (dielectron) reconstructed quantities. The denominator and numerator are binned in reconstructed kinematics, thus also taking into account the minimal resolution effects in y . The combination of the trigger, reconstruction, and lepton identification efficiencies are calculated as:

$$\varepsilon = \frac{N^Z(|y_Z^{\mu\mu(ee)}| < 2.0(1.44), |\eta^{\mu(e)}| < 2.4(1.44), p_T^{\mu(e)} \geq 20 \text{ GeV}/c, \text{ quality cuts})}{N^Z(|y_Z^{\mu\mu(ee)}| < 2.0(1.44), |\eta^{\mu(e)}| < 2.4(1.44), p_T^{\mu(e)} \geq 20 \text{ GeV}/c)}. \quad (5.3)$$

When the data are binned in the Z -boson p_T , y , or event centrality, the corresponding selection is applied to both the numerator and denominator. The overall acceptance is approximately 70% (50%) in the muon (electron) rapidity ranges. The overall efficiency is approximately 85% (55%) in the muon (electron) case in Pb+Pb collisions. In the following sections we will look at these in more detail.

5.4.1 Acceptance and Efficiency Corrections for Dimuons

Acceptance The acceptance measurement for dimuons is shown in Fig. 5.20 as a function of Z boson p_T and y . Since the acceptance is not based on the state of the detector, the acceptance is flat as a function of centrality.

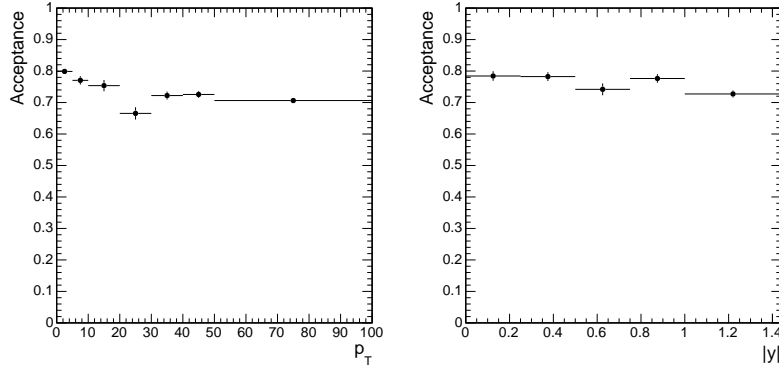


Figure 5.20: Acceptance corrections for dimuons as a function of Z p_T and y evaluated from PYTHIA, in the Pb+Pb collision system.

Efficiency The combined trigger, reconstruction, and muon identification efficiency as function of centrality, Z boson p_T , and y are shown in Fig. 5.21.

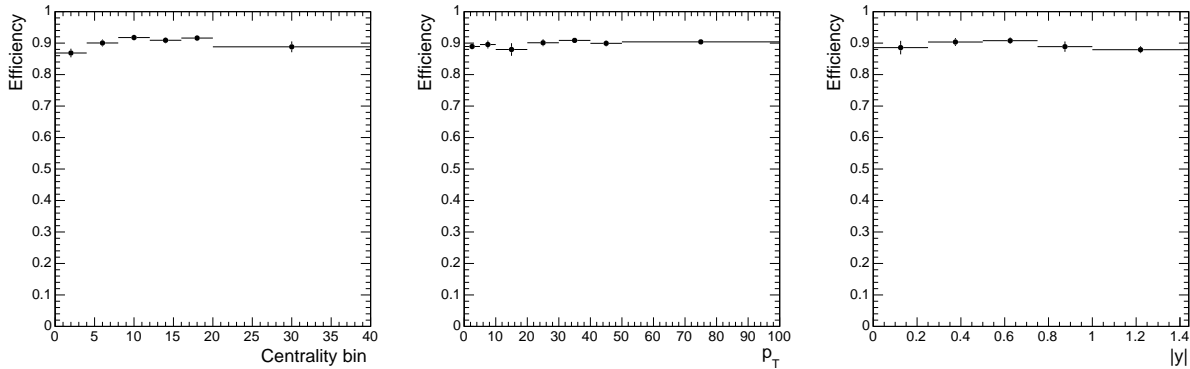


Figure 5.21: Combined trigger, reconstruction, and muon identification efficiency for dimuons in bins of the analysis, in the Pb+Pb collision system.

The final correction to be applied to the raw yields extracted from data is the product of the acceptance and efficiency, $\alpha \times \epsilon$.

5.4.2 Acceptance and efficiency corrections for dielectrons

Acceptance The acceptance measurement for dielectrons is shown in Fig. 5.22 as a function of Z boson p_T and y . Since the acceptance is not based on the state of the detector, the acceptance is flat as a function of centrality.

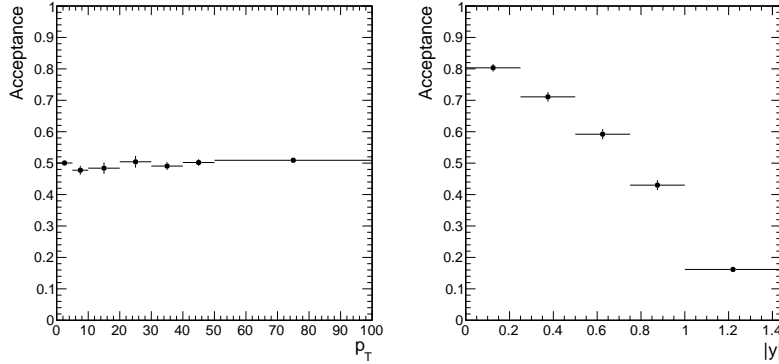


Figure 5.22: Acceptance corrections for dielectrons as a function of Z boson p_T and y evaluated from PYTHIA, in the Pb+Pb collision system. The significant drop in acceptance vs. $|y|$ is due to the limitation of the electron $\eta < 1.44$.

Efficiency The combined trigger, reconstruction, and muon identification efficiency as function of centrality, p_T^Z and y are shown in Fig. 5.23.

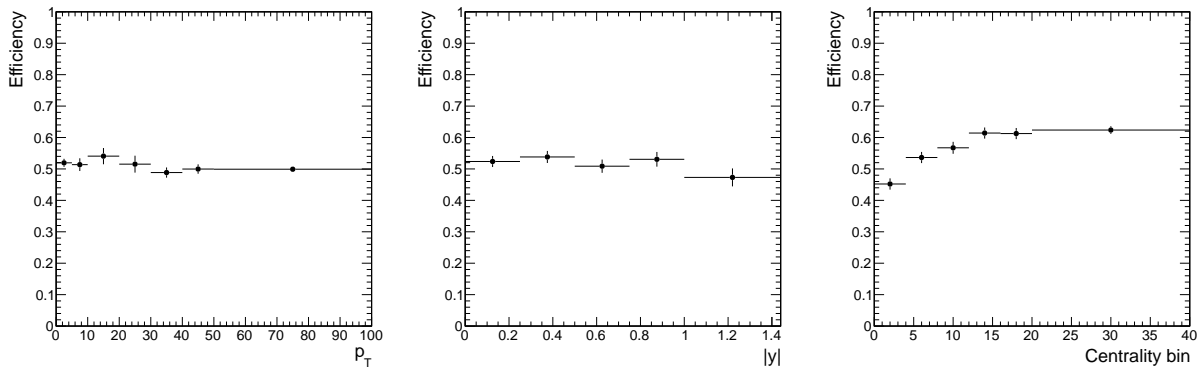


Figure 5.23: Combined trigger, reconstruction, and electron identification efficiency for dielectrons in bins of the analysis in the Pb+Pb collision system.

Electron charge misidentification One of the cuts required for a dielectron to be considered a Z candidate and counted as part of the signal, is that the two electrons have opposite charge.

In the proton-proton environment, electron charge misidentification occurs on the order of 1 time in 1000. In the Pb+Pb environment simulations shown below give a value closer to 1 time in 200. Figure 5.24 shows the number of same-sign pairs that are reconstructed in MC.

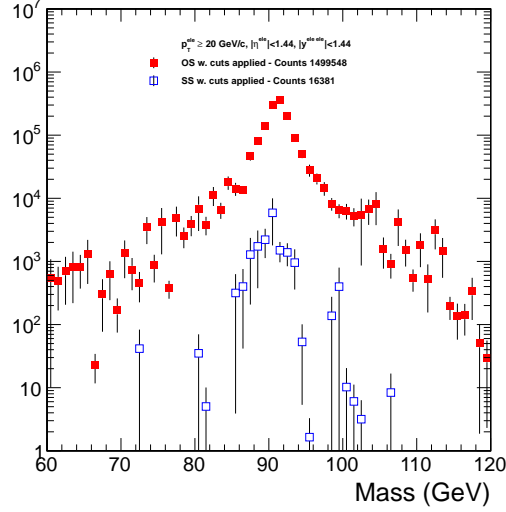


Figure 5.24: Invariant mass of electron pairs in MC in the Pb+Pb collision system, showing same-sign and opposite-sign pairs. All events are from simulated Z s. The red points are electron pairs with reconstructed opposited sign charges and the blue points are electron pairs with reconstructed same sign charges. There are $1.50 \cdot 10^6$ opposite-sign pairs (after weighting), and $1.64 \cdot 10^4$ same-sign pairs.

The relative proportion of same-sign over opposite-sign pairs vs. electron p_T , η , and centrality are shown in Fig. 5.25. There is a significant difference between charge misidentification at very low centrality (very peripheral events show a misidentification rate consistent with the previously stated 1 time in 1000) vs. high centrality, which explains why the effect that is seen in Pb+Pb ($\sim 0.5\%$ effect per electron resulting in $\sim 1\%$ effect per Z) is so much greater than that seen in $p + p$.

5.5 Uncertainties

The overall uncertainties measured are given here. The description of how these uncertainties are calculated is discussed in the following sections. The total systematic uncertainty in the Z yield in Pb+Pb collisions is estimated by adding the different contributions in quadrature. The

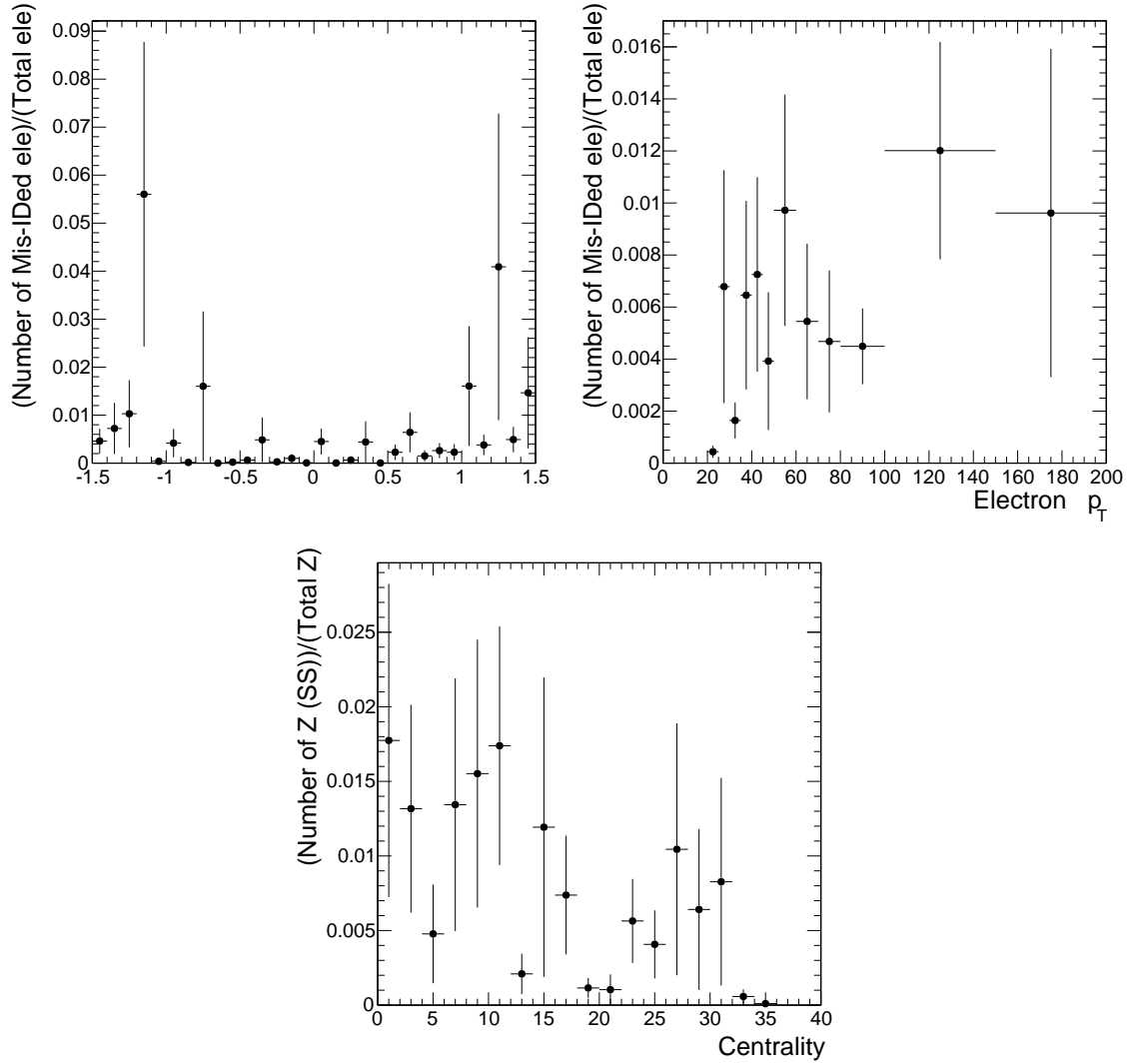


Figure 5.25: Ratio of electrons and Z s reconstructed with incorrect charge over the total electrons and Z s reconstructed in the Pb+Pb collision system. The overall effect for electrons is $\sim 0.5\%$ and thus for Z s is $\sim 1\%$.

uncertainty in the efficiencies is 1.8% for the dimuon channel and 7.4% for the dielectron channel. These estimates are based on the TNP technique for measuring single-particle reconstruction, identification, and trigger efficiencies. The method is done in a way similar to that described in Ref. [78] and is dominated by the statistical uncertainty from data.

The uncertainties coming from the acceptance corrections are less than 2%, as estimated by varying the input p_T and y shapes used to estimate the acceptance. The uncertainty comes from applying a weight to the generated Z p_T and y distributions that varies linearly between 0.7 and 1.3 over the ranges $0 < p_T < 100$ GeV/ c and $0 < |y| < 2.0$ (1.44 for the dielectron channel). The p_T -dependent uncertainty arising from the resolution unfolding is less than 1%, as estimated by varying the generated Z p_T distribution using the same method.

The systematic uncertainty in the remaining background from other physics sources such as semileptonic decays of heavy-flavors is estimated by fitting the lower dilepton mass range (with the Drell-Yan contribution subtracted) to an exponential and extrapolating the fit to higher masses. This fit gives us a conservative systematic uncertainty of 0.5% for the dimuon channel and 2% for the dielectron channel.

The integrated systematic uncertainties for the $Z \rightarrow \mu^+\mu^-$ and the $Z \rightarrow e^+e^-$ channel yields in Pb+Pb collisions are summarized in Table 5.5.

Table 5.5: Summary of the integrated systematic uncertainties on the $Z \rightarrow \mu^+\mu^-$ and $Z \rightarrow e^+e^-$ yields in Pb+Pb.

| | $Z \rightarrow \mu^+\mu^-$ | $Z \rightarrow e^+e^-$ |
|-------------------------------|----------------------------|------------------------|
| Combined Efficiency | 1.8% | 7.4% |
| Acceptance | 0.7% | 0.7% |
| Background | 0.5% | 2.0% |
| N_{MB} | 3.0% | 3.0% |
| Overall (without T_{AA}) | 3.6% | 8.3% |
| T_{AA} (N_{MB} included) | 6.2% | 6.2% |
| Overall | 6.5% | 9.9% |

5.5.1 Background Studies

Although the background for measuring Z boson production in the dimuon and dielectron channels is small, it is important to quantify how small that contribution is. The same-sign pairs give an indication of the background from uncorrelated muon pairs. However other physics sources can contribute opposite-sign pairs that are not reflected in the same-sign distribution, such as $b\bar{b}$ production and $Z \rightarrow \tau^+\tau^-$ where $\tau^\pm \rightarrow \mu^\pm\nu_{\mu^\pm}\bar{\nu}_{\tau^\pm}$.

To get an indication of the background under the Z boson signal, the data distribution is fitted with the distribution predicted by a simulation of embedded and fully reconstructed Z bosons and Drell-Yan. Since the Drell-Yan process is part of the signal in the $[60 - 120]$ GeV/c^2 mass region, the background should be determined from the difference of the Z boson combined with the Drell-Yan production and the data distributions. The difference is fit in the low mass region with exponentials (since the expected backgrounds have a falling exponential shape) in various ranges. The resulting exponential fit function is extrapolated to the signal region. The worst case scenario is used as an upper limit on the expected background.

Muons Figure 5.26 shows the mass distribution of muon pairs in real data on the left and the differences between data and MC fit with exponentials on the right. The only difference between one background fit and the other is the beginning and end of the fit window. The worst case scenario is shown by the green curve. The 1.8% contribution of the remaining background to the the signal region is considered as the systematic on the background.

Electrons Figure 5.27 shows the mass distribution of electron pairs in real data on the left and the differences between data and MC fit with exponentials on the right. The worst case scenario is shown by the black curve. The 2.0% contribution in the signal region is considered as the systematic on the background.

5.5.2 Acceptance and Efficiency Uncertainty from Shape Variation

A systematic uncertainty on the product of the acceptance and efficiency MC correction factor is determined by applying a weight to the generated Z p_T and y distributions that varies linearly from 0.7 to 1.3 (or 1.3 to 0.7) over the ranges $0 < p_T < 100$ GeV/c and $0 < |y| < 2.0$. This accounts for

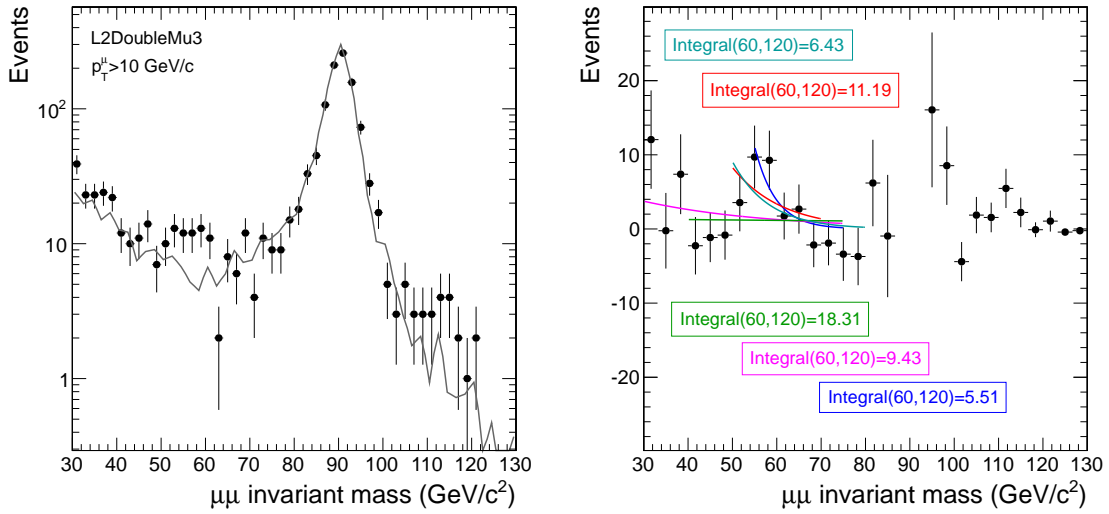


Figure 5.26: (Left) The invariant mass distribution of muon pairs in real data fitted with the mass distribution from Z boson combined with Drell-Yan simulation (the black line). (Right) Difference between the real data mass distribution and the fitted Drell-Yan simulation, together with exponential fits to the lower mass region to estimate the background in the Pb+Pb collision system.

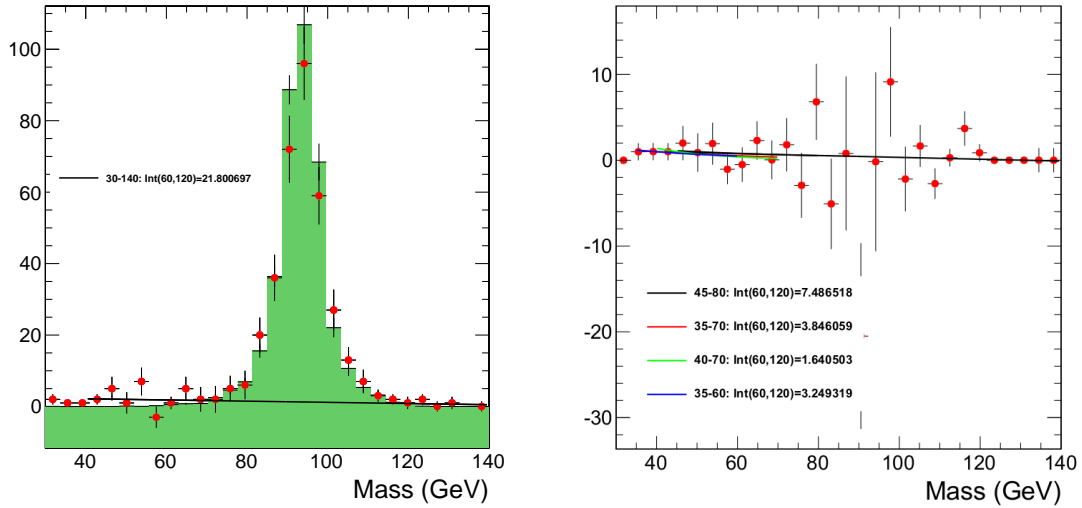


Figure 5.27: (Left) The invariant mass distribution of electron pairs in real data (red circles) fitted with the mass distribution from simulation (green histogram). (Right) Difference between the real data mass distribution and the fitted simulation together with exponential fits to the lower mass region estimating the background in the Pb+Pb collision system.

maximum variations expected from theory in the shapes of the kinematic distributions.

The systematic uncertainty on the acceptance α_{sys} due to the variation of the y and p_T shapes as described above, is estimated as follows. Here α_d is the acceptance without the shape variation:

$$\alpha_{\text{sys}}(p_T, y) = 0.5 \sqrt{(\alpha_d - \alpha_{+30\%(p_T)})^2 + (\alpha_d - \alpha_{-30\%(p_T)})^2 + (\alpha_d - \alpha_{+30\%(y)})^2 + (\alpha_d - \alpha_{-30\%(y)})^2} \quad (5.4)$$

We follow the same method for the efficiency ϵ_{sys} as well as a function of transverse momentum, y and centrality (where ϵ_d is the efficiency without the shape variation):

$$\epsilon_{\text{sys}}(p_T, y) = 0.5 \sqrt{(\epsilon_d - \epsilon_{+30\%(p_T)})^2 + (\epsilon_d - \epsilon_{-30\%(p_T)})^2 + (\epsilon_d - \epsilon_{+30\%(y)})^2 + (\epsilon_d - \epsilon_{-30\%(y)})^2} \quad (5.5)$$

Muon In the dimuon channel, the shape variations used, based on the procedure described above, are illustrated in Figs. 5.28 and 5.29. The results of both acceptance and efficiency uncertainties due to varying the shape are shown in Table 5.6.

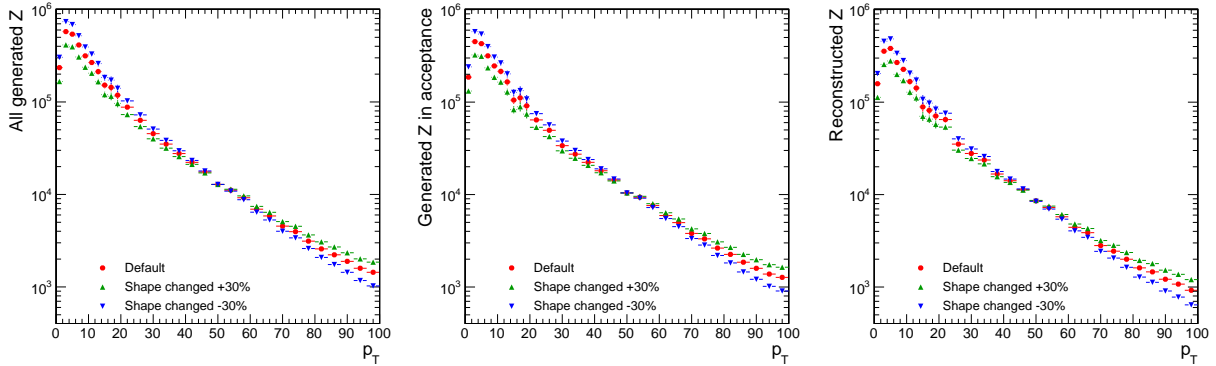


Figure 5.28: (left) All generated Z , (center) Z in acceptance, (right) reconstructed Z for the dimuon channel in the Pb+Pb collision system.

Electrons The shape variations used in the dielectron channel, based on the same procedure are illustrated in Figs. 5.30 and 5.31. Since the underlying distribution of the Z boson p_T and y does not depend on whether the Z boson will decay into a dimuon or dielectron, the left plots of Figs. 5.28 and 5.30 and Figs. 5.29 and 5.31 have identical shapes. The results of both acceptance and efficiency uncertainties are shown in Table 5.7

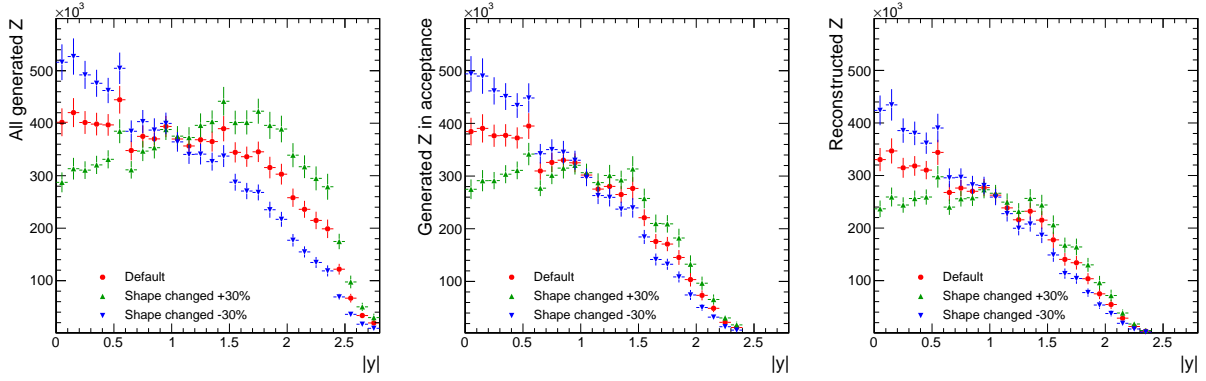


Figure 5.29: (left) All generated Z , (center) Z in acceptance, (right) reconstructed Z for the dimuon channel in the Pb+Pb collision system.

Table 5.6: Fractional dimuon acceptance and efficiency uncertainties as a function of p_T , y , and centrality.

| p_T (GeV/c) | 0 – 5 | 5 – 10 | 10 – 20 | 20 – 30 | 30 – 40 | 40 – 50 | 50 – 100 | |
|---------------------------------------|----------|------------|------------|------------|------------|------------|------------|------------|
| $\alpha_{\text{Syst}}(p_T)$ | 0.021 | 0.018 | 0.022 | 0.018 | 0.018 | 0.014 | 0.013 | |
| $\epsilon_{\text{Syst}}(p_T)$ | 0.008 | 0.002 | 0.001 | 0.004 | 0.004 | 0.008 | 0.007 | |
| $ y^Z $ | 0 – 0.25 | 0.25 – 0.5 | 0.5 – 0.75 | 0.75 – 1.0 | 1.0 – 1.25 | 1.25 – 1.5 | 1.5 – 1.75 | 1.75 – 2.0 |
| $\alpha_{\text{Syst}}(y)$ | 0.0003 | 0.0006 | 0.0002 | 0.0003 | 0.0007 | 0.0011 | 0.0016 | 0.0017 |
| $\epsilon_{\text{Syst}}(y)$ | 0.0007 | 0.0008 | 0.0001 | 0.0006 | 0.0004 | 0.0002 | 0.0015 | 0.0012 |
| Cent (%) | 0 – 10 | 10 – 20 | 20 – 30 | 30 – 40 | 40 – 50 | 50 – 100 | | |
| $\alpha_{\text{Syst}}(\text{cent})$ | 0.019 | 0.020 | 0.019 | 0.021 | 0.020 | 0.021 | | |
| $\epsilon_{\text{Syst}}(\text{cent})$ | 0.004 | 0.002 | 0.003 | 0.003 | 0.004 | 0.001 | | |

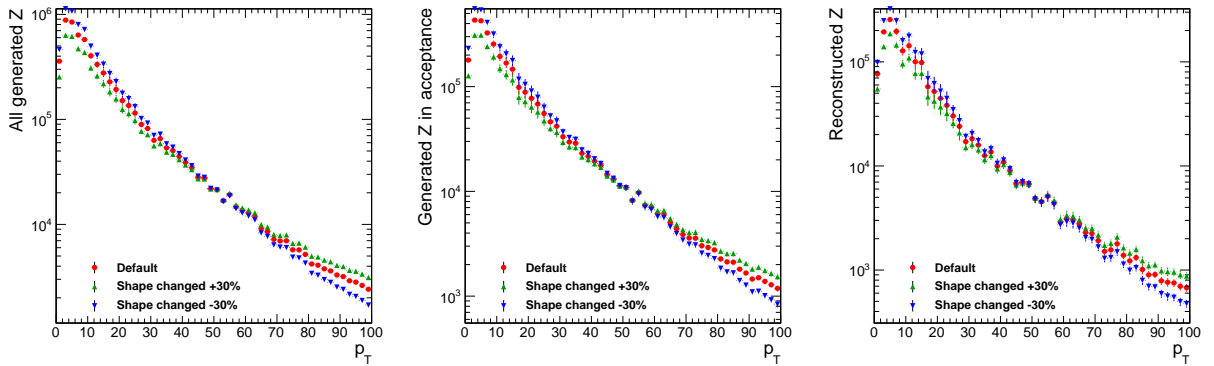


Figure 5.30: (left) All generated Z , (center) Z in acceptance, (right) reconstructed Z for the dielectron channel in the Pb+Pb collision system.

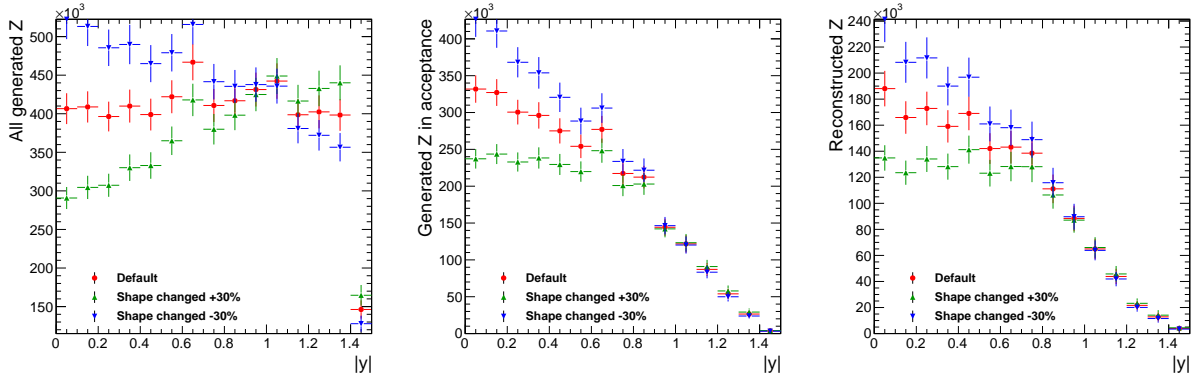


Figure 5.31: (left) All generated Z , (center) Z in acceptance, (right) reconstructed Z for the dielectron channel in the Pb+Pb collision system.

Table 5.7: Fractional uncertainties for dielectrons on acceptance and efficiency as a function of p_T , y , and centrality.

| | | | | | | | |
|---------------------------------------|----------|------------|------------|------------|------------|----------|----------|
| p_T (GeV/ c) | 0 – 5 | 5 – 10 | 10 – 20 | 20 – 30 | 30 – 40 | 40 – 50 | 50 – 100 |
| $\alpha_{\text{Syst}}(p_T)$ | 0.0223 | 0.0217 | 0.0197 | 0.0187 | 0.0169 | 0.0153 | 0.0158 |
| $\epsilon_{\text{Syst}}(p_T)$ | 0.0028 | 0.0028 | 0.0048 | 0.0003 | 0.0010 | 0.0016 | 0.0017 |
| $ y^Z $ | 0 – 0.25 | 0.25 – 0.5 | 0.5 – 0.75 | 0.75 – 1.0 | 1.0 – 1.44 | | |
| $\alpha_{\text{Syst}}(y)$ | 0.0025 | 0.0017 | 0.0003 | 0.0019 | 0.0027 | | |
| $\epsilon_{\text{Syst}}(y)$ | 0.0006 | 0.0014 | 0.0011 | 0.0005 | 0.0011 | | |
| Cent (%) | 0 – 10 | 10 – 20 | 20 – 30 | 30 – 40 | 40 – 50 | 50 – 100 | |
| $\alpha_{\text{Syst}}(\text{cent})$ | 0.0239 | 0.0213 | 0.0226 | 0.0294 | 0.0237 | 0.0203 | |
| $\epsilon_{\text{Syst}}(\text{cent})$ | 0.0006 | 0.0018 | 0.0005 | 0.0023 | 0.0023 | 0.0026 | |

5.5.3 Uncertainty on T_{AA}

The T_{AA} values and uncertainties which are used to scale from $p + p$ to Pb+Pb are shown in Table 4.1. The uncertainties are shown in Table 5.8. The T_{AA} uncertainties were determined through variation of the Woods-Saxon parameters of the nucleus, variation of Glauber model parameters, the uncertainties in the particle production model used to describe the $\sum E_T$ for the CMS data, and the variation of the nucleon-nucleon cross section.

Table 5.8: Uncertainty on T_{AA} .

| Centrality bin | Uncertainty | Centrality bin | Uncertainty |
|----------------|-------------|----------------|-------------|
| 0-10% | 4.3% | 30-40% | 8.5% |
| 10-20% | 5.2% | 40-50% | 10.9% |
| 20-30% | 6.6% | 50-100% | 15.0% |

5.6 Tag and Probe Method

The TNP method is used to extract efficiencies in a data-driven way. It will be used in this analysis to verify the single-lepton triggers, tracking and identification efficiencies calculated from MC. The TNP analysis is done using the official TNP framework, as employed for example in Refs. [79, 80].

TNP makes use of peaks such as the Z where the dilepton pair reconstructed at the correct mass cannot come from something other than real leptons (once the background is subtracted). Well-defined leptons that pass a tight selection are called the “Tag” leptons. They are combined with the other leptons, the “Probe” leptons, and their invariant mass is computed. A “passing probe” is a probe which possesses those criteria for which we want to evaluate/estimate an efficiency.

Some challenges arise in measuring the tracking efficiency because, in the heavy-ion environment, the tracking efficiency and the rate of fake tracks are both correlated with the multiplicity of the underlying Pb+Pb event, i.e. one can have a pair that arises from the combination of losing a true muon and gaining a fake one which gets counted in the numerator for purposes of measuring efficiency. Yet another problem is that measuring the track matching efficiency between the signal in the ECAL or the muon station and an inner track (necessary to promote to a global lepton) is

not straightforward in heavy-ion collisions [79].

Due to these challenges, the TNP method in this analysis is not used for measuring efficiencies but instead is used for comparing MC to data. The difference between the two demonstrates the differences between using our MC for measuring efficiencies and using a data-driven method to calculate efficiencies. We compare the efficiencies obtained with TNP on data with efficiencies obtained with TNP on MC as well as with the efficiencies obtained by the method described earlier. When the results obtained through the different methods agree, we gain confidence in the use of the embedded samples in HYDJET. The level of agreement also gives us a handle on the uncertainties on the calculated efficiencies.

Two tag-probe invariant mass distributions are formed, in the vicinity of the Z mass, according to whether the probe passes or fails the criteria for which the efficiency is being measured. The two mass distributions are then fit simultaneously, and the efficiency ε (and its uncertainty) is extracted as a parameter in the fit,

$$\begin{aligned} N_{\text{pass}} &= \varepsilon \times N_{\text{probes}} \\ N_{\text{fail}} &= (1 - \varepsilon) \times N_{\text{probes}} \end{aligned} \tag{5.6}$$

where N_{probes} , N_{pass} , and N_{fail} are the number of “all probes”, “passing probes”, and “failing probes” respectively.

In the end the values measured are used in the following ways: the ratio of the efficiency found in MC and data is used to scale the efficiencies measured using MC in order to correct for differences between the two datasets; the uncertainties from the MC and data fits are used as the uncertainty associated with the TNP method, as is standard for heavy-ion analyses using TNP because the resulting fluctuations in the fits are driven by limited statistics in data.

5.6.1 TNP Method for Muons

For the TNP for muons, the term “Good Quality”, which will be used through the section, refers to:

- `isTrackerMuon`.
- `isGlobalMuon`.
- `Valid Muon Hits > 0`.
- `Number of Matched Stations > 1`.
- `Global Track $\chi^2/\text{ndof} < 10$` .
- `TrackerLayersWithMeasurement > 4`.
- `PixelLayersWithMeasurement > 0`.

“Good Track Quality” requirement refers to:

- `TrackerLayersWithMeasurement > 4`.
- `PixelLayersWithMeasurement > 0`.

Our acceptance requirement for the single muon is $p_T > 20 \text{ GeV}/c$ and $|\eta| < 2.4$.

5.6.1.1 Muon Trigger Efficiency

The settings used to get the trigger efficiency with the TNP method are the following:

- **Tag:** a Global Muon with “Good Quality” and matched to a single-muon trigger.
- **Probe:** a Global Muon that fulfills all “Good Quality” cuts and is in the acceptance.
- **Passing:** a Probe that can be matched to the dimuon trigger, requiring both muons to have a $p_T > 3 \text{ GeV}/c$ (`HLT_HIL2DoubleMu3`).

The mass range used in the fit is $M \in [60, 120] \text{ GeV}/c^2$ and the mass peak is fitted with a Voigtian function for the passing and failing signal [81]. The passing and failing background is fitted with an exponential. The efficiency of the trigger is estimated to be $97.4 \pm 0.4\%$ (stat) from the fit using Z in real data for our trigger. The fits for MC and data are shown in Appendix B.1.

Figure 5.32 shows the single-muon trigger efficiency as a function of p_T and η for real data in red and for Z s embedded in HYDJET in blue. The agreement between each sample is at the 1% level. The HLT_HIL2DoubleMu3 trigger requires two muons with a p_T greater than 3 GeV/ c . Note that the analysis is restricted to single muons with $p_T > 20$ GeV/ c and so the turn-on curve of the triggers is below the region of interest for the muons we are using. On average the trigger efficiency is very good, 98.2% from TNP with the embedded samples. The ratio of the efficiency found in MC and data is used to scale the efficiencies measured using MC. The uncertainties from the MC and data fits are used for the uncertainty associated with the TNP method.

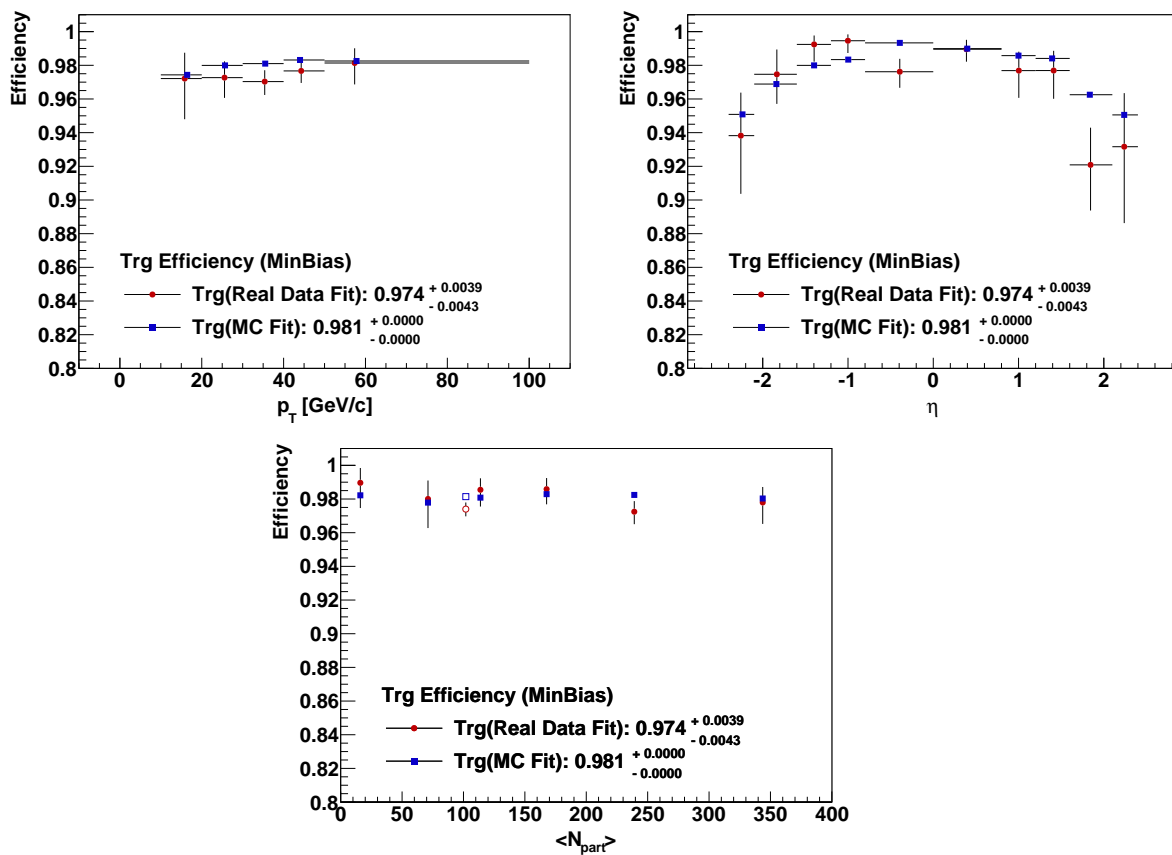


Figure 5.32: Single muon triggering efficiency in the Pb+Pb collision system of the HLT_HIL2DoubleMu3 trigger as a function of p_T on the left and η on the right and N_{part} on the bottom. In red: Z in real data, in blue: Z embedded in HYDJET.

We note here that since we are using a combination of two triggers, one trigger that requires a single muon with a $p_T > 15$ GeV/ c (HLT_HIL2Mu15) and one dimuon trigger (HLT_HIL2DoubleMu3),

it is impossible to simultaneously get the single muon trigger efficiency of the OR of the triggers by looking at the OR of the triggers in TNP. For example, if instead of defining our passing probe as we did before, we defined it as:

- Passing: a Probe that can be matched to either the single or double muon trigger.

we would see no difference in the single muon efficiency. Since the Tag is matched to a single muon trigger with a $p_T > 3 \text{ GeV}/c$, for HLT_HIL2DoubleMu3 (two triggering muons with a $p_T > 3 \text{ GeV}/c$) to be satisfied we only require the probe to be matched to a trigger and have a $p_T > 3 \text{ GeV}/c$. For HLT_HIL2Mu15 to be satisfied the probe must be matched to a trigger and have a $p_T > 15 \text{ GeV}/c$, which is a harder cut than that required for the dimuon trigger. Although the single muon trigger efficiency does not show this to be the case, the single muon trigger does have a higher efficiency to trigger on Z events, since only one of the high- p_T muons coming from the Z needs to trigger. This is equivalent to only getting hit once by the single muon trigger efficiency instead of twice which is the case for the dimuon trigger.

Therefore, it is important to make sure that the MC and data agree for each trigger independently. In adding the Z s that are triggered by HLT_HIL2Mu15, it is important to make sure that the trigger simulation in MC matches well what occurs in data. Defining the settings used to get the trigger efficiency for HLT_HIL2Mu15 on its own:

- Tag: a Global Muon with ‘Good Quality’ and matched to at least one Single Muon Trigger.
- Probe: a Global Muon that fulfills all quality cuts and is in the acceptance.
- Passing: a Probe that can be matched to the Single Muon trigger, requiring a $p_T > 15 \text{ GeV}/c$ trigger.

Figure 5.33 shows the efficiencies measured versus p_T and η for the triggers separately and an OR of the two. The overall agreement between MC and data is within 1%.

5.6.1.2 Muon ID Efficiency

The settings for the method used to estimate the muon identification efficiency are the following :

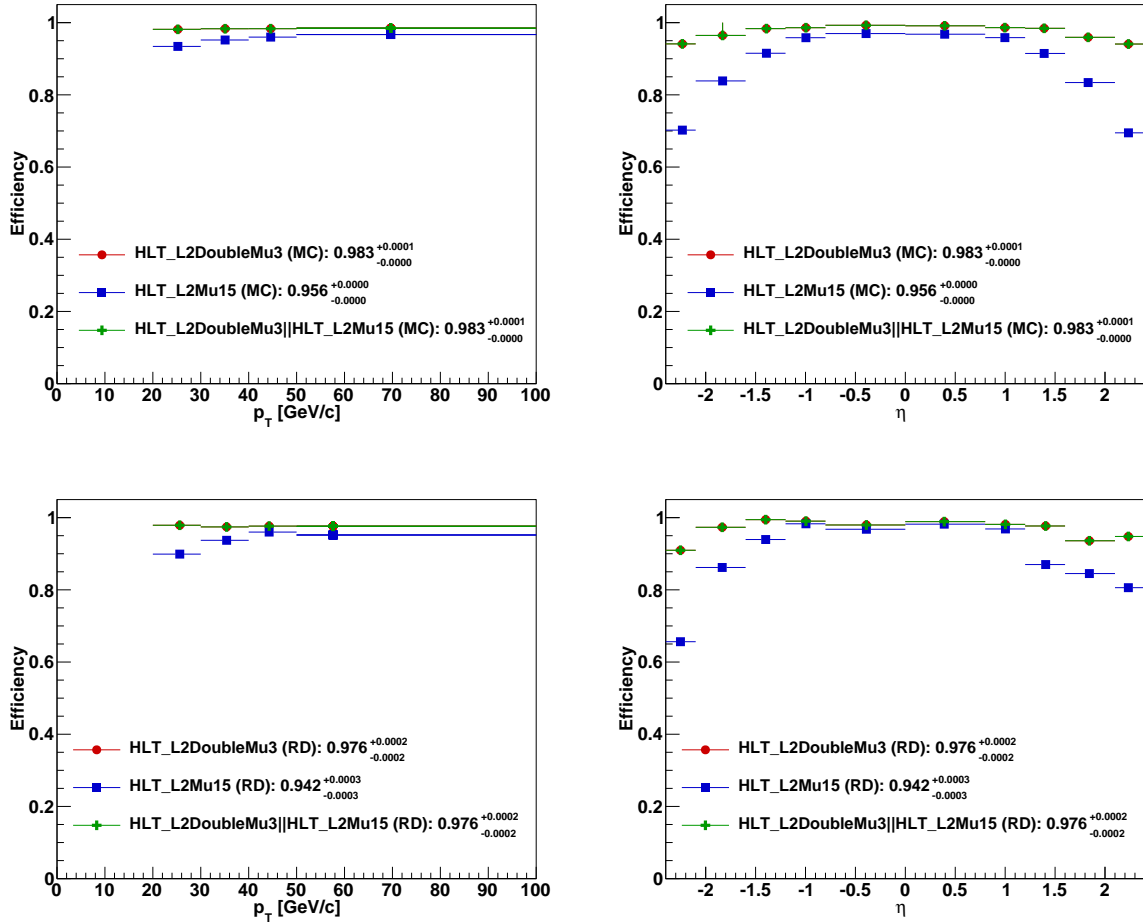


Figure 5.33: Single muon triggering efficiency in the Pb+Pb collision system of the HLT_HIL2DoubleMu3 trigger as a function of p_T on the left and η on the right. Top: MC. Bottom: RD In red: dimuon trigger (completely overlaps with OR trigger). In blue: single muon trigger. In green: OR of the dimuon and single muon trigger.

- Tag: a Global Muon with “Good Quality” and matched to the Double Muon Trigger.
- Probe: Tracker muon in acceptance, passing good track quality cuts.
- Passing: probe that can be matched to a global muon in the acceptance and is “Good Quality”.

The mass range used in the fit is $M \in [60, 120]$ GeV/ c^2 and the mass peak is fitted with a Voigtian function for the passing and failing signal. The passing and failing background is fitted with an exponential. The efficiency for muon identification is estimated to be $97.8 \pm 0.5\%$ (stat) from the fit using Z in real data. The fits for MC and data are shown in Appendix B.1.

Figure 5.34 shows the muon identification efficiency as a function of p_T and η , for real data in red and for Z embedded in HYDJET in blue. The agreement between each sample is at the 1% level. Note that these values are different from those from simulations due to a few missing cuts. The missing cuts are:

- $d_z < 0.5$ mm: distance of closest approach between the muon track and the vertex in the z -direction. This is not currently implemented in the TNP since the variable we first used turned out to be the distance of closest approach between the muon track and the (0,0,0) CMS position in the z -direction.

We note that the results for real data are within 1% of the simulation, thus these cuts do not remove many candidates and that the data and MC distributions we are cutting on agree very well. The ratio of the efficiency found in MC and data is used to scale the efficiencies measured using MC, and the uncertainties from the MC and data fits are used as the uncertainty associated with the TNP method.

5.6.1.3 Muon Track Reconstruction Efficiency

Most of the challenges mentioned earlier with regards to measuring TNP efficiency arise in measuring the inner track reconstruction efficiency. Furthermore, to fit failing TNP pairs becomes challenging due to the poor resolution of the standalone (STA) muons. This results in higher uncertainties

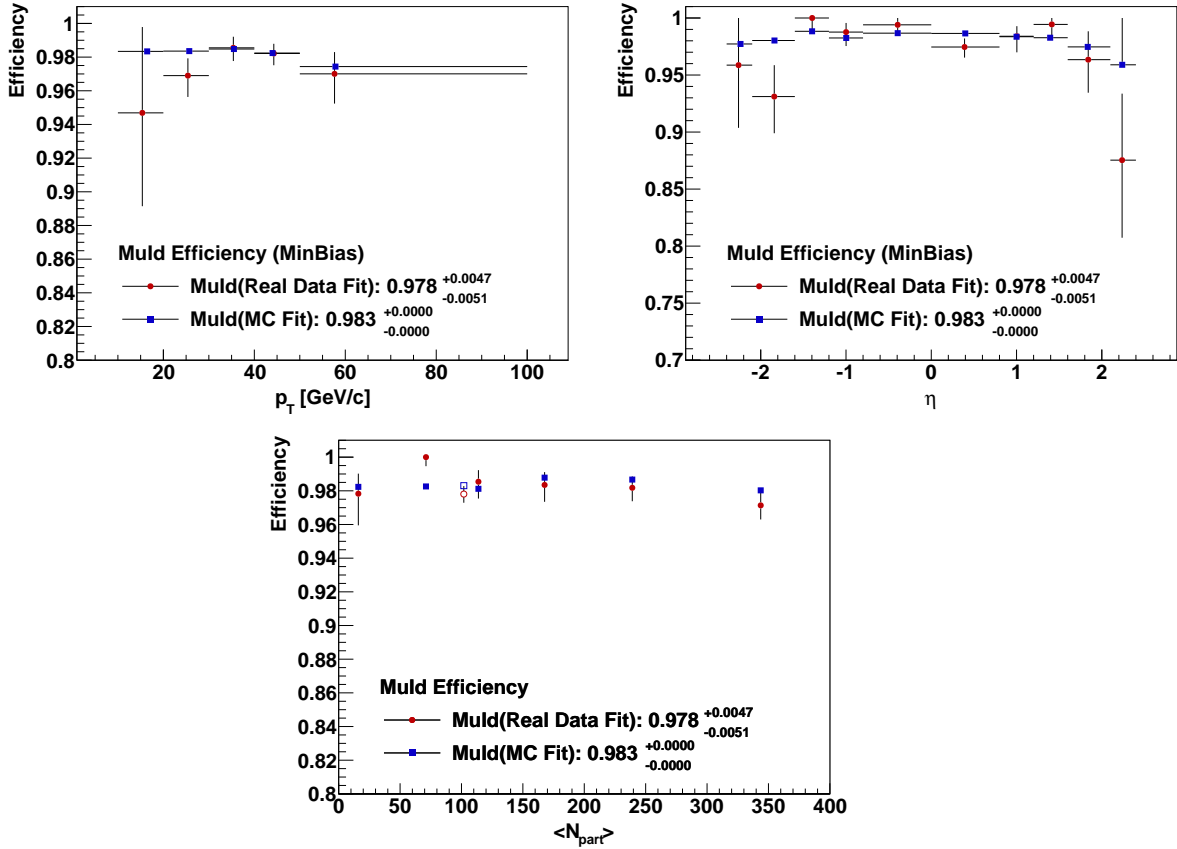


Figure 5.34: Single muon ID efficiency in the Pb+Pb collision system as a function of p_T on the left, η on the right and N_{part} on the bottom. In red: Z in real data, in blue: Z embedded in HYDJET.

than those measured for trigger and muon identification uncertainties, larger differences between data and MC, and poorer fits of the efficiencies.

In order to measure the muon track reconstruction efficiency, we apply the TNP method:

- Tag: a Global muon with “Good Quality” and matched to `HLT_HIL2DoubleMu3`.
- Probe: STA muon with at least one valid hit in the muon station.
- Passing: Probe that fulfills `isGlobalMuon` with “Good Track Quality”.

In order to look at the p_T dependence of the reconstruction efficiency, invariant mass plots are made using the Tag collection, splitting the Probe collection into p_T bins, and forming the invariant mass spectrum using the inner track kinematics of the Tag and the outer track kinematics of the Probe. When looking at the invariant mass peaks split in terms of p_T , a peak at the mass of the Z is observed, as expected, along with a p_T dependent peak of poorly resolved probe muons. This is due to the poor resolution of the probe muon and can be seen most clearly in Fig. 5.36 (left). Because when the inner track kinematics are employed for the probe, these dimuons end up in the Z peak, they are misreconstructed Z s, and therefore should not be considered background.

Since there are so few probe muons at low p_T ($0 \text{ GeV}/c < p_T < 20 \text{ GeV}/c$) that come from the Z and since the outer muon track kinematics are poor, the majority of probes with low outer track p_T are poorly reconstructed. The difference between the generated and reconstructed p_T spectra can be seen in Fig. 5.35. Therefore, following what was done in pp , the reconstruction efficiency is done using probes beginning at $20 \text{ GeV}/c$ [82].

Due to the poorer resolution, the mass range used in the fit is $\in [40, 140] \text{ GeV}/c^2$. The mass peak is fitted with a Voigtian at the Z peak. The passing and failing background is fitted with an exponential. The efficiency of the muon reconstruction is estimated to be $97.7 \pm 0.6\%$ (stat) from the fit using Z in real data. The fits for MC and data are shown in Appendix B.1.

Figure 5.37 shows the muon track reconstruction efficiency as a function of p_T and η , for real data in red and for Z s embedded in HYDJET in blue. Results for real data are within 1% of simulation. The ratio of the efficiency found in MC and data is used to scale the efficiencies measured using MC. The uncertainties from the MC and data fits are the uncertainties associated with the TNP

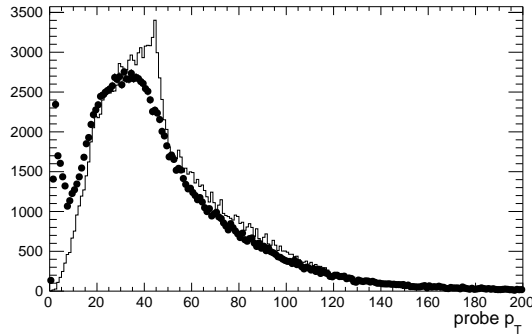


Figure 5.35: The line is the Generated Muon p_T spectrum, and the dots are the probe p_T spectrum using outer track kinematics. Note that at low p_T ($0 \text{ GeV}/c < p_T < 20 \text{ GeV}/c$) there are far fewer generated muons than reconstructed muons, pointing to the fact that most of those reconstructed muons are placed at the incorrect p_T . The inner track kinematics match the generated muon kinematics.

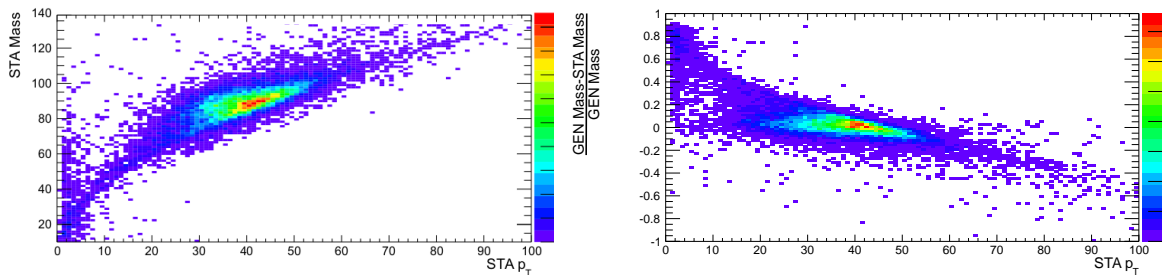


Figure 5.36: In the MC, looking at Z s with a p_T in the $[0,20] \text{ GeV}/c$ range, we observe a probe p_T dependence on the poorly reconstructed Z s. (left) Plotted is the probe's outer track p_T measurement versus the mass of the dimuon using the tag's inner track kinematics and probe's outer track kinematics. (right) Plotted is the probe's outer track p_T measurement versus the difference in the percentage difference between the generated mass of the Z and the reconstructed mass of the Z . This demonstrates the fact that when we focus on low p_T probes we see a second p_T dependent bump in the invariant mass that is signal and must be included in the measurement of the efficiency.

method.

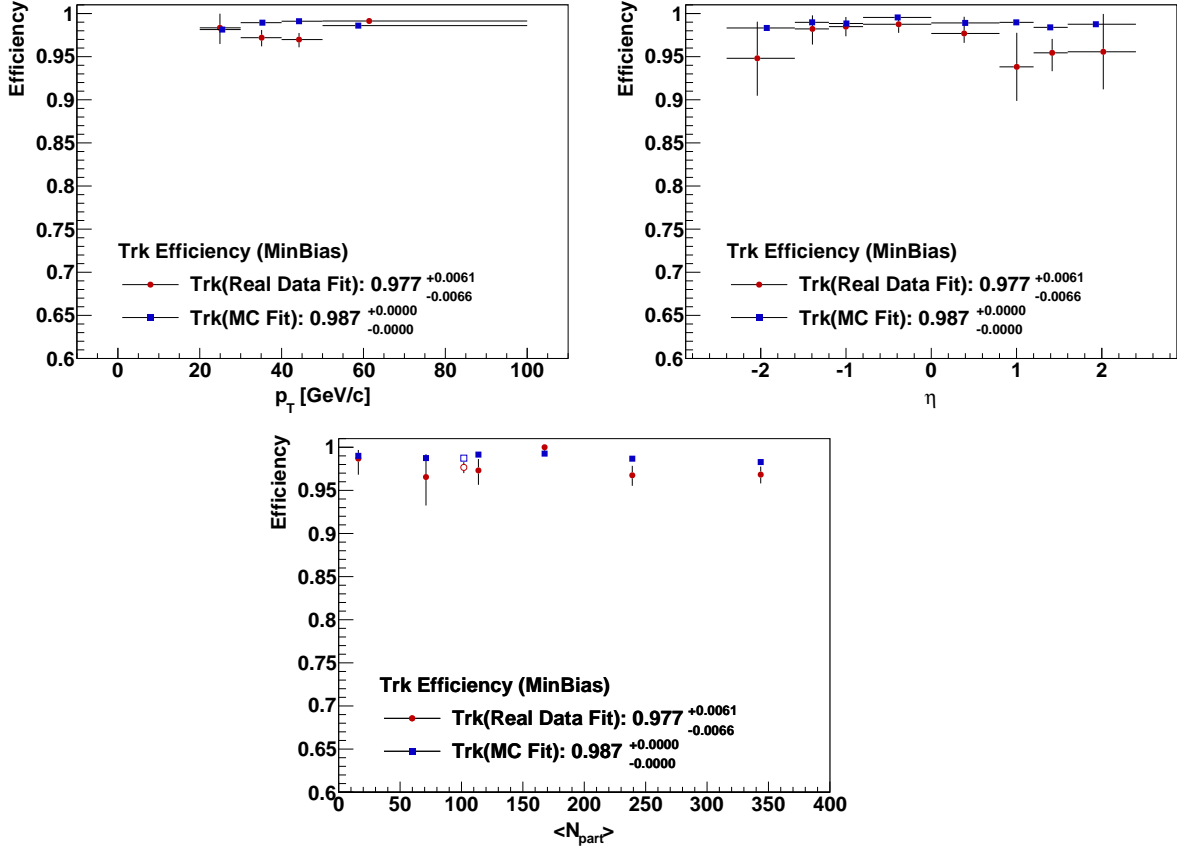


Figure 5.37: Single muon tracking efficiency in the Pb+Pb collision system as a function of p_T on the left, η on the right and N_{part} on the bottom. In red: Z in real data, in blue: Z embedded in HYDJET.

5.6.2 TNP Method for Electrons

For the TNP for electrons, the “Electron ID” requirement is used to match the cut made in the analysis, and refers to:

- $H/E < 0.2$
- $|\sigma_{i\eta i\eta}| < 0.011$
- $|\Delta\eta_{i\eta}| < 0.03$

- $|\Delta\Phi_{i\eta}| < 0.15$
- $|1/E_{sc} - 1/p_{T_track}| < 0.05$
- $d_{xy} < 0.02$

Our acceptance requirement for the single electron is $p_T > 20$ GeV/ c and $|\eta| < 1.44$.

5.6.2.1 Electron Trigger Efficiency

The settings used to get the trigger efficiency with the TNP method are the following:

- Tag: an Electron in Acceptance, passing Electron ID cuts, and matched to the trigger requiring a single energy deposit of $E_T > 20$ GeV (HLT_HISinglePhoton20).
- Probe: an Electron in Acceptance, passing Electron ID cuts.
- Passing: Probe that can be matched to the trigger requiring two energy deposits, one of $E_T > 20$ GeV and one of $E_T > 15$ GeV (HLT_HIPhoton15_Photon20).

The mass range used in the fit is $M \in [60, 120]$ GeV/ c^2 and the mass peak is fitted with a Breit-Wigner function convolved with Crystal-Ball function for the passing and failing signal. The passing and failing background is fit with an exponential. The efficiency of the trigger is estimated to be $98.3 \pm 0.7\%$ (stat) from the fit using Z s in real data for the trigger. The fits for MC and data are shown in Appendix B.3.

Figure 5.38 shows the single electron trigger efficiency as a function of p_T and η , for real data in red and for Z s embedded in HYDJET in blue. The agreement between each set of points is on the 4% level. The HLT_HIPhoton15_Photon20 trigger requires two ECAL objects, one with a p_T greater than 15 and one greater than 20. On average the trigger efficiency in MC is 99.8% from TNP with the embedded samples.

Integrated results for real data differ by about 1.5% from the simulated results. The ratio of the efficiency found in MC and data is used to scale the efficiencies measured using MC. The uncertainties from the MC and data fits are the uncertainties associated with the TNP method.

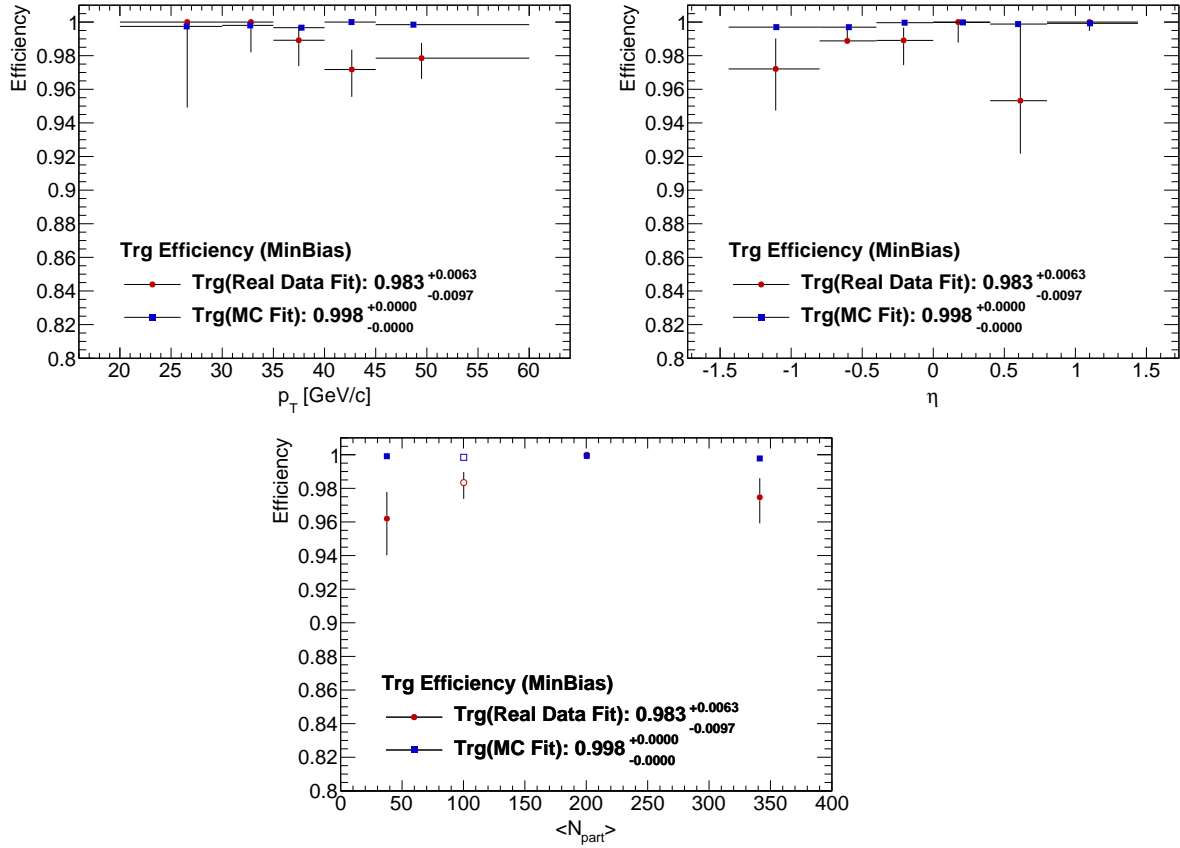


Figure 5.38: Single electron triggering efficiency in the Pb+Pb collision system of the HLT_HIPhoton15_Photon20 trigger as a function of p_T on the left and η on the right and N_{part} on the bottom. In red: Z in real data, in blue: Z embedded in HYDJET.

5.6.2.2 Electron ID Efficiency

The settings for the method used to estimate the electron identification efficiency are the following:

- Tag: an Electron in Acceptance, passing Electron ID cuts, and matched to the diphoton trigger (HLT_HIPhoton15_Photon20).
- Probe: an Electron in Acceptance.
- Passing: Probe that passes Electron ID cuts.

The mass range used in the fit is $M \in [60, 120]$ GeV/ c^2 and the mass peak is fitted with a Breit-Wigner function convolved with Crystal-Ball function for the passing and failing signal. The passing and failing background is fitted with an exponential. The efficiency of the electron identification is estimated to be $89.8 \pm 2.7\%$ (stat) from the fit using Z in real data. The fits for MC and data are shown in Appendix B.3.

Figure 5.39 shows the electron identification efficiency as a function of p_T and η for real data in red and for Z s embedded in HYDJET in blue. The overall agreement between each sample is at the 0.4% level. The ratio of the efficiency found in MC and data is used to scale the efficiencies measured using MC. The uncertainties from the MC and data fits are the uncertainties associated with the TNP method.

5.6.2.3 Electron Track Reconstruction Efficiency

In order to measure the electron track reconstruction efficiency, we apply the TNP method as follows:

- Tag: an Electron in Acceptance, passing Electron ID cuts, and matched to the diphoton trigger (HLT_HIPhoton15_Photon20).
- Probe: SuperCluster in Acceptance, passing $H/E < 0.2$.
- Passing: Probe reconstructed as the super cluster of an electron.

In order to look at the electron track reconstruction efficiency, invariant mass plots are made using the electron track kinematics of the Tag and the super cluster kinematics of the Probe.

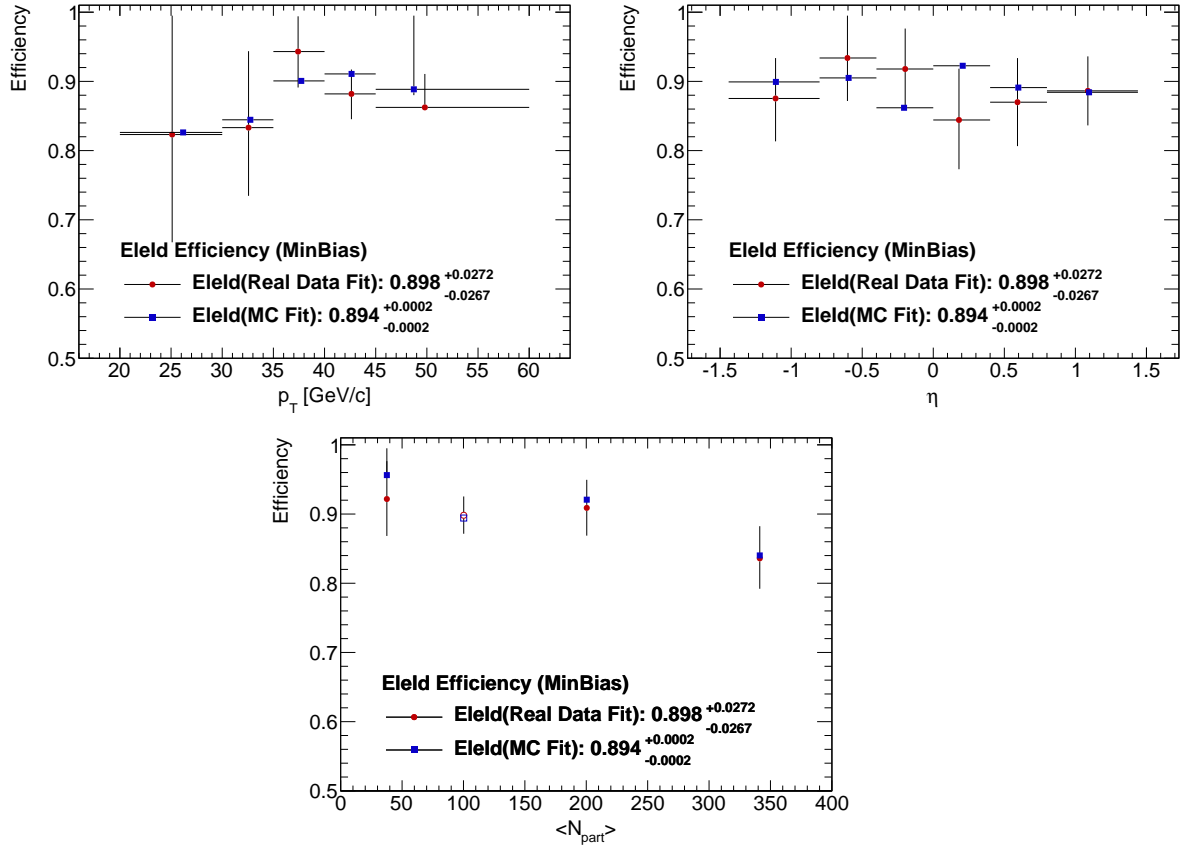


Figure 5.39: Single electron ID efficiency in the Pb+Pb collision system as a function of p_T on the left, η on the right and N_{part} on the bottom. In red: Z in real data, in blue: Z embedded in HYDJET.

Due to the poorer resolution of the super cluster kinematics, the mass range used in the fit is $\in [40, 140]$ GeV/ c^2 and the mass peak is fitted with a Breit-Wigner function convolved with Crystal-Ball function. The passing and failing background is fitted with an exponential times a turn-on curve. The efficiency of the electron reconstruction is estimated to be $84.4 \pm 2.4\%$ (stat) from the fit using Z s from real data. The fits for MC and data are shown in Appendix B.3.

Figure 5.40 shows the track reconstruction efficiency as a function of p_T and η for real data in red and for Z s embedded in HYDJET in blue. The overall results for real data are within 1.2% of simulation. The ratio of the efficiency found in MC and data is used to scale the efficiencies measured using MC. The uncertainties from the MC and data fits are the uncertainties associated with the TNP method.

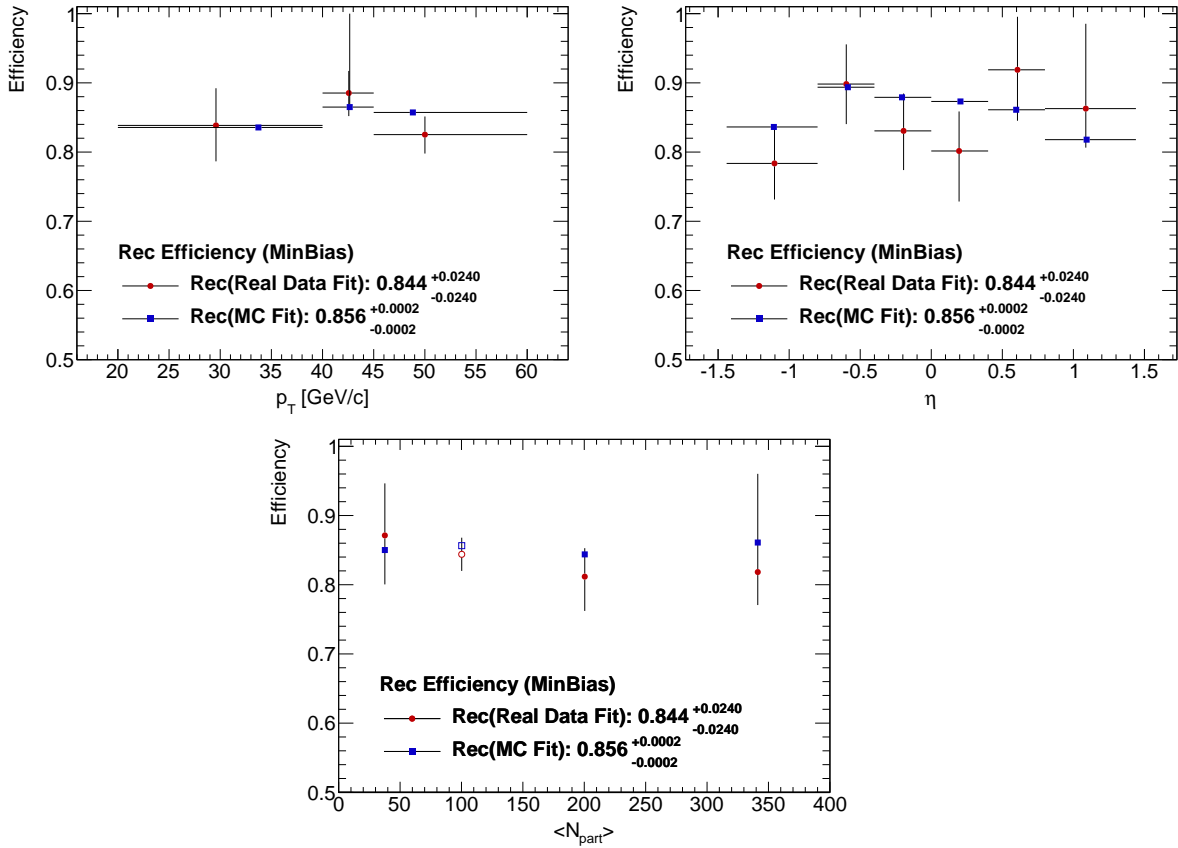


Figure 5.40: Single electron tracking efficiency in the Pb+Pb collision system as a function of p_T on the left, η on the right and N_{part} on the bottom. In red: Z in real data, in blue: Z embedded in HYDJET.

Chapter 6

Analysis of $Z \rightarrow l^+l^-$ in $p + p$ at

$$\sqrt{s} = 2.76 \text{ TeV}$$

The structure of this chapter will follow closely what is done in Chapter 5 for the Pb+Pb collision system. Any differences between the analysis of the two collision systems will be stated in this chapter.

This Chapter begins by covering the cuts to be used in order to remove as much background as possible from fake leptons while still keeping a high efficiency. The effect of these cuts is then used to compare data to MC. The next step is to look at the energy scale and resolution seen in data compared to MC. Due to the improved resolution seen in the $p + p$ environment compared to Pb+Pb, no energy scale or resolution corrections are performed.

Next, we define and measure the signal and background in bins of p_T , and y . The final part of measuring the yields is measuring the overall acceptance and efficiency corrections required to correct for losses in the signal. Finally, a summary of the measurement uncertainties is carried out. In a similar fashion as to what was done in Pb+Pb, each section will describe what is done in general and then will be split into what is done for the muons compared to what is done for the electrons.

6.1 Lepton Selection and Identification

Similar to the Pb+Pb analysis, the strategy is to apply loose cuts which will keep as much signal as possible while removing the majority of the background. The lower occupancy of the CMS calorimeters and muon chambers in $p + p$ at 2.76 TeV provides a clean Z signal in the dimuon channel and a relatively clean Z signal in the dielectron channel.

6.1.1 Muon Identification

The muon identification cuts used in the $p+p$ analysis are the same as those described in Section 5.1.1. Although the $p + p$ environment has a sufficiently low occupancy in the calorimeters to effectively apply isolation cuts, no isolation cuts were applied in this analysis in order to match what was done for the Pb+Pb environment. The variable distributions, and the effect of the cuts, are very similar to those seen in Section 5.1.1.

The cuts listed are studied in the reconstructed MC simulated dataset. The effects of all quality cuts are shown in Table 6.1. The table summarizes the values of the cuts for the analysis and the percentile of signal in simulation kept independently by each cut in the third column and after all the other cuts are applied in the last column. All cuts are applied after applying the trigger selection of one muon with a $p_T > 15$ GeV/ c .

Table 6.1: Quality cuts applied to global muons.

| Cut variable | Cut value | Only this cut | All except this cut |
|------------------|-----------|---------------|------------------------|
| IsTrackerMuon | true | 99.15 % | 96.24% |
| Muon Valid Hits | > 0 | 99.73 % | 96.49% |
| Matched Stations | > 1 | 98.25 % | 97.01% |
| Tracker Layers | > 4 | 99.80 % | 96.42% |
| Pixel Layers | > 0 | 98.86 % | 97.11% |
| GlobalChi2 | < 10 | 99.38 % | 96.72% |
| $ d_z $ | < 0.5 mm | 99.82% | 96.24% |
| $ d_{xy} $ | < 0.02 mm | 99.81 % | 95.25% |
| All cuts applied | | 96.24 % | |

In order to make sure the generated MC is representative of the data, Fig. 6.1 shows the

MC distributions of the relevant cut variables plotted together with the distributions from real data. The reconstructed MC muons coming from the Z are shown in the green histogram and the reconstructed global muons from the Z candidate muon pairs in data are shown by the red points. For each variable plotted all cuts were applied except for the cut on the variable shown. All of the variable distributions are normalized to unity. For most of the variables, the muons from HI data Z candidates (red points) match the distributions from MC Z s (green histogram). Although there may be a slight discrepancy between the distributions of a few variables, the cuts on the variable are loose enough that any differences do not affect the results. This can be shown by taking the ratio of the integral of the distribution passing the cut in both MC and real data (RD), which is shown on each plot. For perfectly matching distributions, this ratio should be equal to 1. The vertical dashed purple lines give the cut values used in the analysis.

Table 6.1 shows that $< 4\%$ of the signal is lost when applying all of the quality cuts. The largest loss comes from requiring more than one matched station, but it also is the muon quality cut responsible for the largest cut on the background.

6.1.2 Electron Identification

The electron identification variables that are cut on in the $p + p$ analysis are the same as those described in Section 5.1.2 although the $p + p$ analysis has more stringent selection cuts in order to match what was done in the $\sqrt{s} = 7$ TeV $p + p$ analyses [7, 8]. The hadronic energy cut is tightened so that $H/E < 0.12$ and the supercluster and track matching requirement in the η direction is tightened so that $|\Delta\eta_{in}| < 0.007$. The variable distributions and the effect of the cuts are significantly different from those seen in Section 5.1.2. The cuts are more efficient in the $p + p$ environment due to the lower occupancy in the calorimeter.

The cuts listed are studied in the reconstructed MC simulated dataset and the effects of all quality cuts are shown in Table 6.2. The table summarizes the values of the cuts for the analysis. The percent of the simulated signal kept by each cut independently is given in the third column while the signal remaining after all other cuts are applied is given in the last column. All cuts are applied after the trigger selection is complete.

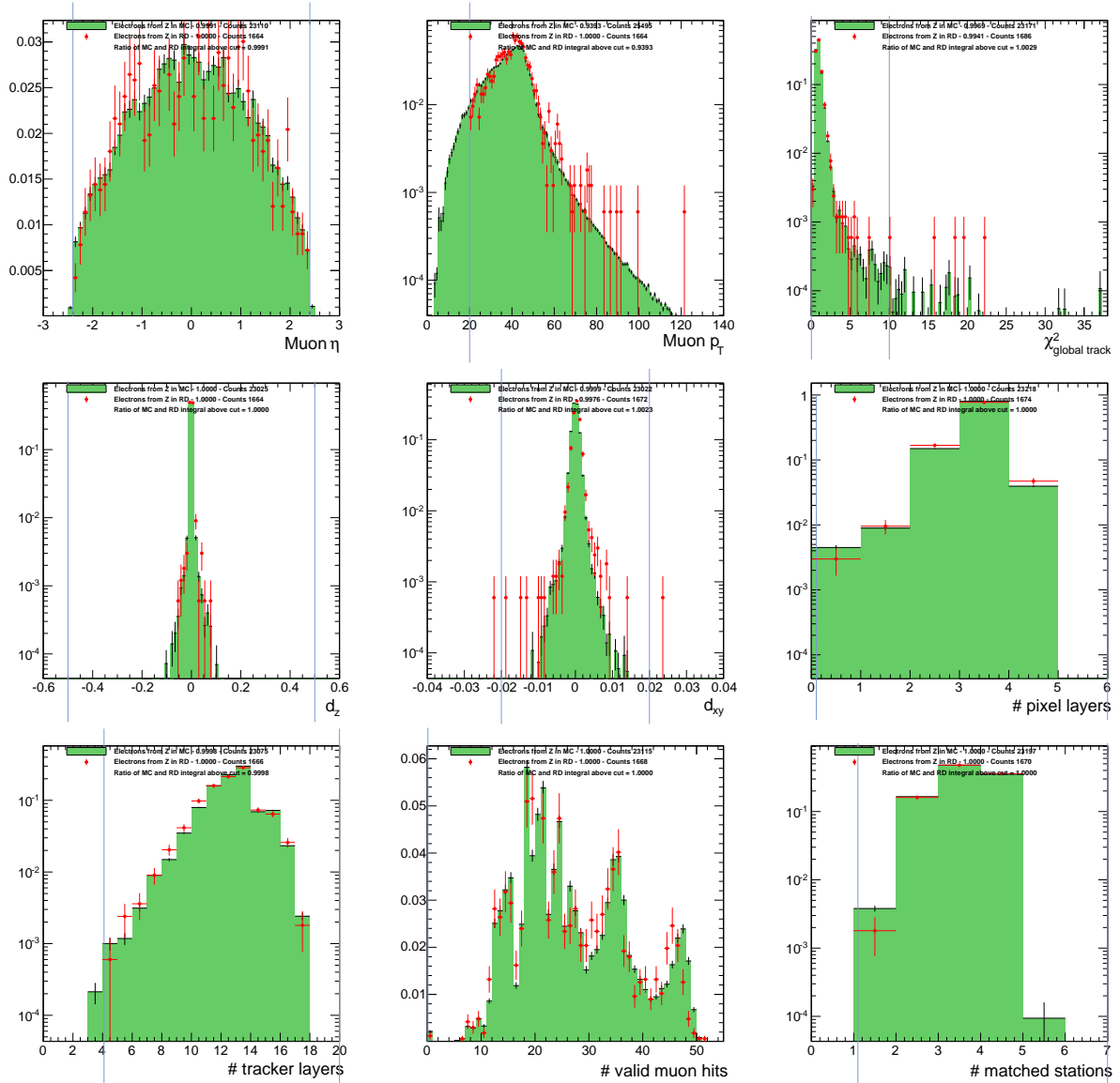


Figure 6.1: Single global muon quality distributions, from PYTHIA generated events with one Z per event (green histogram) and from the real data Z candidates (red points). All other cuts are applied to the muons but the one displayed. The histograms are normalized to unit area. The vertical dashed bars indicate the cut values used.

Table 6.2: Quality cuts applied to global electrons.

| Cut variable | Cut value | Only this cut | All except this cut |
|-------------------------------|-------------|---------------|---------------------|
| H/E | < 0.2 | 99.22% | 92.53 % |
| $ \sigma_{i\eta i\eta} $ | < 0.011 | 98.45% | 92.86 % |
| $ \Delta\eta_{in} $ | < 0.03 | 98.94% | 92.34 % |
| $ \Delta\Phi_{in} $ | < 0.15 | 98.88% | 92.00 % |
| $ d_{xy} $ | < 0.02 mm | 96.37% | 93.64 % |
| $ 1/E_{sc} - 1/p_{T_track} $ | < 0.05 | 96.75% | 93.65 % |
| All cuts applied | | 91.89 % | |

In order to make sure the generated MC is representative of the data, Fig. 6.2 shows the MC distributions plotted together with the distributions from real data without any background subtracted. The reconstructed MC electrons coming from the Z are shown in the green histogram and the reconstructed electrons from the Z candidate electron pairs in data are shown with the red points. For each variable plotted all cuts were applied except for the cut on the variable shown. All of the variable distributions are normalized to unity.

Similar to the effect that was seen in $p + p$, the plot comparing electron $\sigma_{i\eta i\eta}$ in data and MC are significantly different, due to the fact that there is a background present in the data that has a fundamentally different shower shape. In order to subtract the background, sideband subtraction is performed. In this case the mass bins 40–70, and 110–140 GeV/c^2 are used as the sideband regions representing the background, and the values are subtracted from what is seen in the 60–120 GeV/c^2 mass bin. The sideband subtracted results are shown in Fig. 5.3, demonstrating that the removal of background events removes the discrepancy between the data and MC.

6.2 Resolution Corrections

Similarly to Pb+Pb, before the MC can be trusted, it must faithfully reflect the characteristics of the data. An important aspect of the data and MC is the resolution of the mass and p_T of the Z . If these are significantly different, then the difference must be accounted for either through a correction or through assigning an uncertainty associated with that difference.

The first step is to compare the resolutions in data and MC in a data-driven way following

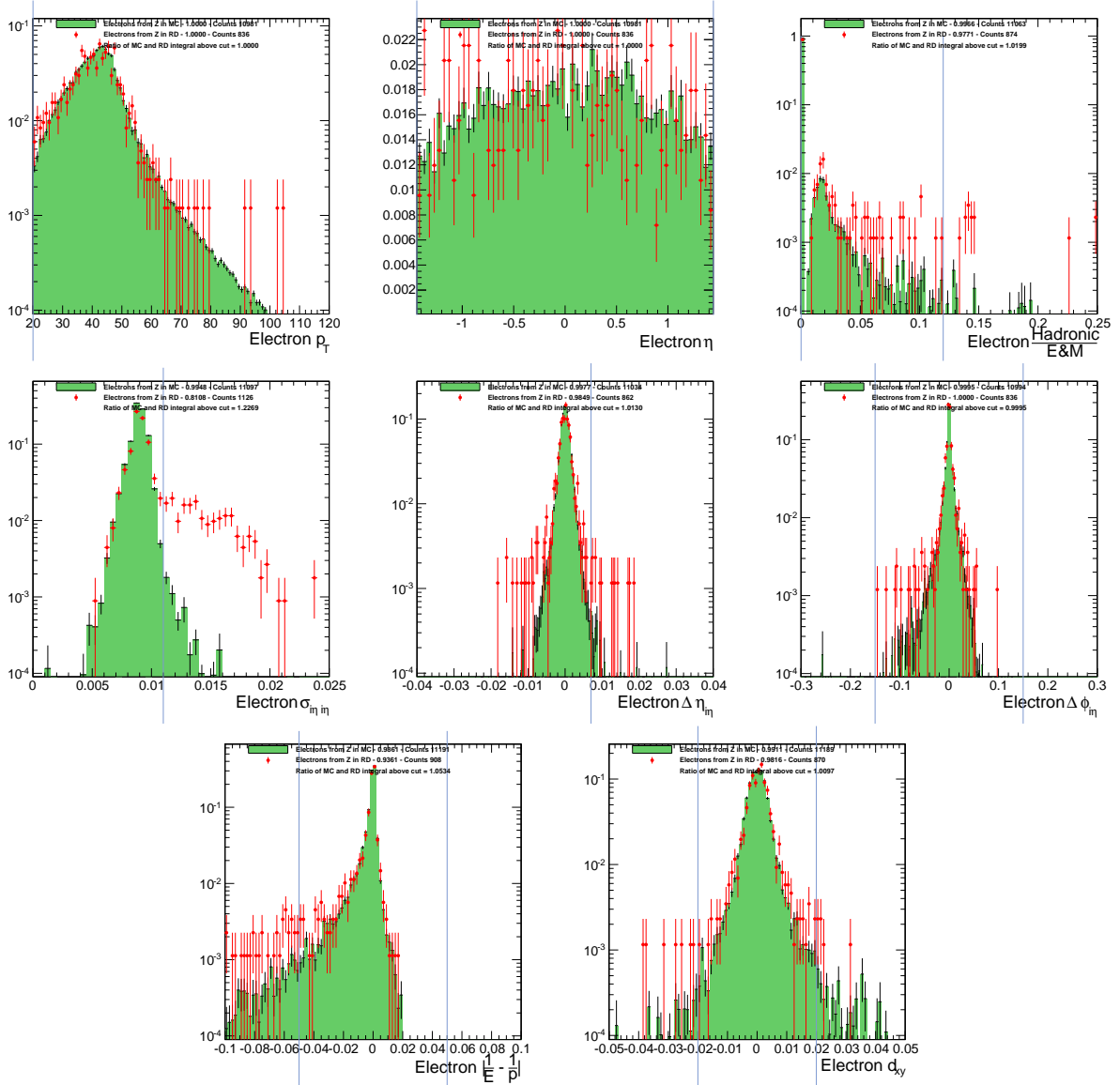


Figure 6.2: Single global electron quality distributions, from PYTHIA generated events with one Z per event (green histogram) and from the real data Z candidates (red points). All other cuts are applied to the electrons except the one displayed. The histograms are normalized to unity. The vertical bars indicate the actual cuts used.

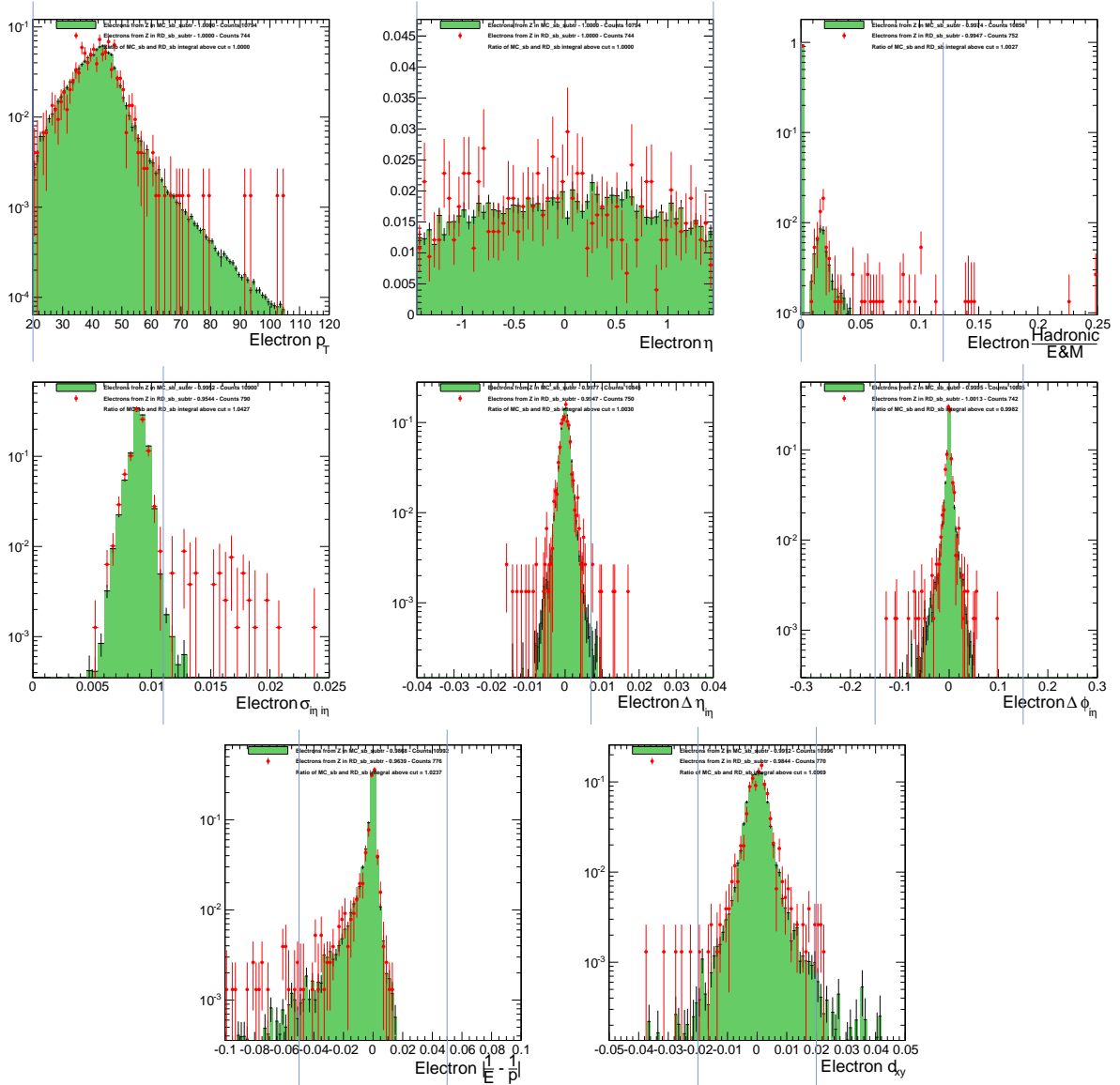


Figure 6.3: Single global electron quality distributions, from PYTHIA generated events with one Z per event (green histogram) and from the real data Z candidates (red points). All other cuts are applied to the electrons but the one displayed. Side-band subtraction is performed, using the mass bins $40 - 70$, and $110 - 140 \text{ GeV}/c^2$ as the sideband regions. The histograms are normalized to unity. The vertical dashed bars indicate the actual cuts used.

what was done in the Pb+Pb analysis and in Ref. [75]. This gives a general sense of the agreement between the two, as well as an idea of the level of resolution effects dealt with. The next step is to look at the peak and resolution of the invariant mass in data compared to MC in order to determine the need for either energy scale corrections to the data or MC oversmearing.

Finally, due to the significant p_T resolution effects that are present due to a combination of detector and final state radiation effects, unfolding is introduced in order to get a final Z p_T spectrum that can be compared to theoretical predictions.

6.2.1 Resolution Study

The resolution study was done by following the Pb+Pb analysis. Separate studies are done for the dimuon and dielectron channels.

6.2.1.1 Resolution Study for Dimuons

Due to the cleanliness of the dimuon signal, the dimuon channel is expected to have a good resolution so that the MC and data agree within statistics. First, we analyze the data in p_T bins while comparing to the expectations from MC simulations. The RD and MC samples are split in the p_T bins of the analysis and the RMS and mean value of the a_l and a_t distributions are computed. Figure 6.4 shows the mean and the RMS of the a_l and a_t distributions for MC truth, for MC simulation and for Z candidates in RD.

Finally, the values of the dimuon mass and p_T resolution are calculated. The results presented in Fig. 6.5 are obtained by splitting into 9 p_T bins and fitting the difference between the generated Z mass or p_T and the reconstructed value to a Gaussian. The individual fit results can be found in Appendix A and are shown in Figs. A.3 and A.7. We find a p_T resolution of better than 3% for $p_T > 30$ GeV/ c and a mass resolution better than 1.4%.

In the end, although there are some differences between the data and MC, these differences are not significant given the errors on the resolution measurement.

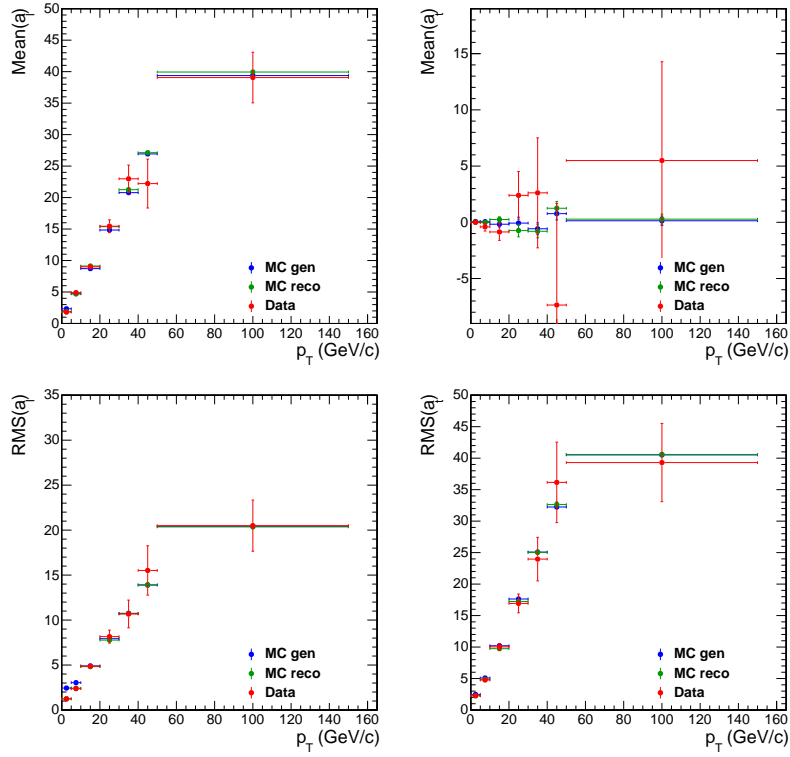


Figure 6.4: The mean (top) and the RMS (bottom) of the a_t (left) and a_l (right) distributions for MC truth, for MC simulation and for Z candidates from real data (blue squares, green triangles, and red circles, respectively), for dimuons.

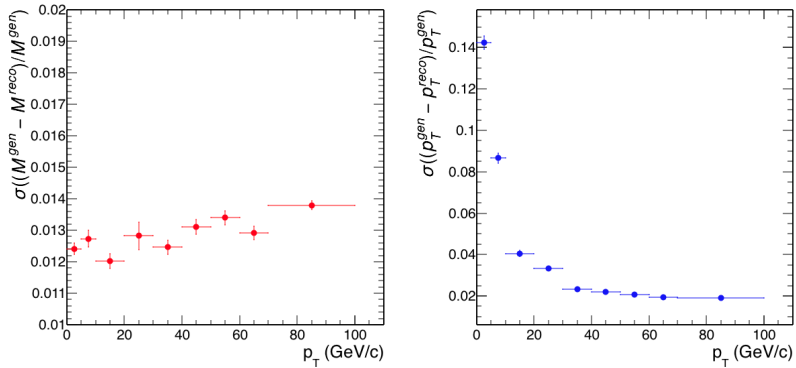


Figure 6.5: The mass resolution (left) and the p_T resolution (right) as a function of the generated p_T of the Z boson from dimuons in the $p + p$ environment.

6.2.1.2 Resolution Study for Dielectrons

Similar to the Pb+Pb analysis, the dielectron channel is expected to have lower resolution than the dimuon channel, although the MC should reflect the decrease in resolution. Following the same steps as for dimuons, we analyze the data in p_T bins while comparing to the expectations from MC simulations. The RD and MC samples are split in the p_T bins of the analysis and the RMS and mean value of the a_l and a_t distributions are computed. Figure 6.6 shows the mean and the RMS of the a_l and a_t distributions for MC truth, for MC simulation and for Z candidates in RD.

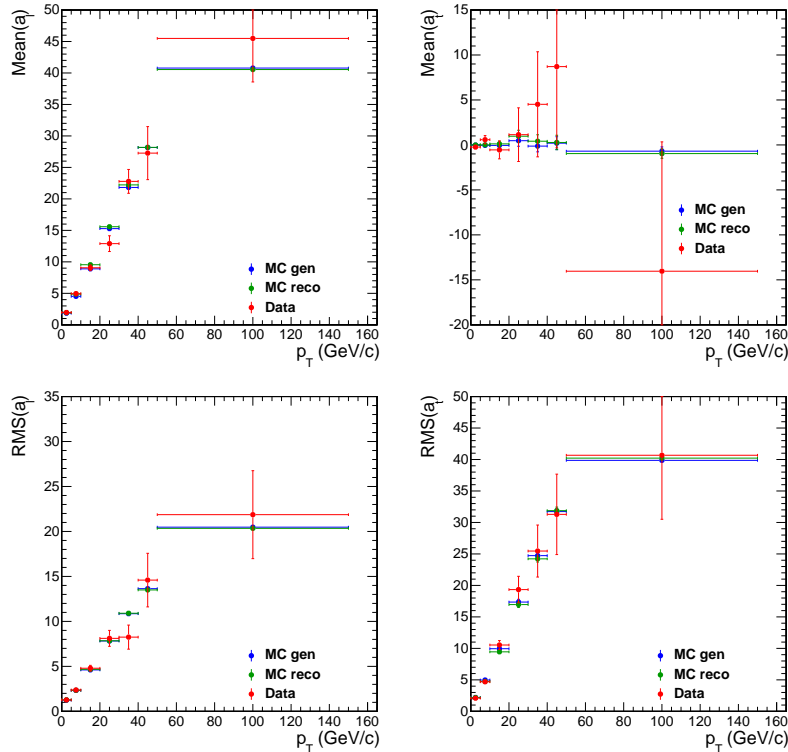


Figure 6.6: The mean (top) and the RMS (bottom) of the a_t (left) and a_l (right) distributions for MC truth, for MC simulation and for Z candidates from real data for dielectrons.

Finally, the values of the dielectron mass and p_T resolution are calculated. The results presented in Fig. 6.5 are obtained by splitting into 9 p_T bins and fitting the difference between the generated Z mass or p_T and the reconstructed value to a Gaussian. The individual fit results can be found in Appendix A and are shown in Figs. A.4 and A.8. We find a p_T resolution of better than 2% for $p_T > 40$ GeV/c, and a mass resolution better than 1.8%.

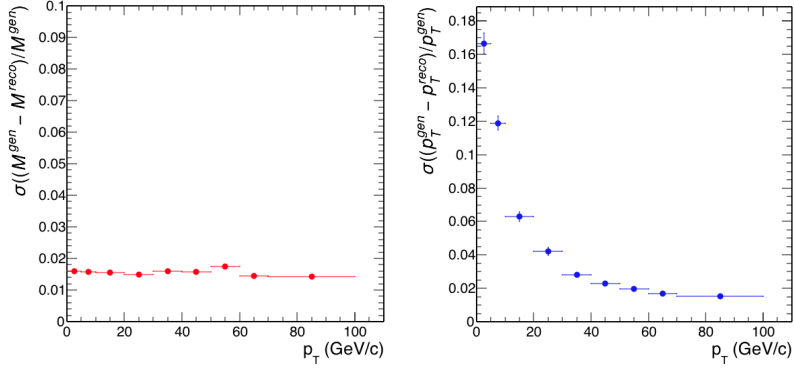


Figure 6.7: The mass resolution (left) and the p_T resolution (right) as a function of the generated p_T of the Z boson from dielectrons in the $p + p$ environment.

The resolution values are within statistical uncertainties although it is important to recognize the significant statistical limitations. These differences will be addressed by applying an energy correction to the data, and oversmearing the MC.

6.2.2 Invariant Mass Comparison

Studying the Z boson comes with the bonus that it provides a prominent peak compared to background processes. This allows for comparing the invariant-mass distribution seen in data compared to that seen in MC. If energy-scale corrections are needed, the Z boson peak will be at a different mass in data compared to MC. If the resolution differs between the two, then the MC must be oversmeared.

6.2.2.1 Invariant Mass for Dimuons

Figure 6.8 shows the invariant-mass distribution for global-global muon pairs from real data after all cuts are made. The solid points are the OS pairs, the open points represent the SS pairs (of which there is one in the dimuon channel) and the red, filled histogram shows the invariant-mass distribution seen in the MC. We can directly get the total number of Z s from counting the number of OS pairs: $N_Z(\text{OS}) = 830$ and subtracting the single SS pair: $N_Z(\text{SS}) = 1$ in the $[60-120]$ GeV/c^2 mass range to get the estimated raw Z yield $N_Z = 829$. This is due to the fact that the number of background events from muons coming from combinatorial background can be estimated by looking

at the number of SS pairs.

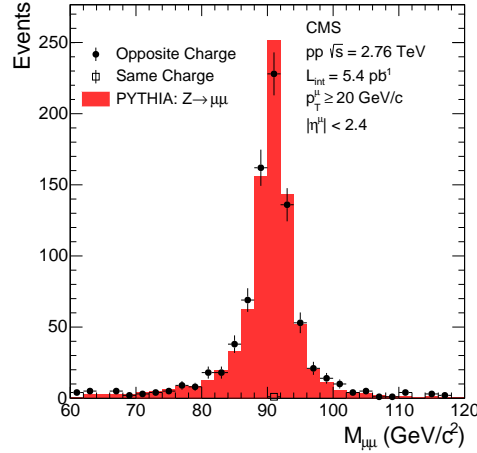


Figure 6.8: Invariant mass of global-global muon pairs in the $p + p$ collision system, after all cuts are made. The solid points represent “Opposite charge” muon pairs in data, and the open point represents the single “Same charge” muon pair. The filled, red histogram represents the MC.

Comparing data and MC, the peaks match, confirming that the muons are reconstructed with the correct energy. The MC appears to have a slightly better resolution than the data, although given the statistics, the resolutions are reasonably similar.

6.2.2.2 Invariant Mass for Dielectrons

Figure 6.9 shows the invariant mass distribution for electron pairs from real data in $p + p$. The solid points are the OS pairs, the open points are the SS pairs and the blue, filled histogram shows the invariant mass in the MC. For the Z boson decaying into two electrons, the background is well represented by the SS pairs (although a charge-misidentification correction will be applied later on). We can get the number of Z s from counting the number of OS pairs: $N_Z(\text{OS}) = 416$ and subtracting the number of SS pairs: $N_Z(\text{SS}) = 17$, resulting in $N_Z(\text{OS} - \text{SS}) = 399$ in the $[60-120]$ GeV/c^2 mass range.

Comparing data and MC, the Z peaks are consistent which confirms that there is no need for an energy scale correction for the electron case. The MC also appears to have a similar resolution to that of the data so that no oversmearing of the MC is required.

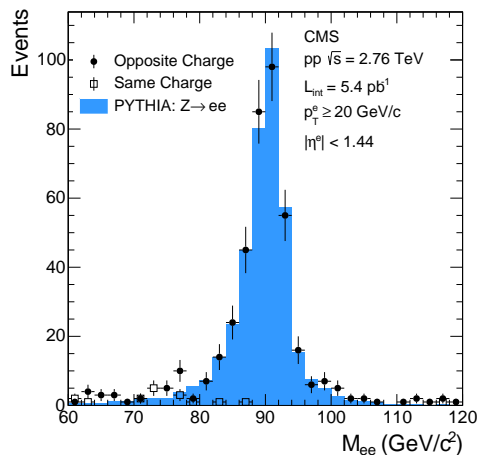


Figure 6.9: Invariant mass of electron pairs in the $p + p$ collision system, after all cuts are made. The solid points represent “Opposite charge” electron pairs in data, and the open points represent the “Same charge” electron pairs. The blue, filled histogram represents the MC.

6.2.3 Energy Correction

Since the background in the muon systems and calorimeters is much smaller in $p + p$ than Pb+Pb, no energy correction is expected to be needed. By looking at the invariant mass distributions in the two decay channels, these expectations are validated, and therefore no energy corrections are carried out in either of the channels.

6.2.4 Oversmearing of the MC

Once the data has been corrected, the Z boson peaks should match. When comparing the resolution of the peak, there may be a significant difference between data and MC, in which case this difference either needs to be corrected for or taken into account in the uncertainties. Similar to Pb+Pb, we must determine whether or not the MC and data distributions are significantly different. This is done using the KS test, which is described in Section 5.2.4.1.

The result of the KS test comparing the data and MC in the dimuon channel in $p + p$ is that 27% of randomly drawn distributions from the MC will fit as well or worse than the data that was recorded. Although this is not excellent agreement, it is good enough to justify keeping the MC resolution as is, without oversmearing. The oversmearing that corrects this difference (as described

for the electron MC in Pb+Pb in Section 5.2.4.2) is insignificant.

The result of the KS test comparing the data and MC in the dielectron channel in $p+p$ is that 47% of randomly drawn distributions from the MC will fit as well or worse than the data that was recorded. This is actually the channel with the best agreement, and therefore no oversmearing of the MC sample is required.

6.2.5 Unfolding

The same process which is described in Section 5.2.5 for correcting for resolution effects in Pb+Pb through unfolding is carried out for $p+p$. The resolution corrections will be at a slightly lower level in $p+p$, since the resolution in $p+p$ has been improved over that in Pb+Pb due to the dramatic reduction in the underlying-event activity.

6.2.5.1 Resolution Unfolding for Dimuons

Using the MC that has been generated, the response matrix shown in Fig. 6.10 is created.

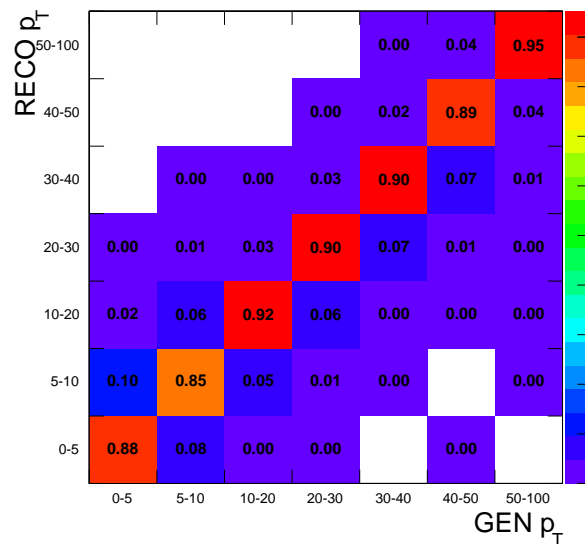


Figure 6.10: Matrix of generated versus reconstructed p_T for the Z boson in the dimuon channel, in the MC used in this $p+p$ analysis.

The response matrix is unfolded, and applied to the data binned in Z boson p_T , in order to

transform the reconstructed Z boson p_T spectrum to the original produced Z boson p_T spectrum.

6.2.5.2 Resolution Unfolding for Dielectrons

For the Z boson analysis for dielectrons, the response matrix (generated p_T versus reconstructed p_T) based on the MC that was generated in the $p + p$ environment is used to unfold the resolution effects with respect to p_T . Figure 6.11 shows the response matrix.

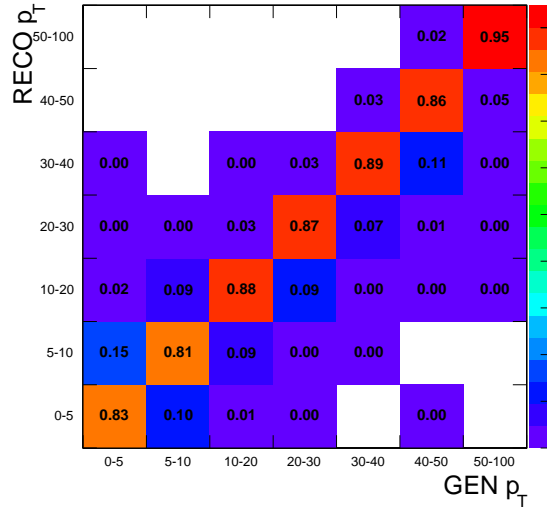


Figure 6.11: Matrix of generated versus reconstructed p_T for the Z boson in the dielectron channel, in the MC used in this $p + p$ analysis.

6.3 Raw Yields

The signal and background estimation are determined the same way in $p + p$ as was done in Pb+Pb. The raw signal (background) yields are determined by counting the number of opposite (same) charged dileptons in the $[60 - 120]$ GeV/c^2 mass range. Those dileptons are required to pass the following acceptance cuts: each muon (electron) has a $p_T^\mu > 20$ GeV/c (20 GeV/c), $|\eta| < 2.4$ (1.44), and each dimuon (dielectron) has $|y| < 2.0$ (1.44). The raw yield is counted in the full integrated bin as well as split into bins of p_T and $|y|$.

6.3.1 Raw Yields in Dimuon Channel

The Z candidates in the dimuon channel are split into bins of p_T and $|y|$ as shown in Table 6.3, with a total integrated value of 830 ± 29 Z bosons. There are no same charge dimuons, so there is no background subtraction done at this point.

Table 6.3: Raw number of Z boson candidates in the dimuon channel in the p_T and y bins used for the analysis, including statistical errors. $p_T^\mu > 20 \text{ GeV}/c$, $|\eta^\mu| < 2.4$ and $|y_{\mu\mu}| < 2.0$.

| p_T (GeV/ c) | 0 – 5 | 5 – 10 | 10 – 20 | 20 – 30 | 30 – 40 | 40 – 50 | 50 – 100 | |
|-------------------|--------------|--------------|--------------|--------------|--------------|-------------|------------|------------|
| N_Z | 250 ± 16 | 202 ± 14 | 217 ± 15 | 81 ± 9 | 32 ± 6 | 18 ± 4 | 30 ± 5 | |
| $ y $ | 0 – 0.25 | 0.25 – 0.5 | 0.5 – 0.75 | 0.75 – 1.0 | 1.0 – 1.25 | 1.25 – 1.5 | 1.5 – 1.75 | 1.75 – 2.0 |
| N_Z | 123 ± 11 | 134 ± 12 | 132 ± 11 | 103 ± 10 | 119 ± 11 | 97 ± 10 | 71 ± 8 | 53 ± 7 |

6.3.2 Raw Yields in Dielectron Channel

The Z candidates in the dielectron channel are split into the same p_T bins as in the dimuon channel but different bins of $|y|$, as shown in Table 6.4. There are 416 ± 20 opposite charge dielectrons and 17 ± 4 same charge dielectrons, resulting in a background subtracted raw yield of 399 ± 21 Z bosons.

Table 6.4: Raw number of Z boson candidates in the dielectron channel in the p_T and y bins used for the analysis, including statistical errors. $p_T^e > 20 \text{ GeV}/c$, $|\eta^e| < 1.44$ and $|y_{ee}| < 1.44$.

| p_T (GeV/ c) | 0 – 5 | 5 – 10 | 10 – 20 | 20 – 30 | 30 – 40 | 40 – 50 | 50 – 100 |
|----------------------|--------------|--------------|--------------|------------|------------|------------|------------|
| N_Z^{OS} | 109 ± 10 | 109 ± 10 | 113 ± 11 | 42 ± 6 | 20 ± 4 | 12 ± 3 | 10 ± 3 |
| N_Z^{SS} | 4 ± 2 | 3 ± 2 | 2 ± 1 | 2 ± 1 | 2 ± 1 | 2 ± 1 | 2 ± 1 |
| $N_Z^{\text{OS-SS}}$ | 105 ± 11 | 106 ± 11 | 111 ± 11 | 40 ± 7 | 18 ± 5 | 10 ± 4 | 8 ± 3 |
| $ y $ | 0 – 0.25 | 0.25 – 0.5 | 0.5 – 0.75 | 0.75 – 1.0 | 1.0 – 1.44 | | |
| N_Z^{OS} | 121 ± 11 | 100 ± 10 | 100 ± 10 | 50 ± 7 | 45 ± 7 | | |
| N_Z^{SS} | 6 ± 2 | 4 ± 2 | 3 ± 2 | 0 ± 0 | 4 ± 2 | | |
| $N_Z^{\text{OS-SS}}$ | 115 ± 11 | 96 ± 10 | 97 ± 10 | 50 ± 7 | 41 ± 7 | | |

6.4 Acceptance and Efficiency

The next step in the measurement is applying acceptance and efficiency corrections. These corrections are calculated as a function of p_T and y , and are defined in the same way as for Pb+Pb in Section 6.4 for Pb+Pb. Since the acceptance corrections are based entirely on the kinematics of the Z bosons produced, the acceptance corrections are identical to those seen in Pb+Pb, with the overall acceptance being approximately 70% (50%) in the muon (electron) rapidity ranges.

When the data are binned in the Z -boson p_T or y , the corresponding selection is applied to both the numerator and denominator. The overall efficiency is approximately 90% (80%) in the muon (electron) case in $p + p$ collisions. The following sections look at these in more detail.

6.4.1 Efficiency Corrections for Dimuons

The combined trigger, reconstruction, and muon identification efficiency as function of Z boson p_T , and y are shown in Fig. 6.12.

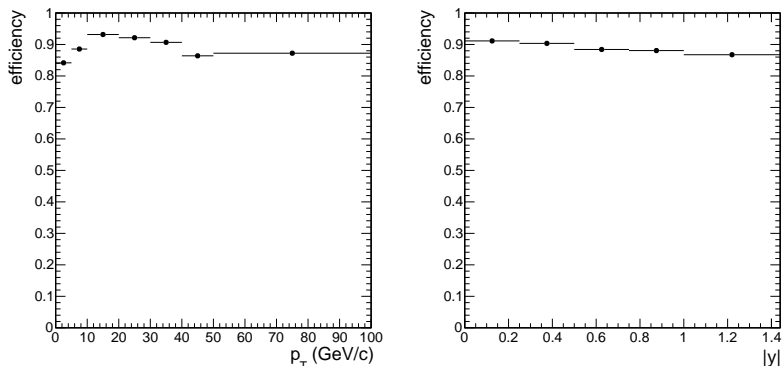


Figure 6.12: Combined trigger, reconstruction, and muon identification efficiency for dimuons in p_T and $|y|$ bins of the $p + p$ analysis.

The final correction to be applied to the raw yields extracted from data is the acceptance \times efficiency ($\alpha \times \epsilon$).

6.4.2 Efficiency Corrections for Dielectrons

The combined trigger, reconstruction, and electron identification efficiency as function of Z p_T and y are shown in Fig. 6.13.

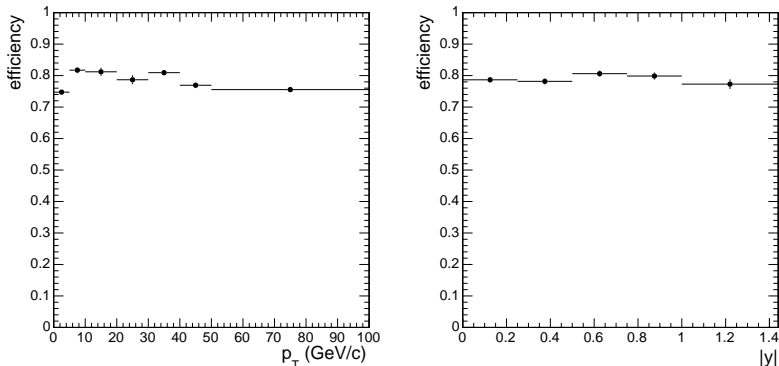


Figure 6.13: Combined trigger, reconstruction, and electron identification efficiency for dielectrons in the $p + p$ collision system in p_T and $|y|$ bins of the $p + p$ analysis.

6.5 Uncertainties

The overall uncertainties measured are given here. The method of getting these uncertainties matches what is done in the Pb+Pb analysis, as described in Section 5.5. The total systematic uncertainty in the Z yield in $p + p$ collisions is estimated by adding the different contributions in quadrature. The uncertainty in the efficiencies is 1.9% for the dimuon channel and 7.7% for the dielectron channel, based on the TNP technique.

The uncertainties coming from the acceptance corrections are identical to those described in Section 5.5.2 for Pb+Pb and will cancel in the measurement of R_{AA} . The systematic uncertainty from the remaining background from other physical sources gives us a systematic uncertainty of 1.0% for the dimuon channel, and 1.0% for the dielectron channel.

The uncertainty in the integrated luminosity of the $p + p$ dataset is 3.7% due to the uncertainty in the calibration of the beam cross section [67].

The integrated systematic uncertainties for the $Z \rightarrow \mu^+\mu^-$ and the $Z \rightarrow e^+e^-$ channel yields in $p + p$ collisions are summarized in Table 6.5.

Table 6.5: Summary of the integrated systematic uncertainty values for the $Z \rightarrow \mu^+\mu^-$ and $Z \rightarrow e^+e^-$ yields in $p + p$.

| | $Z \rightarrow \mu^+\mu^-$ | $Z \rightarrow e^+e^-$ |
|-------------------------------------|----------------------------|------------------------|
| Combined Efficiency | 1.9% | 7.7% |
| Acceptance | 0.7% | 0.7% |
| Background | 1.0% | 1.0% |
| Integrated Luminosity (L_{int}) | 3.7% | 3.7% |
| Overall | 4.3% | 8.6% |

6.5.1 Background Studies

The method for determining the uncertainty on the background follows the same procedure as for Pb+Pb in Section 5.5.1.

Muons Figure 6.14 shows the mass distribution of muon pairs in real data on the left and the differences between data and MC fit with exponentials in the right panel. The only thing that was changed from one background fit to the other is the beginning and end of the fit window. The worst case scenario is shown by the red curve. The 1% contribution of the remaining background to the the signal region is considered to be the systematic on the background.

Electrons Figure 6.15 shows the mass distribution of electron pairs in real data on the left and the differences between data and MC fit with exponentials on the right. The worst case scenario is shown by the red curve. The 1% contribution in the signal region is considered to be the systematic on the background.

6.6 Tag and Probe Method

The TNP method described in Section 5.6 is used to extract efficiencies in a data-driven way for the $p + p$ analysis. As is done in the Pb+Pb analysis, the calculated efficiencies are used in the following ways: the ratio of the efficiency found in MC and data is used to scale the efficiencies measured using MC in order to correct for differences between the two datasets; the uncertainties from the MC and data fits are used as the uncertainty associated with the TNP method, as is standard for heavy-ion analyses using TNP. The fluctuations in the fits are driven by the limited statistics in data.

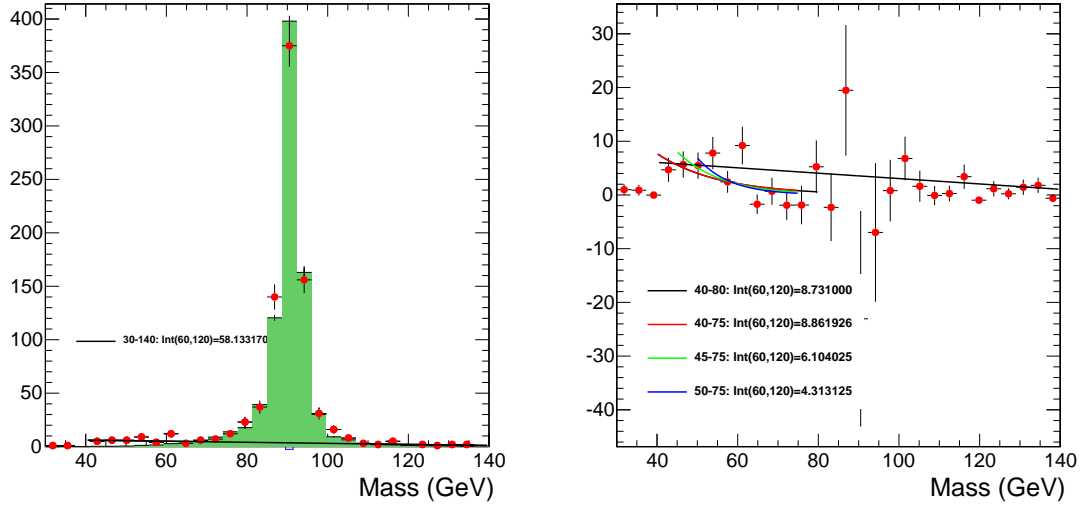


Figure 6.14: (Left) The invariant mass distribution of muon pairs from $p + p$ collisions in real data (red circles) fitted with the mass distribution from simulation (green histogram). The legend in the figure shows the integral of the background fitting before the subtraction. (Right) Difference between the real data mass distribution and the fitted simulation together with exponential fits to the lower mass region estimating the background in the $p + p$ collision system.

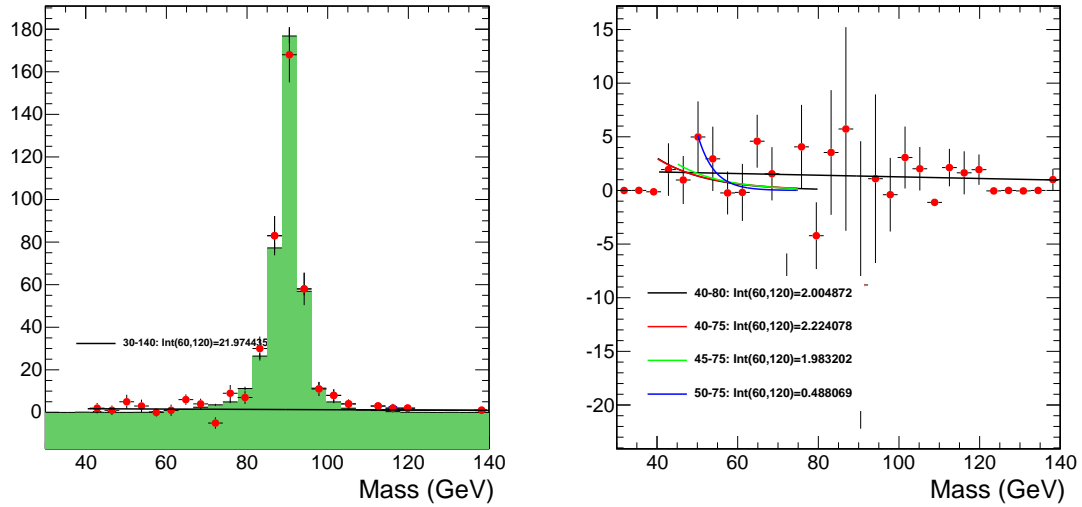


Figure 6.15: (Left) The invariant mass distribution of electron pairs from $p + p$ collisions in real data (red circles) fitted with the mass distribution from simulation (green histogram). The legend in the figure shows the integral of the background fitting before the subtraction. (Right) Difference between the real data mass distribution and the fitted simulation together with exponential fits to the lower mass region estimating the background in the $p + p$ collision system.

6.6.1 TNP Method for Muons

The three single-muon efficiencies: trigger, muon identification, and inner track reconstruction, are measured separately using similar tag and probe definitions to those used in Pb+Pb. Since the quality cuts used in the $p + p$ and Pb+Pb analyses are identical, the definitions for a “Good Quality” muon, and “Good Track Quality” are the same as those described in Section 5.6.1. Our acceptance requirement for a single muon is $p_T > 20 \text{ GeV}/c$ and $|\eta| < 2.4$.

6.6.1.1 Muon Trigger Efficiency

Since the triggers used in the Pb+Pb and $p + p$ analyses are different, the trigger efficiency measurement differs slightly. The settings used to get the trigger efficiency with the TNP method are the following:

- Tag: a Global Muon with “Good Quality” and matched to a single-muon trigger.
- Probe: a Global Muon that fulfills all “Good Quality” cuts and is in the acceptance.
- Passing: a Probe that can be matched to the dimuon trigger, requiring two muons with no explicit p_T cutoff (HLT_HIL2DoubleMu0).

The mass range used in the fit is $M \in [60, 120] \text{ GeV}/c^2$ and the mass peak is fitted with a Voigtian function for the passing and failing signal. The passing and failing background is fitted with an exponential. The efficiency of the trigger is estimated to be $98.6 \pm 0.3\%$ (stat) from the fit using Z in real data for the trigger we are using. The fits for MC and data are shown in Appendix B.2.

Figure 6.16 shows the single-muon trigger efficiency as a function of p_T and η for real data in red and for Z generated in PYTHIA in blue. The overall agreement between each sample is at the 1% level. On average the trigger efficiency is very good, 99.0% from TNP with the generated samples. The ratio of the efficiency found in MC and data is used to scale the efficiencies measured using MC. The uncertainties from the MC and data fits are the uncertainties associated with the TNP method.

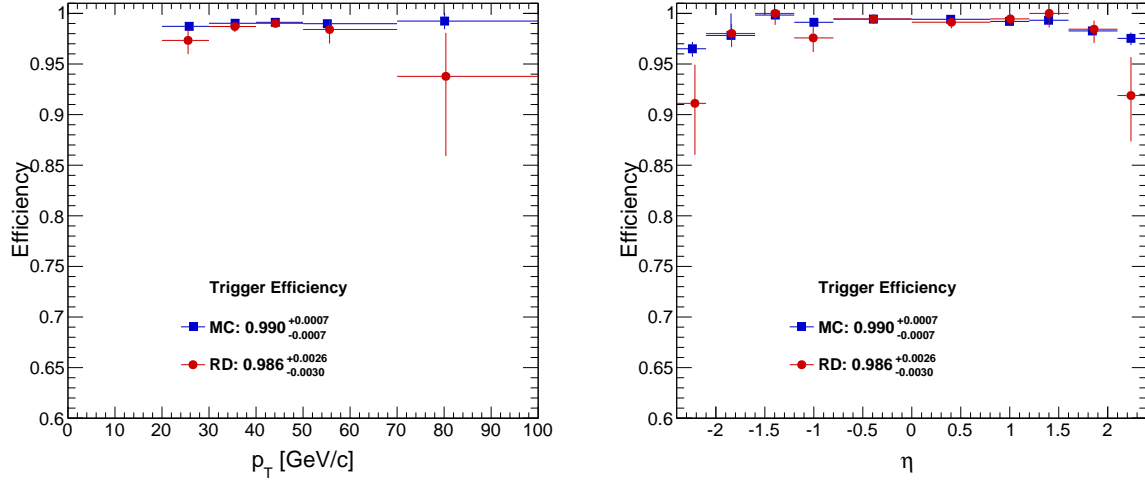


Figure 6.16: Single-muon triggering efficiency of the HLT_HIL2DoubleMu0 trigger used in $p + p$ collisions as a function of p_T on the left, and η on the right. In red: Z in real data, in blue: Z generated with PYTHIA.

6.6.1.2 Muon ID Efficiency

The settings for the method used to measure the muon identification efficiency are the following:

- Tag: a Global Muon with “Good Quality” and matched to the Double Muon Trigger.
- Probe: Tracker muon in acceptance, passing track cuts.
- Passing: probe that can be matched to a global muon in the acceptance and is “Good Quality”.

The mass range used in the fit is $M \in [60, 120]$ GeV/ c^2 and the mass peak is fitted with a Voigtian function for the passing and failing signal. The passing and failing background is fitted with an exponential. The efficiency of the muon identification is estimated to be $98.4 \pm 0.3\%$ (stat) from the fit using Z in real data. The fits for MC and data are shown in Appendix B.2.

Figure 6.17 shows the muon identification efficiency as a function of p_T and η , for real data in red and for Z generated in PYTHIA in blue. These cuts do not remove much signal, and the results for real data are within 0.1% of simulation. The ratio of the efficiency found in MC and data is used to scale the efficiencies measured using MC. The uncertainties from the MC and data fits are

the uncertainties associated with the TNP method.

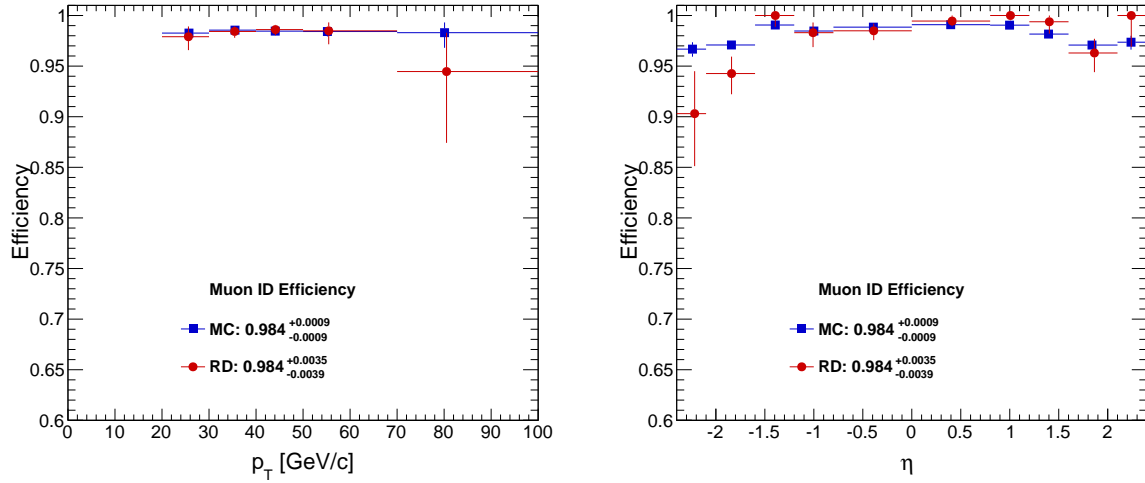


Figure 6.17: Single-muon ID efficiency for $p + p$ collisions as a function of p_T on the left, and η on the right. In red: Z in real data, in blue: Z generated with PYTHIA.

6.6.1.3 Muon Track Reconstruction Efficiency

In order to measure the muon track reconstruction efficiency, we apply the TNP method:

1. Tag: a Global muon with “Good Quality” and matched to HLT_HIL2DoubleMu0
2. Probe: STA muon with at least one valid hit in the muon station
3. Passing: Probe that fulfills isGlobalMuon with “Good Track Quality”.

Due to the poorer resolution, the mass range used in the fit is $\in [40, 140]$ GeV/ c^2 . The mass peak is fitted with a Voigtian at the Z peak. The passing and failing background is fitted with an exponential. The efficiency of the muon-track reconstruction is estimated to be $99.8 \pm 0.4\%$ (stat) from the fit using Z s in real data. The fits for MC and data are shown in Appendix B.2.

Figure 6.18 shows the muon track reconstruction efficiency as a function of p_T and η , for real data in red and for Z generated in PYTHIA in blue. Results for real data are within 1% of the simulation. The ratio of the efficiency found in MC and data is used to scale the efficiencies

measured using MC. The uncertainties from the MC and data fits are the uncertainties associated with the TNP method.

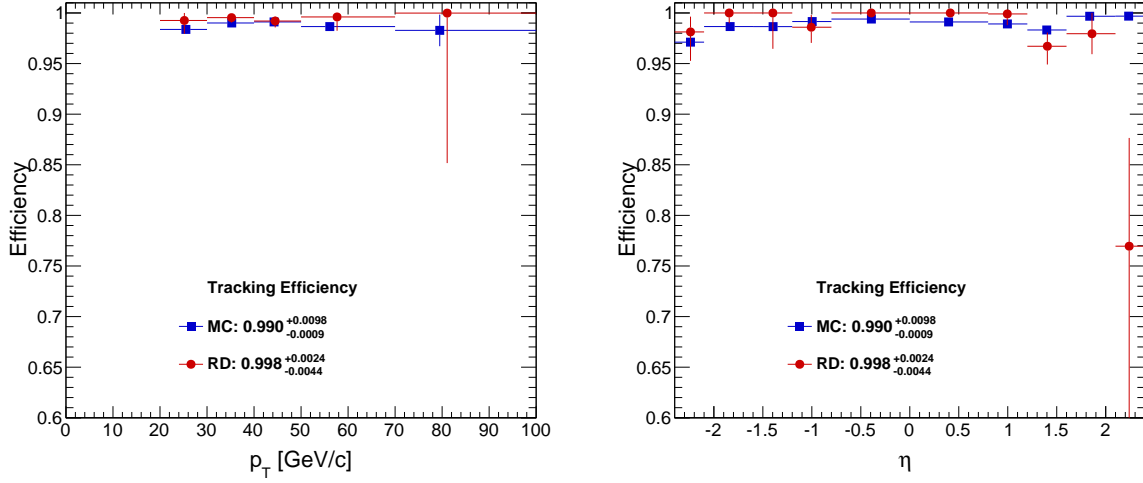


Figure 6.18: Single-muon tracking efficiency for $p + p$ collisions as a function of p_T on the left, and η on the right. In red: Z in real data, in blue: Z generated with PYTHIA.

6.6.2 TNP Method for Electrons

The three single-electron efficiencies: trigger, electron identification, and reconstruction are measured separately using similar tag and probe definitions as those used in Pb+Pb. The quality cuts used (and therefore the “Electron ID” requirements) in the $p + p$ and Pb+Pb analyses are identical except for the following tighter cuts which can be used in the cleaner $p + p$ collision environment without cutting out as much signal as in the Pb+Pb environment:

- $H/E < 0.12$
- $|\Delta\eta_{i\eta}| < 0.007$

Our acceptance requirement for the single electron is $p_T > 20$ GeV/ c and $|\eta| < 1.44$.

6.6.2.1 Electron Trigger Efficiency

Although the event background differs between Pb+Pb and $p + p$, the triggers used in the two analyses have the same requirements although the nomenclature is slightly different. An extra `_NoCaloId` is added in the $p + p$ trigger name since, although there are no significant changes in the trigger, during the $p + p$ run a set of photon triggers containing calorimeter ID cuts were added to the calorimeter trigger menu. The settings used to get the trigger efficiency with the TNP method are the following:

- Tag: an Electron in the acceptance, passing Electron ID cuts, and matched to the trigger requiring a single energy deposit of $E_T > 20$ GeV (`HLT_HISinglePhoton20`).
- Probe: an Electron in the acceptance, passing Electron ID cuts.
- Passing: Probe that can be matched to the trigger requiring two energy deposits, one of $E_T > 20$ GeV and one of $E_T > 15$ GeV (`HLT_HIPhoton15_Photon20` trigger).

The mass range used in the fit is $M \in [60, 120]$ GeV/ c^2 and the mass peak is fitted with a Breit-Wigner function convolved with Crystal-Ball function for the passing and failing signal. The convolution with the Crystal-Ball function is done in order to reflect the energy loss experienced by the electron passing through the detector. The passing and failing background is fit with an exponential. The efficiency of the trigger is estimated to be $99.6 \pm 0.4\%$ (stat) from the fit using Z in real data for the trigger we are using. The fits for MC and data are shown in Appendix B.4.

Figure 6.19 shows the single-electron trigger efficiency as a function of p_T and η , for real data in red and for Z generated in PYTHIA in blue. The agreement between each set of points is on the 1% level. The `HLT_HIPhoton15_Photon20` trigger requires two ECAL objects, one with a p_T greater than 15 GeV/ c and one greater than 20 GeV/ c . On average the trigger efficiency in MC is 99.9% from TNP with the generated samples. The ratio of the efficiency found in MC and data is used to scale the efficiencies measured using MC. The uncertainties from the MC and data fits are the uncertainties associated with the TNP method.

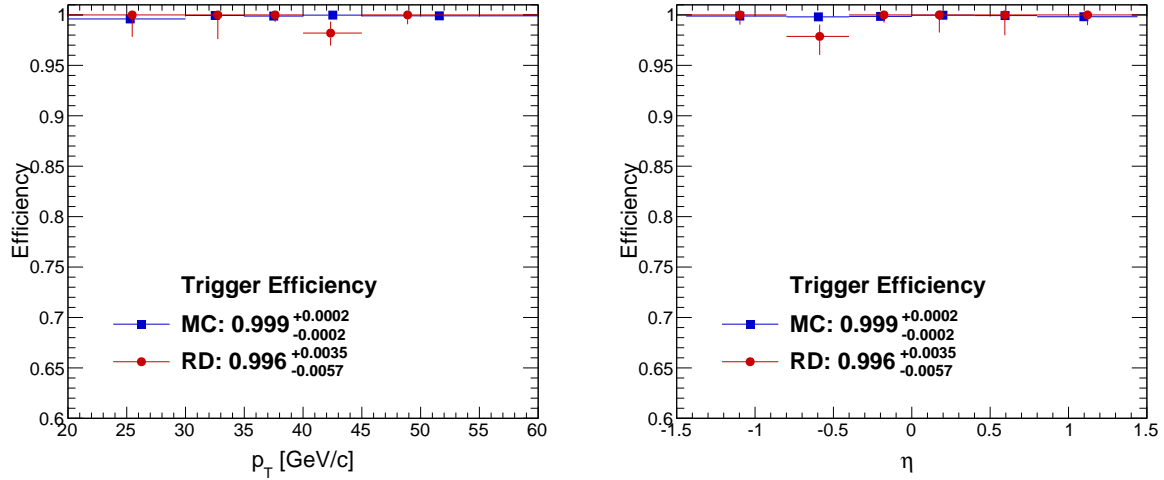


Figure 6.19: Single-electron triggering efficiency of the HLT_HIPhoton15_Photon20 trigger in $p + p$ collisions as a function of p_T on the left, and η on the right. In red: Z in real data, in blue: Z generated with PYTHIA.

Electron ID Efficiency The settings for the method used to estimate the electron identification efficiency are the following:

- Tag: an Electron in the acceptance, passing Electron ID cuts, and matched to the diphoton trigger.
- Probe: an Electron in the acceptance.
- Passing: Probe that passes Electron ID cuts.

The mass range used in the fit is $M \in [60, 120]$ GeV/ c^2 and the mass peak is fitted with a Breit-Wigner function convolved with Crystal-Ball function for the passing and failing signal. The passing and failing background is fitted with an exponential. The efficiency of the electron identification is estimated to be $92.6 \pm 4.0\%$ (stat) from the fit using Z in real data. The fits for MC and data are shown in Appendix B.4.

Figure 6.20 shows the electron identification efficiency as a function of p_T and η for real data in red and for Z generated in PYTHIA in blue. The overall agreement between each sample is at the 2.5% level. The ratio of the efficiency found in MC and data is used to scale the efficiencies

measured using MC. The uncertainties from the MC and data fits are the uncertainties associated with the TNP method.

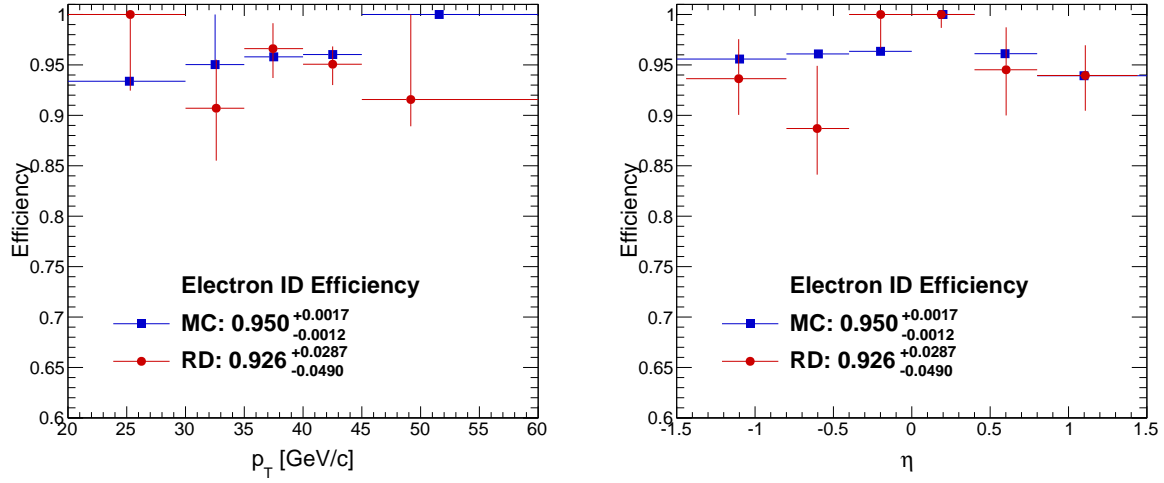


Figure 6.20: Single-electron ID efficiency in the $p + p$ environment as a function of p_T on the left, and η on the right. In red: Z in real data, in blue: Z generated with PYTHIA.

Electron Track Reconstruction Efficiency In order to measure the electron track reconstruction efficiency, we apply the TNP method as follows:

- Tag: an Electron in the acceptance, passing Electron ID cuts, and matched to the diphoton trigger.
- Probe: SuperCluster in the acceptance, passing $H/E < 0.12$.
- Passing: Probe reconstructed as the super cluster of an electron track.

Due to the poorer resolution of the super cluster kinematics, the mass range used in the fit is $\in [40, 140]$ GeV/ c^2 and the mass peak is fitted with a Breit-Wigner function convoluted with a Crystal-Ball function. The passing and failing background is fitted with an exponential times a turn-on curve. The efficiency of the electron reconstruction is estimated to be $96.6 \pm 1.6\%$ (stat) from the fit using Z s in real data. The fits for MC and data are shown in Appendix B.4.

Figure 6.21 shows the electron track reconstruction efficiency as a function of p_T and η for real data in red and for Z generated in PYTHIA in blue. The overall results for real data are within 2.0% of simulation. The ratio of the efficiency found in MC and data is used to scale the efficiencies measured using MC. The uncertainties from the MC and data fits are the uncertainties associated with the TNP method.

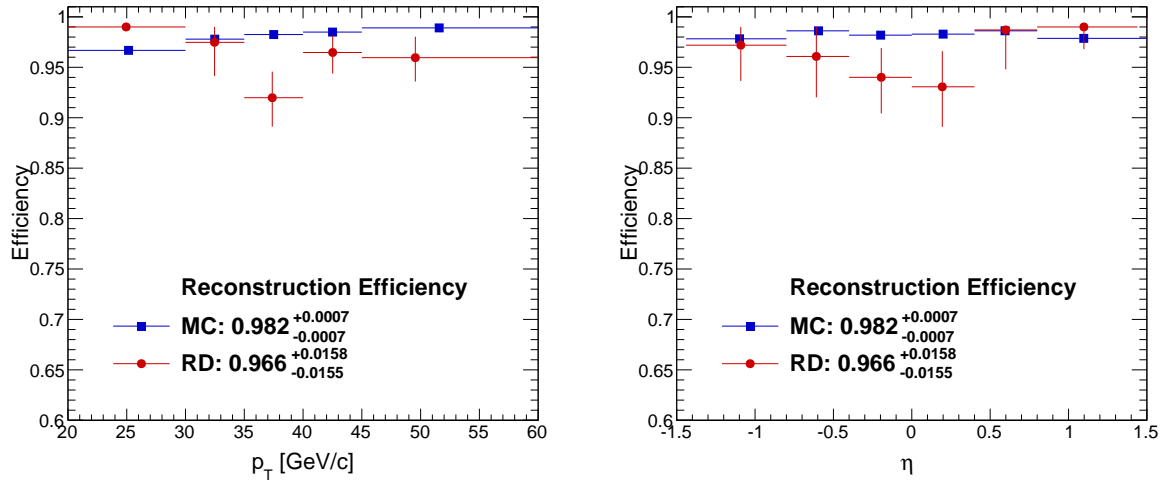


Figure 6.21: Single-electron tracking efficiency in $p + p$ collisions as a function of p_T on the left, and η on the right. In red: Z in real data, in blue: Z generated by PYTHIA.

Chapter 7

Results and Discussion

7.1 Z Yields in Pb+Pb Collisions vs. p_T , y , and Centrality

The Z yield measured in Pb+Pb collisions as a function of event centrality, y , and p_T is compared to $p+p$ NNLO calculations produced by POWHEG, and scaled by an average nuclear overlap function, $d\sigma_{p+p}^Z/dy \times T_{AA}$, as described below and discussed in Ref. [42]. The results from $p+p$ data are presented in Section 7.2 and compared with those from Pb+Pb data in Section 7.3.

The data are divided into independent ranges: 6 in event centrality, 8 (5) in y for the dimuon (dielectron) channel, and 7 in the dilepton p_T . The results are presented in Figs. 7.1, and 7.2. The yields of $Z \rightarrow l^+l^-$ (where l is the combination of the muon and electron channels) per MB event, per unit of y ($dN_{\text{Pb+Pb}}^Z/dy$), and per p_T bin ($d^2N_{\text{Pb+Pb}}^Z/dydp_T$) are computed using the following equations:

$$\frac{dN_{\text{Pb+Pb}}^Z}{dy} = \frac{N_{\text{Pb+Pb}}(Z \rightarrow l^+l^-)}{\alpha \varepsilon N_{\text{MB}} \Delta y} \quad \text{or} \quad \frac{d^2N_{\text{Pb+Pb}}^Z}{dydp_T} = \frac{N_{\text{Pb+Pb}}(Z \rightarrow l^+l^-)}{\alpha \varepsilon N_{\text{MB}} \Delta y \Delta p_T}. \quad (7.1)$$

Here $N_{\text{Pb+Pb}}(Z \rightarrow l^+l^-)$ is the number of Z boson candidates divided into bins of p_T , y , and centrality found in the dimuon or dielectron invariant mass range of 60–120 GeV/ c^2 . They refer to the counts presented in Table 5.3 for dimuons and Table 5.4 for dielectrons. N_{MB} is the number of corresponding MB events corrected for the trigger efficiency, namely $(1.16 \pm 0.03) \times 10^9$ events, α and ε are acceptance and efficiency corrections as described in Section 5.4, and Δy and Δp_T are

the two bin widths in consideration. When the Z -boson yield is divided into centrality bins, N_{MB} is multiplied by the corresponding fraction of the MB cross section included in the bin.

Figure 7.1 shows the centrality dependence of the Z -boson production in Pb+Pb collisions. The $dN_{\text{Pb+Pb}}^Z/dy$ yields per MB event are divided by the nuclear overlap function T_{AA} , which is obtained from the Glauber model as discussed in Section 4.3. This quantity is proportional to the number of elementary nucleon-nucleon collisions $N_{\text{coll}} = T_{AA} \cdot \sigma_{NN}^{\text{in}}$, where σ_{NN}^{in} is the inelastic nucleon-nucleon cross section. The T_{AA} uncertainties are included in the systematic uncertainties depicted as boxes around the data in Fig. 7.1. The event centrality is translated to the average number of participants, N_{part} , as shown in Table 4.1, using the same Glauber model.

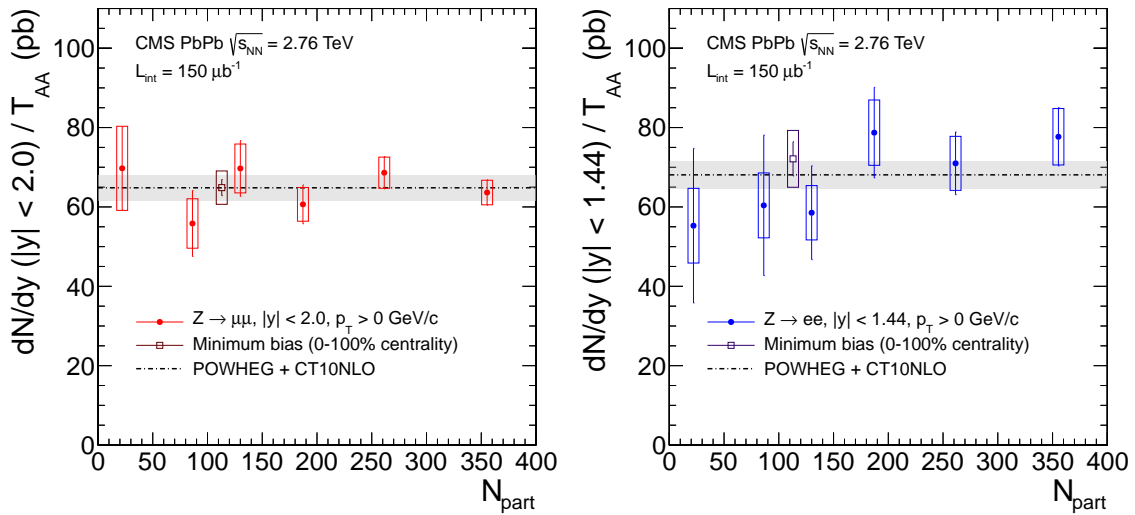


Figure 7.1: Event centrality dependence of the $Z \rightarrow \mu^+\mu^-$ (left) and $Z \rightarrow e^+e^-$ (right) yields per MB event in Pb+Pb collisions, divided by the expected average nuclear overlap function, T_{AA} , which is directly comparable to the $p + p \rightarrow Z \rightarrow l^+l^-$ cross section predicted by the POWHEG generator displayed as a black dashed line assuming no nuclear effects. On the horizontal axis, event centrality is depicted as the average number of participant nucleons, N_{part} (see Table 4.1). Vertical lines (boxes) correspond to statistical (systematic) uncertainties. The theoretical uncertainty of 5% assumed for the POWHEG reference curve is shown by the grey band.

No strong centrality dependence is observed for the yield $(dN_{\text{Pb+Pb}}^Z/dy) \cdot (1/T_{AA})$. The centrality-integrated value is displayed as an open maroon (purple) square for the dimuon (dielectron) channel in Fig. 7.1. For comparison, the dashed line on the plots shows the cross section of the $p + p \rightarrow Z \rightarrow l^+l^-$ process provided by the POWHEG generator interfaced with the PYTHIA 6.424 parton-shower generator.

Higher-order corrections to the cross sections predicted by POWHEG + PYTHIA amount to 3% [83]. Typical NNLO calculations also have a 3% uncertainty in the proton PDFs and are found to agree with 7 and 8 TeV $p + p$ data, as reported in Refs. [7, 9]. Therefore, the POWHEG reference has a typical uncertainty of 5%, as indicated by the grey band. The Z -boson yields in Pb+Pb collisions have been compared with various theoretical predictions, including PDFs that incorporate nuclear effects. The calculated yields are found to be consistent with the results. However, since the nuclear modification is expected to be small, on the order of 3%, compared to the statistical uncertainties, it is not possible to discriminate nuclear effects from the available data.

For the p_T and y dependence of the Z -boson yields, the data are integrated over centrality. Therefore the POWHEG reference is multiplied by the MB $T_{AA} = 5.67 \pm 0.32 \text{ mb}^{-1}$ provided by the Glauber model described in Section 4.3. By construction, this MB T_{AA} is equal to $A^2/\sigma_{\text{Pb+Pb}}^{\text{in}}$, where $A = 208$ is the Pb atomic number and $\sigma_{\text{Pb+Pb}}^{\text{in}} = 7.65 \pm 0.42 \text{ b}$ is the total Pb+Pb inelastic cross section computed from the same Glauber model.

The distribution $d^2N_{\text{Pb+Pb}}^Z/dydp_T$ as a function of the dilepton p_T and the invariant yield as a function of rapidity, $dN_{\text{Pb+Pb}}^Z/dy$ are compared with POWHEG and shown in Fig. 7.2. The y dependence is compared to theoretical predictions which do not incorporate nuclear PDF modifications to the unbound proton PDF (yellow band) and those that do (green band) employing the nuclear PDF EPS09 which includes shadowing and antishadowing, as discussed in Section 2.6.2. No strong deviations from this absolutely-normalised reference are observed. Therefore, we deduce that Z -boson production scales with the number of binary nucleon-nucleon collisions and that nuclear effects such as isospin or shadowing are small compared to the experimental uncertainties.

7.2 Z-Boson Production Cross Section in $p + p$ Collisions

The differential $p + p \rightarrow Z \rightarrow \mu^+\mu^-$ and $p + p \rightarrow Z \rightarrow e^+e^-$ cross sections as a function of p_T and y of the Z -boson candidates selected in the mass range between 60–120 GeV/ c^2 mass and within $|y| < 2.0$ (1.44) in the dimuon (dielectron) channel are obtained from the $p + p$ data at $\sqrt{s} = 2.76 \text{ TeV}$. These distributions are shown in Fig. 7.3. In $p + p$ collisions, the cross section is calculated by dividing the corrected yields by the calibrated integrated luminosity. The differential

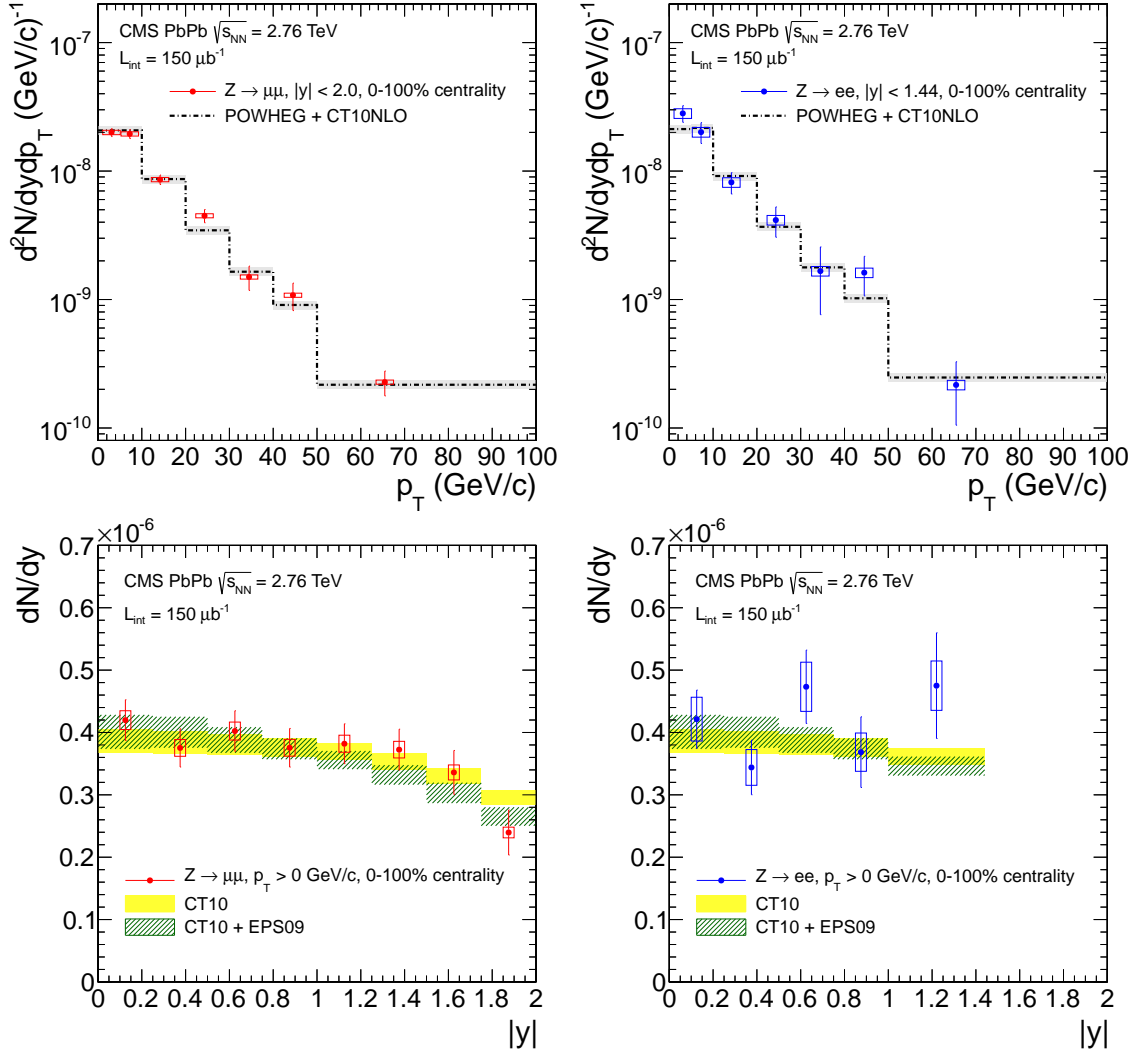


Figure 7.2: The measured Z -boson yields per MB event in Pb+Pb collisions as a function of the Z -boson p_T (top) and y (bottom) for the dimuon (left) and the dielectron (right) decay channels. The yields are compared with $p+p \rightarrow Z \rightarrow l^+l^-$ POWHEG predictions scaled by the MB T_{AA} . The results vs. y are compared to predictions with (green band) and without (yellow band) nuclear modification effects. Vertical lines (boxes) correspond to statistical (systematic) uncertainties. The theoretical uncertainty of 5% assumed for the POWHEG reference curve together with the uncertainty of 6.2% due to the T_{AA} scaling, is shown by the grey band.

cross sections agree with the POWHEG predictions.

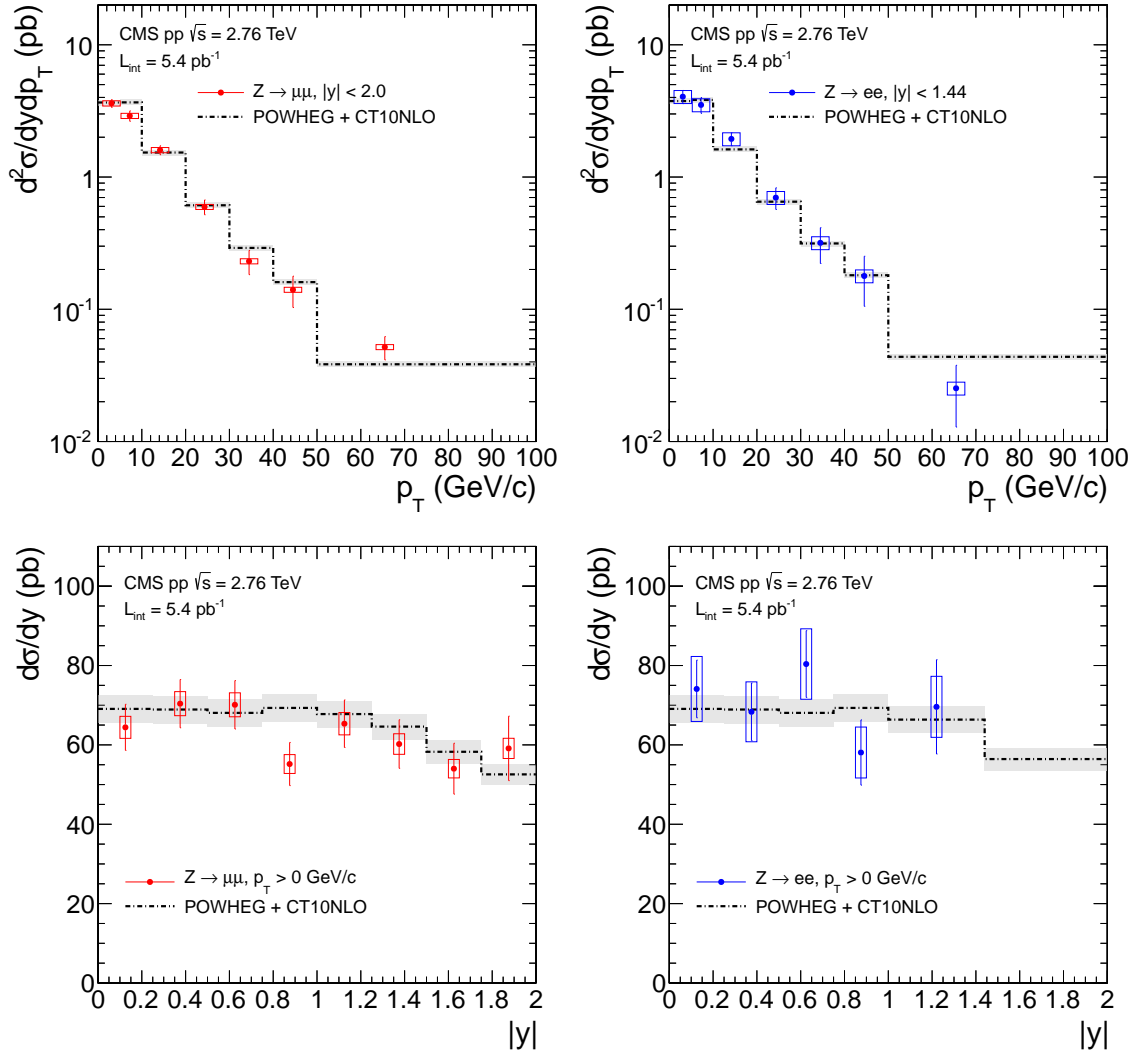


Figure 7.3: The measured Z -boson production cross section in $p + p$ collisions as a function of the Z -boson p_T (top) and y (bottom) for the dimuon (left) and the dielectron (right) decay channels. Results are compared with $p + p \rightarrow Z \rightarrow l^+l^-$ POWHEG predictions. Vertical lines (boxes) correspond to statistical (systematic) uncertainties. The theoretical uncertainty of 5% assumed for the POWHEG reference curve is shown by the grey band.

7.3 Nuclear Modification Factor

Based on Pb+Pb and $p + p$ data at the same centre-of-mass energy, we compute the nuclear modification factor, R_{AA} , for both the dimuon and dielectron channels as a function of the Z -boson p_T , y , and event centrality, as follows:

$$R_{AA} = \frac{N_{\text{Pb+Pb}}^Z}{N_{\text{coll}} \cdot N_{p+p}^Z} = \frac{N_{\text{Pb+Pb}}^Z}{T_{AA} \cdot \sigma_{p+p}^Z} \quad (7.2)$$

where $N_{\text{Pb+Pb}}^Z$ (N_{p+p}^Z) are the yields per MB event measured in Pb+Pb ($p + p$) collisions corrected for acceptance and efficiency, σ_{p+p}^Z refers to the differential cross sections measured from $p + p$ collisions, N_{coll} refers to the average number of nucleon-nucleon collisions for the appropriate centrality selection, and T_{AA} refers to the values of the nuclear overlap function as described in Section 4.3. The R_{AA} values as a function of rapidity, p_T and centrality are shown in Fig. 7.4 (where the points are slightly shifted along the horizontal axis for clarity: negative for muons and positive for electrons), and in Table 7.1. The R_{AA} values show no dependence and, hence, no variation in nuclear effects as a function of p_T , y , or centrality in both muon and electron channels in the kinematic range studied and within the current uncertainties.

7.4 Combination of the Results

According to lepton universality and given the large mass of the Z boson, the Z is expected to decay into the dimuon and dielectron channels with branching ratios within 1% of each other. Also, neither muons nor electrons are expected to interact strongly with the QCD color fields that may be manifest in the medium formed in Pb+Pb collisions. The two channels can therefore be checked against each other and can be used to measure the combined $Z \rightarrow l^+l^-$ yields and R_{AA} , where $Z \rightarrow l^+l^-$ refers to the Z boson decaying into either the dimuon or dielectron channel. Given the errors on the measurements, in the region of overlap between the datasets, the datasets are in agreement. The combination is then done following the Best Linear Unbiased Estimate technique (known as the B.L.U.E. method), as described in Ref. [84].

The combined yields per MB event for Pb+Pb collisions and the combined cross sections for $p+p$

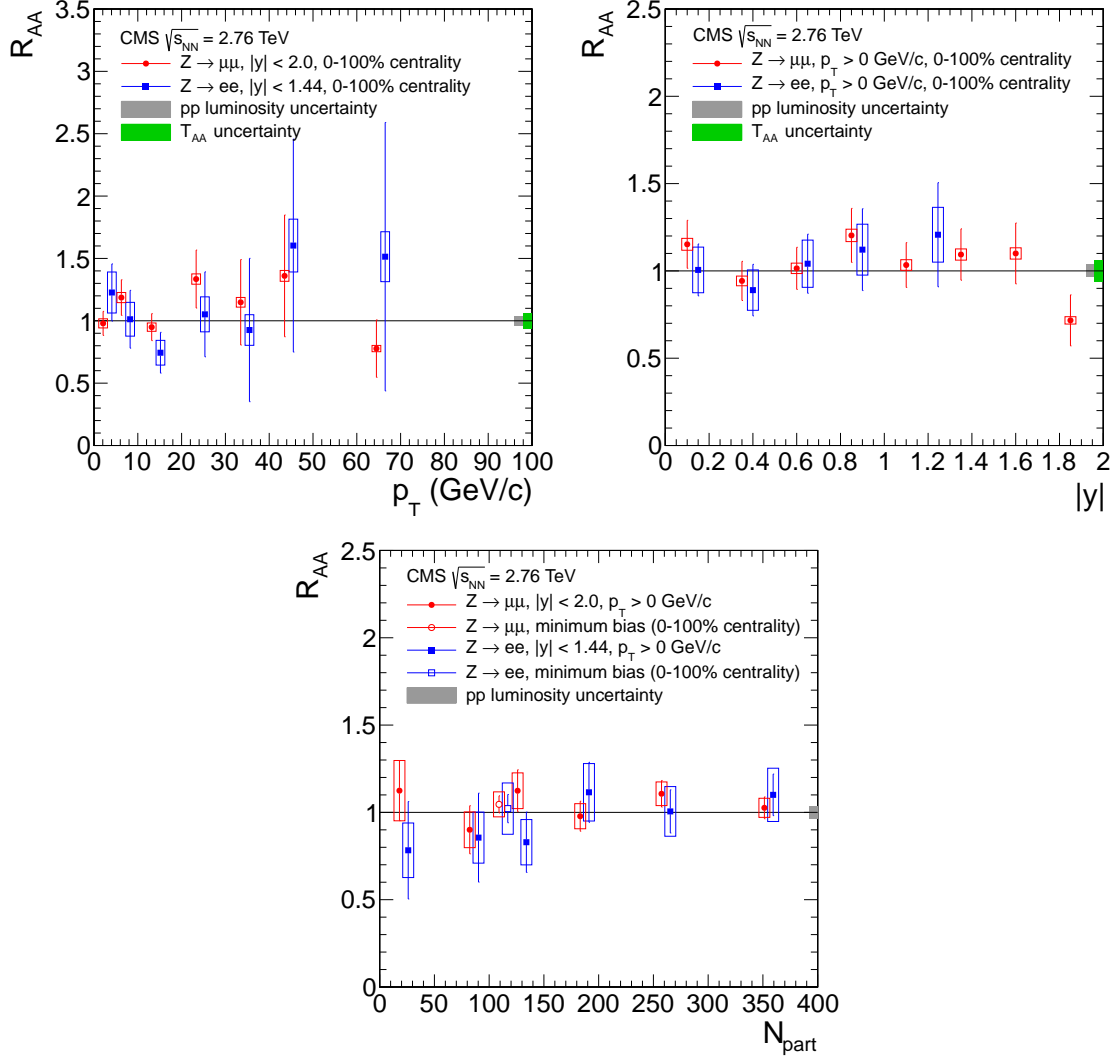


Figure 7.4: The R_{AA} distribution for the $Z \rightarrow e^+e^-$ (blue squares) and $Z \rightarrow \mu^+\mu^-$ (red circles) events as a function of the Z -boson p_T (left), y (right), and N_{part} (bottom). For N_{part} , open points at $N_{\text{part}} \sim 110$ represent the R_{AA} for MB collisions. Points are shifted along the horizontal axis for clarity. The horizontal line at $R_{AA} = 1$ is drawn as reference. Vertical lines (boxes) correspond to statistical (systematic) uncertainties. The grey bar at $R_{AA} = 1$ corresponds to the uncertainty in $p+p$ luminosity and the green bar corresponds to the uncertainty in T_{AA} .

Table 7.1: Nuclear modification factor, R_{AA} , for the $Z \rightarrow \mu^+\mu^-$, e^+e^- and l^+l^- processes as a function of y , p_T , and centrality. The first uncertainty is statistical and the second one is systematic.

| R_{AA} | | | |
|-------------------|----------------------------|--------------------------|--------------------------|
| $ y $ | $Z \rightarrow \mu^+\mu^-$ | $Z \rightarrow e^+e^-$ | $Z \rightarrow l^+l^-$ |
| [0.00, 0.25] | $1.17 \pm 0.14 \pm 0.09$ | $1.01 \pm 0.15 \pm 0.15$ | $1.13 \pm 0.11 \pm 0.09$ |
| [0.25, 0.50] | $0.96 \pm 0.11 \pm 0.07$ | $0.89 \pm 0.15 \pm 0.13$ | $0.96 \pm 0.09 \pm 0.08$ |
| [0.50, 0.75] | $1.03 \pm 0.12 \pm 0.08$ | $1.04 \pm 0.17 \pm 0.15$ | $1.04 \pm 0.10 \pm 0.09$ |
| [0.75, 1.00] | $1.22 \pm 0.16 \pm 0.10$ | $1.12 \pm 0.23 \pm 0.17$ | $1.22 \pm 0.13 \pm 0.10$ |
| [1.00, 1.25] | $1.05 \pm 0.13 \pm 0.08$ | --- | --- |
| [1.25, 1.50] | $1.11 \pm 0.15 \pm 0.09$ | --- | --- |
| [1.00, 1.44] | --- | $1.21 \pm 0.30 \pm 0.18$ | $1.14 \pm 0.10 \pm 0.09$ |
| [1.50, 1.75] | $1.12 \pm 0.18 \pm 0.09$ | --- | $1.12 \pm 0.18 \pm 0.09$ |
| [1.75, 2.00] | $0.73 \pm 0.15 \pm 0.06$ | --- | $0.73 \pm 0.15 \pm 0.06$ |
| p_T (GeV/ c) | | | |
| [0, 5] | $0.99 \pm 0.09 \pm 0.08$ | $1.23 \pm 0.23 \pm 0.19$ | $0.99 \pm 0.09 \pm 0.08$ |
| [5, 10] | $1.20 \pm 0.13 \pm 0.10$ | $1.01 \pm 0.23 \pm 0.15$ | $1.29 \pm 0.14 \pm 0.11$ |
| [10, 20] | $0.96 \pm 0.10 \pm 0.08$ | $0.74 \pm 0.16 \pm 0.11$ | $0.93 \pm 0.10 \pm 0.08$ |
| [20, 30] | $1.36 \pm 0.22 \pm 0.11$ | $1.05 \pm 0.34 \pm 0.16$ | $1.27 \pm 0.20 \pm 0.11$ |
| [30, 40] | $1.17 \pm 0.32 \pm 0.09$ | $0.93 \pm 0.57 \pm 0.14$ | $1.18 \pm 0.31 \pm 0.10$ |
| [40, 50] | $1.38 \pm 0.47 \pm 0.11$ | $1.60 \pm 0.85 \pm 0.24$ | $1.28 \pm 0.40 \pm 0.11$ |
| [50, 100] | $0.79 \pm 0.23 \pm 0.06$ | $1.51 \pm 1.08 \pm 0.23$ | $0.89 \pm 0.28 \pm 0.07$ |
| Centrality | | | |
| [0, 10]% | $1.04 \pm 0.06 \pm 0.07$ | $1.10 \pm 0.12 \pm 0.16$ | $1.10 \pm 0.06 \pm 0.07$ |
| [10, 20]% | $1.12 \pm 0.08 \pm 0.08$ | $1.01 \pm 0.12 \pm 0.15$ | $1.14 \pm 0.08 \pm 0.08$ |
| [20, 30]% | $0.99 \pm 0.09 \pm 0.08$ | $1.12 \pm 0.17 \pm 0.17$ | $1.12 \pm 0.09 \pm 0.09$ |
| [30, 40]% | $1.14 \pm 0.12 \pm 0.11$ | $0.83 \pm 0.17 \pm 0.13$ | $1.06 \pm 0.11 \pm 0.10$ |
| [40, 50]% | $0.91 \pm 0.14 \pm 0.11$ | $0.86 \pm 0.25 \pm 0.15$ | $0.94 \pm 0.14 \pm 0.11$ |
| [50, 100]% | $1.14 \pm 0.17 \pm 0.18$ | $0.78 \pm 0.28 \pm 0.16$ | $1.17 \pm 0.17 \pm 0.18$ |
| [0, 100]% | $1.06 \pm 0.05 \pm 0.08$ | $1.02 \pm 0.08 \pm 0.15$ | $1.10 \pm 0.05 \pm 0.09$ |

collisions are shown in Figs. 7.5 and 7.6, respectively. The dimuon and dielectron measurements share the kinematic region of $|y| < 1.44$. The dependence on p_T and N_{part} of the Z -boson yield and R_{AA} measurements in the combination of the two channels are therefore restricted to $|y| < 1.44$. The dependence on $|y|$ is shown with the combined measurements for $|y| < 1.44$, extended by the dimuon measurements into the range $1.5 < |y| < 2.0$.

The results as a function of p_T , y , and centrality are compared with predictions from the POWHEG generator. The measurements agree with the theoretical calculations within the combined statistical and systematic uncertainties. The current precision of the measurements cannot distinguish between the unbound proton PDF sets and the modified nuclear PDF sets.

To calculate the combined R_{AA} , the combined dilepton yields in Pb+Pb and $p + p$ data are obtained and then the R_{AA} ratio is calculated based on these values. The combined R_{AA} values are in Table 7.1 and in Fig. 7.7. The R_{AA} for the combination of the two channels shows no dependence and no variation in nuclear effects as a function of p_T , y , or centrality. This demonstrates that within uncertainties, Z -boson production is not modified in Pb+Pb collisions compared with $p + p$ collisions scaled by the number of elementary nucleon-nucleon collisions.

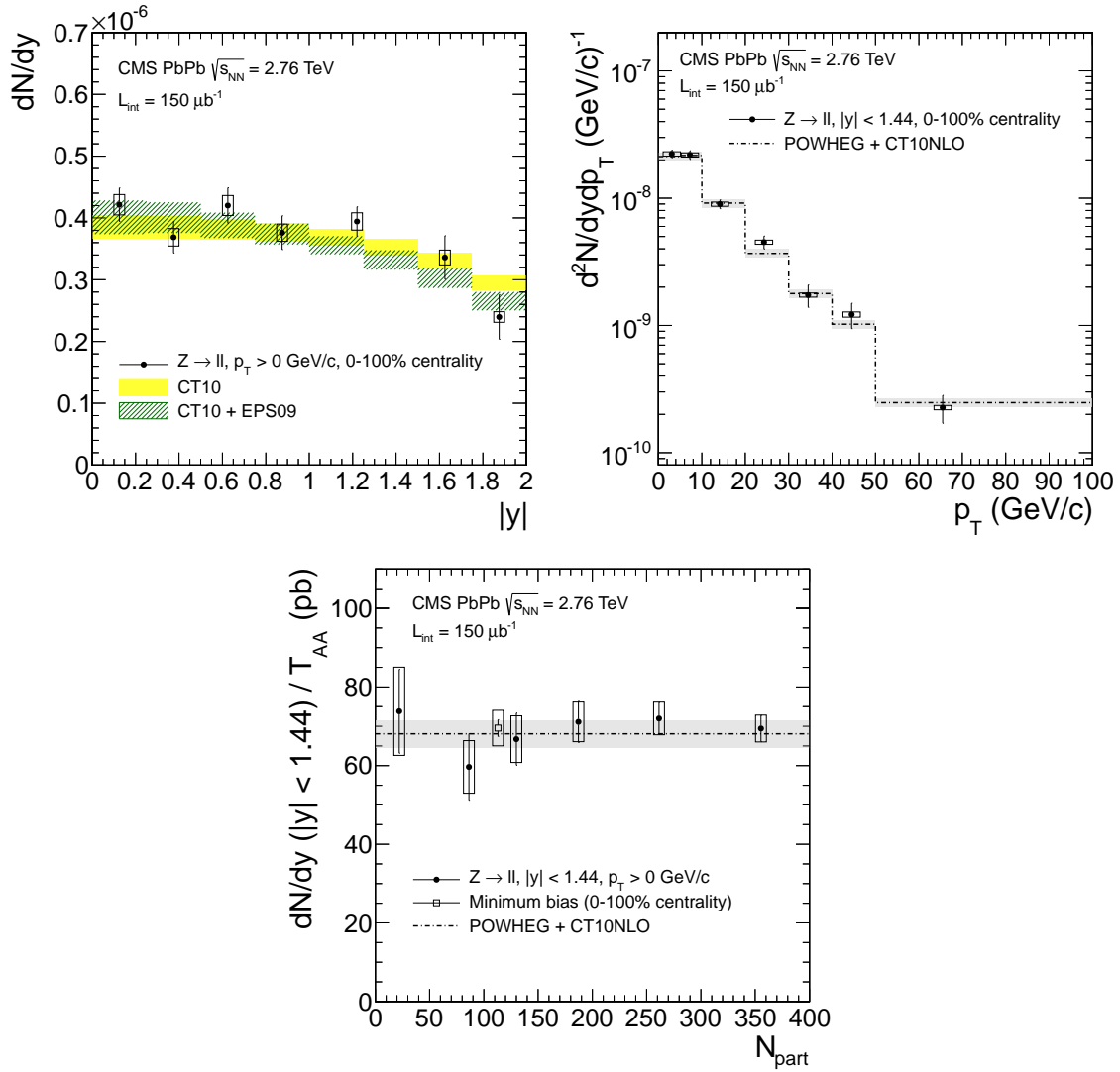


Figure 7.5: The measured $Z \rightarrow l^+l^-$ yields per MB event in Pb+Pb collisions, shown for the combined dilepton channel as a function of the Z -boson y (top left), p_T (top right), and N_{part} (bottom). For the y dependence, the measurements from dimuons and dielectrons are combined for $|y| < 1.44$, while the dimuon measurements are shown for $1.5 < |y| < 2.0$. The yields are compared with $p + p \rightarrow Z \rightarrow l^+l^-$ POWHEG predictions. The results vs. y are compared to predictions with (green band) and without (yellow band) nuclear modification effects. Vertical lines (boxes) correspond to statistical (systematic) uncertainties. The theoretical uncertainty of 5% assumed for the POWHEG reference curve is shown by the grey band.

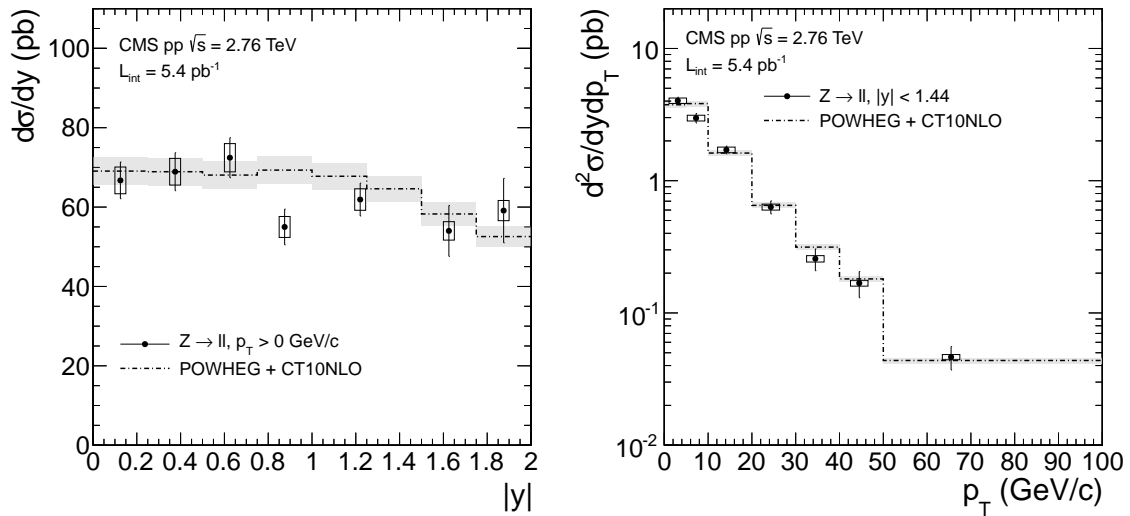


Figure 7.6: The measured $Z \rightarrow l^+l^-$ cross section in $p + p$ collisions, shown for the combined dilepton channel as a function of the Z -boson y (left) and p_T (right). For the y dependence, the measurements from dimuons and dielectrons are combined for $|y| < 1.44$, and the dimuon measurements are shown for $1.5 < |y| < 2.0$. Results are compared with $p + p \rightarrow Z \rightarrow l^+l^-$ POWHEG predictions. Vertical lines (boxes) correspond to statistical (systematic) uncertainties. The theoretical uncertainty of 5% assumed for the POWHEG reference curve is shown by the grey band.

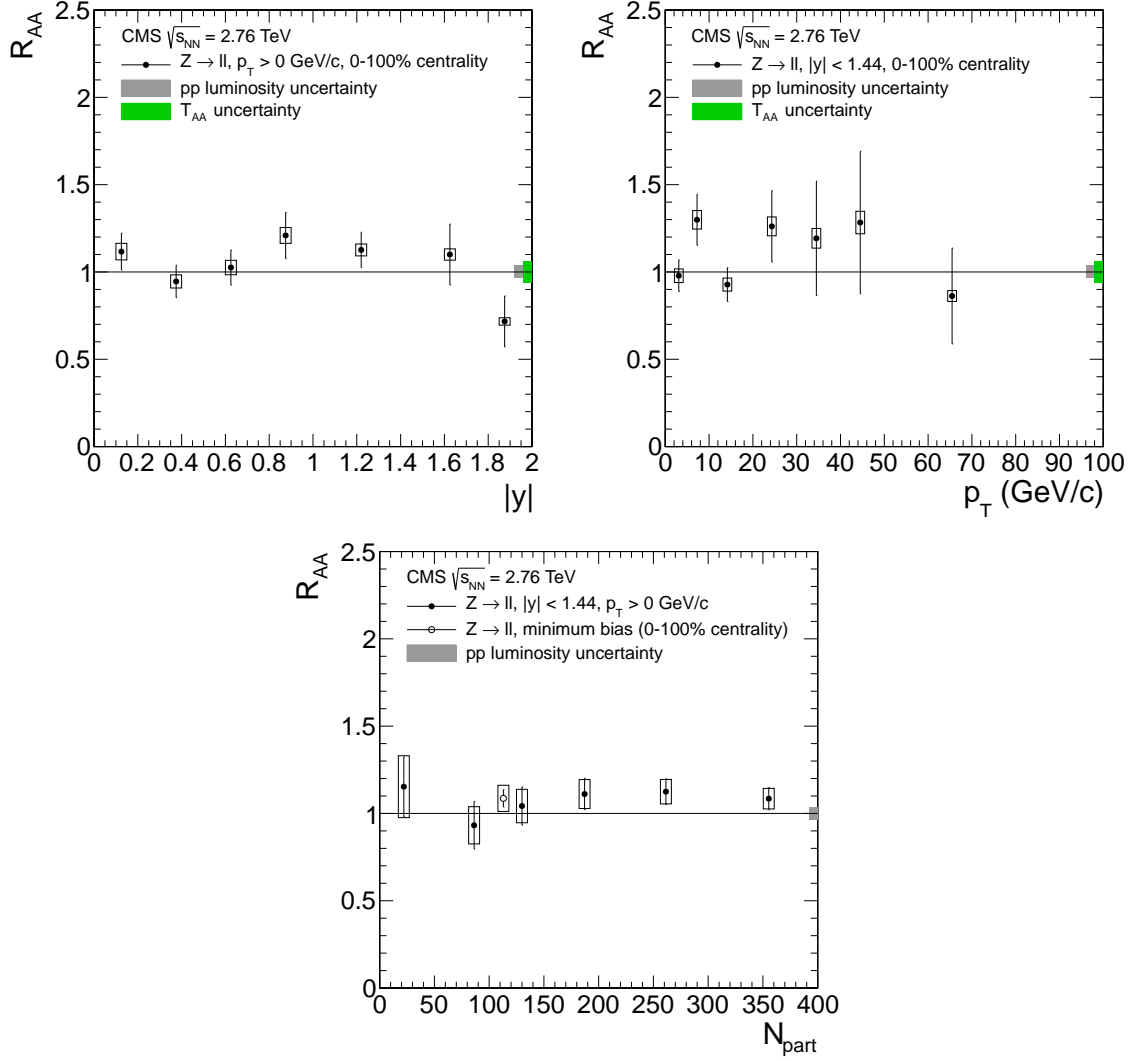


Figure 7.7: The Z -boson R_{AA} values for the combination of the dimuon and dielectron channel, as a function of y (top left), p_T (top right), and N_{part} (bottom). The horizontal line at $R_{AA} = 1$ is drawn as reference. Vertical lines (boxes) correspond to statistical (systematic) uncertainties. Grey bar at $R_{AA} = 1$ corresponds to uncertainty in $p + p$ luminosity and green bar corresponds to uncertainty of T_{AA} .

Chapter 8

Conclusion

The yield of Z bosons in Pb+Pb collisions at $\sqrt{s_{NN}} = 2.76$ TeV has been measured as a function of p_T , y , or centrality, in both the dimuon and dielectron channels with an integrated luminosity of approximately $150 \mu\text{b}^{-1}$. Within uncertainties, no centrality dependence is observed once the yields are normalized by the number of binary nucleon-nucleon collisions. Also, given the experimental uncertainties, which begin on the order of 10%, the measurement as a function of p_T , y , and centrality cannot distinguish between theoretical predictions for Z boson yields which do and do not incorporate nuclear PDF modifications to the unbound proton PDF (such as the EPS09 nuclear PDF), since these two scenarios differ by less than those uncertainties.

The $Z \rightarrow \mu^+\mu^-$ and $Z \rightarrow e^+e^-$ cross sections have also been measured in $p+p$ collisions at the same energy with an integrated luminosity of 5.4 pb^{-1} . The Z -boson production cross sections in $p+p$ vs. p_T and y also agree with theoretical proton-proton cross sections.

Using the Pb+Pb and $p+p$ data, the nuclear modification factor, R_{AA} , has been calculated. The centrality-integrated R_{AA} is found to be 1.06 ± 0.05 (stat.) ± 0.08 (syst.) in the dimuon channel and 1.02 ± 0.08 (stat.) ± 0.15 (syst.) in the dielectron channel. The two channels are also combined in their shared kinematic range of $|y| < 1.44$, resulting in a centrality-integrated R_{AA} measurement of 1.10 ± 0.05 (stat.) ± 0.09 (syst.) for Z -boson production decaying to either two electrons or two muons. The uncertainties are larger in this combined channel than the dimuon channel due to the loss of a significant portion of Z bosons decaying to dimuons outside of the

limited y region.

The R_{AA} measurements show no significant nuclear modification as a function of p_T , y , or centrality in both the dimuon and dielectron channels in the entire kinematic range studied.

The results found are consistent with the expectation that Z -boson production in Pb+Pb collisions is unmodified by the hot-nuclear-matter effects expected from the formation of the QGP. The statistical and systematic uncertainties of the measurement are larger than the expected size of the cold nuclear matter effects, and therefore no further conclusion regarding the magnitude of such effects can be made. These results demonstrate that the Z boson can serve as an *in situ* control for processes expected to be heavily modified in the QGP, as well as eventually being a powerful tool in measuring the properties of the cold nuclear matter effects present in heavy-ion collisions.

Appendix A

Mass and p_T resolution distributions

A.1 Mass Resolution Plots - Pb+Pb

The plots of the dimuon mass are shown in Figure A.1 for dimuons in Pb+Pb, and Figure A.2 for dielectrons in Pb+Pb.

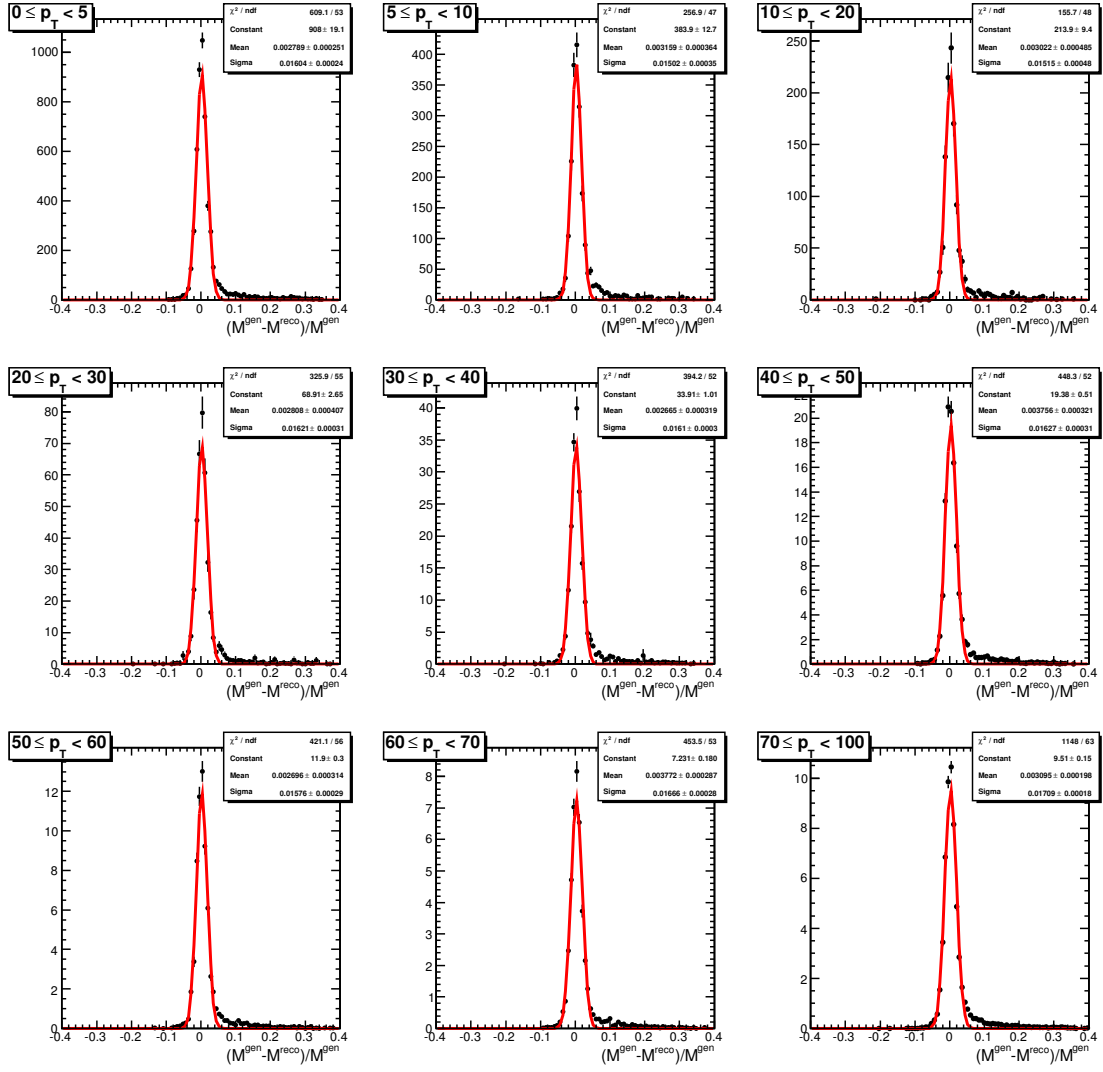


Figure A.1: The mass resolution distributions for dimuons fitted with a gaussian function in bins of p_T for Pb+Pb.

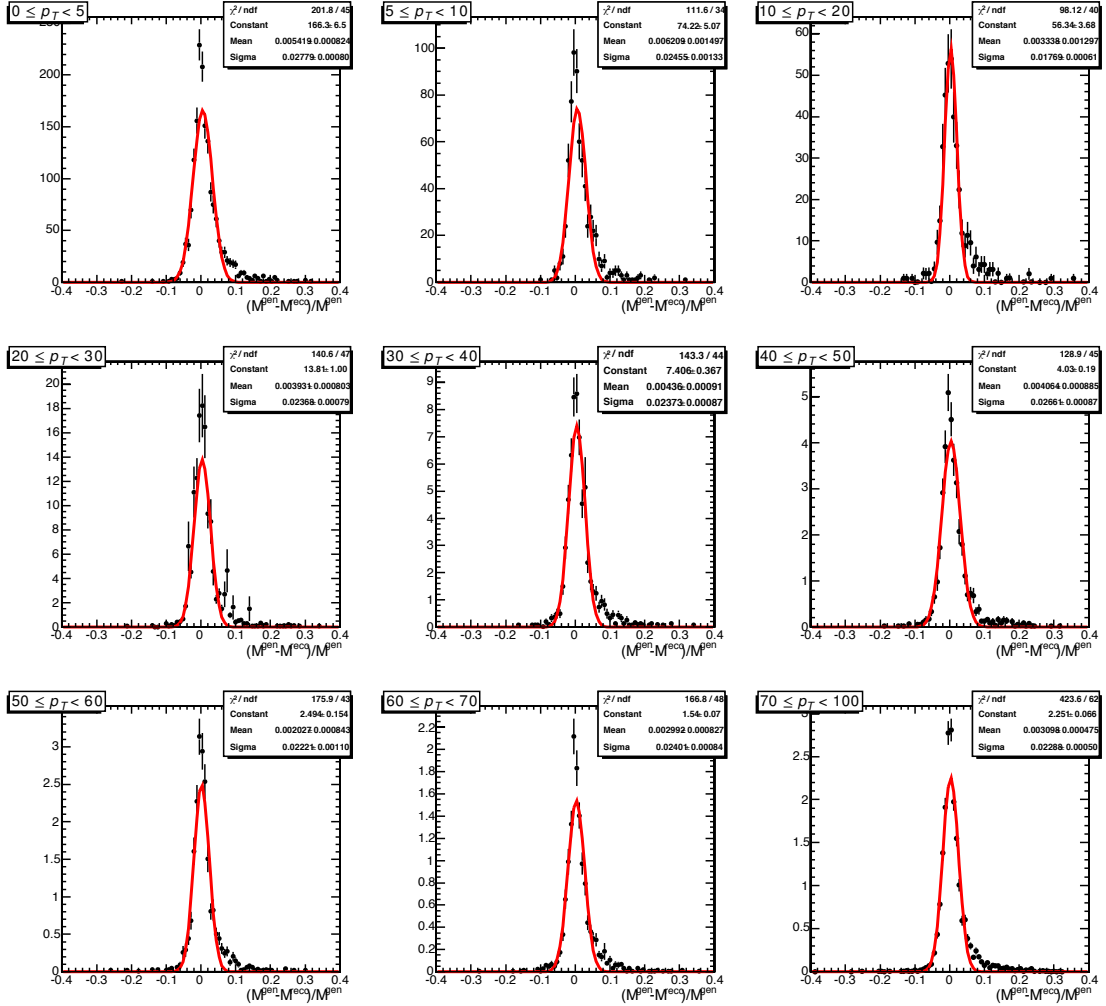


Figure A.2: The mass resolution distributions for dielectrons fitted with a gaussian function in bins of p_T for Pb+Pb.

A.2 Mass Resolution Plots - $p + p$

The plots of the dimuon mass are shown in Figure A.3 for dimuons in $p + p$, and Figure A.4 for dielectrons in $p + p$.

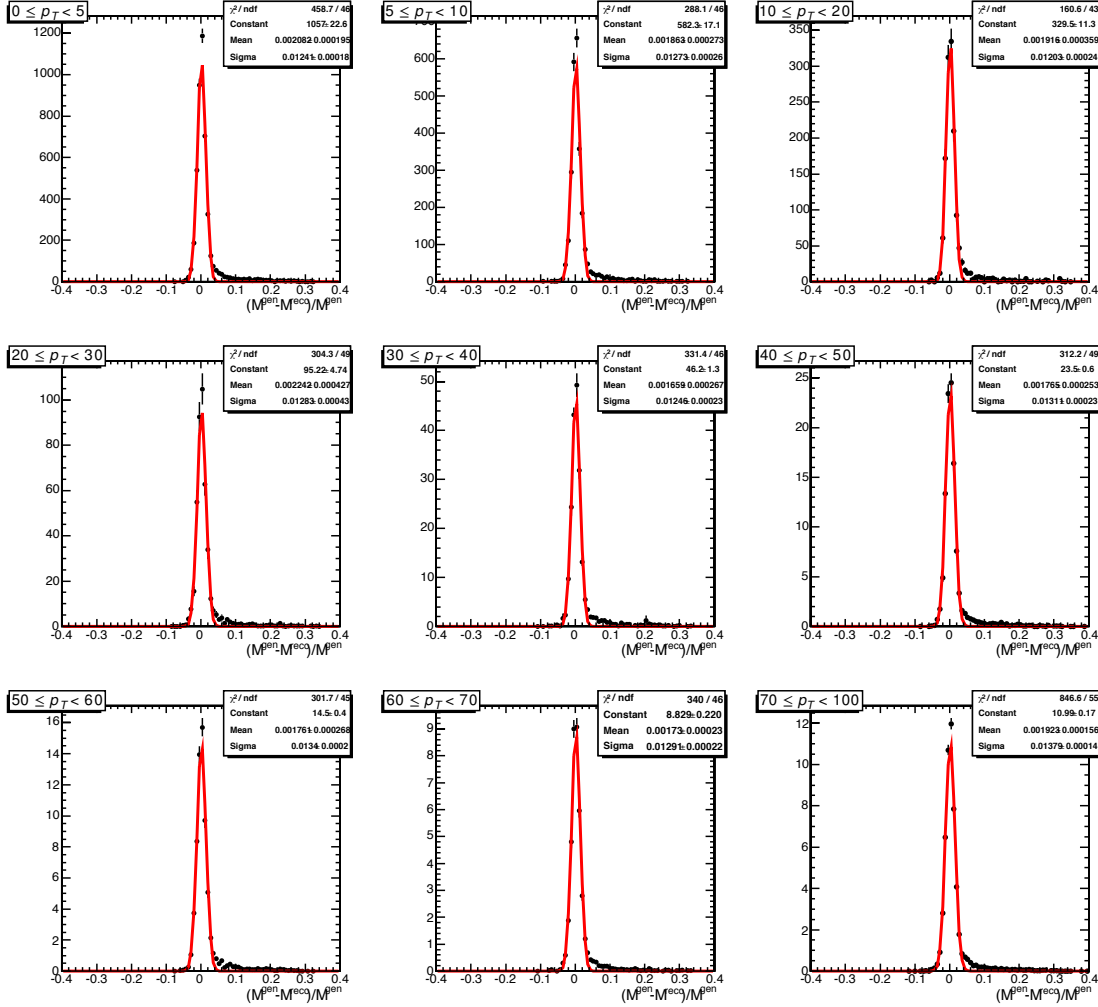


Figure A.3: The mass resolution distributions for dimuons fitted with a gaussian function in bins of p_T for $p + p$.

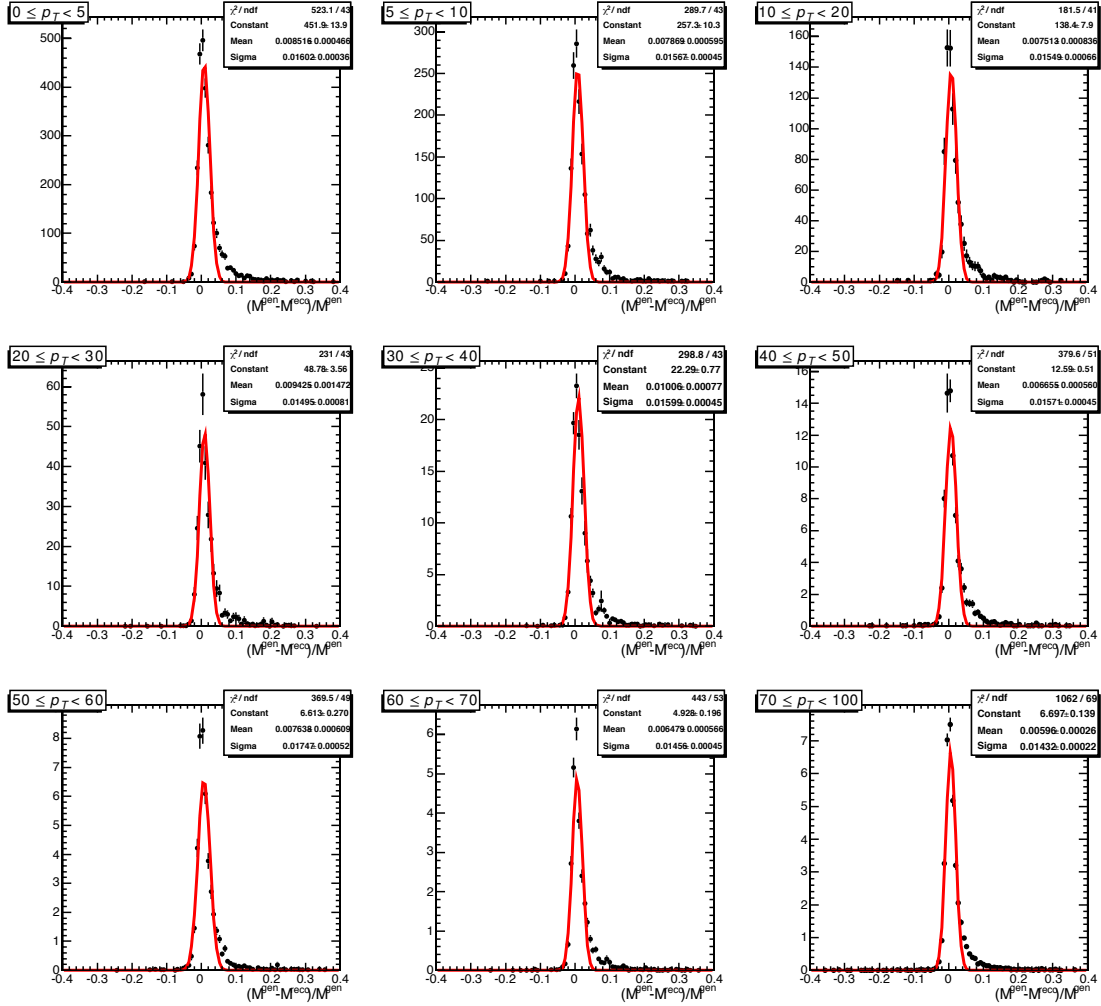


Figure A.4: The mass resolution distributions for dielectrons fitted with a gaussian function in bins of p_T for $p + p$.

A.3 Transverse Momentum Resolution Plots - Pb+Pb

The plots of the dimuon p_T are shown in Figure A.5 for dimuons in Pb+Pb, and Figure A.6 for dielectrons in Pb+Pb.

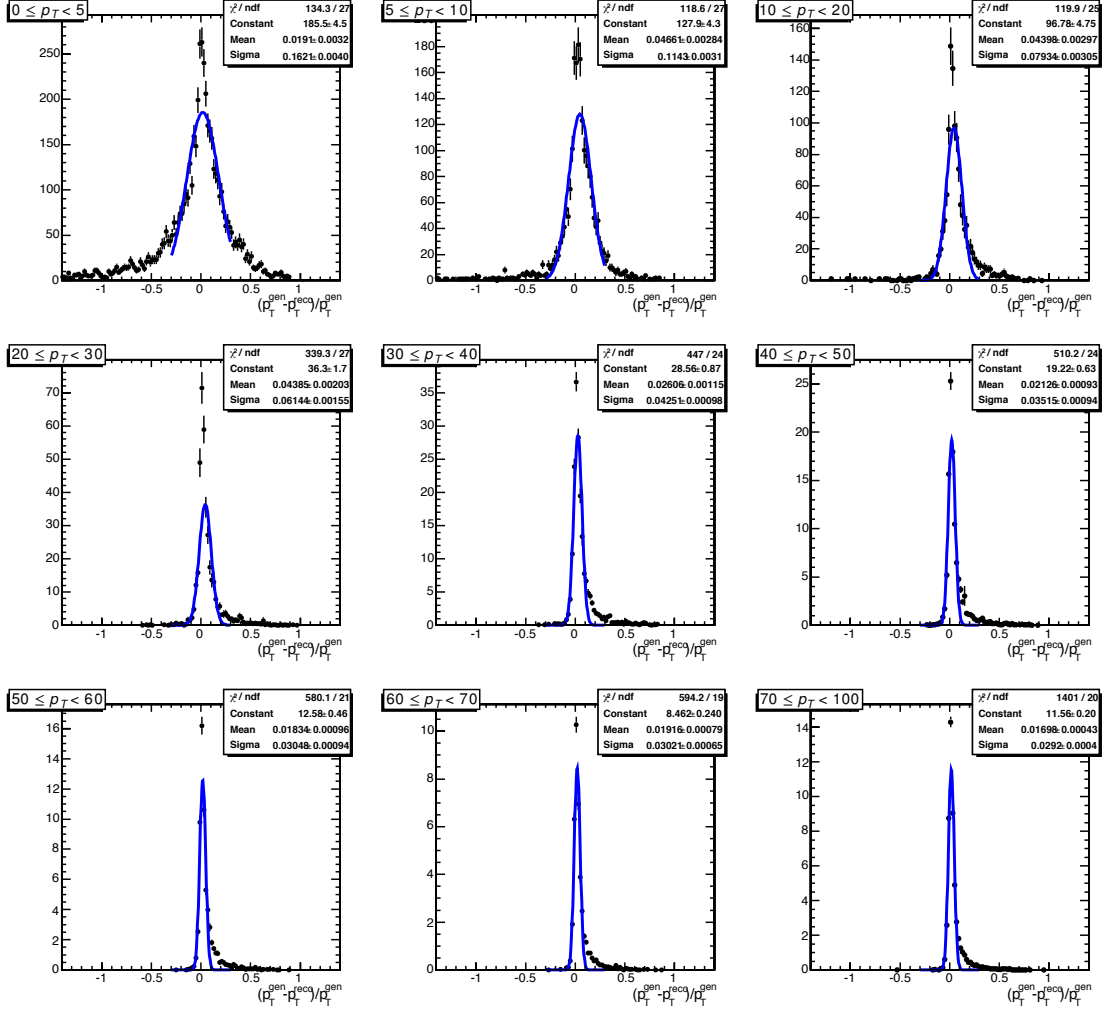


Figure A.5: The p_T resolution distributions for dimuons fitted with a gaussian function in bins of p_T for Pb+Pb.

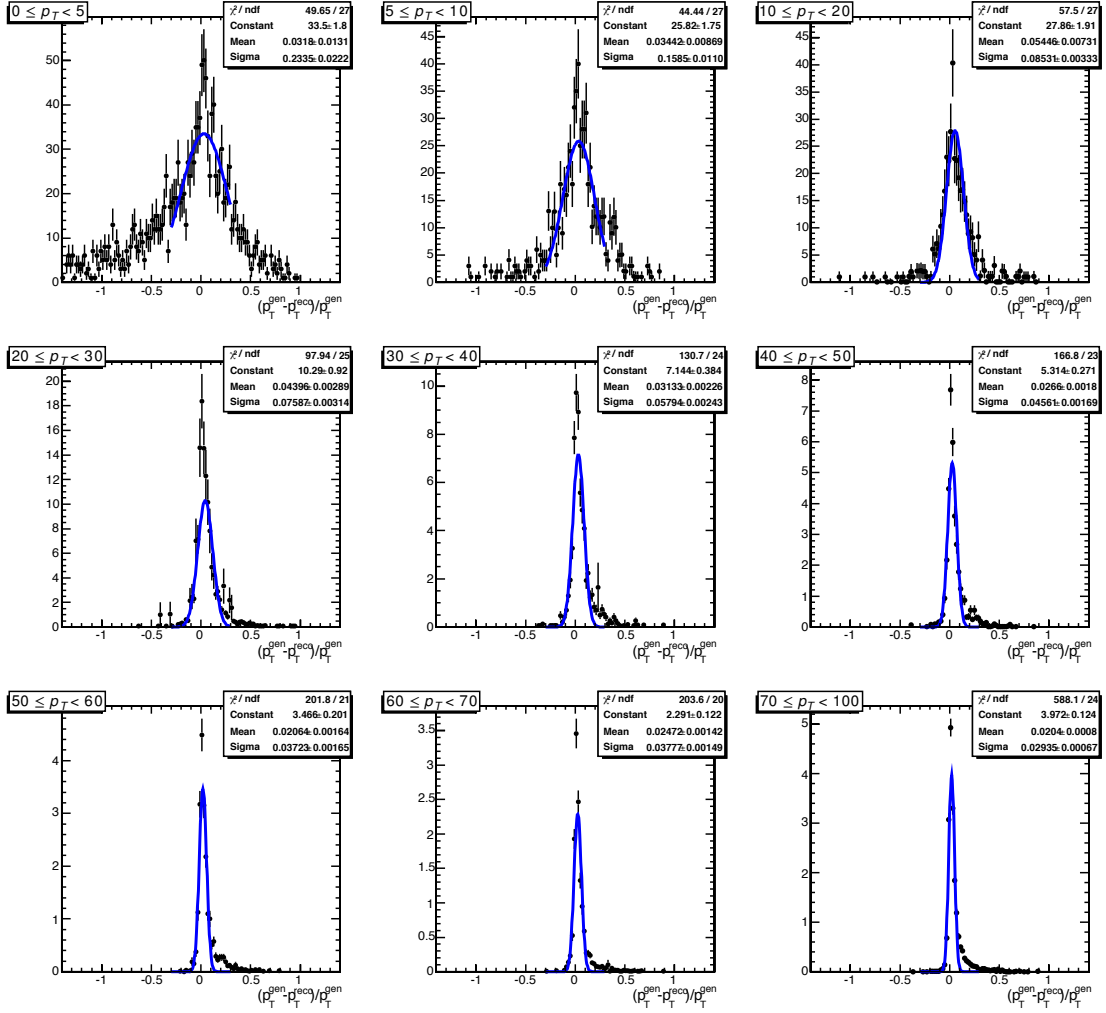


Figure A.6: The p_T resolution distributions for dielectrons fitted with a gaussian function in bins of p_T for Pb+Pb.

A.4 Transverse Momentum Resolution Plots - $p + p$

The plots of the dimuon p_T are shown in Figure A.7 for dimuons in $p + p$, and Figure A.8 for dielectrons in $p + p$.

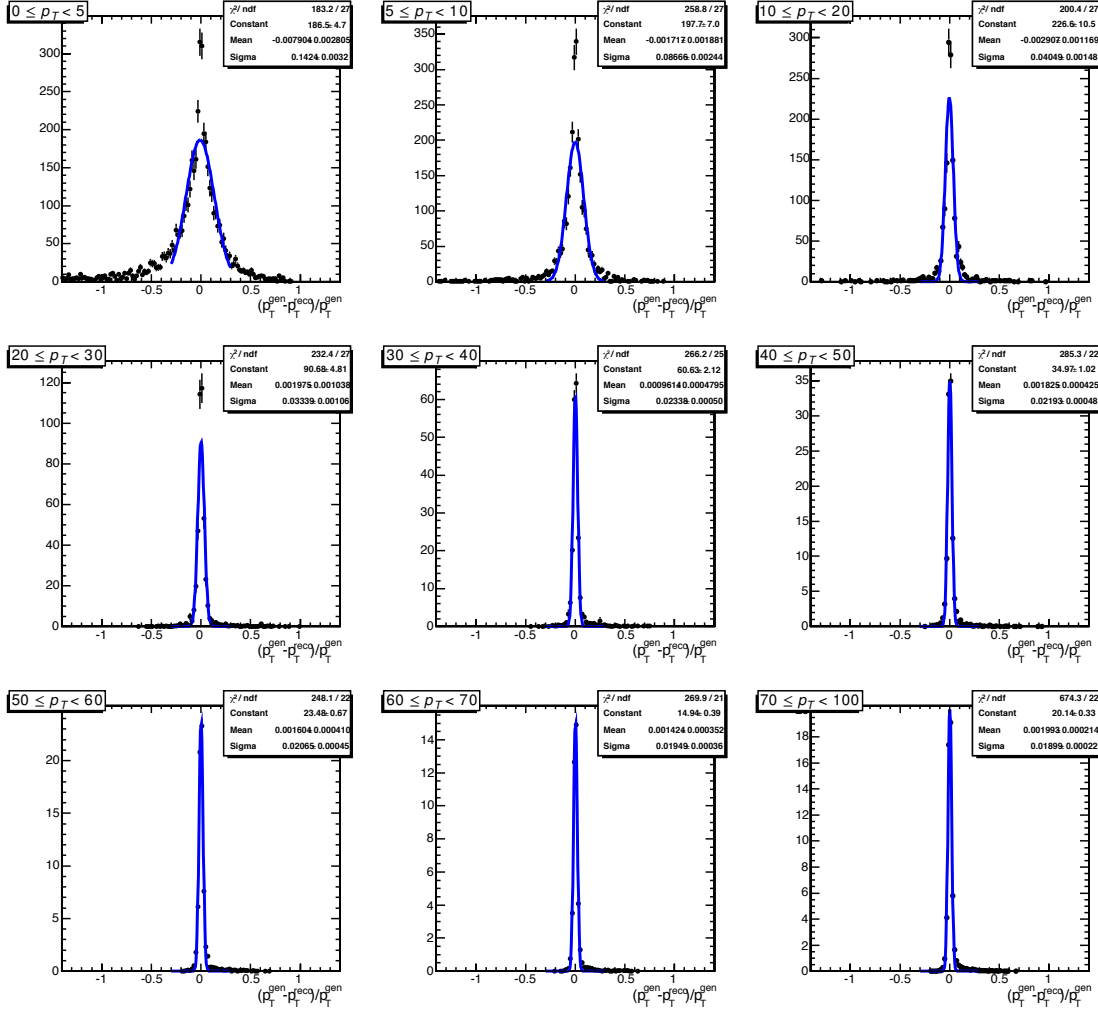


Figure A.7: The p_T resolution distributions for dimuons fitted with a gaussian function in bins of p_T for $p + p$.

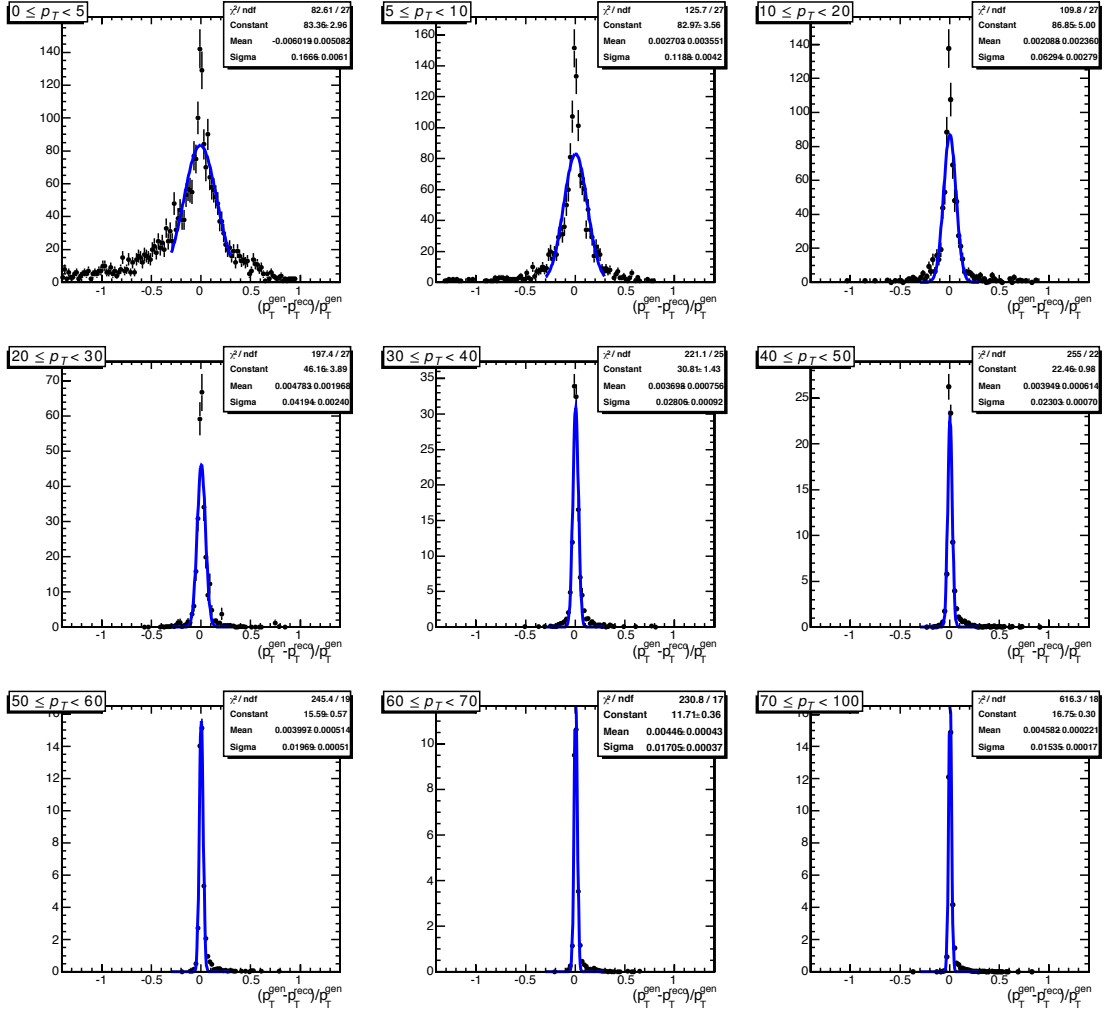


Figure A.8: The p_T resolution distributions for dielectrons fitted with a gaussian function in bins of p_T for $p + p$.

Appendix B

Tag and Probe

The purpose of this appendix is to compile a representation of the fits used for the Tag and Probe method. For the plots that are shown, the top left plot shows the “Passing Probes”, the top right plot shows the “Failing Probes”, the bottom left plot shows “All Probes”, and the bottom right portion of the plot shows the details of the fit. For the plots included in this appendix, the kinematic ranges for the tag and probe muons are as follows:

The kinematic range for the muons is $p_T > 20 \text{ GeV}/c$, $|\eta| < 2.4$.

- For single muons:

- Trigger Efficiency: $p_T > 20 \text{ GeV}/c$, $|\eta| < 2.4$.
- Muon ID Efficiency: $p_T > 20 \text{ GeV}/c$, $|\eta| < 2.4$.
- Track Reconstruction Efficiency: $p_T > 20 \text{ GeV}/c$, $|\eta| < 2.4$.

- For single electrons:

- Trigger Efficiency: $p_T > 20 \text{ GeV}/c$, $|\eta| < 1.44$.
- Muon ID Efficiency: $p_T > 20 \text{ GeV}/c$, $|\eta| < 1.44$.
- Track Reconstruction Efficiency: $p_T > 20 \text{ GeV}/c$, $|\eta| < 1.44$.

- In Pb+Pb:

- The plots shown in Pb+Pb are centrality integrated.

B.1 Tag and Probe Mass Plots - Muons in Pb+Pb

In the dimuon channel in Pb+Pb, there is a measurement of the trigger efficiency, muon ID efficiency, and reconstruction efficiency.

Trigger Efficiency - dimuons

The mass range used in the fit is $M \in [60, 120]$ GeV/c^2 and the mass peak is fitted with a Voigtian function for the passing and failing signal. The passing and failing background is fit to an exponential. The efficiency of the trigger in data is estimated to be $97.4 \pm 0.4\%$ (stat) from the fit using the Z boson as seen in Figure B.1. For MC, the efficiency of the trigger is measured to be 98.1%, as seen in Figure B.2. The functions for fitting MC and data are the same.

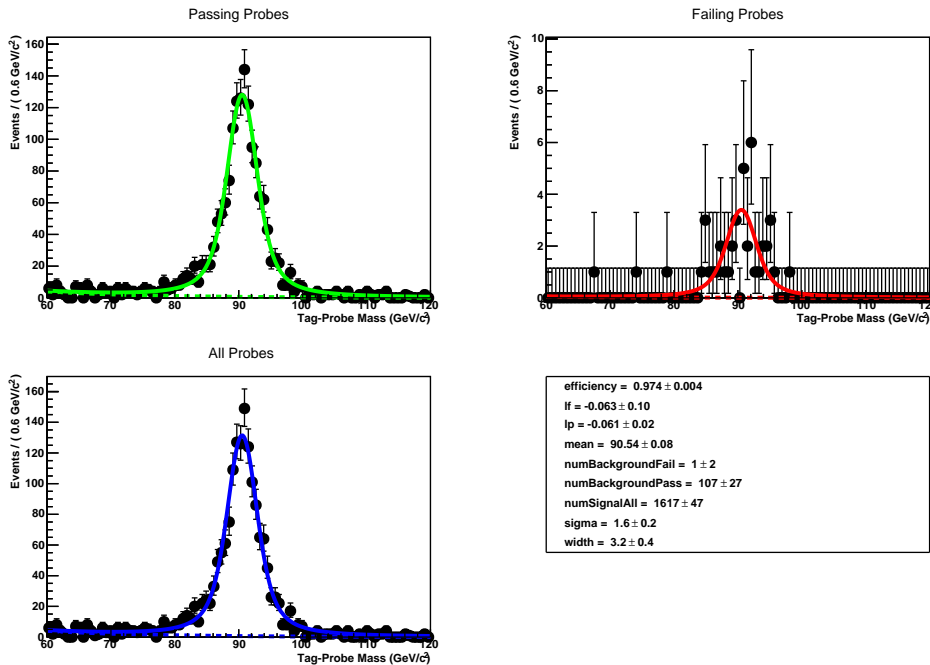


Figure B.1: DiMuon: A plot of the overall trigger efficiency as measured by tag and probe in Pb+Pb data. (top left) “Passing Probes”, (top right) “Failing Probes”, (bottom left) “All Probes”, (bottom right) details of the fit. The kinematic range for the muons is $p_T > 20 \text{ GeV}/c$, $|\eta| < 2.4$.

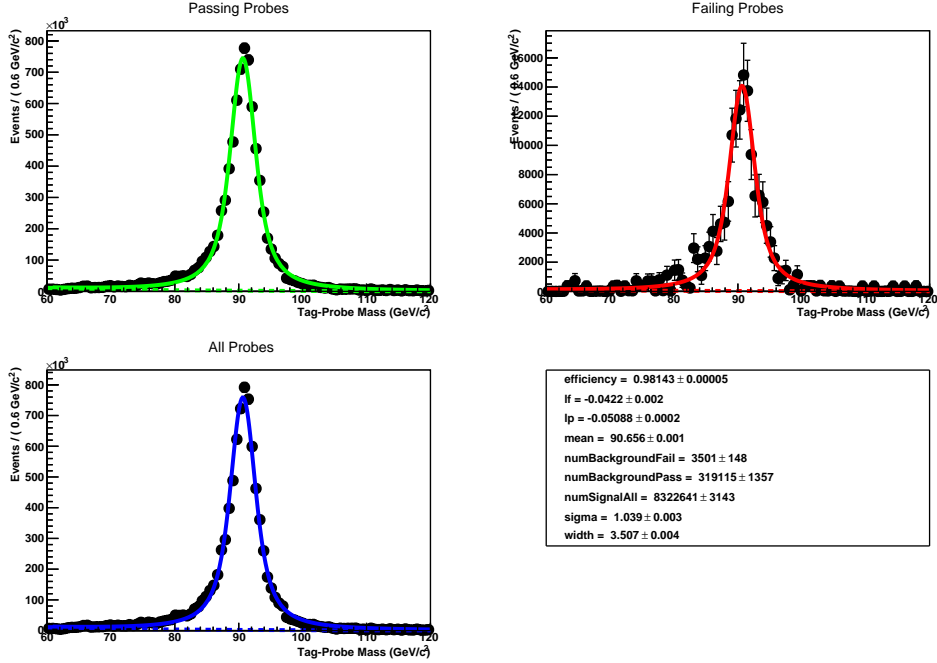


Figure B.2: DiMuon: A plot of the overall trigger efficiency as measured by tag and probe in Pb+Pb MC. (top left) “Passing Probes”, (top right) “Failing Probes”, (bottom left) “All Probes”, (bottom right) details of the fit. The kinematic range for the muons is $p_T > 20 \text{ GeV}/c$, $|\eta| < 2.4$.

Muon ID Efficiency - Muons in Pb+Pb

The mass range used in the fit is $M \in [60, 120] \text{ GeV}/c^2$ and the mass peak is fitted with a Voigtian function for the passing and failing signal. The passing and failing background is fit to an exponential. The efficiency of the muon matching and identification is estimated to be $97.8 \pm 0.5\%$ (stat) from the fit using the Z boson as seen in Figure B.3. For MC, the efficiency of the MuID is measured to be 98.3%, as seen in Figure B.4. The functions for fitting MC and data are the same.

Inner-Track Reconstruction Efficiency - Muons in Pb+Pb

Due to the poorer resolution, the mass range used in the fit is $\in [40, 140] \text{ GeV}/c^2$. The mass peak is fitted with a Voigtian at the Z peak. The passing and failing background is fit to an exponential. The efficiency of the muon inner-track reconstruction is estimated to be $97.7 \pm 0.6\%$ (stat) from the fit using the Z boson as seen in Figure B.5. For MC, the reconstruction efficiency is measured

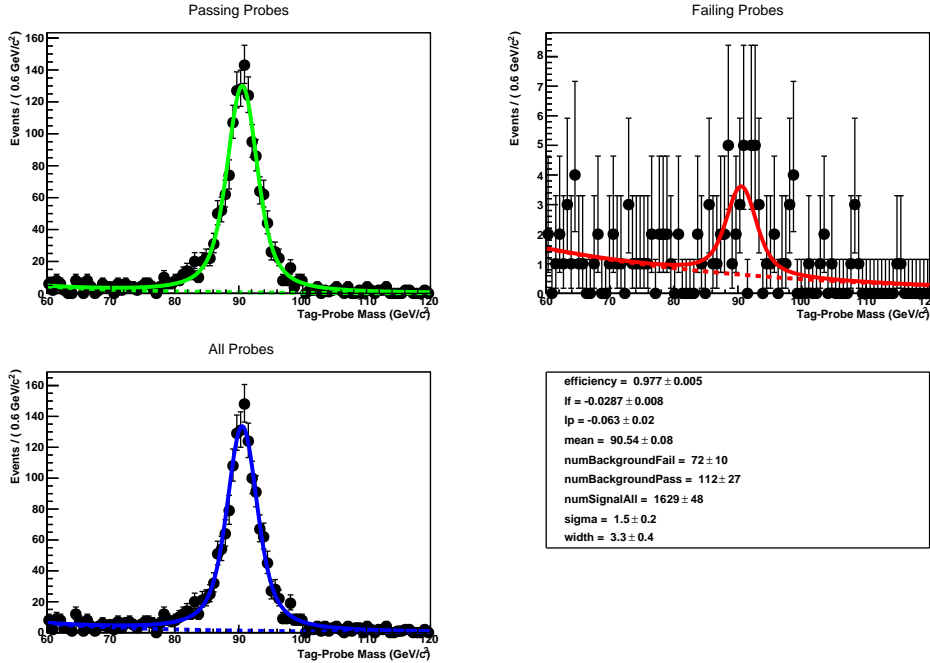


Figure B.3: DiMuon: A plot of the overall muon ID efficiency as measured by tag and probe in Pb+Pb data. (top left) “Passing Probes”, (top right) “Failing Probes”, (bottom left) “All Probes”, (bottom right) details of the fit. The kinematic range for the muons is $p_T > 20$ GeV/c, $|\eta| < 2.4$.

to be 98.7%, as seen in Figure B.2. The functions for fitting MC and data are the same.

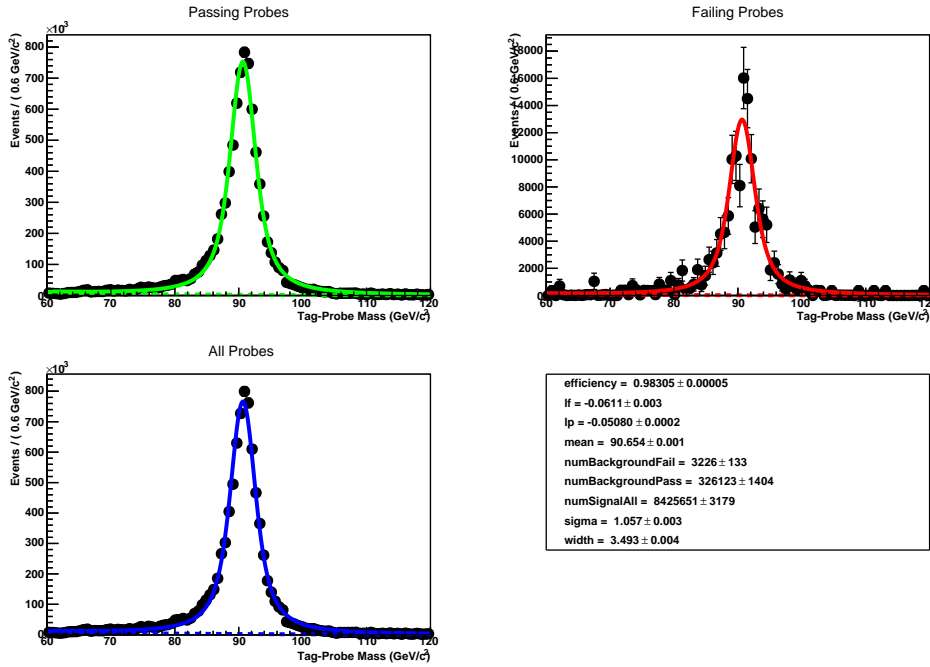


Figure B.4: DiMuon: A plot of the overall muon ID efficiency as measured by tag and probe in Pb+Pb MC. (top left) “Passing Probes”, (top right) “Failing Probes”, (bottom left) “All Probes”, (bottom right) details of the fit. The kinematic range for the muons is $p_T > 20$ GeV/ c , $|\eta| < 2.4$.

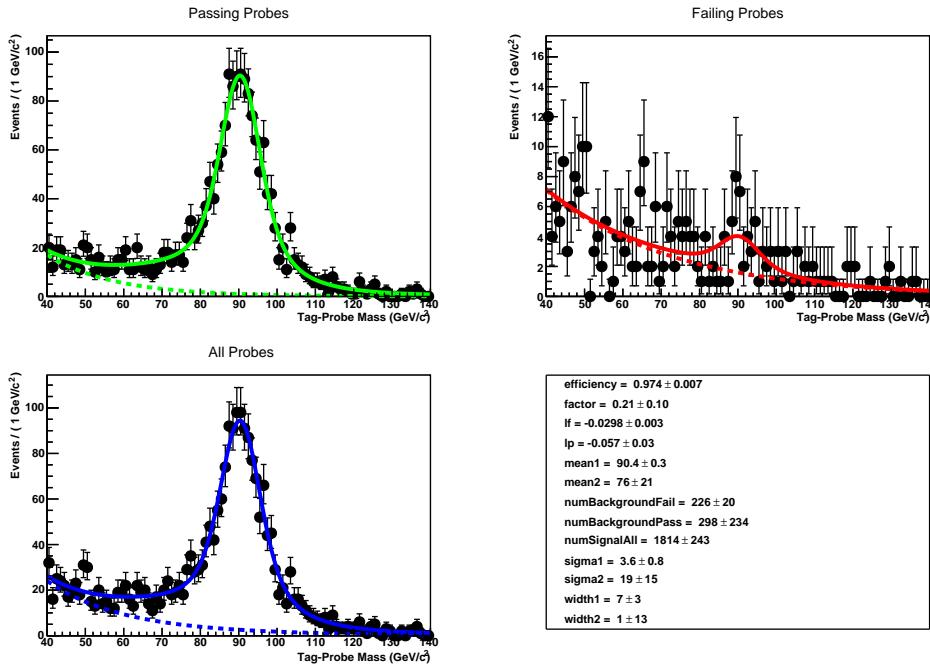


Figure B.5: DiMuon: A plot of the overall muon inner-track reconstruction efficiency as measured by tag and probe in Pb+Pb data. (top left) “Passing Probes”, (top right) “Failing Probes”, (bottom left) “All Probes”, (bottom right) details of the fit. The kinematic range for the muons is $p_T > 20$ GeV/c, $|\eta| < 2.4$.

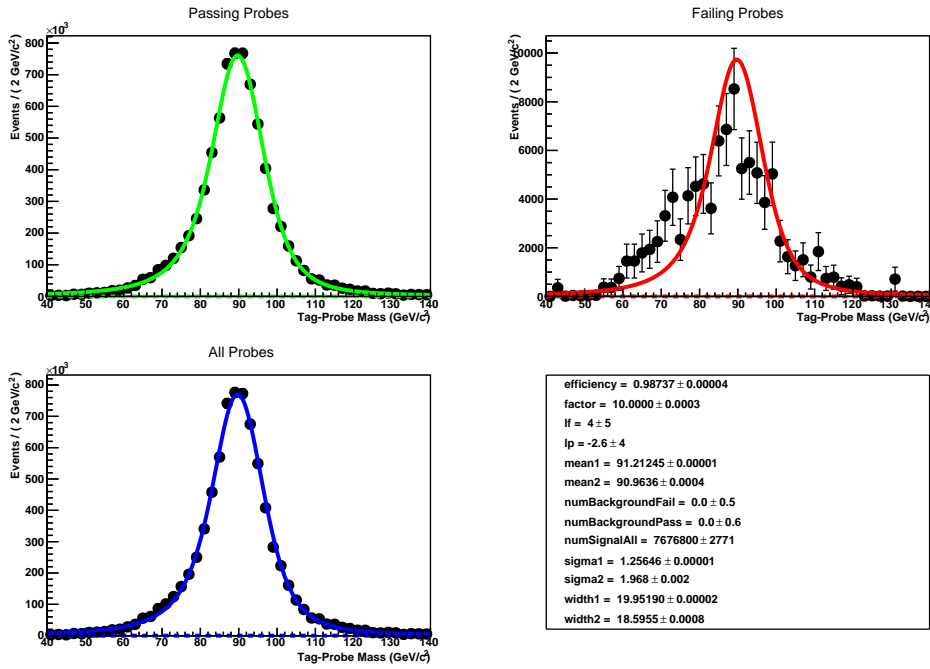


Figure B.6: DiMuon: A plot of the overall muon inner-track reconstruction efficiency as measured by tag and probe in Pb+Pb MC. (top left) “Passing Probes”, (top right) “Failing Probes”, (bottom left) “All Probes”, (bottom right) details of the fit. The kinematic range for the muons is $p_T > 20$ GeV/c, $|\eta| < 2.4$.

B.2 Tag and Probe Mass Plots - Muons in $p + p$

In the dimuon channel in $p + p$, there is a measurement of the trigger efficiency, muon ID efficiency, and reconstruction efficiency.

Trigger Efficiency - dimuons

The mass range used in the fit is $M \in [60, 120]$ GeV/c^2 and the mass peak is fitted with a Voigtian function for the passing and failing signal. The passing and failing background is fit to an exponential. The efficiency of the trigger in data is estimated to be $98.6 \pm 0.3\%$ (stat) from the fit using the Z boson as seen in Figure B.7. For MC, the efficiency of the trigger is measured to be 99.0%, as seen in Figure B.8. The functions for fitting MC and data are the same.

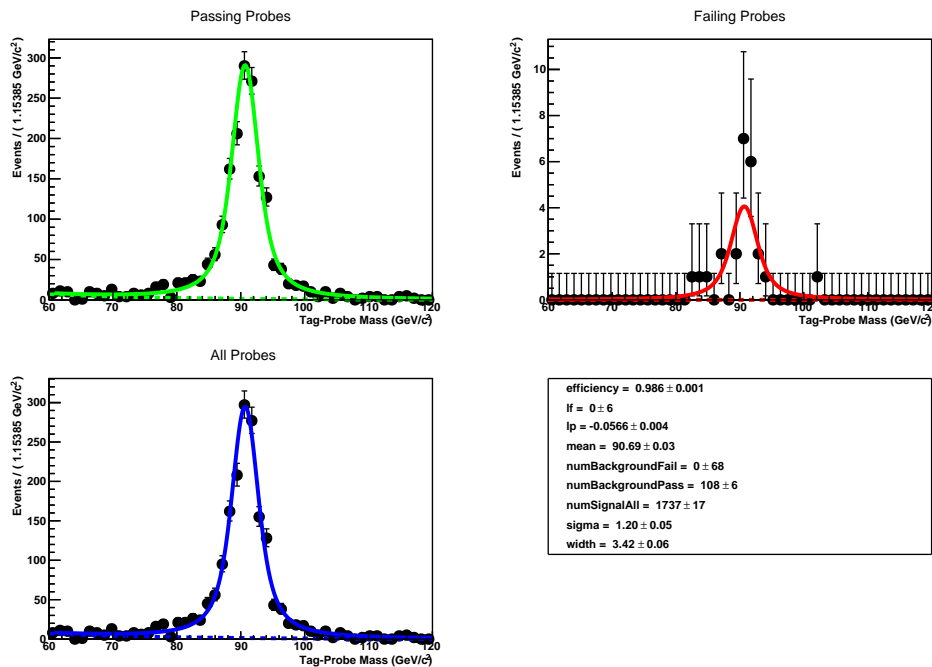


Figure B.7: DiMuon: A plot of the overall trigger efficiency as measured by tag and probe in $p + p$ data. (top left) “Passing Probes”, (top right) “Failing Probes”, (bottom left) “All Probes”, (bottom right) details of the fit. The kinematic range for the muons is $p_T > 20$ GeV/c , $|\eta| < 2.4$.

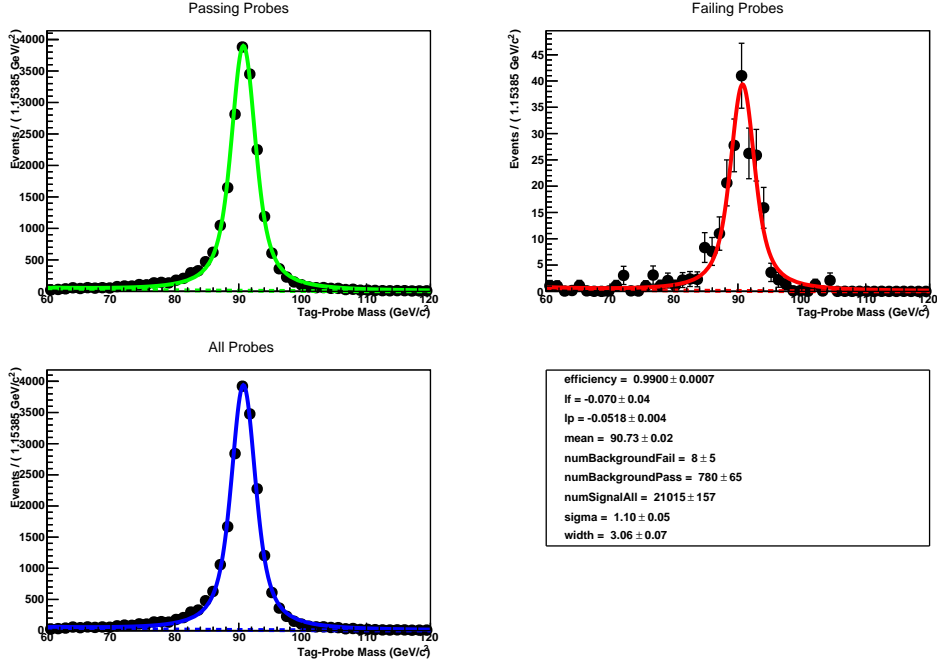


Figure B.8: DiMuon: A plot of the overall trigger efficiency as measured by tag and probe in $p + p$ MC. (top left) “Passing Probes”, (top right) “Failing Probes”, (bottom left) “All Probes”, (bottom right) details of the fit. The kinematic range for the muons is $p_T > 20$ GeV/ c , $|\eta| < 2.4$.

Muon ID Efficiency - Muons in $p + p$

The mass range used in the fit is $M \in [60, 120]$ GeV/ c^2 and the mass peak is fitted with a Voigtian function for the passing and failing signal. The passing and failing background is fit to an exponential. The efficiency of the muon matching and identification is estimated to be $98.4 \pm 0.3\%$ (stat) from the fit using the Z boson as seen in Figure B.9. For MC, the efficiency of the MuID is measured to be 98.4%, as seen in Figure B.10. The functions for fitting MC and data are the same.

Inner-Track Reconstruction Efficiency - Muons in $p + p$

Due to the poorer resolution, the mass range used in the fit is $\in [40, 140]$ GeV/ c^2 . The mass peak is fitted with a Voigtian at the Z peak. The passing and failing background is fit to an exponential. The efficiency of the muon inner-track reconstruction is estimated to be $99.8 \pm 0.4\%$ (stat) from the fit using the Z boson as seen in Figure B.11. For MC, the reconstruction efficiency is measured

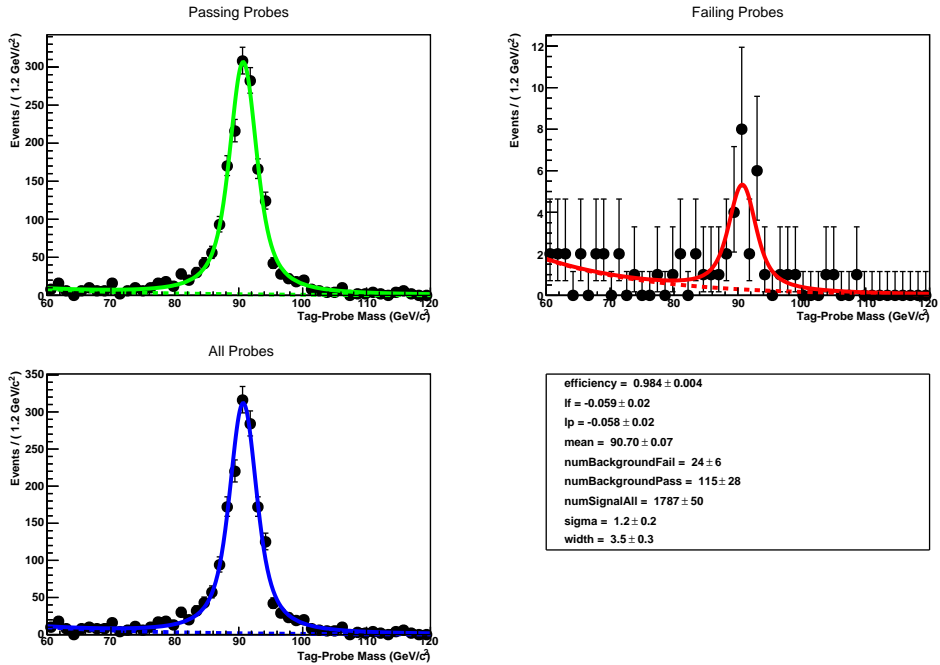


Figure B.9: DiMuon: A plot of the overall muon ID efficiency as measured by tag and probe in $p + p$ data. (top left) “Passing Probes”, (top right) “Failing Probes”, (bottom left) “All Probes”, (bottom right) details of the fit.

to be 99.0%, as seen in Figure B.12. The functions for fitting MC and data are the same.

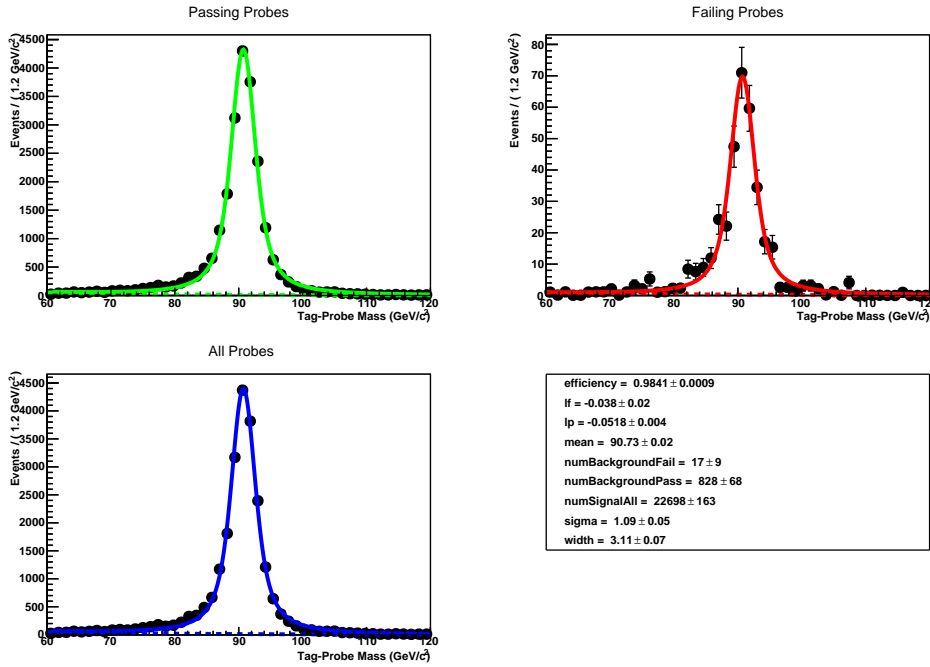


Figure B.10: DiMuon: A plot of the overall muon ID efficiency as measured by tag and probe in $p + p$ MC. (top left) “Passing Probes”, (top right) “Failing Probes”, (bottom left) “All Probes”, (bottom right) details of the fit. The kinematic range for the muons is $p_T > 20$ GeV/ c , $|\eta| < 2.4$.

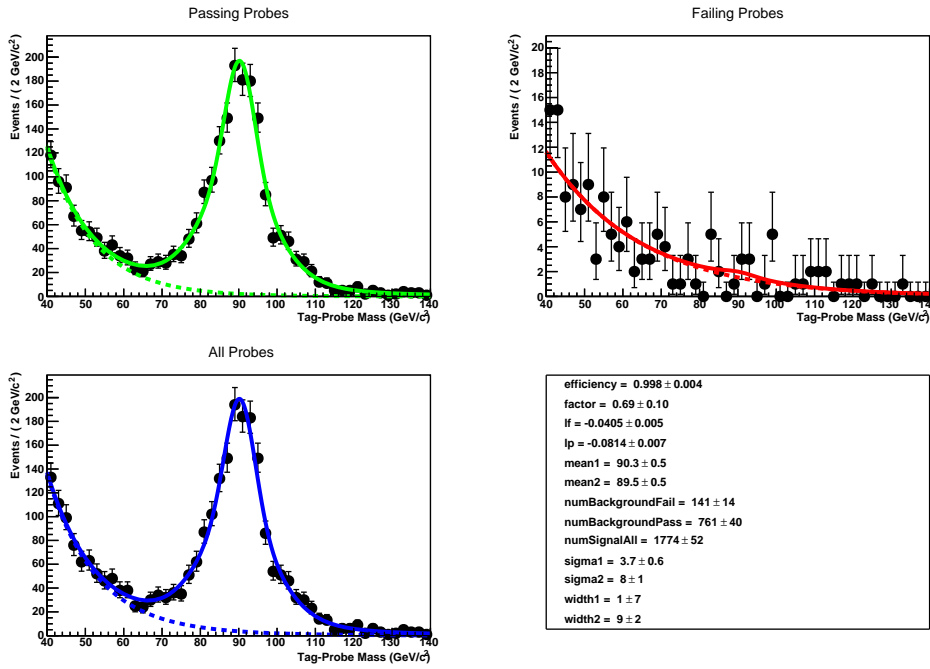


Figure B.11: DiMuon: A plot of the overall muon inner-track reconstruction efficiency as measured by tag and probe in $p + p$ data. (top left) “Passing Probes”, (top right) “Failing Probes”, (bottom left) “All Probes”, (bottom right) details of the fit. The kinematic range for the muons is $p_T > 20$ GeV/ c , $|\eta| < 2.4$.

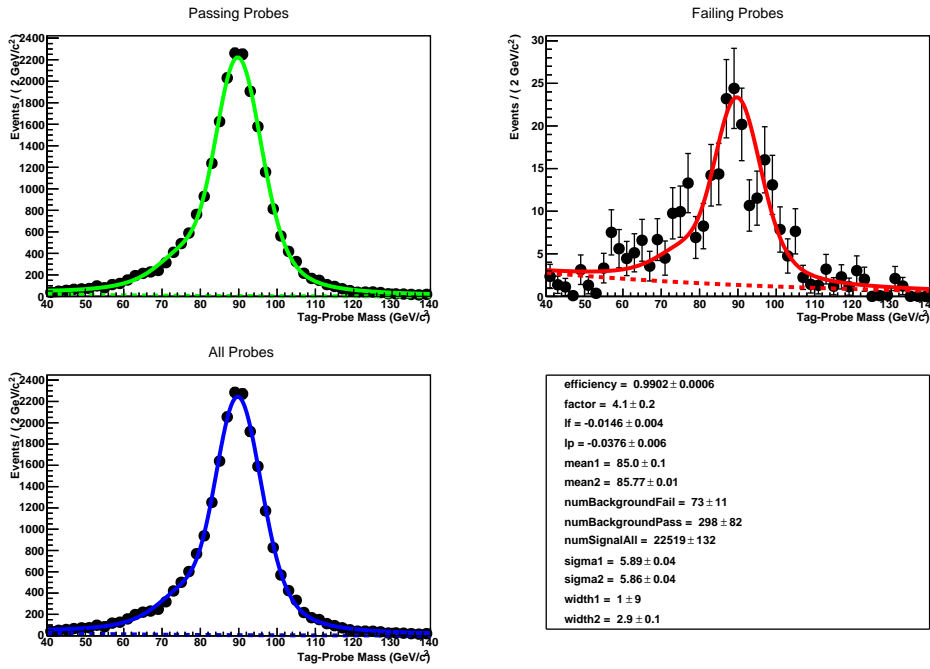


Figure B.12: DiMuon: A plot of the overall muon inner-track reconstruction efficiency as measured by tag and probe in $p + p$ MC. (top left) “Passing Probes”, (top right) “Failing Probes”, (bottom left) “All Probes”, (bottom right) details of the fit. The kinematic range for the muons is $p_T > 20$ GeV/ c , $|\eta| < 2.4$.

B.3 Tag and Probe Mass Plots - Electrons in Pb+Pb

In the dielectron channel in Pb+Pb, there is a measurement of the trigger efficiency, electron ID efficiency, and reconstruction efficiency.

Trigger Efficiency - Electrons in Pb+Pb

The mass range used in the fit is $M \in [60, 120]$ GeV/c^2 and the mass peak is fitted with a Breit-Wigner function convolved with a Crystal-Ball function for the passing and failing signal. The convolution with the Crystal-Ball function is done in order to reflect the energy loss experienced by the electron passing through the detector. The passing and failing background is fit with an exponential. The efficiency of the trigger is estimated to be $98.3 \pm 0.7\%$ (stat) from the fit using Z in real data for the trigger we are using.

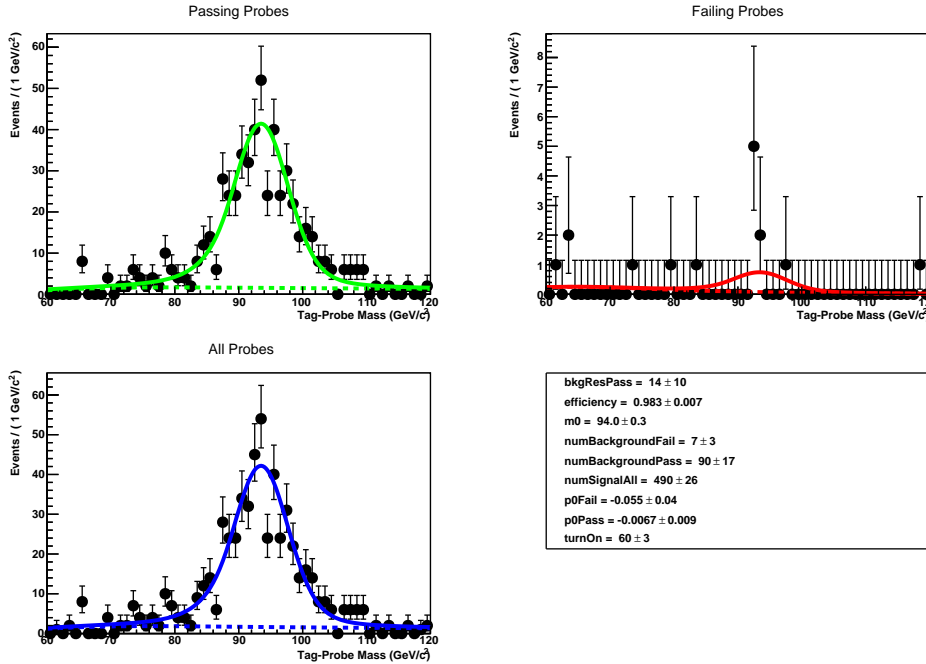


Figure B.13: DiElectron: A plot of the overall trigger efficiency as measured by tag and probe in Pb+Pb data. (top left) “Passing Probes”, (top right) “Failing Probes”, (bottom left) “All Probes”, (bottom right) details of the fit. The kinematic range for the electrons is $p_T > 20$ GeV/c , $|\eta| < 1.44$.

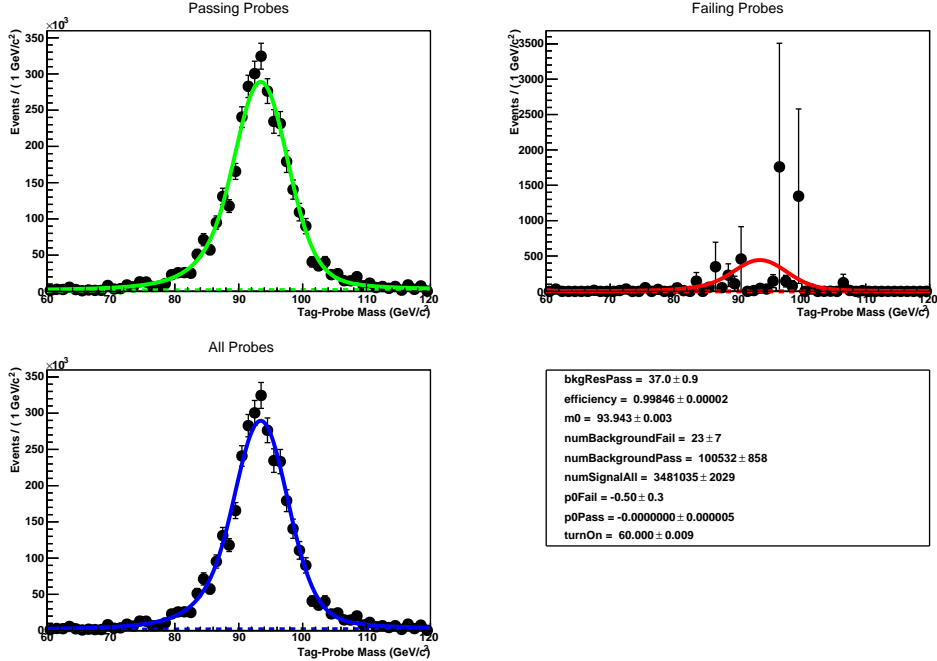


Figure B.14: DiElectron: A plot of the overall trigger efficiency as measured by tag and probe in Pb+Pb MC. (top left) “Passing Probes”, (top right) “Failing Probes”, (bottom left) “All Probes”, (bottom right) details of the fit. The kinematic range for the electrons is $p_T > 20$ GeV/ c , $|\eta| < 1.44$.

Electron ID Efficiency - Electrons in Pb+Pb

The mass range used in the fit is $M \in [60, 120]$ GeV/ c^2 and the mass peak is fitted with a Breit-Wigner function convolved with a Crystal-Ball function for the passing and failing signal. The passing and failing background is fit to an exponential. The efficiency of the electron matching and identification is estimated to be $89.8 \pm 2.7\%$ (stat) from the fit using Z in real data.

Inner-Track Reconstruction Efficiency - Electrons in Pb+Pb

Due to the poorer resolution of the super cluster kinematics, the mass range used in the fit is $\in [40, 140]$ GeV/ c^2 and the mass peak is fitted with a Breit-Wigner function convolved with a Crystal-Ball function. The passing and failing background is fit to an Exponential times a turn-on curve. The efficiency of the electron reconstruction is estimated to be $84.4 \pm 2.4\%$ (stat) from the fit using Z in real data.

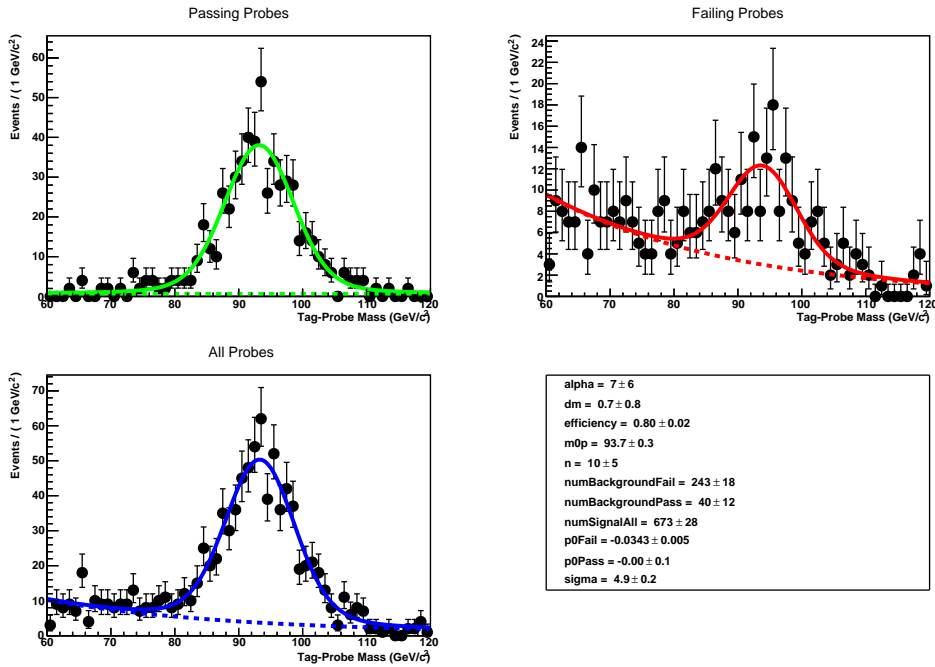


Figure B.15: DiElectron: A plot of the overall electron identification efficiency as measured by tag and probe in Pb+Pb data. (top left) “Passing Probes”, (top right) “Failing Probes”, (bottom left) “All Probes”, (bottom right) details of the fit. The kinematic range for the electrons is $p_T > 20$ GeV/ c , $|\eta| < 1.44$.

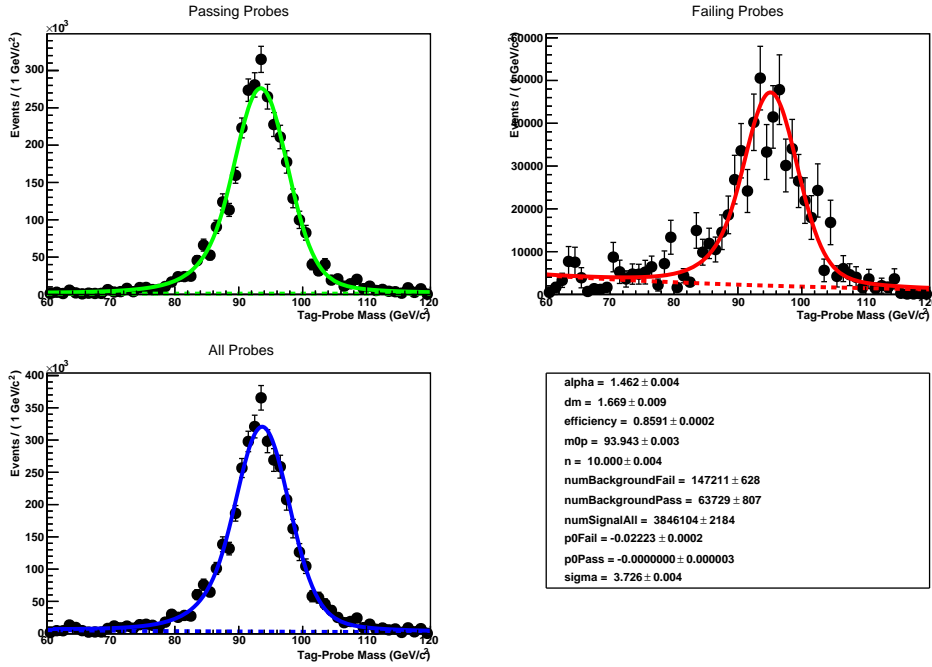


Figure B.16: DiElectron: A plot of the overall electron identification efficiency as measured by tag and probe in Pb+Pb MC. (top left) “Passing Probes”, (top right) “Failing Probes”, (bottom left) “All Probes”, (bottom right) details of the fit. The kinematic range for the electrons is $p_T > 20$ GeV/ c , $|\eta| < 1.44$.

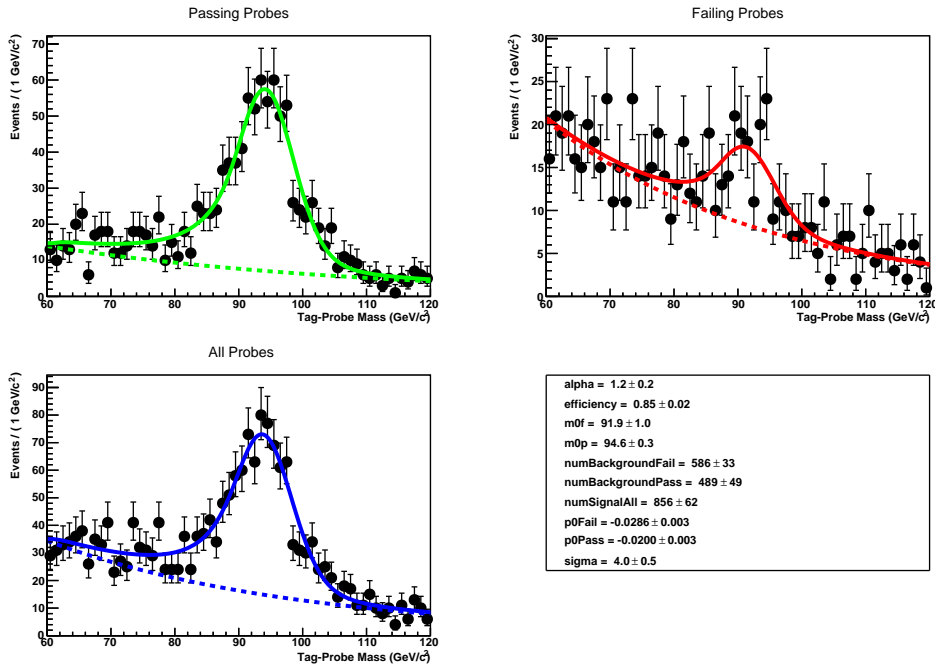


Figure B.17: DiElectron: A plot of the overall electron track reconstruction efficiency as measured by tag and probe in Pb+Pb data. (top left) “Passing Probes”, (top right) “Failing Probes”, (bottom left) “All Probes”, (bottom right) details of the fit. The kinematic range for the electrons is $p_T > 20 \text{ GeV}/c$, $|\eta| < 1.44$.

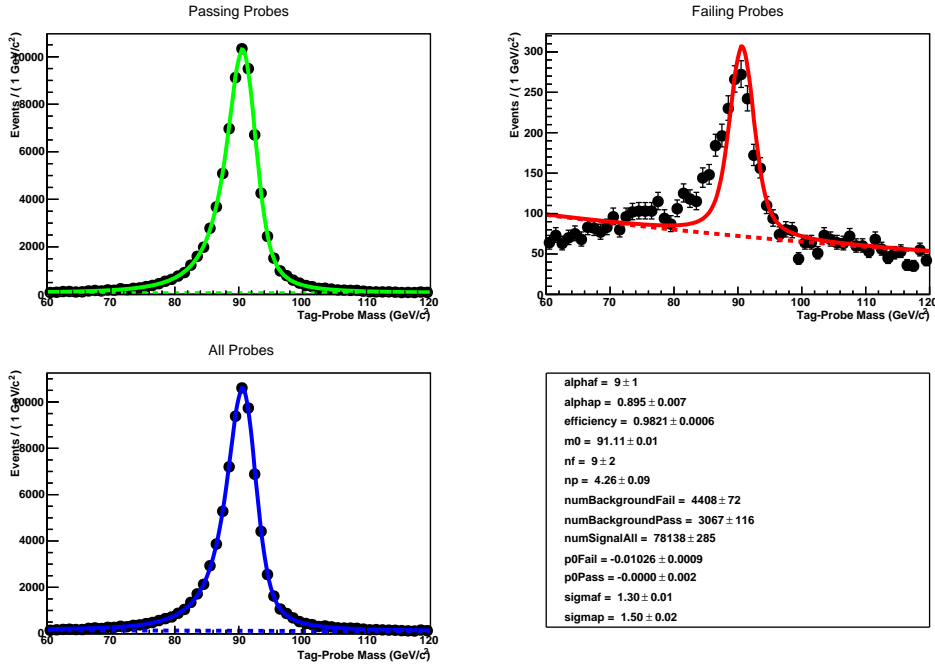


Figure B.18: DiElectron: A plot of the overall electron track reconstruction as measured by tag and probe in Pb+Pb MC. (top left) “Passing Probes”, (top right) “Failing Probes”, (bottom left) “All Probes”, (bottom right) details of the fit. The kinematic range for the electrons is $p_T > 20$ GeV/ c , $|\eta| < 1.44$.

B.4 Tag and Probe Mass Plots - Electrons in $p + p$

In the dielectron channel in $p + p$, there is a measurement of the trigger efficiency, electron ID efficiency, and reconstruction efficiency.

Trigger Efficiency - Electrons in $p + p$

The mass range used in the fit is $M \in [60, 120]$ GeV/c^2 and the mass peak is fitted with a Breit-Wigner function convolved with a Crystal-Ball function for the passing and failing signal. The passing and failing background is fit with an exponential. The efficiency of the trigger is estimated to be $99.6 \pm 0.4\%$ (stat) from the fit using Z in real data for the trigger we are using.

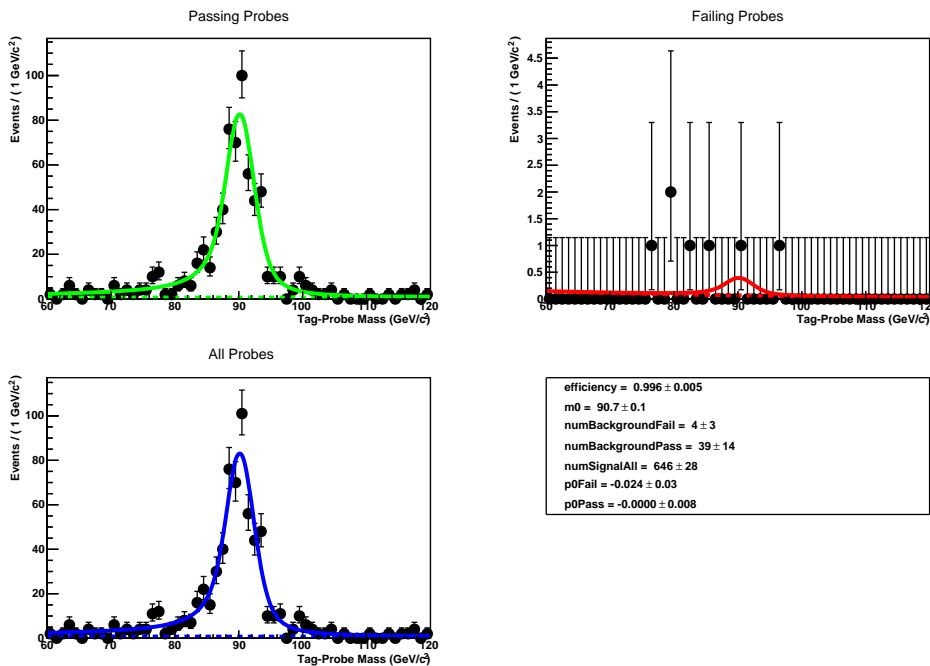


Figure B.19: DiElectron: A plot of the overall trigger efficiency as measured by tag and probe in $p + p$ data. (top left) “Passing Probes”, (top right) “Failing Probes”, (bottom left) “All Probes”, (bottom right) details of the fit. The kinematic range for the electrons is $p_T > 20$ GeV/c , $|\eta| < 1.44$.

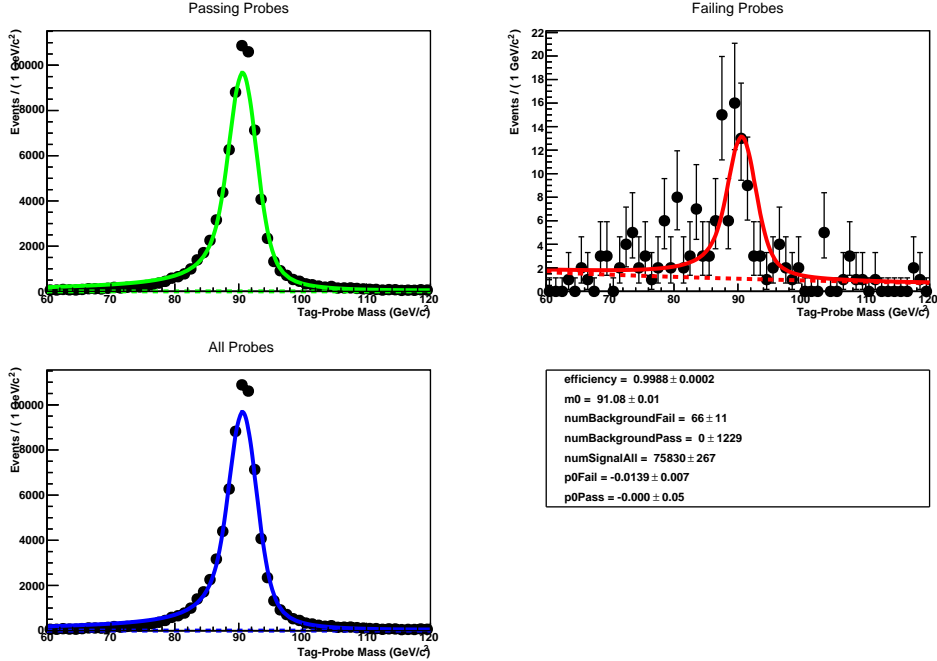


Figure B.20: DiElectron: A plot of the overall trigger efficiency as measured by tag and probe in $p + p$ MC. (top left) “Passing Probes”, (top right) “Failing Probes”, (bottom left) “All Probes”, (bottom right) details of the fit. The kinematic range for the electrons is $p_T > 20$ GeV/ c , $|\eta| < 1.44$.

Electron ID Efficiency - Electrons in $p + p$

The mass range used in the fit is $M \in [60, 120]$ GeV/ c^2 and the mass peak is fitted with a Breit-Wigner function convolved with a Crystal-Ball function for the passing and failing signal. The passing and failing background is fit to an exponential. The efficiency of the electron matching and identification is estimated to be $89.8 \pm 2.7\%$ (stat) from the fit using Z in real data.

Inner-Track Reconstruction Efficiency - Electrons in $p + p$

Due to the poorer resolution of the super cluster kinematics, the mass range used in the fit is $\in [40, 140]$ GeV/ c^2 and the mass peak is fitted with a Breit-Wigner function convolved with a Crystal-Ball function. The passing and failing background is fit to an Exponential times a turn-on curve. The efficiency of the electron reconstruction is estimated to be $84.4 \pm 2.4\%$ (stat) from the fit using Z in real data.

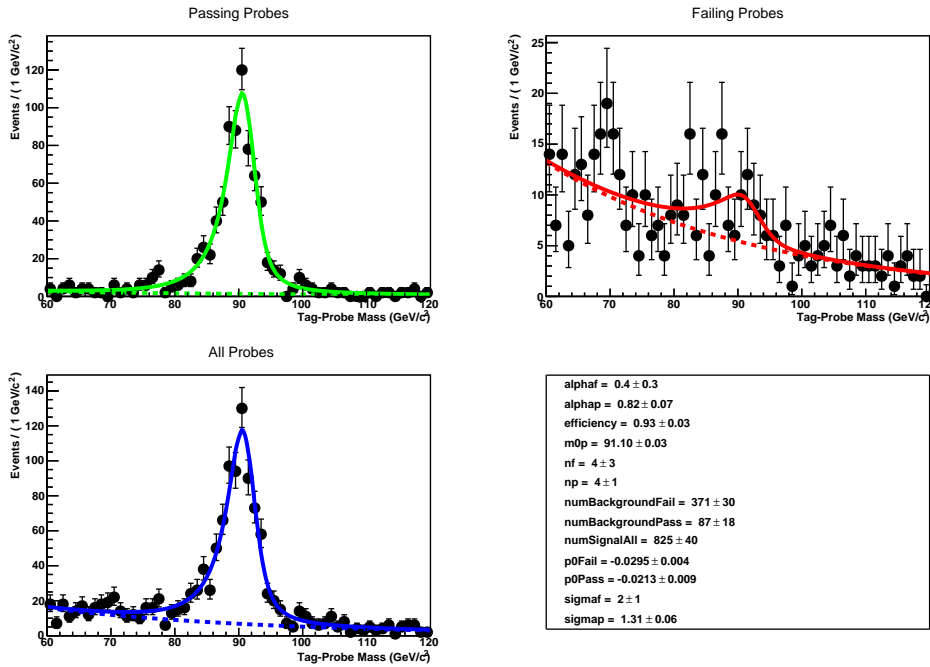


Figure B.21: DiElectron: A plot of the overall electron identification efficiency as measured by tag and probe in $p + p$ data. (top left) “Passing Probes”, (top right) “Failing Probes”, (bottom left) “All Probes”, (bottom right) details of the fit. The kinematic range for the electrons is $p_T > 20$ GeV/ c , $|\eta| < 1.44$.

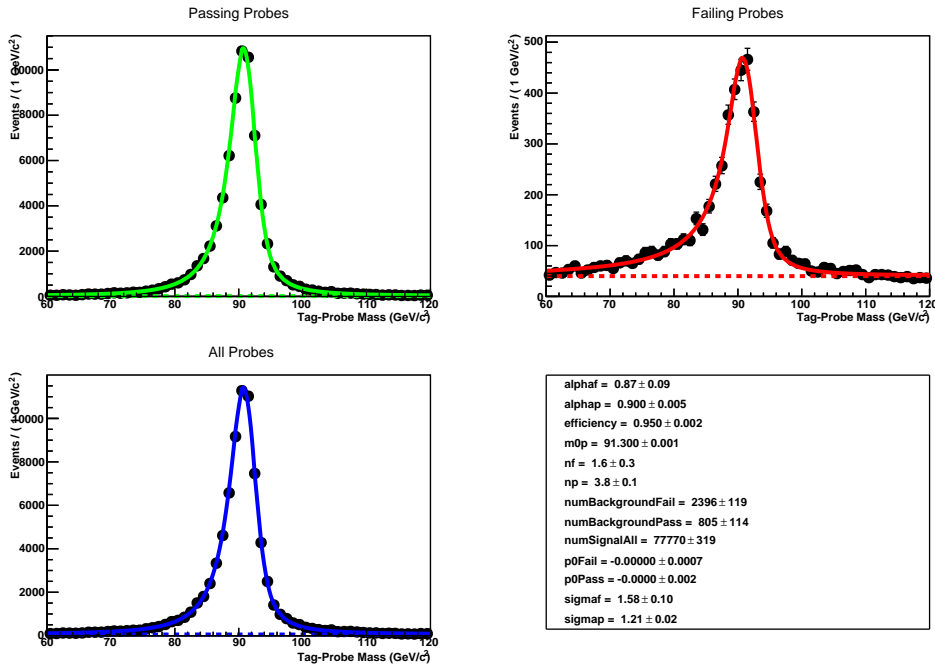


Figure B.22: DiElectron: A plot of the overall electron identification efficiency as measured by tag and probe in $p + p$ MC. (top left) “Passing Probes”, (top right) “Failing Probes”, (bottom left) “All Probes”, (bottom right) details of the fit. The kinematic range for the electrons is $p_T > 20$ GeV/ c , $|\eta| < 1.44$.

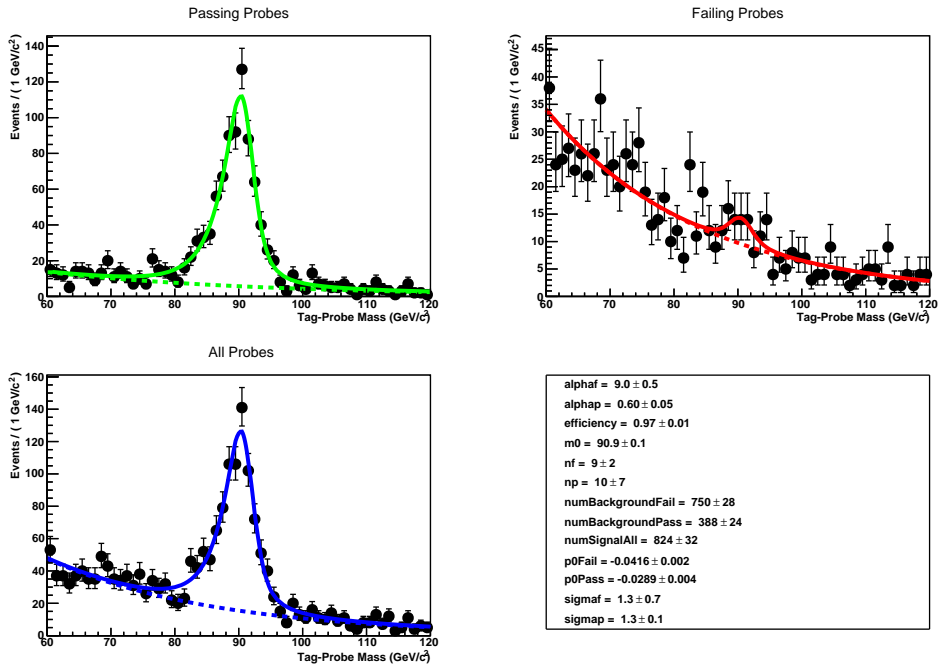


Figure B.23: DiElectron: A plot of the overall electron track reconstruction efficiency as measured by tag and probe in $p + p$ data. (top left) “Passing Probes”, (top right) “Failing Probes”, (bottom left) “All Probes”, (bottom right) details of the fit. The kinematic range for the electrons is $p_T > 20 \text{ GeV}/c$, $|\eta| < 1.44$.

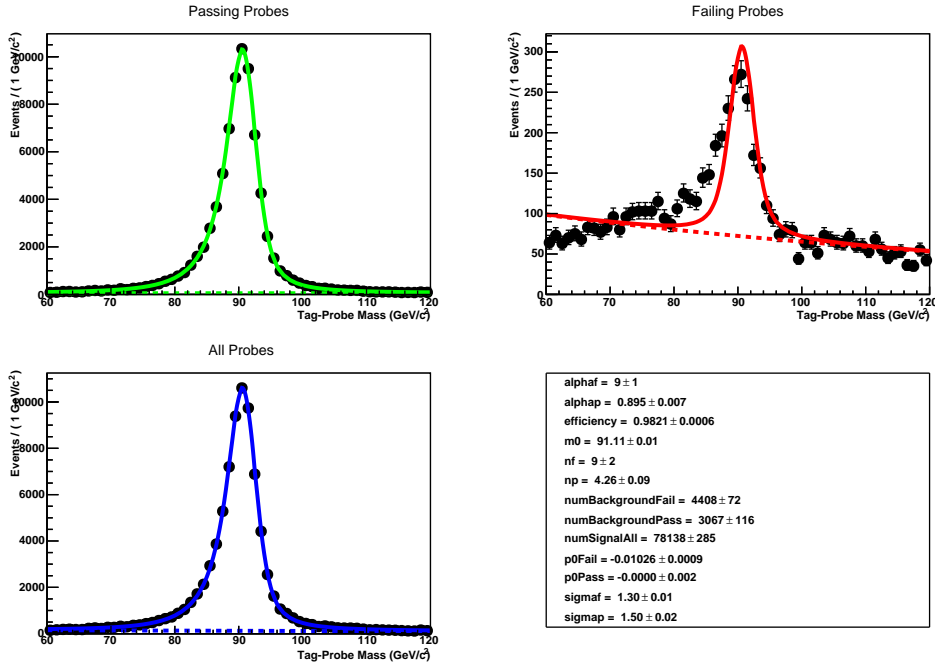


Figure B.24: DiElectron: A plot of the overall electron track reconstruction as measured by tag and probe in $p + p$ MC. (top left) “Passing Probes”, (top right) “Failing Probes”, (bottom left) “All Probes”, (bottom right) details of the fit. The kinematic range for the electrons is $p_T > 20$ GeV/ c , $|\eta| < 1.44$.

Bibliography

- [1] G. Arnison *et al.*, “Experimental Observation of Lepton Pairs of Invariant Mass Around 95 GeV/ c^2 at the CERN SPS Collider,” *Phys. Lett. B*, vol. 126, p. 398, 1983.
- [2] P. Bagnaia *et al.*, “Evidence for $Z \rightarrow e^+e^-$ at the CERN $\bar{p}p$ collider,” *Phys. Lett. B*, vol. 129, p. 130, 1983.
- [3] S. Schael *et al.*, “Electroweak Measurements in Electron-Positron Collisions at W -Boson-Pair Energies at LEP,” *Phys. Rept.*, vol. 532, p. 119, 2013.
- [4] S. Schael *et al.*, “Precision electroweak measurements on the Z resonance,” *Phys. Rept.*, vol. 427, pp. 257–454, 2006.
- [5] D. Acosta *et al.*, “First measurements of inclusive W and Z cross sections from Run II of the Tevatron collider,” *Phys. Rev. Lett.*, vol. 94, p. 091803, 2005.
- [6] S. Abachi *et al.*, “ W and Z boson production in $p\bar{p}$ collisions at $\sqrt{s} = 1.8$ TeV,” *Phys. Rev. Lett.*, vol. 75, p. 1456, 1995.
- [7] S. Chatrchyan *et al.*, “Measurement of the Inclusive W and Z Production Cross Sections in $p + p$ Collisions at $\sqrt{s} = 7$ TeV,” *JHEP*, vol. 1110, p. 132, 2011.
- [8] S. Chatrchyan *et al.*, “Measurement of the Rapidity and Transverse Momentum Distributions of Z Bosons in $p + p$ Collisions at $\sqrt{s} = 7$ TeV,” *Phys. Rev. D*, vol. 85, p. 032002, 2012.
- [9] S. Chatrchyan *et al.*, “Measurement of inclusive W and Z boson production cross sections in $p + p$ collisions at $\sqrt{s} = 8$ TeV,” *Phys. Rev. Lett.*, vol. 112, p. 191802, 2014.

- [10] G. Aad *et al.*, “Measurement of the inclusive W^\pm and Z/γ^* cross sections in the electron and muon decay channels in pp collisions at $\sqrt{s} = 7$ TeV with the ATLAS detector,” *Phys. Rev. D*, vol. 85, p. 072004, 2012.
- [11] V. Kartvelishvili, R. Kvatadze, and R. Shanidze, “On Z and Z +jet production in heavy-ion collisions,” *Phys. Lett. B*, vol. 356, p. 589, 1995.
- [12] G. Kunde, H. van Hecke, K. Hessler, and C. Mironov, “ Z -tagged quark jets at the Large Hadron Collider,” *Eur. Phys. J. C*, vol. 61, no. 4, pp. 785–788, 2009.
- [13] R. Neufeld, I. Vitev, and B.-W. Zhang, “The Physics of Z/γ^* -tagged jets at the LHC,” *Phys. Rev. C*, vol. 83, p. 034902, 2011.
- [14] H. Paukkunen and C. A. Salgado, “Constraints for the nuclear parton distributions from Z and W production at the LHC,” *JHEP*, vol. 1103, p. 071, 2011.
- [15] R. Neufeld, I. Vitev, and B.-W. Zhang, “A possible determination of the quark radiation length in cold nuclear matter,” *Phys. Lett. B*, vol. 704, p. 590, 2011.
- [16] R. Vogt, “Shadowing effects on vector boson production,” *Phys. Rev. C*, vol. 64, p. 044901, 2001.
- [17] S. Chatrchyan *et al.*, “Study of Z boson production in Pb+Pb collisions at $\sqrt{s_{NN}} = 2.76$ TeV,” *Phys. Rev. Lett.*, vol. 106, p. 212301, 2011.
- [18] S. Chatrchyan *et al.*, “Study of W boson production in Pb+Pb and $p+p$ collisions at $\sqrt{s_{NN}} = 2.76$ TeV,” *Phys. Lett. B*, vol. 715, p. 66, 2012.
- [19] S. Chatrchyan *et al.*, “Measurement of isolated photon production in $p+p$ and Pb+Pb collisions at $\sqrt{s_{NN}} = 2.76$ TeV,” *Phys. Lett. B*, vol. 710, p. 256, 2012.
- [20] P. W. Higgs, “Broken Symmetries and the Masses of Gauge Bosons,” *Phys. Rev. Lett.*, vol. 13, pp. 508–509, Oct 1964.
- [21] F. Englert and R. Brout, “Broken Symmetry and the Mass of Gauge Vector Mesons,” *Phys. Rev. Lett.*, vol. 13, pp. 321–323, Aug 1964.

- [22] S. Chatrchyan *et al.*, “Observation of a new boson at a mass of 125 GeV with the CMS experiment at the LHC,” *Phys. Lett. B*, vol. 716, no. 1, pp. 30 – 61, 2012.
- [23] G. Aad *et al.*, “Observation of a new particle in the search for the Standard Model Higgs boson with the ATLAS detector at the LHC,” *Phys. Lett. B*, vol. 716, no. 1, pp. 1 – 29, 2012.
- [24] M. W. Commons, “Wikipedia, File:Standard Model of Elementary Particles.svg,” 2006.
- [25] S. L. Glashow, “Partial-symmetries of weak interactions,” *Nucl. Phys.*, vol. 22, pp. 579–588, Feb. 1961.
- [26] A. Salam and J. Ward, “Weak and Electromagnetic Interactions,” *Il Nuovo Cimento Series 10*, vol. 11, no. 4, pp. 568–577, 1959.
- [27] S. Weinberg, “A Model of Leptons,” *Phys. Rev. Lett.*, vol. 19, pp. 1264–1266, Nov 1967.
- [28] F. Hasert *et al.*, “Observation of Neutrino Like Interactions Without Muon Or Electron in the Gargamelle Neutrino Experiment,” *Phys. Lett. B*, vol. 46, pp. 138–140, 1973.
- [29] G. Arnison *et al.*, “Experimental Observation of Isolated Large Transverse Energy Electrons with Associated Missing Energy at $\sqrt{s} = 540$ GeV,” *Phys. Lett. B*, vol. 122, pp. 103–116, 1983.
- [30] G. Arnison *et al.*, “Experimental observation of lepton pairs of invariant mass around 95 GeV/ c^2 at the CERN SPS collider,” *Phys. Lett. B*, vol. 126, no. 5, pp. 398 – 410, 1983.
- [31] J. Beringer *et al.*, “Review of Particle Physics,” *Phys. Rev. D*, vol. 86, p. 010001, 2012.
- [32] S. Bethke, “World Summary of α_s (2012),” *Nucl. Phys. Proc. Suppl.*, vol. 234, pp. 229–234, 2013.
- [33] T. Matsui and H. Satz, “J/ ψ -Suppression by Quark-Gluon Plasma Formation,” *Phys. Lett. B*, vol. 178, no. 4, pp. 416–422, 1986.
- [34] S. Chatrchyan *et al.*, “Observation of sequential Upsilon suppression in Pb+Pb collisions,” *Phys. Rev. Lett.*, vol. 109, p. 222301, 2012.

- [35] L. Adamczyk *et al.*, “Suppression of Upsilon Production in d+Au and Au+Au Collisions at $\sqrt{s_{NN}} = 200$ GeV,” *Phys. Lett. B*, vol. 735, p. 127, 2014.
- [36] S. Digal, P. Petreczky, and H. Satz, “Quarkonium feed down and sequential suppression,” *Phys. Rev. D*, vol. 64, p. 094015, 2001.
- [37] A. Ali and G. Kramer, “Jets and QCD: A Historical Review of the Discovery of the Quark and Gluon Jets and its Impact on QCD,” *Eur. Phys. J. H*, vol. 36, pp. 245–326, 2011.
- [38] R. Hwa and X. Wang, *Quark-Gluon Plasma 4*, ch. Energy Loss in a Strongly Coupled Thermal Medium and the Gauge-String Duality. World Scientific Publishing Company, Incorporated, 2010.
- [39] J. Adams *et al.*, “Evidence from d+Au measurements for final state suppression of high p_T hadrons in Au+Au collisions at RHIC,” *Phys. Rev. Lett.*, vol. 91, p. 072304, 2003.
- [40] S. Chatrchyan *et al.*, “Observation and studies of jet quenching in Pb+Pb collisions at $\sqrt{s_{NN}} = 2.76$ TeV,” *Phys. Rev. C*, vol. 84, p. 024906, 2011.
- [41] S. Chatrchyan *et al.*, “Observation of a new boson at a mass of 125 GeV with the CMS experiment at the LHC,” *Phys. Lett. B*, vol. 716, pp. 30–61, 2012.
- [42] M. L. Miller, K. Reygers, S. J. Sanders, and P. Steinberg, “Glauber modeling in high energy nuclear collisions,” *Ann. Rev. Nucl. Part. Sci.*, vol. 57, p. 205, 2007.
- [43] A. Martin, W. Stirling, R. Thorne, and G. Watt, “Parton distributions for the LHC,” *Eur. Phys. J. C*, vol. 63, pp. 189–285, 2009.
- [44] K. Eskola, H. Paukkunen, and C. Salgado, “EPS09: A New Generation of NLO and LO Nuclear Parton Distribution Functions,” *JHEP*, vol. 0904, p. 065, 2009.
- [45] A. Adames *et al.*, “Shadowing in inelastic scattering of muons on carbon, calcium and lead at low x_{Bj} ,” *Zeit. für Phy. C Part. Fiel.*, vol. 67, no. 3, 1995.
- [46] D. A. *et al.*, “Nuclear dependence of dimuon production at 800 gev,” *Phys. Rev. Lett.*, vol. 64, pp. 2479–2482, May 1990.

- [47] P. Amaudruz *et al.*, “A Reevaluation of the nuclear structure function ratios for D, He, Li-6, C and Ca,” *Nucl. Phys. B*, vol. 441, pp. 3–11, 1995.
- [48] M Arneodo *et al.*, “The A dependence of the nuclear structure function ratios,” *Nucl. Phys. B*, vol. 481, no. 12, pp. 3 – 22, 1996.
- [49] J J Aubert *et al.*, “The ratio of the nucleon structure functions $F2_n$ for iron and deuterium,” *Phys. Lett. B*, vol. 123, p. 275, 1983.
- [50] J Seely *et al.*, “New Measurements of the European Muon Collaboration Effect in Very Light Nuclei,” *Phys. Rev. Lett.*, vol. 103, p. 202301, Nov 2009.
- [51] L Weinstein *et al.*, “Short Range Correlations and the EMC Effect,” *Phys. Rev. Lett.*, vol. 106, p. 052301, 2011.
- [52] A. Accardi, N. Armesto, M. Botje, S. Brodsky, B. Cole, *et al.*, “Hard probes in heavy-ion collisions at the LHC: pdfs, shadowing and p+A collisions,” 2004.
- [53] R. Vogt, “Shadowing and absorption effects on J/psi production in d+A collisions,” *Phys. Rev. C*, vol. 71, p. 054902, 2005.
- [54] G. Aad *et al.*, “The ATLAS Experiment at the CERN Large Hadron Collider,” *JINST*, vol. 3, p. S08003, 2008.
- [55] K. Aamodt *et al.*, “The ALICE experiment at the CERN LHC,” *JINST*, vol. 3, p. S08002, 2008.
- [56] S. Chatrchyan *et al.*, “The CMS experiment at the CERN LHC,” *JINST*, vol. 3, p. S08004, 2008.
- [57] J. Alves, A. Augusto *et al.*, “The LHCb Detector at the LHC,” *JINST*, vol. 3, p. S08005, 2008.
- [58] L. Evans and P. Bryant, “LHC Machine,” *JINST*, vol. 3, p. S08001, 2008.
- [59] S. Chatrchyan *et al.*, “Energy calibration and resolution of the CMS electromagnetic calorimeter in $p + p$ collisions at $\sqrt{s} = 7$ TeV,” *JINST*, vol. 8, p. P09009, 2013.

- [60] J. Pilot, “Photographs of CMS,” July 2013.
- [61] T. McCauley and L. Taylor, “CMS Higgs Search in 2011 and 2012 data: candidate ZZ event (8 TeV) with two electrons and two muons.” CMS Collection., Jul 2012.
- [62] CMS Collaboration, “CMS collision events: first lead ion collisions.” CMS Collection., Nov 2010.
- [63] T. McCauley, “CMS collision events: candidate Upsilon’s in heavy-ion collisions - Dec 2010.” CMS Collection., May 2011.
- [64] CMS Collaboration, “CMS collision events: first Z bosons detected in heavy-ion collisions.” CMS Collection., Nov 2010.
- [65] T. Dahms, “Quarkonia and heavy-flavour production in CMS,” *Nucl. Phys. A*, vol. 910-911, no. 0, pp. 91 – 97, 2013. Hard Probes 2012 5th International Conference on Hard and Electromagnetic Probes of High-Energy Nuclear Collisions.
- [66] B. Alver, M. Baker, C. Loizides, and P. Steinberg, “The PHOBOS Glauber Monte Carlo,” 2008.
- [67] CMS Collaboration, “Luminosity Calibration for the 2013 Proton-Lead and Proton-Proton Data Taking,” CMS Physics Analysis Summary CMS-PAS-LUM-13-002, 2013.
- [68] S. Chatrchyan *et al.*, “Dependence on pseudorapidity and centrality of charged hadron production in PbPb collisions at a nucleon-nucleon centre-of-mass energy of 2.76 TeV,” *JHEP*, vol. 1108, p. 141, 2011.
- [69] J. Beringer *et al.*, “Review of Particle Physics,” *Phys. Rev. D*, vol. 86, p. 010001, 2012.
- [70] T. Sjostrand, S. Mrenna, and P. Z. Skands, “PYTHIA 6.4 Physics and Manual,” *JHEP*, vol. 0605, p. 026, 2006.
- [71] S. Agostinelli *et al.*, “GEANT4: A Simulation toolkit,” *Nucl. Instrum. Meth.*, vol. A506, p. 250, 2003.

- [72] I. Lokhtin and A. Snigirev, “A Model of jet quenching in ultrarelativistic heavy-ion collisions and high- p_T hadron spectra at RHIC,” *Eur. Phys. J. C*, vol. 45, p. 211, 2006.
- [73] W. Adam, R. Fruhwirth, A. Strandlie, and T. Todorov, “Reconstruction of electrons with the Gaussian sum filter in the CMS tracker at LHC,” *eConf*, vol. C0303241, p. TULT009, 2003.
- [74] CMS Collaboration, “Electron reconstruction and identification at $\sqrt{s} = 7$ TeV,” CMS Physics Analysis Summary CMS-PAS-EGM-10-004, 2010.
- [75] D0 Collaboration, “ $ZZ \rightarrow l^+l^- \nu\bar{\nu}$ production in $p\bar{p}$ collisions at $\sqrt{s} = 1.96$ TeV,” *FERMILAB-PUB-08-267-E*, 2008.
- [76] J. Massey, Frank J., “The Kolmogorov-Smirnov Test for Goodness of Fit,” *Jour. Am. Stat. Assoc.*, vol. 46, no. 253, pp. pp. 68–78, 1951.
- [77] B. W. Commons, “Wikipedia, File:KS Example.png,” 2013.
- [78] S. Chatrchyan *et al.*, “Suppression of non-prompt J/ψ , prompt J/ψ , and $\Upsilon(1S)$ in Pb+Pb collisions at $\sqrt{s_{NN}} = 2.76$ TeV,” *JHEP*, vol. 1205, p. 063, 2012.
- [79] CMS Collaboration, “Quarkonium production in Pb+Pb collisions,” CMS Note AN 2011/062, 2011.
- [80] I. Shipsey, N. Leonardo et al (for the Upsilon team), “Measurement of the inclusive Upsilon production cross section in $p + p$ collisions at $\sqrt{s} = 7$ TeV,” CMS Note 2010/040, 2010.
- [81] J. Olivero and R. Longbothum, “Empirical fits to the voigt line width: A brief review,” *Jour. Quant. Spec. Rad. Tran.*, vol. 17, no. 2, pp. 233 – 236, 1977.
- [82] G. Petrucciani and L. Perrozzi, “Private Communication.”
- [83] S. Catani, L. Cieri, G. Ferrera, D. de Florian, and M. Grazzini, “Vector boson production at hadron colliders: a fully exclusive QCD calculation at NNLO,” *Phys. Rev. Lett.*, vol. 103, p. 082001, 2009.

- [84] L. Lyons, D. Gibaut, and P. Clifford, “How to Combine Correlated Estimates of a Single Physical Quantity,” *Nucl. Instrum. Meth.*, vol. A270, p. 110, 1988.